

LEABHARLANN CHOLÁISTE NA TRÍONÓIDE, BAILE ÁTHA CLIATH | TRINITY COLLEGE LIBRARY DUBLIN
Ollscoil Átha Cliath | The University of Dublin

Terms and Conditions of Use of Digitised Theses from Trinity College Library Dublin

Copyright statement

All material supplied by Trinity College Library is protected by copyright (under the Copyright and Related Rights Act, 2000 as amended) and other relevant Intellectual Property Rights. By accessing and using a Digitised Thesis from Trinity College Library you acknowledge that all Intellectual Property Rights in any Works supplied are the sole and exclusive property of the copyright and/or other IPR holder. Specific copyright holders may not be explicitly identified. Use of materials from other sources within a thesis should not be construed as a claim over them.

A non-exclusive, non-transferable licence is hereby granted to those using or reproducing, in whole or in part, the material for valid purposes, providing the copyright owners are acknowledged using the normal conventions. Where specific permission to use material is required, this is identified and such permission must be sought from the copyright holder or agency cited.

Liability statement

By using a Digitised Thesis, I accept that Trinity College Dublin bears no legal responsibility for the accuracy, legality or comprehensiveness of materials contained within the thesis, and that Trinity College Dublin accepts no liability for indirect, consequential, or incidental, damages or losses arising from use of the thesis for whatever reason. Information located in a thesis may be subject to specific use constraints, details of which may not be explicitly described. It is the responsibility of potential and actual users to be aware of such constraints and to abide by them. By making use of material from a digitised thesis, you accept these copyright and disclaimer provisions. Where it is brought to the attention of Trinity College Library that there may be a breach of copyright or other restraint, it is the policy to withdraw or take down access to a thesis while the issue is being resolved.

Access Agreement

By using a Digitised Thesis from Trinity College Library you are bound by the following Terms & Conditions. Please read them carefully.

I have read and I understand the following statement: All material supplied via a Digitised Thesis from Trinity College Library is protected by copyright and other intellectual property rights, and duplication or sale of all or part of any of a thesis is not permitted, except that material may be duplicated by you for your research use or for educational purposes in electronic or print form providing the copyright owners are acknowledged using the normal conventions. You must obtain permission for any other use. Electronic or print copies may not be offered, whether for sale or otherwise to anyone. This copy has been supplied on the understanding that it is copyright material and that no quotation from the thesis may be published without proper acknowledgement.

Modelling and Monitoring Geomagnetically Induced Currents in Ireland

A dissertation submitted to the University of Dublin
for the degree of Doctor of Philosophy

Seán Blake
Trinity College Dublin, September 2017

School of Physics
University of Dublin
Trinity College



Declaration

I declare that this thesis has not been submitted as an exercise for a degree at this or any other university and it is entirely my own work.

I agree to deposit this thesis in the University's open access institutional repository or allow the library to do so on my behalf, subject to Irish Copyright Legislation and Trinity College Library conditions of use and acknowledgement.

Na

Si **Date:** 27-FEB-18

Thesis 11514

For my parents

Abstract

This thesis is the first detailed study of the effects of geomagnetic storms and geomagnetically induced currents (GICs) on the Irish power network.

In order to better monitor geomagnetic storms in Ireland, a network of geomagnetic observatories (MagIE) was set up to complement Met Éireann's Valentia observatory. Two permanent magnetometer installations with realtime communications were established in Birr and Armagh to improve realtime geomagnetic coverage. Each site calculates local K-indices in near-realtime. These K-indices, along with the MagIE data can be found at www.RosseObservatory.ie. Geolectric fields were also measured in Sligo and Leitrim at temporary installations. A test magnetometer installation identified Malin Head as a suitable site for a future addition to the MagIE network.

In order to estimate how geomagnetic disturbances drive GICs in the Irish power network, a detailed high-voltage power network model was constructed. This model takes into account the types of transformers and their winding resistances. In addition, some of the substations have associated grounding resistance information, and 15 transformers have ground switches. This detailed model was subjected to a battery of tests to identify substations which are particularly susceptible to GICs. The 400 kV Moneypoint substation in the West of Ireland was found to be by far the most susceptible substation to GICs.

GICs were simulated in the Irish power network model for different recent storms using the spherical elementary current systems (SECS) method of geomagnetic field interpolation, and both the MT and thin-sheet methods of calculating surface electric fields. The detailed power

network was imposed on the electric fields and GICs were calculated at each substation. The resulting GICs were compared to measured GICs at a single transformer. It was found that the MT method of calculating electric fields coupled with a uniform 400 Ωm resistivity model gave the most accurate calculated GICs.

Using this model, the March 1989, November 1991 and October 2003 storms were simulated. A maximum GIC value of 168 A was calculated for the Moneypoint substation for the March 1989 geomagnetic storm.

Finally, an estimation of a 1-in-100 year GIC event was calculated using two methods. The first used a previously calculated estimate for a 1-in-100 year geomagnetic storm. This value was used to scale an historic storm, and a maximum GIC value of 255 A was calculated for Moneypoint. The second estimate was made by calculating 25 years of GICs from 1991 to 2015, and fitting both a power law and lognormal distribution. These fits were extrapolated to estimate a large event. The power law gave an estimate of 258 A. The same value for the lognormal distribution was a more conservative 178 A.

Acknowledgements

First and foremost, I would like to acknowledge and thank my supervisor Prof. Peter Gallagher for his enthusiasm and guidance during my research. The administrative and technical staff of the Trinity School of Physics are also deserving of praise, particulary Joe McCauley.

Colin Hogg of the DIAS Geophysics Section deserves hearty thanks for his expertise and advice on the world of geophysics, as do all of the staff of DIAS. I would also like to thank Alan Jones for his contribution to the MT portion of this project.

I sincerely thank Ciarán Beggan, Gemma Richardson and Alan Thomson of the British Geological Survey for their invaluable scientific contribution to this project, as well as their hospitality during my stays in Edinburgh. I'd like to acknowledge David Bell and the other staff of EirGrid. Without their input, this research could not exist.

I consider myself extraordinarily fortunate to be able to call all of the members of the Astrophysical Research Group (past and present) my friends as well as mere colleagues. Without our side-projects and friendship, I would have gone mad long ago.

Joan Campanyà deserves a special mention, for teaching me the mysterious ways of MT, as well as listening to my incessant complaints in his distinctly Catalan stress-free manner.

I would like to thank the rest of my family (Sarah, Alan, Juli, Mam and Dad) for their patience and support in all aspects of my life.

Finally, I would like to thank the Amy, for all of the laughter and love.

This work was funded by the Irish Research Council's Enterprise Partnership Scheme with EirGrid.

List of Publications

1. **Blake, S.P.**, Gallagher, P.T., McCauley, J., Jones, A.G., Hogg, C., Campanyà, Beggan, C.D., Thomson, A.W.P., Kelly, G.S., & Bell, D.
   "Geomagnetically Induced Currents in the Irish Power Network During Geomagnetic Storms"
   Space Weather, 2016

2. **Blake, S.P.**, Gallagher, P.T., Campanyà, Beggan, C.D., Thomson, A.W.P., Kelly, G.S., & Bell, D.
   "Complete Irish HV Power Network Model for GICs"
   in preparation, 2018

3. **Blake, S.P.**, Gallagher, P.T., Campanyà, Hogg, C., Beggan, C.D., Thomson, A.W.P., Kelly, G.S., & Bell, D.
   "GIC calculations for 25 Years in the Irish Power Network"
   in preparation, 2018

Contents

List of Figures xi

List of Tables xv

1 Introduction 1

1.1 Geomagnetically Induced Currents 1

1.2 GICs in Power Systems 5

1.2.1 Effect on Transformers 7

1.3 GIC Mitigation 9

1.4 Studying GICs 9

1.5 Aims of this Work 11

2 The Drivers of GICs 13

2.1 The Sun as a Driver for Space Weather 13

2.1.1 Solar Wind and Coronal Holes 14

2.1.2 Coronal Mass Ejections 15

2.1.3 Solar Flares 16

2.1.4 Solar Energetic Particles 18

2.2 Earth's Magnetic Environment 18

2.2.1 Magnetosphere 18

2.2.2 Ionosphere 20

2.2.3 Magnetic Reconnection 21

2.2.4 Magnetic storms and Substorms 22

2.3 Geoelectric Field Induction 23

3 Monitoring Geomagnetic Storms **26**
3.1 Origin of Magnetic Observatories 26
3.1.1 INTERMAGNET 27
3.2 The Irish Magnetometer Network (MagIE) 29
3.2.1 Equipment 31
3.2.2 Deployment 33
3.2.3 MagIE Observatories 35
3.2.4 Difficulties Encountered during MagIE Operation 39
3.3 Quantifying Geomagnetic Disturbances 41
3.3.1 K-Index 42
3.3.2 Kp-Index 45
3.3.3 Dst Index 46
3.4 Summary 47

4 Spherical Elementary Current Systems **49**
4.1 Spherical Elementary Current Systems 49
4.2 Interpolating Geomagnetic Storms in Ireland 55
4.2.1 Valentia as sole measurement for Ireland 58
4.2.2 SECS-interpolated geomagnetic field using INTERMAGNET sites only 58
4.2.3 SECS-interpolated geomagnetic field using INTERMAGNET and MagIE sites 59
4.2.4 Summary 62

5 Magnetotellurics and The Thin-Sheet Method **63**
5.1 Magnetotellurics 64
5.1.1 Description of MT 65
5.1.1.1 MT Sources 65
5.1.1.2 Maxwell's Equations 66
5.1.1.3 Assumptions of MT 67
5.1.1.4 Boundary Conditions 68
5.1.1.5 Diffusion Equations and EM Skin-Depth 68
5.1.2 MT Transfer Function and Dimensionality 71
5.1.2.1 Homogenous Earth 73

5.1.2.2 1D Earth 74
5.1.2.3 2D Earth 80
5.1.2.4 3D Earth 83
5.1.3 MT Inverse Problem 83
5.1.4 Other MT Considerations 86
5.1.5 MT Measurements in Ireland 86
5.2 The Thin-Sheet Method 89
5.2.1 The Thin-Sheet Equation 90
5.2.2 Computing the Thin-Sheet Approximation 91
5.2.3 Comparing MT and Thin-Sheet Methods 95
5.3 Summary 96

6 GIC Modelling in the Irish Power Network 99
6.1 Modelling GICs in a Power Network 99
6.1.1 Modelling Different Voltage Levels 101
6.1.2 Power Network Model Generator 102
6.2 The Irish Power Network 104
6.2.1 Irish Network Models 108
6.3 Network Sensitivity Tests 112
6.3.1 Application of Uniform Electric Field 112
6.3.1.1 Electric Field Orientation 115
6.3.2 Ground Resistance Analysis 117
6.3.3 Effect of Adding Lower Voltages to Network 122
6.3.4 Minimising GIC with Ground Switches 124
6.4 Summary 127

7 Modelling GICs During Recent Storm Events 130
7.1 Measured GIC Data in Ireland 131
7.1.1 Choosing Recent Events 132
7.1.2 Cleaning GIC Measurements 138
7.1.3 Goodness-Of-Fit Measures 139
7.2 Simple Power Network Response 139
7.3 Detailed Power Network Response 144
7.3.1 Homogenous 400 Ωm Earth 145

7.3.2 400 Ωm Earth with Conductive Sea 148
7.3.3 MT Derived Resistivity Model 152
7.4 Summary and Discussion 154

8 Simulating Historical Storm Events **157**
8.1 Historical Event Case Studies 157
8.1.1 13-14 March 1989 160
8.1.2 08-10 November 1991 163
8.1.3 29-31 October 2003 165
8.1.4 Historical Simulations Discussion 165
8.2 Extreme Event Analysis 169
8.2.1 Scaled Geomagnetic Storm 169
8.2.2 Extrapolating 25 Years of GIC Calculations 171
8.3 Extreme Event Discussion 176

9 Conclusions and Future Work **178**
9.0.1 MagIE 178
9.0.2 Power Network Modelling 179
9.0.3 Simulating GICs in Ireland During Geomagnetic Storms . . 180
9.1 Future Work 181

References **184**

List of Figures

1.1 The space weather chain of events. 2
1.2 New York Times headline on Carrington Event. 3
1.3 How GICs enter a power network. 6
1.4 Half-cycle saturation and BH curve of a transformer. 7

2.1 Interplanetary magnetic field schematic. 16
2.2 The Sun and Parker spiral. 17
2.3 The Earth's magnetosphere. 19
2.4 High altitude current systems. 21
2.5 Magnetic Reconnection 22
2.6 Geoelectric field induction 24

3.1 Carrington event in Greenwich 28
3.2 Magnetic observatory coordinate system. 29
3.3 MagIE and INTERMAGNET observatories 30
3.4 MagIE recording times 31
3.5 Lemi-417 MT kit 33
3.6 Fluxgate magnetometer schematic 34
3.7 Birr magnetometer installation 36
3.8 Armagh magnetometer installation 37
3.9 Leitrim and Sligo MT sites 38
3.10 Malin Head site 39
3.11 Magnetometer temperature at Birr 41
3.12 Lightning strike at Birr 42
3.13 Solar quiet estimation 46

3.14 K-index at Birr for St. Patrick's Day storm. 47

4.1 Sketch of spherical elementary current systems 50
4.2 Ground magnetic effect of of divergence-free elementary current . . 52
4.3 Magnetic measurements in Ireland during the 22-23 June 2015 storm. 56
4.4 SECS interpolation across Ireland 60
4.5 Measured and modelled horizontal geomagnetic field in Ireland . . . 61

5.1 Skin depth vs. resistivity and period 72
5.2 Dimensionality of subsurface 73
5.3 Four different synthetic resistivity profiles. 79
5.4 Effect 2-layer resistivity profiles on calculated E-fields. 82
5.5 Calculated E-Fields in Leitrim using homogenous and layered Earth models. 85
5.6 Resistivity of various depth intervals in the Irish geology down to 200 km as given by the MT model. 88
5.7 Thin-Sheet Earth Model 89
5.8 Effect of grid size on electric field estimates 92
5.9 Thin-sheet response using different characteristic periods. 93
5.10 Thin-sheet conductivity model for Ireland 94
5.11 Coastal effect with thin-sheet model 95
5.12 Comparison between thin-sheet and MT calculated electric field. . . 97

6.1 Two-winding and autotransformer schematics 102
6.2 Auto and two-winding transformers GIC treatment 103
6.3 Details of a substation given by the Power Network Model Generator 105
6.4 The Horton *et al.* (2012) model network 106
6.5 The Horton *et al.* (2012) GIC comparison 107
6.6 EirGrid Transmission Schematic 109
6.7 Power network models A and B 110
6.8 Response of models A and B to a uniform 1 V km^{-1} electric fields . 114
6.9 Sum of GICs in model B due to uniform electric field of varying direction 116
6.10 Peak GICs in substations to angle 116

6.11 Maximum GICs in substations per angle 117
6.12 Locations of substations with measured grounding resistance 118
6.13 Histogram of known substation grounding resistances 119
6.14 GICs due to a Northward electric field with varying grounding resistances 121
6.15 Varying GICs due to assumed grounding resistances 122
6.16 Calculated GICs when including different voltage levels 123
6.17 Proportional difference in calculated GICs when the 110 kV network is added 125
6.18 Effect of grounding and isolating 15 transformers in the network. . . 126
6.19 Isolating Substations in the Irish network one by one 127

7.1 Woodland Hall effect probe 132
7.2 Measured magnetic field in Birr during the five recent events 134
7.3 Untreated and cleaned GIC data. 136
7.4 GIC data cleaning process. 137
7.5 Measured and calculated GIC using the simple network Model A . . 141
7.6 GIC distribution in the simple power network model 143
7.7 Measured and calculated GIC using network Model B for a homogenous 400 Ωm Earth 147
7.8 Measured and calculated GIC using network Model B for a 400 Ωm Earth with a conductive sea 150
7.9 Difference in calculated GIC when the conductive sea is added to a 400 Ωm halfspace model. 151
7.10 Measured and calculated GIC using network Model B for the MT derived ground model. 153
7.11 Measured and calculated GIC in Woodland for the 27-28 March 2017 event. 155

8.1 Results for the simulation of the March 1989 storm. 159
8.2 Cumulative GIC amplitudes in Moneypoint for each of the three historical storms. 161
8.3 Results for the simulation of the November 1991 storm. 162
8.4 Results for the simulation of the October 2003 Halloween storm. . . 164

8.5 Maximum GIC and proportion of GIC per substation for each of the three historical events. 167
8.6 The ten substations which experienced the largest GICs during each of the historical events. 168
8.7 Scaled 2003 Halloween storm 170
8.8 GIC from 100-year extreme event estimate 171
8.9 Locations used for 25 year GIC simulations 172
8.10 Normalised sum of GIC values from the 25 years of simulations . . . 173
8.11 Histogram and CCDF of 25 years of GIC calculations 176

List of Tables

3.1 K-index values and limits for MagIE sites and Niemegk 44
3.2 Values for m used in FMI method. 45

4.1 Errors in interpolating geomagnetic field in Ireland. 57

6.1 Details from power network models A and B 111

7.1 Recent events chosen to test GIC calculations 133
7.2 Goodness of fit measures for the calculated GICs using network Model A. 142
7.3 Goodness of fit measures for the calculated GICs using network Model B and a 400 Ωm Earth. 146
7.4 Goodness of fit measures for the calculated GICs using network Model B and a 400 Ωm Earth with a conductive sea 149
7.5 Goodness of fit measures for the calculated GICs using network Model B and the MT derived resistivity model 152

8.1 Maximum values for historical storms 158

1 Introduction

With the ever-increasing reliance on digital and electric technologies in the last two centuries, society has become exposed to an array of potentially damaging space weather effects. These hazards include disruption to radio and GPS communications, damage to satellites, and increased radiation risk to polar flights. Arguably the most potentially disruptive space weather effect (and the main subject of this thesis) are geomagnetically induced currents (GICs). In this chapter, GICs and their effects are discussed. Following this, the strategy for studying GICs in Ireland is outlined, along with a summary of the other chapters in this thesis.

Geomagnetically Induced Currents

GICs and all other space weather effects are driven ultimately by activity on the Sun (see Figure 1.1). The Sun is a dynamic star, constantly emitting radiation and matter into the Solar System. Such solar activity, in the form of the solar wind, solar flares, coronal mass ejections (CMEs) and associated solar energetic particle events (SEPs) can all interact with the Earth's magnetosphere and ionosphere, causing it to react and change in time.

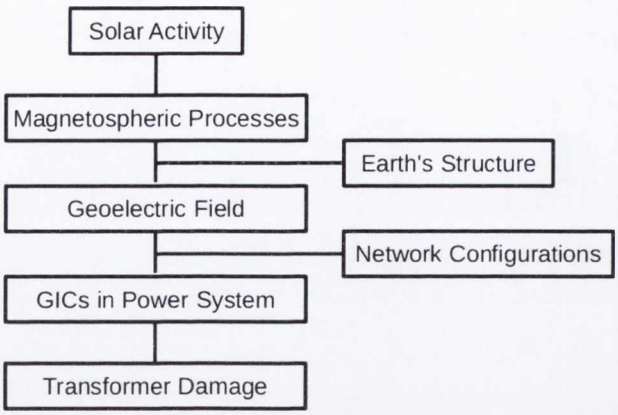
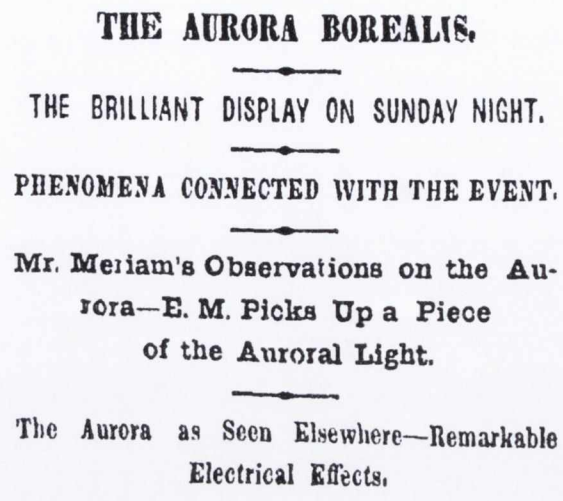


Figure 1.1: The chain of events which lead from the Sun to transformer damage on terrestrial power networks. After Pirjola (2000).

Up until the 1800s, the only visible effect of this Sun-Earth interaction were the aurorae at the poles. These were recorded first in oral traditions, then as written records all around the globe. The earliest datable observations of the aurorae have been found on Babylonian tablets written in 567 BC (Stephenson *et al.*, 2004), and records of aurorae exist in Japanese and Chinese records from at least 600 AD (Kataoka *et al.*, 2017). The aurora australis was possibly sighted and recorded in 1640 in the southern hemisphere (Willis *et al.*, 2009), but appears in indigenous oral traditions stretching back much earlier (Hamacher, 2014).

The variations in the Earth's magnetic field due to the Sun induces electric fields in the surface of the Earth. These surface electric fields drive GICs in any grounded network of conductors, particularly during periods of geomagnetic unrest. They can damage gas pipelines and telecommunication cables (Pirjola, 2000), and disrupt railway signalling equipment (Eroshenko *et al.*, 2010). Most importantly, they pose a risk to grounded power systems, the kind all developed nations employ to generate and transmit electrical power. GICs were first theorised by Davy (1821), and were first observed in grounded telegraph systems in the 1800s.

The most famous example of GICs in telegraph systems is the Carrington storm of September 1859, the largest geomagnetic storm event to date. This event is still used as a benchmark example of a large geomagnetic storm (Cliver *et al.*, 2004;



THE AURORA BOREALIS.

THE BRILLIANT DISPLAY ON SUNDAY NIGHT.

PHENOMENA CONNECTED WITH THE EVENT.

Mr. Meriam's Observations on the Aurora—E. M. Picks Up a Piece of the Auroral Light.

The Aurora as Seen Elsewhere—Remarkable Electrical Effects.

Figure 1.2: Headline from the New York Times, 5th September 1859. On the subject of the widespread aurora, the article goes on to say: *"What is the origin of this remarkable phenomena? The ancients asked the question, and the moderns reply by repeating the interrogation. The most popular theory attributes it to electricity, but that agent has been made responsible for everything which men did not know how to account for otherwise."*

Green & Boardsen, 2006; Nevanlinna, 2005; Siscoe *et al.*, 2006). The 1859 storm is noted as also being the first solar flare ever observed (Cliver, 2006). This flare was observed on September 1st 1859 by both Carrington (1860) and Hodgson (1860). Approximately 17 hours later, the great geomagnetic storm began. It was large enough that the magnetic recorder at the Kew observatory was driven off its scale.

Apart from the variations in magnetic recordings in observatories, fantastic aurorae were seen around the world (see Figure 1.2). The storm was of such magnitude that the aurorae were seen as far South as Cuba (Nevanlinna, 2005). These displays were accompanied by disruption to telegraph communications from GICs (Boteler, 2006). Operators around the world experienced electrical shocks from their telegraph equipment. In some cases, the operators could disconnect their batteries and still communicate with their colleagues, such was the magnitude of GICs which flowed in their equipment.

While there may have been communication disruptions, the extent of the ground-based effects of the storm was limited to telegraph systems. There were no grounded power systems in operation during the Carrington event. If a geomag-

netic storm of the same magnitude were to occur today, the effects would be much more widespread and damaging, given the proliferation of grounded power networks. A Carrington-type event could damage or disrupt power networks around the world simultaneously.

The cost of a hypothetical catastrophic GIC event goes far beyond the cost of repairing affected transformers (themselves expensive pieces of infrastructure). A sustained electrical blackout in an area will severely disrupt food and water supplies, not to mention the disruption to essential services such as hospitals, waste management, and transport. If a space weather event is large enough to destroy a sufficient number of transformers in a region, it could take months to fully repair a network. For particular transformers, it can take up to years to integrate them fully into a network.

It has been estimated that the direct economic cost incurred from disruption to electricity is only 49% of the total macroeconomic cost of an extreme event, with the rest of the cost attributed to the inevitable disruption to global supply chains (Oughton *et al.*, 2017). The threat posed by extreme space weather events has been studied from an economic or insurance point of view in numerous studies (see for example Oughton *et al.* (2016); Schrijver *et al.* (2014)), and the economic loss to arise from such a worst-case scenario has been estimated to be as much as $40 billion per day for the US alone (Schrijver *et al.*, 2014). Such a scenario may precipitate social unrest in large cities (Centra Tech, 2011).

The studies mentioned above are focussed on the hypothetical worst-case scenarios. Thankfully, such a catastrophic GIC event has not occurred since power networks have become ubiquitous. A widespread GIC event that causes immediate and permanent damage to multiple transformers appears unlikely, although the risk posed from GIC-related heating is still under debate (Pulkkinen *et al.*, 2017). GICs have, however, damaged power networks in the past. The most famous example of GICs disabling a power network occurred in 1989 in the Canadian Hydro-Québec power system (Bolduc, 2002). During this event, the power system experienced instabilities due to GICs which led to a complete blackout. Damages to network components totalling $13.2 million were seen. Worse than this was the nine hour blackout which followed, causing 'knock-on' economic losses of approximately $2.9 billion. The same event saw a transformer in New Jersey damaged due

to GICs. In 2003, a similar geomagnetic storm damaged transformers in Sweden, leading to temporary blackout (Pulkkinen *et al.*, 2003c).

Space weather effects are now a recognised risk on a government level. Severe space weather is seen as much as a threat to society as adverse terrestrial weather on the UK national risk register (as of 2011), and in 2016, the US Congress passed the Space Weather Research and Forecasting Act. These highlight the importance of studying space weather and its effects.

Countries at higher latitudes ($> 60°$ N) are at particular risk from GICs, where geomagnetic disturbances are larger and more frequent (Pirjola, 2000). Studies of GICs in high-latitude countries have been conducted in Finland (Pulkkinen *et al.*, 2001; Viljanen *et al.*, 2004), Sweden (Pulkkinen *et al.*, 2003c; Wik *et al.*, 2008), Norway (Myllys *et al.*, 2014), Canada (Bolduc, 2002; Boteler *et al.*, 1989) and others.

It is now known that GICs can contribute to the failure of transformers in low-latitude and midlatitude countries through repeated heating of transformer insulation (Gaunt, 2014; Gaunt & Coetzee, 2007). Geomagnetic storms can cause wear on transformers, leading to reduced efficiency, and eventual failure months after the event, even if typical geomagnetic variations are small.

Countries of middling and lower latitudes have also studied GICs in their power networks. These countries include Austria (Bailey *et al.*, 2017), Spain (Torta *et al.*, 2014, 2017), China (Liu *et al.*, 2016; Zhang *et al.*, 2015), New Zealand (MacManus *et al.*, 2017; Marshall *et al.*, 2012), Australia (Marshall *et al.*, 2013), South Africa (Koen & Gaunt, 2003; Ngwira *et al.*, 2011), Ireland (Blake *et al.*, 2016b), Scotland (McKay & Whaler, 2006), the UK as a whole (Beggan, 2015; Kelly *et al.*, 2017; McKay, 2003; Thomson *et al.*, 2005), Greece (Zois, 2013) and Brazil (Trivedi *et al.*, 2007), among others.

GICs in Power Systems

Transformers are employed in power networks to step-up or step-down the voltage of electricity for efficient transmission (Paynter & Toby-Boydell, 2011). Electrical energy produced at a power plant is immediately stepped up in voltage via a

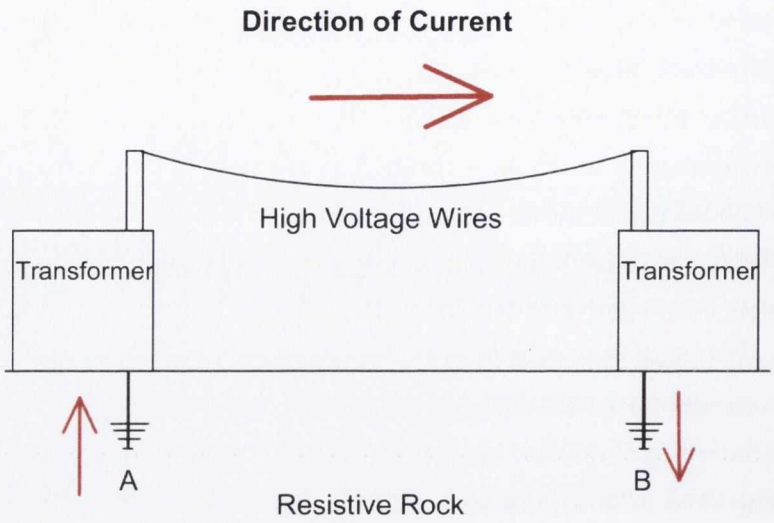


Figure 1.3: How GICs enter a power network.

transformer and transmitted over long distances using either overhead or underground transmission lines. The transmitted voltages are then reduced in another transformer to levels usable by either domestic or commercial customers.

High-voltage power transmission networks use three-phase AC with transformers to convert between voltage levels (Boteler & Pirjola, 2014). Where these three-phase transmission lines are connected to Y-connected transformers, the windings converge at a neutral point, which then connects to the ground. During normal operation no current flows through this ground (as each of the AC currents in the three phases sum to zero). Should an imbalance occur, the ground allows a safe discharge path for stray currents. It is this connection to ground which allows GICs to enter a network.

At their simplest, transformers consist of two magnetic coils wound around separate sides of a magnetic core. An alternating voltage is applied to the primary coil, which creates an alternating current through the coil. This current produces an alternating magnetic flux in the magnetic core, which in turn generates a current in the secondary coil. The number of windings in each of the coils determines the resulting voltage.

When the Earth's magnetic field alters with time due to solar effects, a surface electric field is induced (see Chapter 2). The grounded transformers and the low

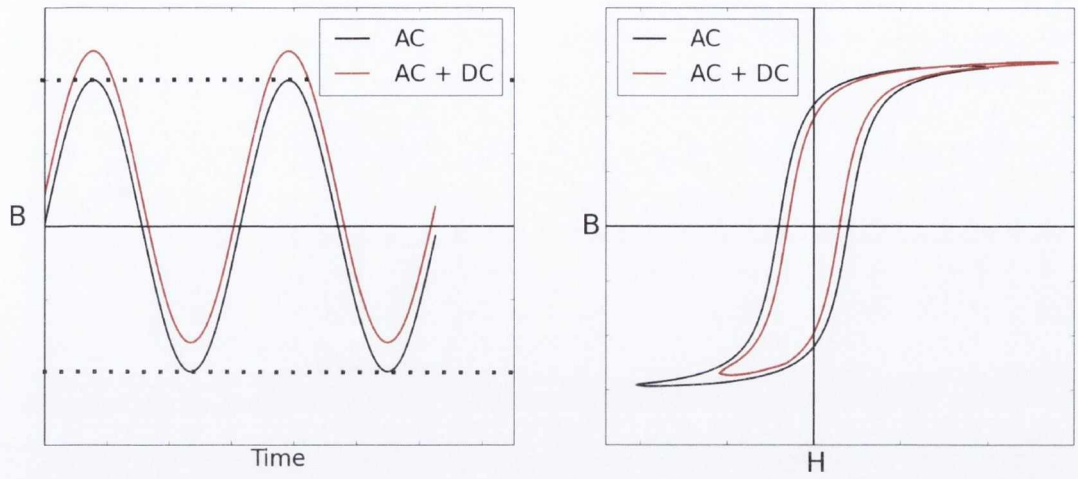


Figure 1.4: Left: half-cycle saturation in a transformer. The dotted lines delimit the normal operating range for a transformer. Right: BH curve of a transformer. The addition of the GIC shifts it off the linear portion of the plot, where they transformers operate normally.

resistance transmission lines they are connected to effectively serve as a short-circuit for ground currents (see Figure 1.3). Once the GIC flows through the network, it is distributed according to Kirchoff and Ohm's laws, which depend on the topology and resistance of the network. It is the current flowing through the transformers that can cause damage and disruption to the network.

Effect on Transformers

In the normal operation of a transformer, the magnetic flux density within the magnetic core will alternate sinusoidally around zero. Depending on the magnetic material used in the core, this will result in a different BH loop: a graph of magnetic flux density B to magnetic field intensity H within the magnetic core.

As transformers are designed for AC use, the introduction of a quasi-DC GIC (which alternate at $\sim$1 Hz, much lower than the 50-60 Hz of conventional transformers) will offset the magnetic flux density sinusoid, leading to half-cycle saturation (see Figure 1.4). Transformers are built to be very efficient, and operate on the linear portion of the BH curve, so the addition of even a small GIC can cause significant saturation every half-cycle (Gaunt & Coetzee, 2007).

The main problems that are associated with this half-cycle saturation are transformer heating, the introduction of harmonics, and reactive power losses (Pulkkinen *et al.*, 2017). Transformers will be more or less susceptible to GICs and their effects depending on the type, make, model and condition of an individual transformer (Girgis & Vedante, 2012).

Transformer Heating

Under normal conditions, most magnetic flux in the transformer will remain in the magnetic core. With an added DC component, the non-magnetic shields used to control magnetic flux in the transformer will begin to hold more and more flux. This can cause eddy currents and heating. Large and sustained GICs have the potential to completely destroy the transformer in this manner, and repeated heating of the transformer can damage its thermal insulation, leading to reduced performance and lifespan (Gaunt & Coetzee, 2007; Koen & Gaunt, 2003). In extreme cases, a transformer can be damaged beyond use in a single geomagnetic event.

Harmonic Generation

Transformers that are half-cycle saturated are a source of even and odd harmonics (Dong *et al.*, 2001). Transformers are normally built to cope with only odd harmonics. This can result in tripping of circuit breakers and the reduced performance of control systems when GICs are introduced. Harmonics generated by GICs caused the Hydro-Quebec blackout in 1989 (Bolduc, 2002).

Reactive Power Losses

Saturated transformers have a higher reactive power consumption. Large changes in the reactive and real power balance can cause voltage fluctuations in the system (Pulkkinen *et al.*, 2017), as well as reducing the efficiency of the transformer. This lack of stability can lead to a lack of synchronism or faults within a system.

GIC Mitigation

Devices such as capacitor banks can be installed at transformer grounds, effectively blocking DC currents from entering the network. These devices are costly and complex to install however, rendering them unsuitable for large networks with thousands of transformers (Kappenman *et al.*, 1997). Blocking a transformer in a substation may simply act to reroute GIC to other grounded elements of network as well.

Newer transformers can be built to be robust to GIC effects. However, transformers normally have lifespans of decades, so replacing all the transformers in a network is prohibitively expensive.

A common approach to managing GICs in a power network is to rely on geomagnetic forecasts, coupled with simulations of a network. Forecasts of geomagnetic activity are regularly given by institutions such as the British Geological Survey (www.bgs.ac.uk) and the National Oceanic and Atmospheric Administration Space Weather Prediction Center (www.swpc.noaa.gov). Using these forecasts, power operators can implement mitigation strategies in their networks, provided the GIC risks of different substations have been identified (an objective for the Irish power network in this thesis). This may involve opening or closing network connections to reroute GICs away from vulnerable substations.

This strategy is not without its risks however. Forecasting the extent and intensity of geomagnetic storms is frequently inaccurate. Implementing mitigation strategies for false positive forecasts may be costly for a network operator. They also require knowledge of how the network will respond to different storms. This knowledge is acquired either by measuring GICs or simulating them.

Studying GICs

There are different ways of measuring GICs in a power network. The simplest is to attach a Hall Effect probe to the ground of a transformer, to directly measure the passage of GICs to and from the ground. This is the most common method of measuring GICs. However, fitting Hall Effect probes to existing transformers can

be a disruptive exercise to the operation of a power network (David Bell, EirGrid, 2016, personal communication).

GICs can also be measured by their magnetic signature under high-voltage (HV) power lines by utilizing the differential magnetometer method (Matandirotya *et al.*, 2015, 2016). This method is currently under development, and has yet to be used on a large scale.

The long-term effect of GICs on a transformer can be studied by monitoring the gas composition inside the transformer housing. Moodley & Gaunt (2012) developed an 'energy triangle', which can be used to track the degradation of a transformer after repeated heating from GICs. This method is useful for showing the long-term effect of GICs, but cannot be used to quantify the exact levels of GIC in a transformer.

Ideally, every transformer in a power network would have a Hall Effect probe on its neutral grounding to measure GICs. In reality, it is rare for networks to have more than a handful of instruments to directly measure GICs (MacManus *et al.* (2017) and references therein). The most commonly used approach to study GICs is therefore to simulate GICs in power networks.

This process can be separated into two parts (Pirjola, 2002; Viljanen & Pirjola, 1994):

1. The geophysical step: determining the horizontal surface geoelectric field. This depends on the variations in the geomagnetic field, as well as the conductivity structure of the Earth's subsurface.

2. The engineering step: determining the GICs in a network driven by the geoelectric fields. This requires knowledge of the power network: its connections and the resistivity of its elements.

As most countries (particularly in the northern hemisphere) have long-term geomagentic measurements, GICs from historical geomagnetic storm events can be estimated in a network, even if GIC measurements from that time do not exist.

Aims of this Work

To date, there are no recordings of GICs damaging elements of the Irish power network (David Bell, EirGrid, personal communication). Furthermore, there are no recordings of GICs at all in the Irish power network prior to 2015 (*The Irish Times* does however report that Irish telegraphs were disturbed by a 'mysterious atmospheric influence' on numerous occasions in the early 1900's.). Ireland is a small and mid-latitude (51.4° – 55.4° N) country. Both of these factors limit the size of GICs which could cause potential damage to transformers in Ireland.

Since August 2015, Ireland has had a single Hall effect probe in one substation to continuously measure GICs. This device clearly shows GICs during recent moderate geomagnetic storms. The effects of larger historical storms on the rest of the network is unknown, however. Given the long-term threat GICs pose to even mid-latitude countries, it is worth quantifying the risk GICs pose the Irish power network in detail.

The objectives of this work can be separated into two parts:

1. To develop and maintain a magnetic observatory network around Ireland to better monitor the effects geomagnetic storm events.

2. To model GICs in the Irish power network for historical geomagnetic storm events. From these simulations, assess the magnitude, frequency and distribution of large GIC events in Ireland. Identify substations that are more susceptible to GICs.

Each chapter in this thesis is outlined below:

- Chapter 2: Describes the solar events which trigger magnetospheric and ionospheric changes. These events are the ultimate drivers of space weather hazards including GICs.

- Chapter 3: Lists the sources of geomagnetic data used in this thesis. MagIE, the Irish magnetometer network is described, including equipment and locations used, as well as difficulties encountered in maintaining geomagnetic observatories.

- Chapter 4: Outlines spherical elementary current systems (SECS), a method of interpolating geomagnetic fields across an area during geomagnetic storms. A test case in Ireland is used to determine how including more or less geomagnetic observations affects the accuracy of SECS.

- Chapter 5: Describes two methods of calculating geoelectric fields: the magnetotelluric (MT) and thin-sheet methods. Different simplifications to the MT method are outlined, and practical considerations of the thin-sheet method are explored. Different resistivity models of the Earth are explored.

- Chapter 6: Outlines the Lehtinen & Pirjola (1985) method of calculating GICs in a power network model. The Irish power network is described and modelled for GIC simulations. These models are subjected to a battery of tests to explore the impact the assumptions used in their construction have on calculated GICs.

- Chapter 7: Five recent geomagnetic storm events and their effects on the Irish power network are simulated using the methods described in Chapters 4, 5 and 6. The resulting GICs in one substation are compared to measured GICs. Different resistivity models are used and compared.

- Chapter 8: Three large historical storm events are simulated for the Irish power network and analysed. The GIC amplitudes of a 1-in-100 years geomagnetic storm event is estimated using a scaled historical storm and 25 years of geomagnetic data.

2

The Drivers of GICs

In this chapter, the chain of phenomena that lead to GICs are explored, from solar events through to the induction of geoelectric fields. The different solar phenomena that interact with the Earth's magnetic field are described, along with the Earth's magnetosphere and atmospheric electric current systems. Geomagnetic storms and substorms are defined. The induction of geoelectric fields in the Earth's surface is briefly outlined.

The Sun as a Driver for Space Weather

The Sun is the ultimate driver of space weather effects, be they aurorae, terrestrial communication disruptions or GICs. Radiation and particles are constantly being ejected from the Sun in the form of the solar wind, coronal mass ejections (CMEs) and solar flares. The energy and particles from these events propagate into the Solar System, where they may interact with the Earth's magnetosphere and upper atmosphere, leading to GICs and other space weather phenomena.

The frequency of solar flares, coronal holes and CMEs are closely related to a roughly 11-year cycle known as the solar cycle. This cycle is measured by the number of active regions on the Sun's surface. These dark regions (or sunspots)

are transient, magnetically complex regions which can last up to several months (Phillips, 1992). Sunspots are associated with solar flares and CMEs, and are often the origin for these phenomena. Every 22 years, the polarity of the Sun's magnetic field changes in a magnetic reversal event due to dynamo activity in the solar activity (DeRosa *et al.*, 2012).

Currently, in 2017, we are approaching the next 'solar minimum' portion of the solar cycle. This means that less sunspots are appearing on the Sun, and less associated flares and CMEs with which to drive geomagnetic storms. It is important to note that although the frequency of solar events decreases and increases with the solar cycle, large events that can cause geomagnetic storms can occur at every part of the solar cycle. For example, the 2003 Halloween storm occurred as the solar cycle was approaching solar minimum.

Solar Wind and Coronal Holes

The solar wind is the continuous stream of plasma (mostly protons and electrons, with some heavier ions) which is ejected into the solar system from the Sun's atmosphere (Parker, 1965). The hot atmosphere at the base of the solar corona contains a strong embedded magnetic field which expands outward, accelerating particles into the solar system (Lewis, 2004). The speed of this outgoing plasma varies with location of origin. The 'fast solar wind' has speeds > 500 kms^{-1} and originates from the open field lines of coronal holes, dark regions of low density plasma in the outer solar atmosphere (Cranmer, 2009).

The 'slow solar wind' has speeds <500 kms^{-1} comes from closed magnetic field areas of the Sun (Ohmi *et al.*, 2004). Whilst the fast solar wind can leave the Sun with speeds up to several thousand kms^{-1}, by the time the solar wind is at one astronomical unit, it is usually reduced to ~ 450 kms^{-1} (Lowrie, 2007). The Sun has its own magnetic field structure which is frozen into the matter it ejects into the solar system. At Earth, this has a magnetic field strength of approximately 6 nT.

This structure is thought to be six regions of alternating positive and negative magnetic polarity in the plane of the ecliptic (Lewis, 2004). Around the solar equator, the solar magnetic field lines in the corona are closed, and this constrains

the emitted plasma. At higher and lower latitudes, the magnetic field lines are open and directed radially outwards (see Figure 2.1). A current sheet separates the open field lines of the northern and southern hemispheres. As the Sun rotates, the magnetic field (which is frozen into the solar wind particles) is dragged into an Archimedean spiral (known as the Parker spiral, see Figure 2.2). This magnetic structure which radiates from the Sun is known as the interplanetary magnetic field (IMF).

The rotation of the Sun takes around 27 days to complete at the equator (Phillips, 1992). Coronal holes and sunspots can survive several rotations of the Sun before dissipating. This can lead to repeated high speed solar wind directed at Earth every 27 days. There are less associated CME and solar flare events as sunspots become less common during the solar minimum portion of the solar cycle. During these periods, coronal holes and the solar wind become more important as drivers of geomagnetic effects.

Coronal Mass Ejections

Coronal mass ejections are spectacular large-scale eruptions which occur in the solar atmosphere. They arise when magnetic field lines with fixed points on the Sun's surface twist and become distorted. Eventually, these magnetic field lines reconnect, releasing huge amounts of magnetic energy (Forbes, 2000). This typically propels somewhere between $10^{11} - 10^{13}$ kg of plasma into the solar system at speeds up to 3000 kms^{-1} (Chen, 2011). CMEs expand quickly to fill volumes many times that of the Sun as they travel outwards. CMEs are composed of plasma, and so experience a Lorentz force from the IMF, which slightly curves their trajectories (Byrne *et al.*, 2010; Maloney & Gallagher, 2010; Temmer *et al.*, 2015).

If CMEs comes into contact with the Earth's magnetosphere, they cause it to deform and change temporarily, releasing energy and particles into the near-Earth environment. As well as the speed and size of the CME, the magnetic orientation of the CME can affect the impact it will have on the Earth's magnetosphere. A southward oriented CME will have a larger effect than a northward oriented CME for reasons outlined below (see Section 2.2.3). Knowing the orientation of an interplanetary CME is one of the major challenges with operational space weather

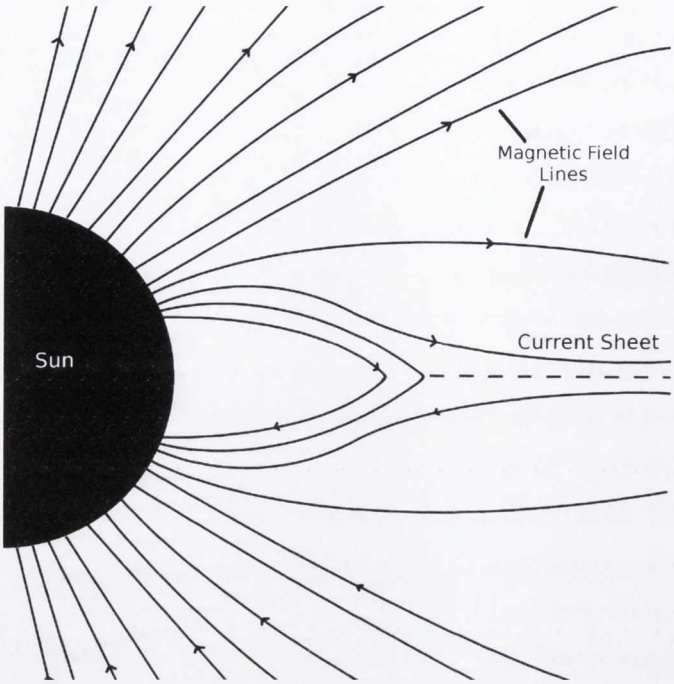


Figure 2.1: A schematic of the solar (or interplanetary) magnetic field during solar minimum. The high speed solar wind originates at higher latitudes where there are open magnetic field lines. A current sheet exists around the equator of the Sun, where magnetic field lines directed away from the Sun are brought into close contact with field lines in the opposite direction. After Phillips (1992).

forecasting. From eruption to 'collision' with the Earth's magnetosphere usually takes around 2-3 days, but CMEs have been known to travel from the Sun to Earth in as little as 17 hours (Schrijver & Siscoe, 2010). CMEs are associated with many of the largest geomagnetic storm events on record (Yermolaev *et al.*, 2005).

Solar Flares

Solar flares are the most powerful explosions in the solar system, with the release of massive amounts of energy (up to 10^{25} J) in the form of radiation in a matter of minutes (Schrijver, 2009). Solar flares occur when magnetic reconnection on the solar surface accelerates electrons to high speeds into the solar atmosphere. These electrons are then decelerated and release either hard ($>$ 10 keV) or soft ($<$ 10 keV) X-rays. Flares are classed by increasing energy. They are either B, C, M or the largest, X-class based on peak X-ray flux as measured by the GOES

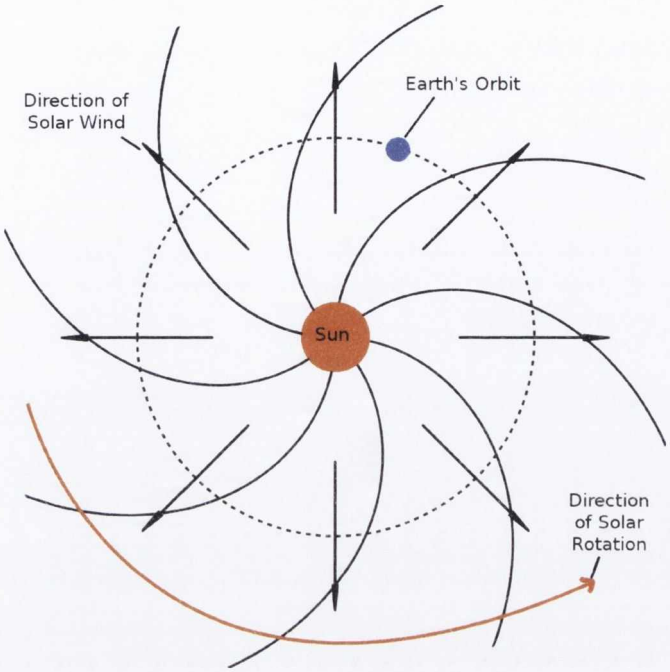


Figure 2.2: The Parker spiral. The radially emitted solar wind particles carries the solar magnetic field into the Solar System. As the Sun rotates, an Archimedean spiral is formed.

spacecraft.

The radiation from flares can damage spacecraft and are a hazard to astronauts. Important to GICs, solar flares can also ionise part of the Earth's upper atmosphere, which contributes to the ionosphere. This extra ionization allows currents to move in the Earth's atmosphere, changing the measured magnetic field at the Earth's surface. A major negative effect of solar flares is the disruption of radio-based communications on Earth due to changes in the ionosphere (see Section 2.2.2).

Solar flares are often precursors to, or accompanied by CMEs. Flares were seen before the famous Carrington geomagnetic storm event (Carrington, 1860) and the 2003 Halloween storms (NOAA, 2003), for example. Operationally, one first observes a flare as their effects are being felt on Earth and at satellites. As such, they are often predicted by observing the conditions of their parent sunspot (McCloskey *et al.*, 2010).

Solar Energetic Particles

Solar energetic particles (SEPs) are highly accelerated particles (mostly protons and electrons) that are released from the Sun during disturbances such as flares or CMEs (Ryan *et al.*, 2000). These particles can have energies of GeV, and can be dangerous to both satellites and astronautical activities. SEPs can ionize part of the Earth's atmosphere in a similar manner to solar flares, which can alter the magnetic field measured at the Earth's surface (see Section 2.2.2).

Earth's Magnetic Environment

The geomagnetic field measured at the surface of the Earth is a superposition of magnetic fields from a number of different sources. These include the Earth's internal magnetic field and numerous current systems in the atmosphere and beyond.

The Earth's internal magnetic field is maintained by the movement of charge (molten iron and nickel) in the Earth's core (McFadden *et al.*, 1991). This magnetic field has a magnitude of approximately 3×10^{-5} nT at the Earth's equator and 6×10^{-5} T at the poles (Chave & Jones, 2012). In the absence of any external forces on the magnetic field, it can be approximated as a magnetic dipole with poles tilted roughly 11° off the Earth's axis of rotation. This intrinsic magnetic field changes slowly with time, and so by itself does not contribute to geomagnetic storms. It is the interaction between the magnetosphere and the Sun that causes the magnetic variations which drive GICs.

Magnetosphere

The Earth's magnetosphere is the region of space around Earth in which the terrestrial magnetic field dictates the motion of charged particles (see Figure 2.3). The Earth's magnetosphere extends asymmetrically into space, with the dayside hemisphere of the magnetosphere compressed due to the solar wind. The border of the magnetosphere is located where the Earth's magnetic pressure balances the solar wind pressure. i.e., where

$$P_{mag} = \frac{B^2}{2\mu_0} = \frac{1}{2}\rho_{sw} v_{sw}^2 = P_{sw} \tag{2.1}$$

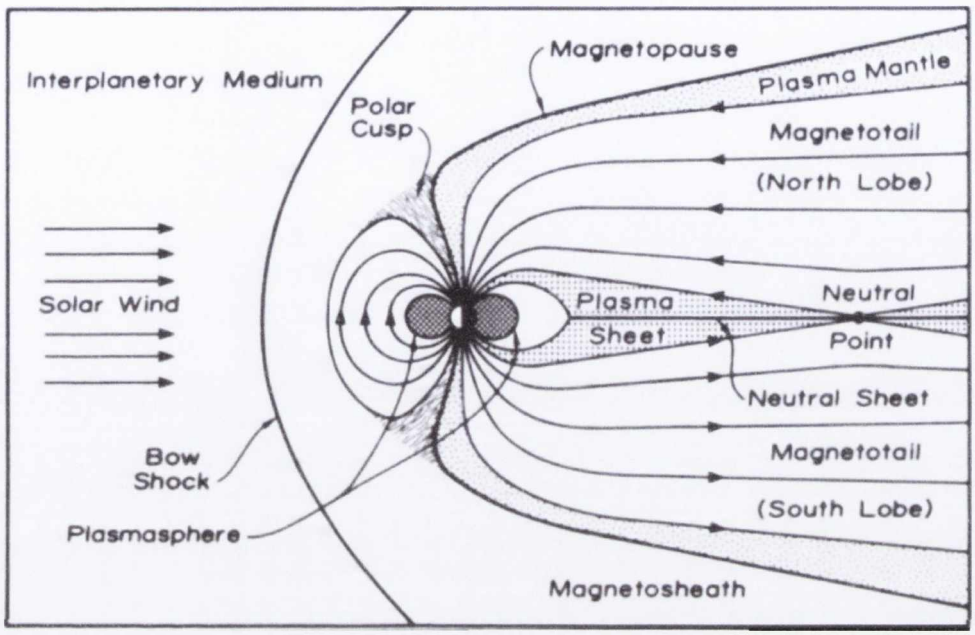


Figure 2.3: The Earth's magnetosphere (Russell, 1993).

where subscripts *mag* and *sw* refer to magnetic and solar wind, B is magnetic field, μ_0 is magnetic permeability of free space, ρ is density and v is velocity. This boundary, the magnetopause, is normally at a distance of around 15 Earth radii, although this is quite sensitive to the pressure of the solar wind (Russell, 1993). The nightside hemisphere of the magnetosphere is elongated and weakened, with open magnetic field lines known as the magnetotail. A current sheet separates two regions of oppositely directed open magnetic field lines, and contains plasma with ion temperatures of up to 5×10^7 K (Seki *et al.*, 2003).

Within the magnetosphere there are two toroidal regions of trapped plasma known as the Van Allen belts. The closest belt contains mostly MeV protons and ions, and the belt further out is mostly composed of electrons with energies of the order of 100 keV (Hudson *et al.*, 2008). During geomagnetic events (such as a CME impacting the Earth's magnetosphere), the density of the Van Allen Belts increases (Rothwell & McIlwain, 1960), and can pose a risk to satellites in the form of increased drag.

The motion of charged particles makes up a number of electrical current systems in the Earth's atmosphere and magnetosphere. One such current system is

the equatorial ring current. This current is caused by the longitudinal drift of particles and resides between 10,000 and 60,000 km in altitude (Daglis *et al.*, 1999). Changes in this current are measured using the disturbed storm time index (Dst, see Section 3.3.3), a proxy for geomagnetic storm intensity. The more particles that are injected into the magnetosphere and ring current, the more negative the Dst value becomes.

The other main current systems in the magnetosphere are the Chapman-Ferraro currents which flow at the dayside magnetopause, and the tailside currents in the nightside magnetosphere (Olsen & Claudia, 2016).

Ionosphere

At high altitudes in the Earth's atmosphere, particles are ionised by UV and X-ray radiation from the Sun. As the air is rare at altitude, collisions are too infrequent to result in rapid recombination, and a weak plasma is formed (Schubert *et al.*, 2015). This region is known as the ionosphere, and extends from about 60-1,000 km above the Earth. The presence of the electrons and ions allows for radio communications around the world (Rishbeth, 1988). The ionosphere and the ground act as a waveguide for radio signals, allowing communications across the globe. Typical electron densities in the ionosphere can range from 10^8 to 10^{12} m^{-3}.

As in the magnetosphere, there are a number of current systems (or electrojets) present in the ionosphere. At mid-latitudes there are the solar quiet currents. These flow clockwise in the southern hemisphere, and anti-clockwise in the Northern Hemisphere, with foci of about $\pm 30°$ (Olsen & Claudia, 2016). These systems are driven by the convective motion of plasma in the atmosphere. The magnetic signature from these currents gives the solar regular (S_r) variation in terrestrial magnetic measurements. This diurnal variation is most apparent on days without geomagnetic storms (see Section 3.3.1). Near the equator, both solar quiet current vortices flow from West to East. This forms the equatorial electrojet.

Towards the poles, there are more complicated systems of currents. Field-aligned currents (FAC's) flow along the Earth's magnetic field lines to the Earth's atmosphere at high latitudes (Scott, 2015), serving as the primary coupling between the polar ionosphere and magnetosphere (Le *et al.*, 2010; Olsen & Claudia,

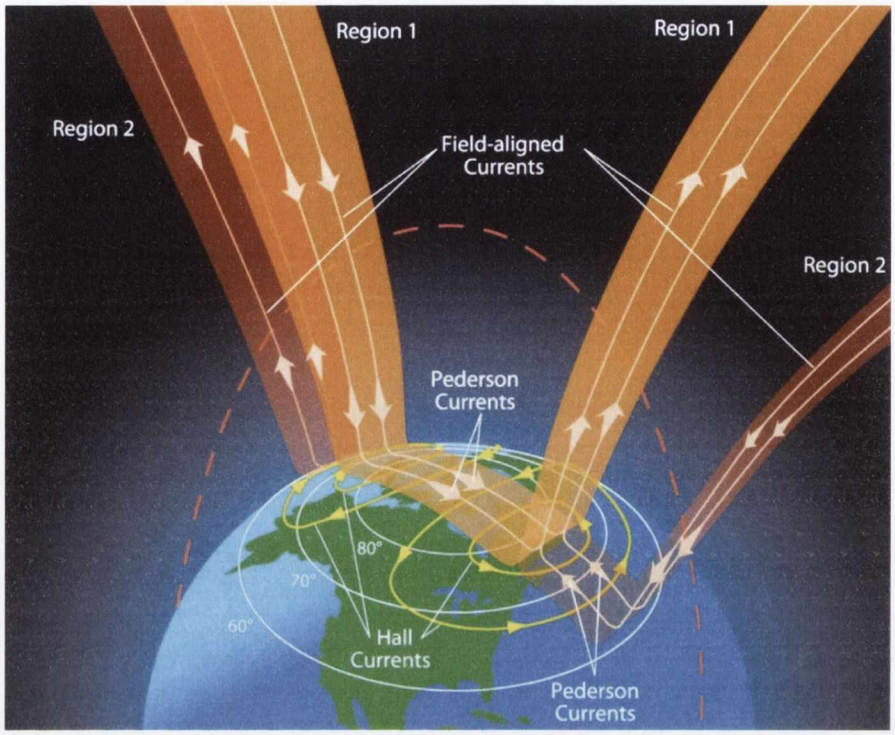


Figure 2.4: High altitude ionospheric current systems. Le *et al.* (2010)

2016). These currents are also known as Birkeland currents, after the scientist who first theorised them (Birkeland, 1908). These currents exist as two rings with opposite polarities. The two rings are known as region 1 (higher latitude) and region 2 (lower latitude). A schematic of this region is shown in Figure 2.4.

Pedersen currents connect the two FAC regions across the polar cap. Two auroral electrojets flow parallel to the Earth's surface at about 100 km altitude beneath the Birkeland currents. These currents carry millions of A, and contribute greatly to the measured magnetic field at the Earth's surface (Schubert *et al.*, 2015). During geomagnetic disturbances, these electrojets creep South.

Magnetic Reconnection

The main mechanism for energy transfer between particles from the Sun and the magnetosphere occurs through the process of magnetic reconnection. This is where anti-parallel magnetic field lines which are moving towards each other

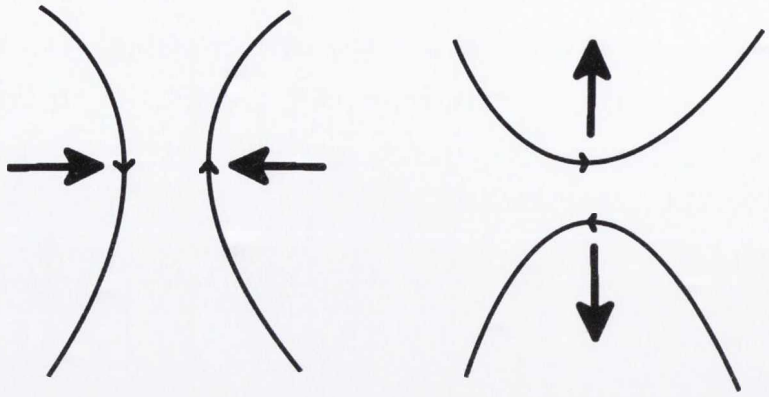


Figure 2.5: Magnetic reconnection. Two antiparallel field lines moving towards each other (left) merge field lines and reconnect in a different orientation. The magnetic field lines are then expelled from the point of reconnection (right). This process occurs on the Sun, and in the interaction between the IMF and CMEs with the magnetosphere.

realign themselves to convert magnetic energy into kinetic and thermal energy via particle acceleration (see Figure 2.5).

This process occurs at the dayside of the magnetosphere. If an incoming CME or the solar wind has a southward oriented magnetic field component, there will be a large magnetic gradient between it and the Earth's magnetospause. This gradient creates a localised diffusive region where the magnetic field lines are no longer frozen in the plasma. They are then 'cut' and reconnected to form different field lines, and move away as the magnetic tension force seeks to straighten them out. The net result of the magnetic reconnection is the conversion of the magnetic energy of particles to thermal and kinetic energy (Schrijver & Siscoe, 2010). A similar process occurs during the formation of CMEs on the surface of the Sun, and in the magnetotail during substorms (see below).

Magnetic storms and Substorms

Geomagnetic disturbances can be broadly separated into two categories: storms and substorms. Geomagnetic storms are prolonged periods of geomagnetic disturbance which can last several days. They begin when enhanced energy transfer from the IMF of the solar wind to the magnetosphere, which leads to an intensification of the ring current (Chave & Jones, 2012). This happens particularly

when the solar wind has a negative B_z component, which aids reconnection at the magnetopause. This can trigger a series of substorms (explained below), and transport energetic particles into the magnetosphere.

Geomagnetic storms have three phases, which are classed according the the change in the Dst index. The initial phase lasts from minutes to hours, and sees an increase in the Dst by tens of nT. The second or main phase lasts up to hours, and sees Dst take a large negative values of several hundred nT. The final recovery phase lasts up to several days, and sees the Dst return to pre-storm levels.

Substorms are shorter disturbances that can occur during geomagnetic storms, or in otherwise geomagnetically quiet times. They also occur regularly frequently, and are accompanied by the movement of the auroral electrojets to lower latitudes. Substorms have been known for many decades (Atkinson, 1966), although there are controversies regarding their exact function (Akasofu, 1989). A substorm consists of three phases: a growth phase, an expansion phase and a recovery phase (Chave & Jones, 2012). The magnetic signature of each is visible in ground-based magnetic measurements.

The growth phase begins when solar wind with a negative B_z transfers energy to the magnetosphere, and is characterised by a small decrease in the ground magnetic field intensity. Dungey (1961) proposed that the negative B_z causes reconnection to occur at the dayside of the magnetosphere. Magnetic energy is then transported and stored in the lobes of the magnetotail. A plasmoid and new current sheet forms in the magnetotail, and the substorm expansion phase begins. This is characterised by a sharp decrease in magnetic field intensity, and the auroral ovals expand towards both the poles and the equator. This process is known as the Dungey Cycle.

Finally, magnetic reconnection occurs again in the magnetotail, the plasmoid is released down the magnetotail. This is the recovery phase. The surface magnetic field returns to pre-substorm levels over time.

Geoelectric Field Induction

The following simple case for electric field induction is described in Boteler & Pirjola (2016). The Earth's surface geomagnetic field varies with time during the

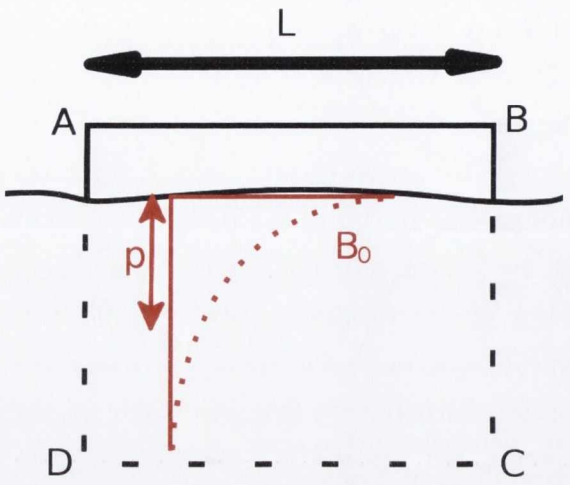


Figure 2.6: Geoelectric field induction in a loop ABCD. The line AB represents a power line aboce ground. The surface magnetic field B_0 attenuates to $1/e$ its value at depth p. After Boteler & Pirjola (2016)

periods of activity listed above. According to Faraday's law, wherever there is a changing magnetic field, an electromotive force ϵ is produced. Assuming a time variation of the form $e^{i\omega t}$, we can compute:

$$\epsilon = -\frac{d\Phi}{dt} \tag{2.2}$$

where Φ is magnetic flux. Consider the loop ABCD in Figure 2.6, where the side AB represents a power line of length L. In this case, variations in the magnetic field are incident on the loop. The surface magnetic field has a value B_0, which attenuates with depth z.

$$B = B_0 e^{-z/\delta} \tag{2.3}$$

where δ is the complex skin-depth and B_0 is the surface magnetic field. This value is related to the conductivity of the subsurface, and gives the depth to which an electromagnetic wave will propagate in a medium where it has attenuated by a factor of $1/e$ (see Section 5.1.1.5 for more). To find the sum of magnetic flux through the loop ABCD, an integral from the surface to an infinite depth is

required:

$$\Phi = \int_0^\infty Bdz \times L = \delta B_0 L \tag{2.4}$$

Subbing into Faraday's Law, the electric field is given as:

$$\epsilon = \oint_{ABCD} Edl = -\frac{d\Phi}{dt} = -i\omega\delta B_0 L \tag{2.5}$$

If the electric field is equal to zero at infinite depth, and there is no horizontal electric field along AD or BC, the emf is given by the integral of the electric field along side AB

$$\oint_{ABCD} Edl = E_0 L = -i\omega\delta B_0 L \tag{2.6}$$

Dropping L from each side:

$$E_0 = -i\omega\delta B_0 \tag{2.7}$$

The surface electric field is dependent on the surface magnetic field and the conductivity of the subsurface (contained within δ). This forms the basis of calculating surface electric fields.

For GIC-related studies, there are a number of different methods of calculating surface electric fields, although all require the same two inputs: a magnetic field (or ionospheric current which produces one) and an Earth conductivity model. The conductivity structures can be as simple as a homogenous Earth, or one that varies in every dimension.

The most commonly used approaches to calculating surface electric fields in GIC studies are the complex image method (Pirjola & Viljanen, 1998), the plane-wave method (Cagniard, 1953) and the thin-sheet method (Vasseur & Weidelt, 1977). In this thesis, the plane-wave (or magnetotelluric) and thin-sheet methods are employed to calculate surface electric fields in Ireland. These two methods are explored in Chapter 5.

3

Monitoring Geomagnetic Storms

As mentioned in Chapter 1, this thesis can be separated into two distinct parts. The first part, which is the subject of this chapter, is a practical task. It deals with the deployment and maintenance of the Irish Magnetometer Network (MagIE), which was set up to monitor the magnetic and electric effects of geomagnetic storms in Ireland. The data from this network are crucial inputs for the GIC simulations, which will be detailed in later chapters.

Origin of Magnetic Observatories

Although the aurorae were a widely known phenomenon for millenia the world over, it wasn't until the early 1700s that the link between the aurorae and geomagnetism was found. Anders Celsius in Sweden noted that the aurorae were accompanied by disturbances of the geomagnetic field, and together with George Graham in London, they concluded that these magnetic disturbances were not merely local effects (Cliver, 1994). Continuous magnetic measurements at that time were still sparse, however. As navigation in the 1800s relied heavily on magnetic methods, it became apparent that a worldwide network of magnetic observatories would yield both scientific and practical navigational value (Cawood, 1979)

Beginning with Gauss and Weber in 1834, multiple nations embarked on their own enthusiastic 'magnetic crusades', to make as many geomagnetic measurements in as many locations as possible across the globe (Clark, 2007; Stern, 2002). These Victorian scientists included the Dubliner Edward Sabine, who recognised that geomagnetic activity mirrored the sunspot cycle in 1852 (Sabine, 1852).

As a result of these efforts, permanent magnetic observatories were set up around the world to continuously monitor changes in the Earth's magnetic field strength and declination. By 1841, there were a total of 53 magnetic observatories around the globe (Stern, 2002). These observatories included Greenwich (1836), Toronto (1840), Mumbai (1841) and Trinity College Dublin (1835). These sites used early magnetometers to measure the Earth's magnetic field, and some were operational during the famous Carrington event (see Figure 3.1 and Cliver & Dietrich (2013)). Whilst the magnetometer in Trinity College was operating for this event, the records for the 1859 year have, unfortunately, since gone missing.

Since this event, magnetometers and variometers have been set up across the world to measure local and global effects. Data from these sites are used to contribute to global models of the Earth's magnetic field, such as the International Geomagnetic Reference Field, which is now in its 12th generation (Thébault *et al.*, 2015). Most of these were set up in Europe and the Northern hemisphere, and would often take hourly measurements before digitisation. Modern systems most frequently have 1-minute and occasionally 1-second digital data feeds.

Magnetic observatories measure the magnetic field in three dimensions (see Figure 3.2). The horizontal B_x and B_y components measure the strength of the magnetic field pointing in geographic North and East respectively. This coordinate system is maintained throughout this thesis. The two main sources for magnetic data used throughout this thesis are the INTERMAGNET and MagIE networks, both of which are described below.

INTERMAGNET

Since the widespread digitisation of geomagnetic data and improvements in data transfer, the International Real-time Magnetic Observatory Network (INTERMAGNET, www.intermagnet.org) was set up to adopt automatic geomagnetic

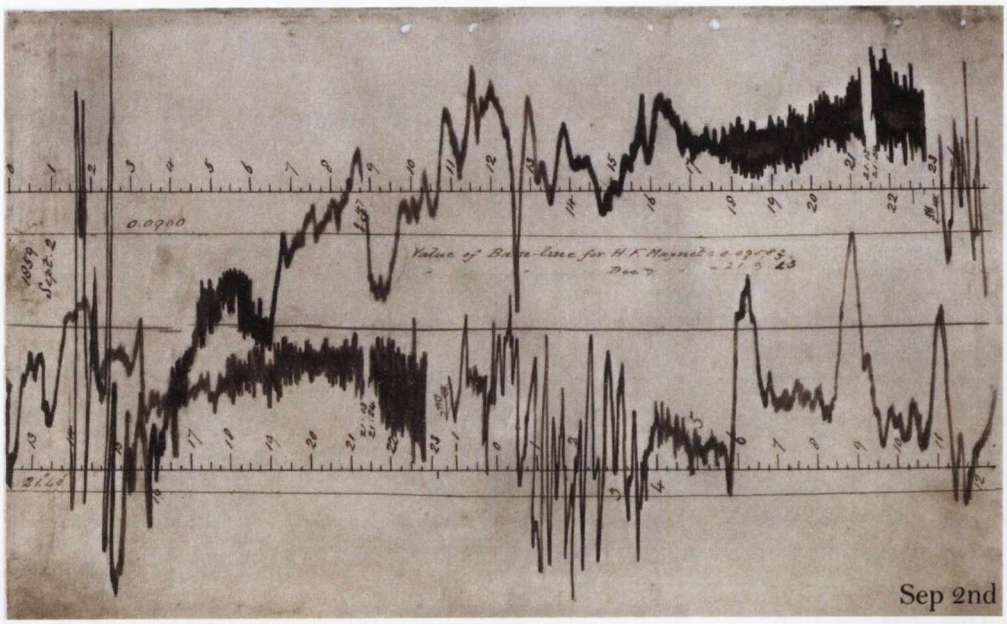


Figure 3.1: Carrington event magnetogram taken in Greenwich, U.K. Reading the data on such magnetograms can be problematic for multiple reasons. Provided the medium is sufficiently intact, recordings of particularly large storms could have variations which went off scale or even off page. www.geomag.bgs.ac.uk/education/carrington.html. Further discussion on 1859 measurements can be found in Cliver & Dietrich (2013)

observatories with satellite communications. The network now comprises of approximately 150 magnetic observatories around the world which conform to particular data and construction standards. Each magnetic observatory produces absolute measurements and data of the requisite quality for secular variation studies of the geomagnetic field (St-Louis, 2012). The magnetometers in these observatories must have a resolution of 0.1 nT, and provide one-minute magnetic field values in a standard format, which can be downloaded from the INTERMAGNET site. Many INTERMAGNET sites operate multiple magnetometers for redundancy (such as the British Geological Survey operated observatories in Britain). Recently, INTERMAGNET has been focussing on producing one second data at each of the sites which contribute to the project.

Met Éireann, the Irish national meteorological service, operates the Valentia observatory in Kerry. This is the only INTERMAGNET observatory in Ireland. Valentia observatory was set up in 1886 beside the Irish junction of the then trans-

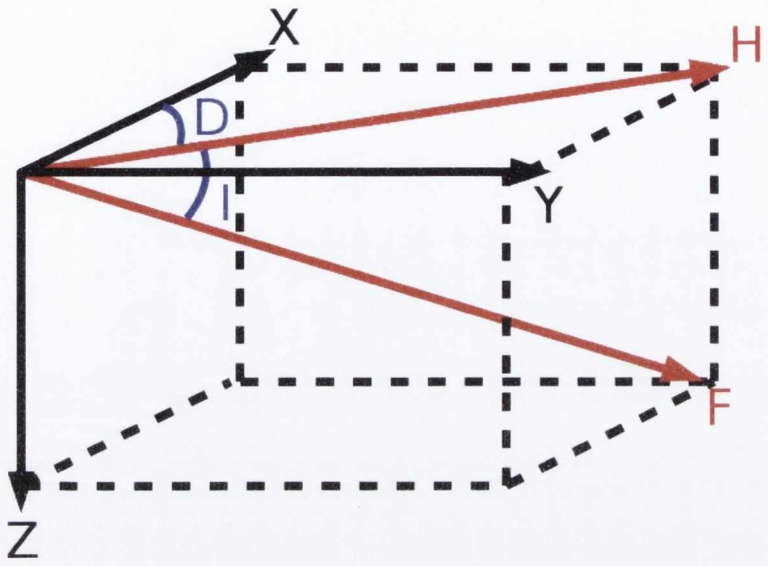


Figure 3.2: Magnetic observatory coordinate system. The coordinates X and Y point geographic North and East respectively. The horizontal (H) component is the vector sum of X and Y. The declination angle (D) is the angle between X and H. The total intensity (F) is the vector sum of all three magnetic components. It makes an inclination angle I with the surface.

atlantic cable (Cullum & Fitzgerald, 1889), and has digitised data available from the 1980s to the present. Valentia currently operates both fluxgate magnetometers (to measure declination and inclination) and proton magnetometers to measure the absolute intensity of the geomagnetic field.

The Irish Magnetometer Network (MagIE)

Since 2012, Trinity College Dublin and the Dublin Institute for Advanced Studies Geophysics Section (DIAS) have installed and maintained a number of geomagnetic and geoelectric observatories in Ireland. These observatories are collectively called the Irish Magnetometer Network (or MagIE). Each observatory operates with a single magnetometer (detailed below). The location of these sites are shown, along with some INTERMAGNET sites, in Figure 3.3. Of the five MagIE sites, Birr, Armagh and Malin Head are currently still installed. Birr and Armagh are permanently housed with a realtime data connection, data for which can be found

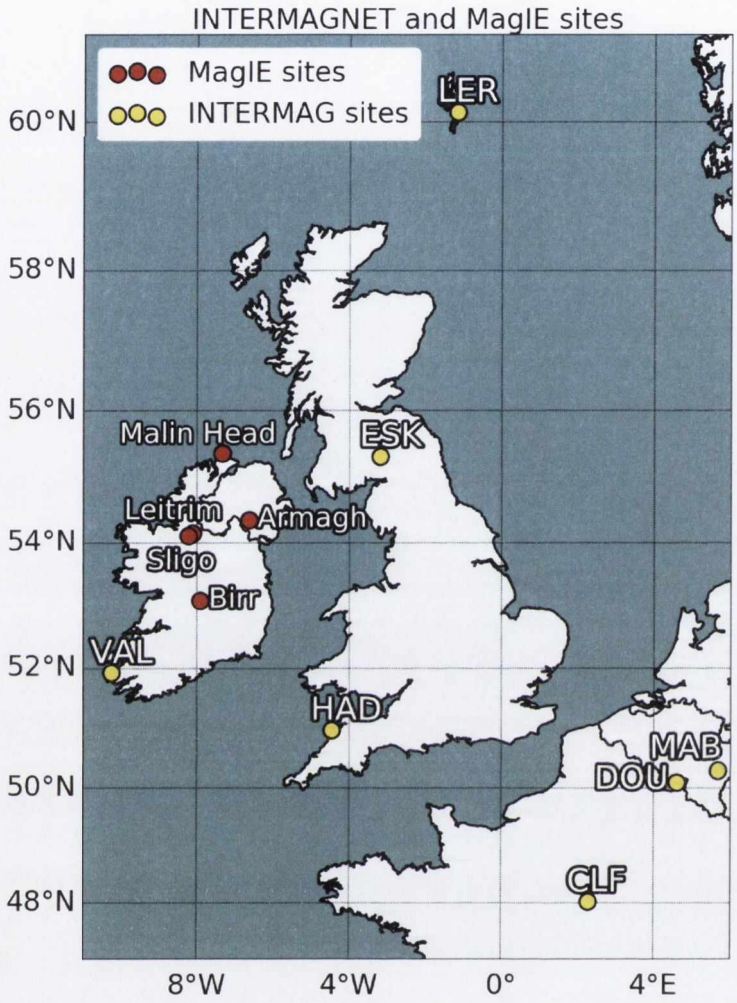


Figure 3.3: MagIE and INTERMAGNET sites in Ireland, Britain and continental Europe. The location of the MagIE sites are as follows: Birr 53.09°N, 7.92°W; Sligo 54.12°N, 8.22°W; Leitrim 54.16°N, 7.92°W, Armagh 54.35°N, 6.65°W and Malin Head 55.37°N, 7.34°W.

on www.rosseobservatory.ie. The time for during which each site was recording is shown in Figure 3.4.



Figure 3.4: Recording time ranges for each of the MagIE magnetic observatories. Armagh had two test magnetometers installed, and one permanent. Leitrim and Sligo each recorded geomagnetic as well as geoelectric data. Birr had a large number of missed days in 2017 due to construction at the site.

Equipment

Each MagIE site uses the third generation Long-Period Magnetotelluric Instrument LEMI-417M to record geomagnetic and, if possible, geoelectric fields (www.lemisensors.com). These instruments are designed for long-period magnetotelluric soundings (<1 Hz). Each instrument is comprised of a fluxgate magnetometer, a set of electrodes (although not always present), a recording unit and a GPS antenna for timestamping (see Figure 3.5).

The LEMI-417M unit samples at 1s, and writes binary files of approximately 2 MB per day to a flash card. If not powered from a mains source, a LEMI can be powered for approximately four to six weeks by a 105 Ah battery. After this time, it is necessary to replace the depleted battery with a charged one, and transfer the data from the flash card on board the data logger to local storage.

Fluxgate Magnetometer

Although the LEMI-417M magnetometer has a proprietary design, a general description of a fluxgate magnetometer is as follows:

A fluxgate magnetometer usually consists of ring cores of a magnetically permeable alloy around which two separate coil windings are wrapped: the drive winding and the sense winding. An alternating current is applied to the drive winding, which will induce equal and opposite magnetic fields in the two halves of the core (see Figure 3.6). In the absence of an external magnetic field, these magnetic fields will cancel out, and there will be no net change of flux detected in the sense winding. With the addition of an external field, the half core generating a magnetic field in the direction of the external field will saturate sooner than the other half, and the magnetic fields from the hemispheres will no longer cancel out. This will lead to a net change of flux in the sense winding, and a voltage will be induced proportional to the strength of the external field.

In order to get a 3D representation of the magnetic field (as the LEMI system does), three orthogonal fluxgate magnetometers are likely used in the LEMI system to give values for B_x, B_y and B_z. The LEMI magnetometer has a measurement range of $\pm$ 68000 nT, with a resolution of 0.01 nT. According to the manufacturers' specifications, there is an expected temperature drift of <0.2 nT per °C. An annual temperature range of 30°C (a reasonable value for Ireland) would therefore result in a temperature drift of 6 nT.

Electrodes

The electrodes normally used with the LEMI system are small plastic cylinders with a porous ceramic bottom filled with a copper sulphide solution. However, the electrodes used in this study were the Phoenix Geophysics (www.phoenix-geophysics.com) non-polarising lead-lead chloride solution (Pb-PbCl) electrodes, based on the design of Petiau & Dupis (1980).

The top of each cylinder has a cable which is connected to the data recorder. Each of the four electrodes is buried in a hole up to 1 m deep for long-term surveys (Chave & Jones, 2012), and is covered with a saline fluid to aid electrical contact with the ground. Particular care needs to be taken to ensure that the whole of

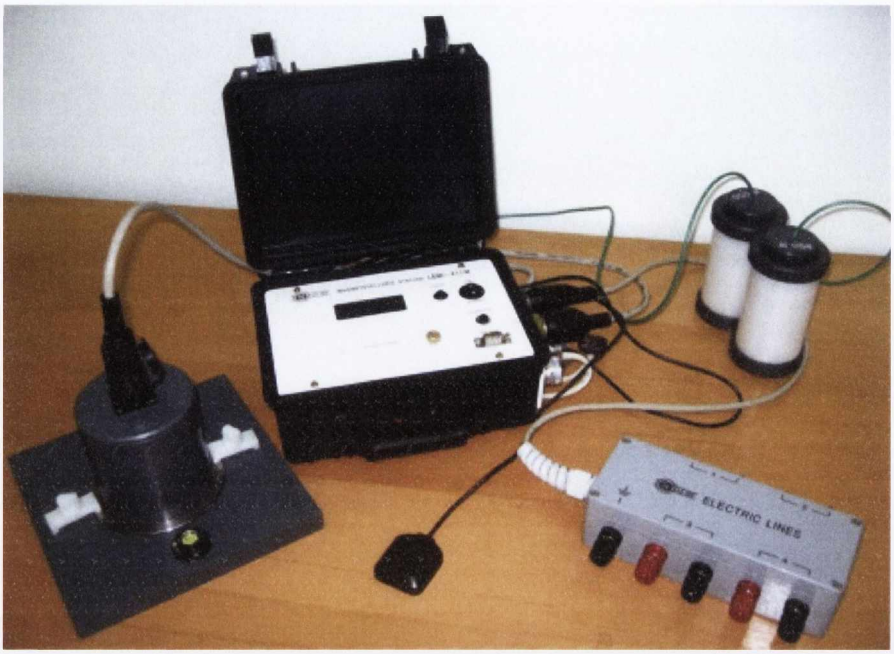


Figure 3.5: The 3rd generation LEMI-417M kit. Fluxgate magnetometer is left, recording device centre, and electrodes background right. Foreground right is the module to connect electrodes to the data logger. The electrodes in this picture (background right) are filled with a copper sulphide solution, rather than the lead-chloride electrodes used in this study. From www.isr.lviv.ua/lemi417.htm.

the base of the electrode is in contact with the soil. Four electrodes are used together to make two orthogonal dipoles approximately 80 m long. Each dipole then measures the electric potential in the ground between the two electrodes. Generally, the drier the soil, the more resistive the connection between electrodes. In particularly dry soil, it may be necessary to bury the electrodes in buckets of conductive liquid, in order to ensure electrical contact with the soil. This is not an issue in the wet soil of Ireland, and electrodes can be buried straight into the ground.

Deployment

Deploying the LEMI system involves choosing an appropriate location and setting up each of the elements of the system. The first consideration for location is for the safety of the device. By necessity, the equipment will need to be left unattended for

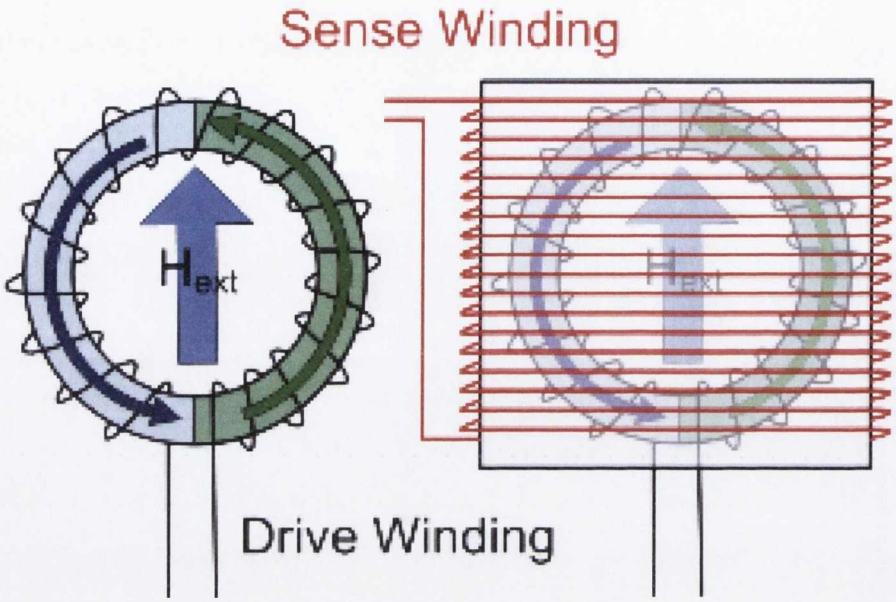


Figure 3.6: Fluxgate magnetometer schematic. The drive winding induces two equal and opposite magnetic fields in each hemisphere of the core. Only with the addition of an external magnetic field H_{ext}, will the sense winding give a voltage. From www.imperial.ac.uk/space-and-atmospheric-physics.

a long period of time for continuous geomagnetic monitoring (unless in controlled grounds such as an observatory). An area less likely to be frequented by people or animals is desirable for uninterrupted recording.

The next consideration is if electric field measurements are required. If this is not the case, most areas free of magnetic materials can be used to host a magnetometer.

If electric fields are required, there are a number of further considerations to account for. Any instances of nearby electric power cables or habitation can easily pollute the electric field data beyond use (although some cleaning can be performed). Electrified railways, power systems and electric fences in particular are to be avoided for electric field measurements (Chave & Jones, 2012). Apart from electromagnetic noise, the topography and nature of soil can also affect the electric field measurements. It is better to have a flat area with at least 30 cm of topsoil and few trees (to minimise vibration from wind).

Previous magnetotelluric studies by DIAS Geophysics were used to characterise

suitable areas which were free from anthropogenic noise in Ireland (Rao *et al.*, 2014). Once a suitable location was found, the magnetometer is buried approximately 90 cm in the ground and oriented towards either magnetic or geographic North. It is then connected to the data logger, which is connected to a GPS for accurate timestamping. If electrodes are required, four are laid in two perpendicular dipoles, usually 80 m long and oriented North-South and East-West. These electrodes are buried in holes up to 1 m deep as mentioned above, and connected to the data logger for recording. Magnetic data are then recorded at 1 s intervals.

MagIE Observatories

Each of the MagIE sites are listed below with further details as to their setup.

Birr (53.09°N, 7.92°W)

A magnetometer was initially installed in the Birr demesne towards the end of 2012 as part of the Rosse Solar-Terrestrial Observatory (www.rosseobservatory.ie). Initially, the magnetometer was buried oriented magnetic North, with a mains power supply and connection to a computer which hosted the data.

In 2015, the magnetometer was oriented geographic North and permanently housed in a custom built chamber. The orientation of the magnetometer to geographic North was achieved in the following manner. First, the latitude and longitude of the magnetometer's position was noted using a GPS system. The declination θ (angle between magnetic and geographic North) was noted using the declination calculator on www.ngdc.noaa.gov. The magnetometer was installed oriented magnetic North initially, and then rotated manually $\theta°$ until it was oriented geographic North. This method of orientation is quick, and requires no specialist equipment, but relying on a declination calculator may introduce errors in the orientation. For greater precision, devices such as declinometers could be used to orient magnetometers.

The magnetometer housing consists of a plastic inspection chamber set into a concrete base and buried approximately 90 cm below the surface. The magnetometer sits on an adjustable nylon plinth which is set into the concrete, allowing for future levelling adjustments should the magnetometer shift orientation. The



Figure 3.7: The Birr permanent magnetometer installation. Left: the plinth set in concrete upon which the magnetometer sits. Right: the inspection chamber before being buried. The thermal insulation can be seen on the left beside the trench.

water-tight inspection chamber was then filled with fibreglass for passive thermal insulation. An image of the Birr magnetometer setup is shown in Figure 3.7.

The entire magnetometer and data logger area was enclosed with a sturdy wooden fence constructed with brass screws. Electric field measurements were made in Birr for approximately six months in 2013, and for the first half of 2014, but the proximity of Birr town led to poor data quality in the E_y component, and so electric field measurements were discontinued.

Armagh (54.35°N, 6.65°W)

A magnetometer was installed in Armagh Observatory at the start of 2015 in order to test if the location was suitable for geomagnetic measurements. After this, another magnetometer was installed in a different site on the observatory grounds. The data from both of these magnetometers needed to be read from a flash drive on the data loggers, and their batteries needed to be charged evey six weeks.

The data returned from these two magnetometers were considered stable and clean, identifying Armagh as a suitable location for a permanent installation. This



Figure 3.8: The Armagh Observatory permanent magnetometer installation. Left: the inspection chamber which housed the magnetometer before being buried. Right: the inspection chamber which housed the data logger.

was installed and oriented geographic North (as with the Birr magnetometer) in 2015. The location at Armagh observatory also meant that a mains power and realtime communications setup in the same fashion as Birr could be readily installed. This installation can be seen in Figure 3.8.

Leitrim and Sligo (54.16°N, 7.92°W & 54.12°N, 8.22°W)

In order to confirm that modelled electric fields are returning sensible values, it is necessary to have electric field measurements. As mentioned above, measuring electric fields is significantly more difficult than measuring geomagnetic fields. Remote areas away from possible electrical interference (such as towns) are favourable (see Section 3.2.2). A site in remote cut forestry in Leitrim, near Lough Allen, was chosen for a magnetometer and electrodes installation. The area had been identified as giving good (low-noise) electric field measurements in previous DIAS magnetotelluric surveys (Colin Hogg, DIAS, personal communication, 2015).

In mid-2015, Coillte (the Irish semi-state forestry company which maintained the land), required the Leitrim site for replanting, and so the equipment was uninstalled. Another site approximately 10 km to the West of the Leitrim site was



Figure 3.9: Left: site in Leitrim near Lough Allen. The broken terrain prevented electric-field cables from being buried. Right: the author at the Sligo site. The solar panel can be seen facing South to capture the Sun in Sligo.

identified in Sligo, again in Coillte maintained cut forestry. In late 2015, a full magnetometer plus electrodes site was was installed there with a solar panel to trickle-charge the power supply, and ensure continuous measurements. The data was retrieved in person from the site until late 2016 when Coillte again required the field for replanting, and the equipment was uninstalled. Both the Leitrim and Sligo sites can be seen in Figure 3.9.

Malin Head (55.37°N, 7.34°W)

A temporary site was installed in Malin Head, in 2015 as it was the most northerly point on the island of Ireland on a weather station maintained by Met Éireann. This magnetometer-only site was installed with a solar panel in order to ascertain if the location was suitable for a permanent installation (as in Birr and Armagh). This site can be seen in Figure 3.10. The data quality from this site is considered stable and noise-free enough to warrant a future permanent magnetometer installation, similar to Birr and Armagh, in the future.

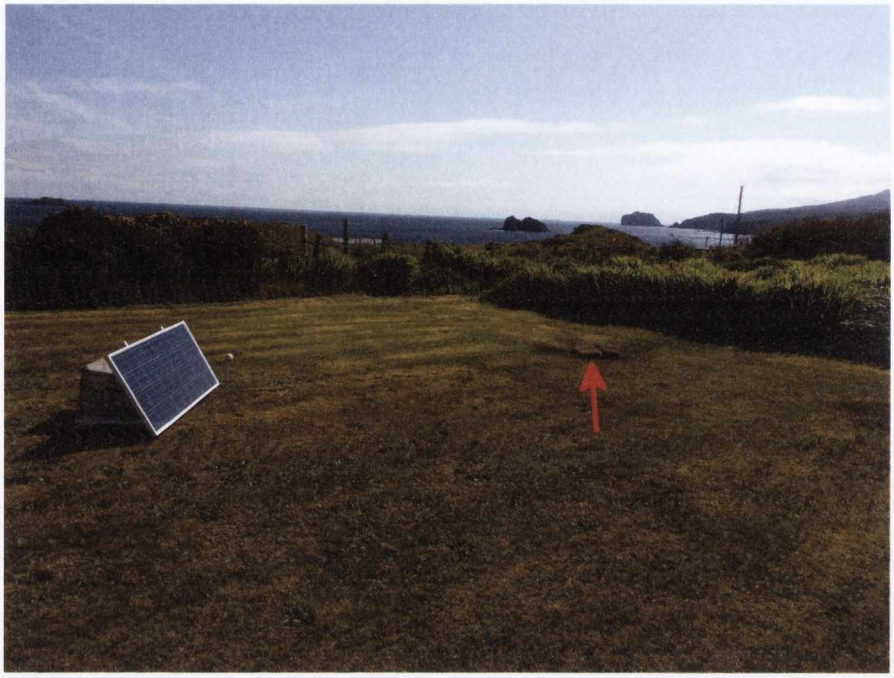


Figure 3.10: The Malin Head magnetometer site at the northernmost tip of Ireland. To the left is the solar panel and GPS receiver. To the right, beneath the cut earth, is where the magnetometer is buried (indicated with a red arrow).

Difficulties Encountered during MagIE Operation

The setup and maintenance of each of the geomagnetic sites in MagIE came with a number of operational problems. Some of these problems and their solutions are listed below.

Power Supplies

For many of our sites, a particular problem was with our power supplies. For our remote temporary sites (i.e., those installed without mains supply power), the batteries sometimes discharged quicker than expected. This can happen particularly in cold weather. As these sites were only visited every six weeks or so, this resulted in lost (or rather unrecorded) data. This can be seen for Leitrim in Figure 3.4. A solution to this was the installation of solar panels to ensure that the system was kept powered. These solar panels functioned well even during the winter in Sligo.

In Birr, there was an unstable power supply, which led to power dropouts (as

can be seen in Figure 3.4). This shut down the computers which logged the data. Fortunately, in most of these cases, the magnetometer and data logger system kept recording. This meant that the data could be retrieved directly from the flash card at a later date, and the data catalogue could be backfilled.

Wildlife

A problem with our locations which took electric field measurements was local wildlife. Despite the construction of the electrode cables (RGS8 cable: copper core surrounded by plastic, with metal shielding and a plastic finish), animals such as deer, hare and sheep can occasionally chew through them. In an ideal location, electric field lines would be buried to prevent this from happening. In the case of Leitrim, however, the nature of the cut forestry meant that this was impossible to do. Animals managed to chew through one of the electrode dipole's cables, meaning that electric field data was not recorded in a dipole in Leitrim. This electrode cable was replaced at the next maintenance visit, and the cables were hidden as best as was possible, given the terrain. Fortunately, there were no more cables chewed through for the duration of the installation.

Waterproofing

Although the LEMI magnetometers can operate normally in wet conditions, it was decided that the permanent housing constructed in Birr and Armagh would need to be waterproof, in order to effectively control temperature and minimise magnetometer drift. Each cylindrical section of the magnetometer housing seen in Figure 3.7 was sealed with a sealant gel during construction. It turned out that this gel was unsuitable for the kind of plastic in our housing, and failed to keep out water after a period of particularly heavy rainfall. A number of different sealants were applied on different occasions until the chamber remained completely dry. A sealant suitable for the type of plastic which made up the housing was found. Figure 3.11 shows the temperature the Birr magnetometer before and after permanent housing.

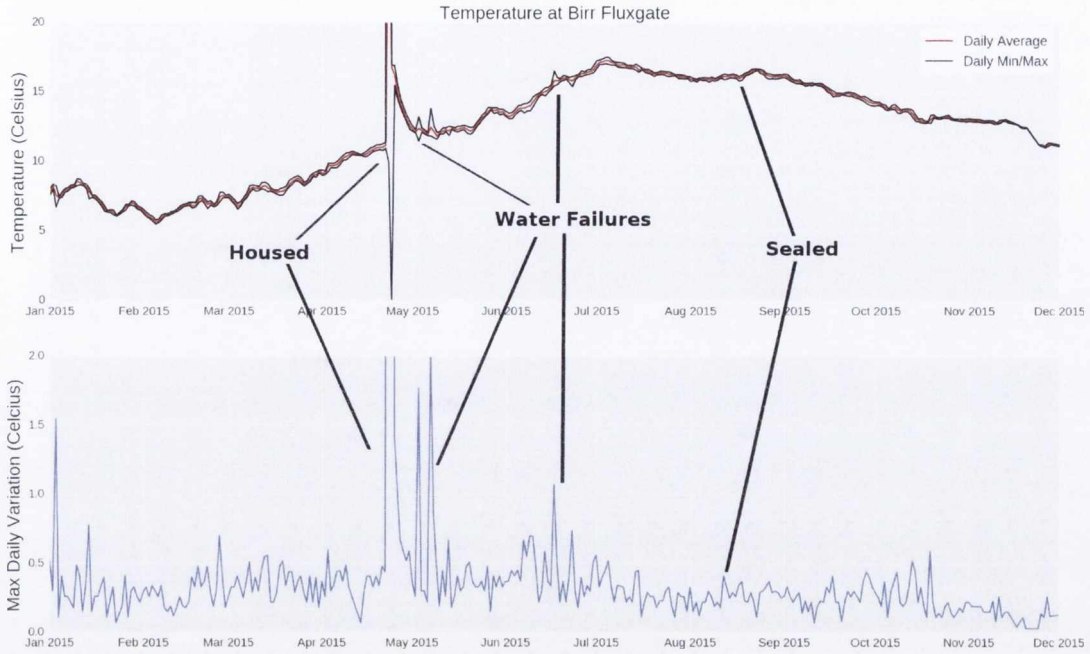


Figure 3.11: The top plot shows average temperature per day (red), with max and min bounding lines (black). The bottom plot shows the maximum daily variation. The large jump in both plots in May shows when the magnetometer was permanently housed. On the 2 May 2015 there was heavy rainfall, which broke the sealants on the magnetometer housing. This was repaired, but failed again on 17 June 2015. It was finally sealed correctly on 12 August 2015. It has remained sealed and dry since.

Lightning

Finally, the most damaging hazard encountered was lighting. On 20 March 2014, lightning struck at the Birr observatory. The lightning strike damaged one of the data loggers beyond use. Temporary surface electric field measurements were being taken in a nearby field, and these measurements show a massive jump just as our data logger stopped recording. This is shown in Figure 3.12.

Quantifying Geomagnetic Disturbances

There exist a number of different indices which give a shorthand quantification of a geomagnetic disturbance. These indices are used to classify geomagnetic

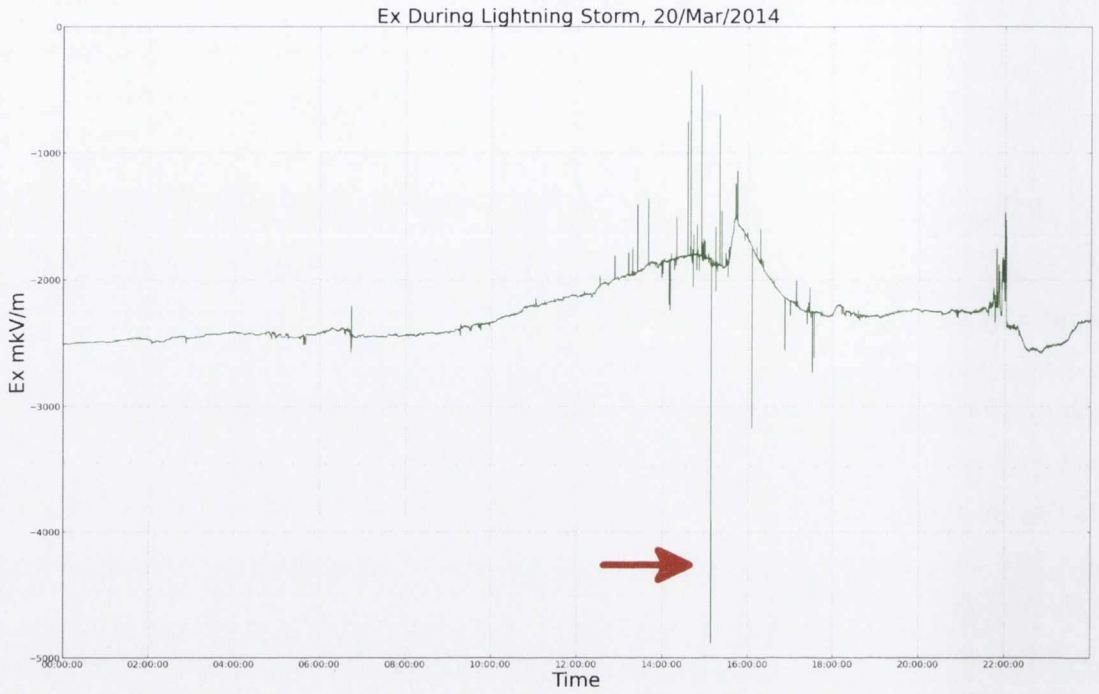


Figure 3.12: Electric field measurements taken approximately 300 m from our Birr magnetometer. The large spike (indicated with a red arrow) shows the time of the lightning strike which damaged the data logger.

storms and aid space weather research, as well as more broadly informing global geomagnetic models (Reay *et al.*, 2011).

K-Index

The K (K for *Kennziffer*, or indicator) index is designed to quantify the level of disturbance caused by the influence of the solar wind at a single location using magnetic measurements (Clark, 1992; Reay *et al.*, 2011). It is a quasi-logarithmic scale from 0 to 9 which quantifies the local variation in the horizontal components of the geomagnetic field. A value of K=0 corresponds to completely quiet conditions (with minimal variation beyond the diurnal variation), whereas K=9 corresponds to a severe storm.

The K-index was introduced by Bartels *et al.* (1939), and gives eight three-hour interval values per day. It is designed such that the daily variation in the magnetic field due to the convection of ionospheric currents (the solar-regular or solar-quiet

curve, S_r) is ignored. Once S_r is subtracted from the magnetic time series for a single day, the maximum variations for each of the horizontal components is taken for each three-hour bin. These numbers (in nT) correspond to a predetermined table which gives the K-value. These values are scaled for each site so that each location should give approximately the same values over time (Bartels *et al.*, 1939), regardless of geomagnetic latitude.

The difficulty in calculating the K-index is the estimation of the S_r curve. On a geomagnetically quiet day, this is a simple enough process, with the S_r curve easily identifiable. However, it becomes more complicated for a disturbed day, when the S_r curve is obscured by magnetospheric and ionospheric activity. Before the digitisation of data, K-indices were hand scaled from analogue magnetograms (Bitterly *et al.*, 1997), where skilled observers would estimate S_r variations for the day and scale the K-values appropriately (Reay *et al.*, 2011). This was a time-consuming and naturally subjective exercise, leading to disagreements between observers and a delay in the access to the indices (Menvielle *et al.*, 1995).

Since the digitisation of data, a number of different digital scaling methods have been suggested. Menvielle *et al.* (1995) lists 12 such algorithms, and subjected a number of them to tests: comparing calculated K-index values with hand-scaled values. These algorithms include adaptive smoothing of geomagnetic data as used by BGS (Clark, 1992), frequency filtering methods and decomposition methods.

Menvielle *et al.* (1995) found the Finnish Meteorological Institute method (FMI) to be the best method of producing K-values in good agreement with hand scaled values. This method is what is used at the MagIE observatories, and is described in detail below.

FMI Method

The FMI method can be applied to calculate K-indices for any observatory around the world, assuming a correct scaling factor is used. As the intensity of geomagnetic perturbations increases with geomagnetic latitude, each observatory must choose an appropriate upper limit, K9, which will inform the rest of the scale. This is done by using the scale values at Niemegk using the following formula:

$$R^X_{lim,i} = R^X_{lim,9} \times R^{NGK}_{lim,i} / R^{NGK}_{lim,9}, \qquad i = 0, 1, 2, ..., 8, 9 \tag{3.1}$$

Table 3.1: K-index values and limits for MagIE sites and Niemegk. An upper value of 540 nT was chosen for Birr and Armagh.

K-Index Value	Limits of Range Classes, nT (Niemegk)	Limits of Range Classes, nT (Birr and Armagh)
0	0–5	0–5.4
1	5–10	5.4–10.8
2	10–20	10.8–21.6
3	20–40	21.6–43.2
4	40–70	43.2–75.6
5	70–120	75.6–129.6
6	120–200	129.6–216.0
7	200–330	216.0–356.4
8	330–500	356.4–540.0
9	500+	540+

Where the ith range limit for a site ($R^{X}_{lim,i}$) is compared to the range limits for Niemegk ($R^{NGK}_{lim,i}$). For Birr and Armagh, upper values of 540 nT are used. This value was used as it gave K-index values which best matched those seen in Hartland, Britain. The range limits used for Birr, Armagh and Niemegk are shown in Table 3.1. These values are then used in the steps below to calculate the local K-index (Stankov *et al.*, 2010):

1. The raw magnetometer data are binned into average minute values. It is then cleaned with a moving hour-long window. Any values which deviate more than 3σ are discarded.

2. The variation between the maximum and minimum of the two horizontal magnetic components (B_x and B_y) for each three hour bin (00-03 UT, 03-06 UT, 06-09 UT, etc.). is calculated. For each three hour bin, the largest variation in either B_x or B_y is compared to Table 3.1 to get an initial K-index K_1.

3. For each hour of the day, the average horizontal values for that hour $\pm(K_1 + m)$ minutes are calculated, where m is a constant which depends on the time of day (see Table 3.2). Together, these points give a rough estimate of the

Table 3.2: Values for m used in calculating approximate solar regular curve. This table is not dependent on time of year.

Hour of Day	m
00–03	120
03–06	60
06–18	0
18–21	60
21–00	120

solar-regular variation S_r. This estimated solar-regular variation can be seen in Figure 3.13 for quiet and disturbed periods.

4. This solar-regular variation is smoothed and subtracted from the data. A second K-index is then found (K_2) as in Step 2.

5. Steps 3 and 4 are repeated with K_2, and a final K-index is found for the day.

Example K-indices for the St. Patrick's Day storm at Birr are shown in Figure 3.14. Calculated K-indices for Birr and Armagh are calculated every five minutes and can be found at www.rosseobservatory.ie. If a K-index value of 5 or greater is registered at Birr, an automated notification email is sent out to a list of interested people. The Python program used to calculate the K-index is available at www.github.com/TCDSolar.

Kp-Index

The planetary K-index (Kp) is derived from the local K-index. It is used to communicate the disturbance of the Earth's magnetic field on a global scale, and is calculated from a weighted average of local K-indices for different regions. The Kp scale has values in the form: 0, 1-, 1o, 1+, 2-... 9o. The National Oceanic and Atmospheric Administration Space Weather Prediction Center (NOAA SWPC) update a Kp-index every three hours. This is calculated from 13 geomagnetic observatories between 44 and 60° northern or southern geomagnetic latitude.

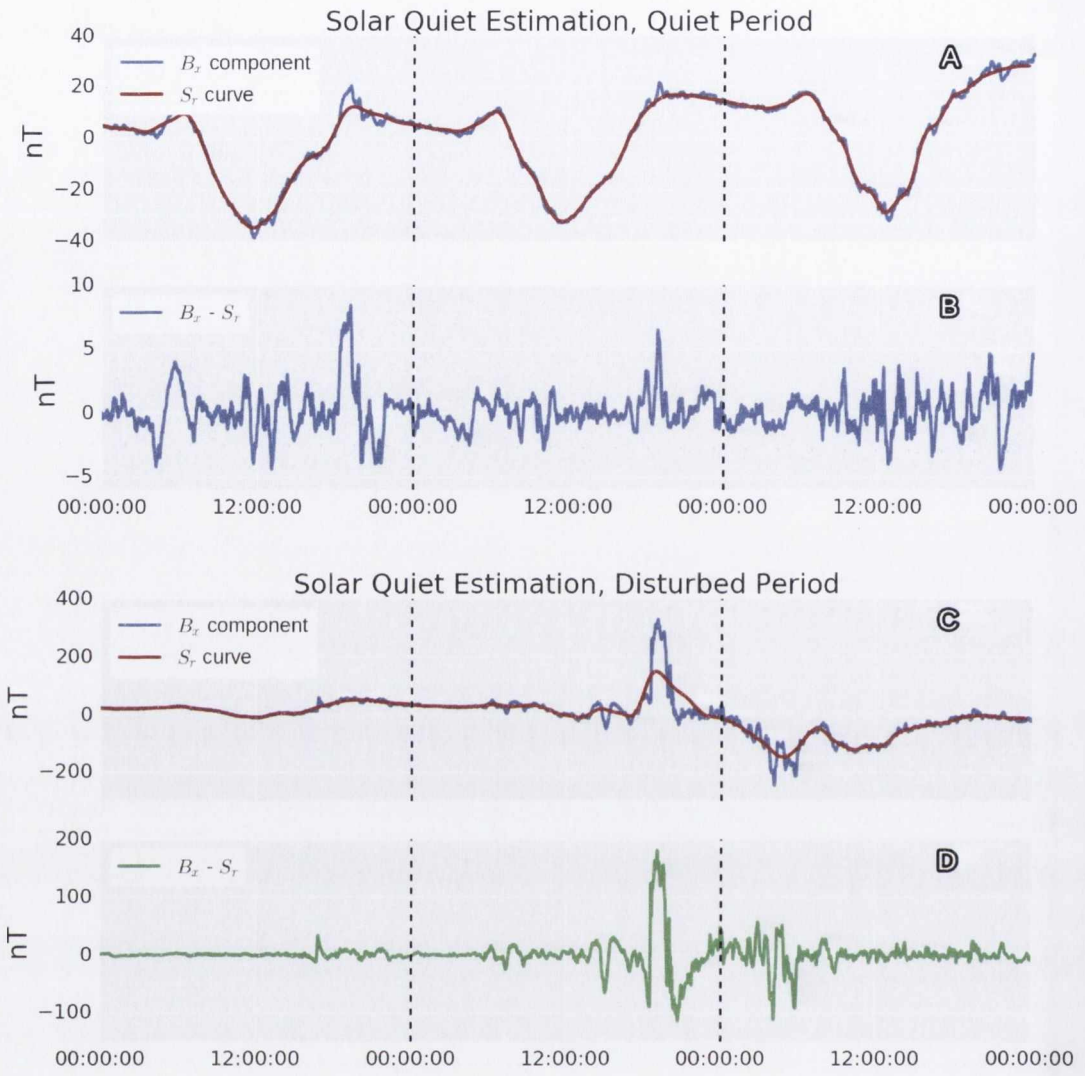


Figure 3.13: Measured B_x and estimated solar quiet curve for a quiet period (A and B) and a disturbed period (C and D). Figures A and C show measured B_x (blue) and calculated S_r using the FMI method (red). Figures B and D show B_x minus S_r for the quiet and disturbed periods respectively. These time series are what are used to calculate the K-index. The y-axis scale is different in the above plots for quiet and disturbed times.

Dst Index

The disturbed storm time (Dst) index is an indicator of magnetic activity constructed using hourly means of the horizontal component H at four equatorial

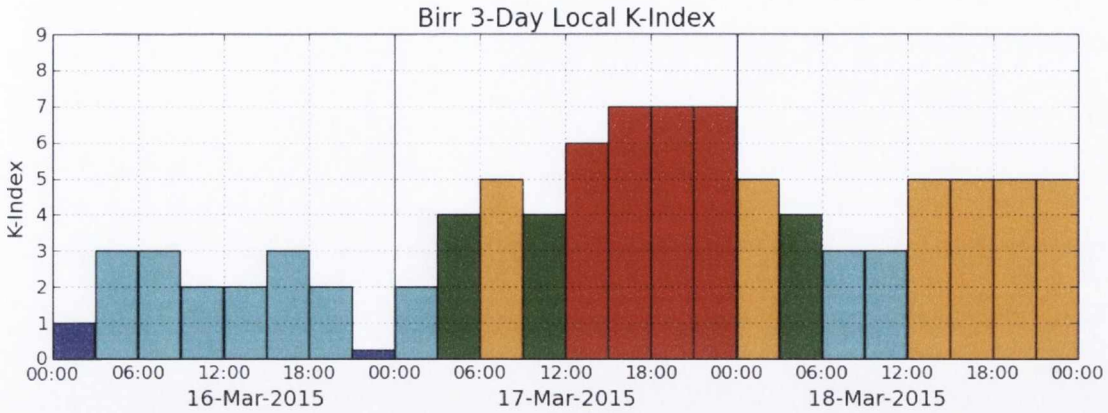


Figure 3.14: Three day local K-index at Birr for the St. Patrick's Day Storm. This was calculated using the FMI method. K-indices for Birr and Armagh can be found at www.rosseobservatory.ie.

magnetometer stations, and is given in nT. It is used as a proxy for measuring the globally symmetrical equatorial electrojet (or ring current) in the magnetosphere. Near the Equator, the North component of the magnetic field variation is dominated by this ring current. The Dst is a measure of the hourly average of this perturbation (Chave & Jones, 2012). The larger the amplitude of the negative value for the Dst, the more disturbed the occasion. The 2003 Halloween storms had a peak Dst of -383 nT (Marshall *et al.*, 2012), whereas the 1859 Carrington event had an estimated Dst of -850 nT (Siscoe *et al.*, 2006). Dst values can be found at the World Data Center for Geomagnetism (wdc.kugi.kyoto-u.ac.jp).

Summary

In order to study geomagnetic storm events in a region, it is necessary to have good spatial and temporal coverage of permanent geomagnetic observatories. In Ireland, Valentia observatory was the only long-term magnetic observatory from the 1800's to 2012. Since 2012, Trinity College and DIAS Geophysics have set up MagIE, the Irish magnetometer network to complement Met Éireann's Valentia observatory.

MagIE is composed of a number of temporary and permanent magnetic observatories across Ireland. Of these observatories, Birr and Armagh are currently

permanently installed. Each have a realtime data link to MagIE, and contribute data to www.rosseobservatory.ie. At each of these sites, a local K-index is calculated, and warning emails are sent out if eleveated activity is detected. Malin Head is currently a temporary installation, without realtime data connections. The data it has produced has been noise-free, and it would be a suitable location for a permanent magnetometer installation in the future. Leitrim and Sligo were two temporary sites which measured both E and B-fields. The equipment at Sligo was removed in late 2016, and currently there are no long-term electric field measurements in Ireland.

The data from each of these sites are used as inputs for GIC simulations. When simulating an historical geomagnetic storm, the more magnetic observatories one uses as inputs, the greater the accuracy of the calculations. This can be seen in Chapter 4. The following chapters detail each of the modelling steps needed to ultimately calculate GIC from magnetic data.

4

Spherical Elementary Current Systems

In this chapter, we outline the interpolation of measured magnetic fields across Ireland using spherical elementary current systems (SECS) during geomagnetic storm events. For this project, a Matlab SECS program provided by the British Geological Survey (Ciarán Beggan, BGS, personal communication, 2014) was ported to Python, and adapted for use in Ireland. The Python program was parallelised for speedier calculations. The interpolated magnetic fields from SECS are used as inputs for calculating electric fields, as will be shown in later chapters.

Spherical Elementary Current Systems

The Spherical Elementary Current Systems (SECS) technique is a method of interpolating horizontal surface geomagnetic fields to any given location using known geomagnetic measurements. It achieves this by assuming that the varying component of the magnetic field on the ground can be represented by a system of divergence-free equivalent currents in the ionosphere (although it has been used with satellite data to calculate actual ionospheric currents (Amm, 2001)). These equivalent currents are solved for true input magnetic data (from INTERMAGNET and MagIE sites, for example; see Chapter 3). The magnetic field at any

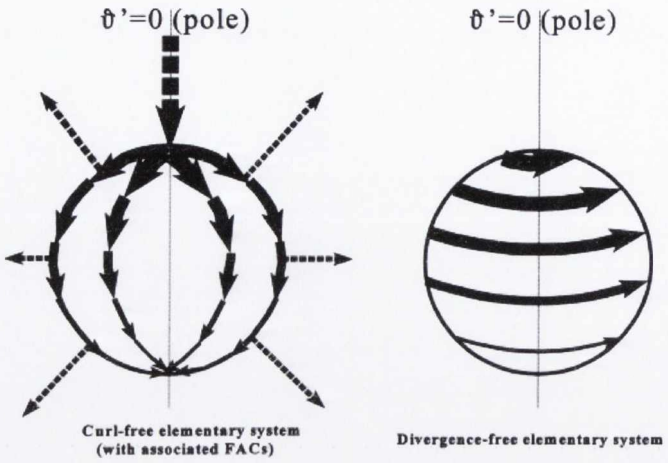


Figure 4.1: Sketch of spherical elementary current systems. On the left is a curl-free elementary system with field-aligned currents (FACs). This system does not produce any magnetic effect below the ionosphere, and so is not used in the SECS calculations. On the right is a divergence-free elementary system. After Amm & Viljanen (1999).

point on the ground can then be calculated as the sum of magnetic effects from these constructed currents.

The SECS method of interpolating the geomagnetic field from measurements was established by Amm (1997) and Amm & Viljanen (1999). It has been shown to be suitable for both high density local interpolation (Pulkkinen *et al.*, 2003a,b) and large-scale interpolation with sparse true magnetic measurements (McLay & Beggan, 2010).

The following is a summary description of the SECS method as appears in Amm (1997) and particularly Amm & Viljanen (1999). Amm (1997) derived two expressions for curl-free and divergence-free basis functions. These basis functions are known as elementary current systems (see Figure 4.1) in spherical geometry (r, θ, ϕ), which can be expanded to represent any ionospheric current system, regardless of the prevailing conductances or electric fields of the ionosphere. These functions are given below.

$$\mathbf{J}_{df}(r') = \frac{I_{0,df}}{4\pi R_I} \cot\left(\frac{\theta'}{2}\right) e_{\phi'} \tag{4.1}$$

$$\mathbf{J}_{cf}(r') = \frac{I_{0,cf}}{4\pi R_I}\cot\left(\frac{\theta'}{2}\right)e_{\theta'} \tag{4.2}$$

Where $\mathbf{J}_{df}(r')$ and $\mathbf{J}_{cf}(r')$ are divergence-free and curl-free currents, r', θ' and ϕ' are the radial, colatitude and longitude coordinates of the pole of the current system, R_I is the radius of the ionosphere and $I_{0,df}$ and $I_{0,cf}$ are the scaling factors (or currents) for the current systems.

By applying Helmholtz' theorem, which decomposes any vector field into curl-free and divergence-free components, Amm (1997) showed that the equivalent ionospheric current density ($\mathbf{J}_{eq}$) can be written as a sum of the elementary current systems described in Equations 4.1 and 4.2.

$$\mathbf{J}_{eq}(r) = \mathbf{J}_{cf}(r) + \mathbf{J}_{df}(r) \tag{4.3}$$

$$\mathbf{J}_{eq}(r) = \int\int \frac{\mathrm{div}_h\mathbf{J}(r')}{4\pi R_I}\cot\left(\frac{\theta}{2}\right)e_\theta d^2r' + \int\int \frac{\mathrm{curl}_h\mathbf{J}(r')}{4\pi R_I}\cot\left(\frac{\theta}{2}\right)e_\phi d^2r' \tag{4.4}$$

Where r' is the location of the pole of the spherical coordinate system. The magnetic field at Earth is a superposition of magnetic effects from a number of different sources in the ionosphere. These include Hall, Pedersen and field-aligned currents (FACs; see Chapter 2). However, Fukushima's Theorem shows that the curl free part of Equation 4.4 cancels any magnetic field component from FACs below the ionosphere. It can then be disregarded (Amm, 1997). Using Gauss' and Stoke's laws to change $\int\int_{K_r r\to 0}[\mathrm{curl}\mathbf{J}(r')]_r d^2r'$ to I_{df}, and disregarding the curl-free component of Equation 4.4, we get the following.

$$\mathbf{J}_{eq}(r) = \int\int \frac{I_{df}(r)}{4\pi R_I}\cot\left(\frac{\theta}{2}\right)e_\theta d^2r' \tag{4.5}$$

In order to calculate the ground magnetic field effect of $\mathbf{J}_{df}$, Amm & Viljanen (1999) derived $\mathbf{A}$, the current system's potential vector. It was shown that for a point with radius $r < R_I$ and pole angle θ' from the pole of the elementary current system, the magnetic field contribution of a divergence-free elementary current

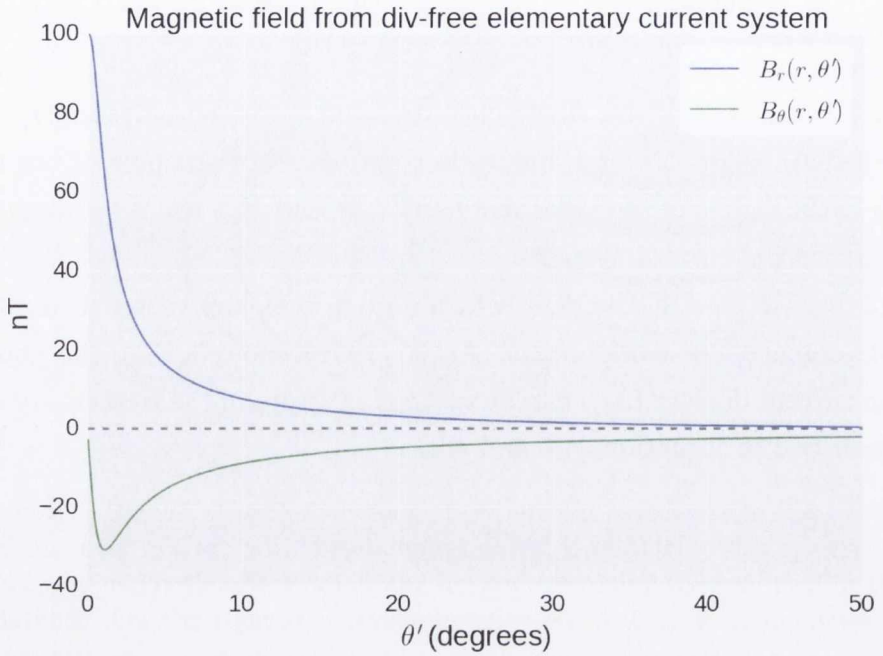


Figure 4.2: Ground magnetic effect of of divergence-free elementary current system with a scaling factor $I_0 = 10000$ A, as a function of colatitude. After Amm & Viljanen (1999).

system $\mathbf{J}_{df}$ with scaling factor I_0 flowing at $r = R_I$ is given by

$$B_{r'}(r,\theta') = \frac{\mu_0 I_0}{4\pi r}\left(\frac{1}{\sqrt{1-\frac{2r\cos\theta'}{R_I}+(\frac{r}{R_I})^2}}-1\right) \tag{4.6}$$

$$B_{\theta'}(r,\theta') = -\frac{\mu_0 I_0}{4\pi r\sin\theta'}\left(\frac{\frac{r}{R_I}-\cos\theta'}{\sqrt{1-\frac{2r\cos\theta'}{R_I}+(\frac{r}{R_I})^2}}+\cos\theta'\right) \tag{4.7}$$

The ground magnetic effect of an divergence-free elementary current system described by Equations 4.6 and 4.7 at the Earth's surface for a current of 10 kA is shown in Figure 4.2. It shows that $B_{r'}$ is largest when directly beneath the pole of the elementary current system. $B_{\theta'}$ starts at 0, and decreases to its minimum at approximately 1 degree from the pole. The amplitudes of both $B_{r'}$ and $B_{\theta'}$ decrease quickly with angle.

The ground magnetic field measurements can be related to the scaling factors

of the SECS with the following matrix formulation

$$\mathbf{Z} = \mathbf{T} \cdot \mathbf{I} \tag{4.8}$$

Where $\mathbf{Z}$ is the n_{obs} magnetic field measurements in the form

$$\mathbf{Z} = \begin{pmatrix} Z_{1,\theta} \\ Z_{1,\phi} \\ Z_{2,\theta} \\ Z_{2,\phi} \\ \vdots \\ Z_{n_{obs},\theta} \\ Z_{n_{obs},\phi} \end{pmatrix} \tag{4.9}$$

$\mathbf{I}$ is the unknown vector of scaling factors for the SECS in the form

$$\mathbf{I} = \begin{pmatrix} I_{0,df,1} \\ I_{0,df,1} \\ \vdots \\ I_{0,df,n_{el}} \end{pmatrix} \tag{4.10}$$

$\mathbf{T}$ is a matrix of geometrical factors which relate the SECS to ground measurements. It takes the form

$$\mathbf{T} = \begin{pmatrix} T_{11,\theta} & T_{12,\theta} & \cdots & T_{1n_{el},\theta} \\ T_{11,\phi} & T_{12,\phi} & \cdots & T_{1n_{el},\phi} \\ T_{21,\theta} & T_{22,\theta} & \cdots & T_{2n_{el},\theta} \\ T_{21,\phi} & T_{22,\phi} & \cdots & T_{2n_{el},\phi} \\ \vdots & \vdots & \vdots & \vdots \\ T_{n_{obs}1,\phi} & T_{n_{obs}2,\phi} & \cdots & T_{n_{obs}n_{el},\phi} \end{pmatrix} \tag{4.11}$$

Where each element of $\mathbf{T}$ in the form $T_{\{k,l\},\{\theta,\phi\}}$ relates the θ or ϕ component of the ground magnetic effect of an elementary current system with a scaling factor of 1 A and its pole at r_l, to an observation point r_k (Equations 4.6 and 4.7).

The problem is then solving for $\mathbf{I}$

$$\mathbf{I} = \mathbf{T}^{-1} \cdot \mathbf{Z} \tag{4.12}$$

Typically, the number of ground magnetic measurements is less than the number of SECS required to give a reasonable approximation of actual currents in the ionosphere. As such, Equation 4.12 is poorly conditioned. Singular value decomposition (SVD) is then employed to separate out the badly conditioned elements of $\mathbf{T}$. SVD decomposes a matrix $\mathbf{T}$ into

$$\mathbf{T} = \mathbf{U}\,\omega\mathbf{V}^{\mathbf{T}} \tag{4.13}$$

Where $\mathbf{U}$ and $\mathbf{V}^{\mathbf{T}}$ are orthogonal matrices, and ω is a diagonal matrix where $\omega_{m,m}, m = 1...n_{el}$ are the singular values of $\mathbf{T}$. By setting any of the diagonal values of ω which are less than 0.01 times the maximum value of ω to zero, the badly conditioned parts of $\mathbf{T}$ are separated out. $\mathbf{I}$ is then solved using

$$\mathbf{I} = \mathbf{V}(\mathrm{diag}(\omega_{m,m}))\mathbf{U}^{\mathbf{T}}\,\mathbf{B} \tag{4.14}$$

Once $\mathbf{I}$ is solved, the magnetic effect of the SECS at any ground point can be computed. It is important to reiterate that the elementary current systems found using the above method are only representative of the actual currents flowing in the ionosphere. Actual magnetic measurements at a site may include magnetic contributions from local magnetic anomalies. If used as an input for SECS, these purely local effects will be assumed to be caused by ionospheric currents, which can lead to inaccuracies in the SECS calculation. In addition, the steps taken to solve for $\mathbf{I}$ also mean that the equivalent currents give slightly smoothed magnetic fields at the surface.

The following sections describe the use and limitations of SECS in Ireland during a geomagnetic storm event.

Interpolating Geomagnetic Storms in Ireland

As described in Chapter 3, Ireland is a small country with multiple geomagnetic observatories currently operating. Valentia observatory, the oldest magnetic observatory in Ireland, has digital data available from 1989. The oldest MagIE observatory in Birr has been recording only since 2012. For different historical geomagnetic storm events, there will therefore be a different number of geomagnetic observatories available to use as inputs for interpolating the geomagnetic field via SECs. As will be shown in the following section, the number of geomagnetic inputs one has affects the accuracy of a SECS interpolated geomagnetic field across even a small area such as Ireland.

In order to assess how the number of magnetic inputs affect the interpolated geomagnetic field, three scenarios were investigated for the 22-23 June 2015 geomagnetic storm. This storm had a maximum planetary K-index of 8+, and was chosen as four geomagnetic observatories were functioning in Ireland for its duration. The three scenarios are as follows:

1. Use Valentia's geomagnetic data as sole measurement for the whole of Ireland, and compare it to the measured data at the MagIE sites.

2. Interpolate the geomagnetic field across Ireland using SECS with only INTERMAGNET site data as inputs.

3. Interpolate the geomagnetic field using SECS with INTERMAGNET and MagIE site data as inputs.

The ratio of estimated and measured horizontal magnetic field (B_h^{obs}/B_h^{int}), the root-mean-square-difference (RMSD) and peak differences between measured and calculated magnetic field ($B_h^{obs} - B_h^{int}$) for each of the scenarios listed above at each MagIE site can be seen in Table 4.1.

The RMSD is defined as

$$\mathrm{RMSD}_{oc} = \sqrt{\frac{\sum_{i=1}^{N}(o_i - c_i)^2}{N}} \tag{4.15}$$

where o_i and c_i are the ith observed and calculated points from a total of N.

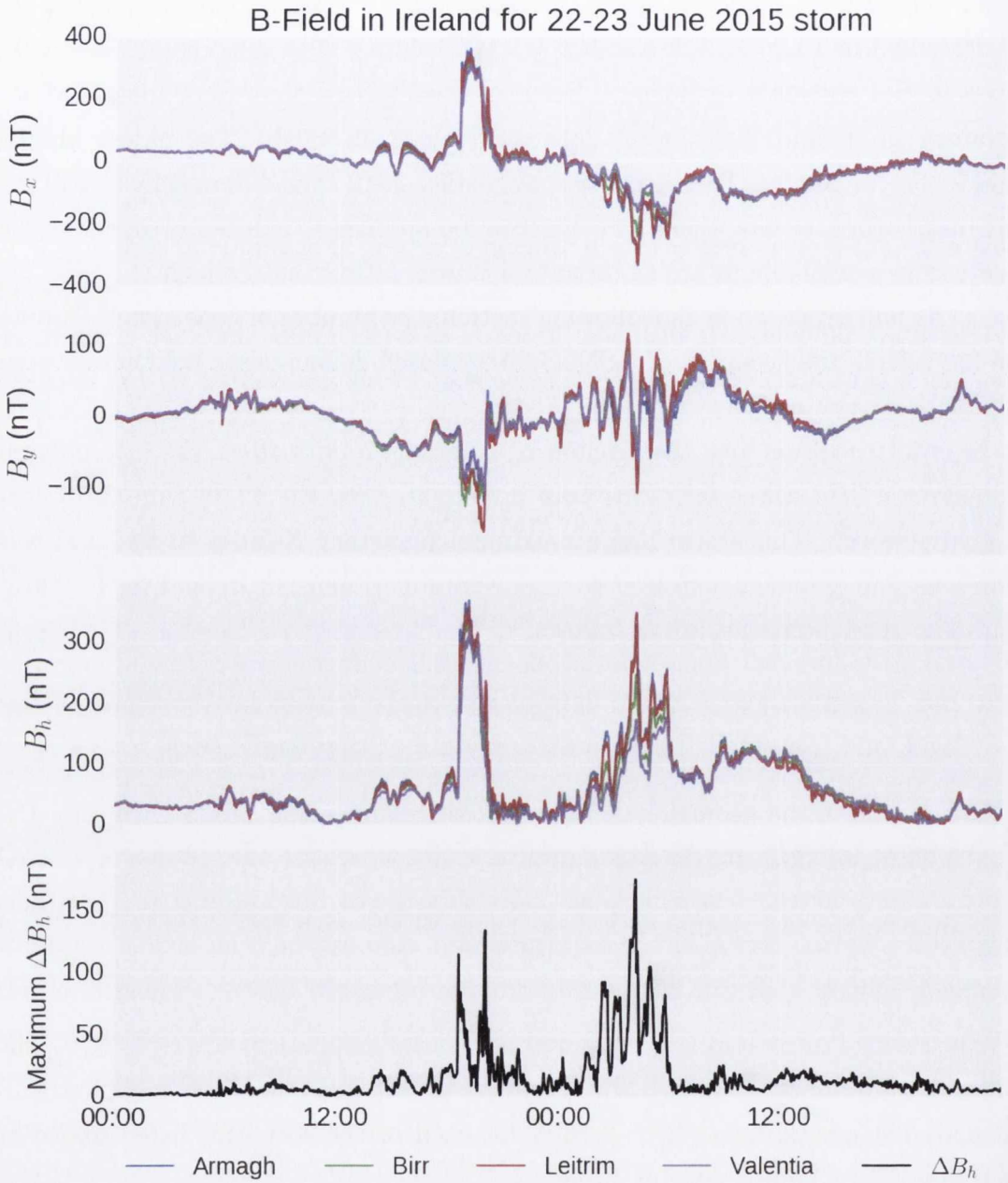


Figure 4.3: Magnetic measurements in Ireland during the 22-23 June 2015 storm. Four magnetic observatories were operating during the storm. The top three plots show the measured B_x, B_y and B_h components at each site. The bottom plot shows the largest difference between each of the sites during the storm.

Table 4.1: The errors in interpolating the geomagnetic field in Ireland during the 22-23 June 2015 geomagnetic storm using different inputs. B_h^{obs} and B_h^{int} refer to the observed and interpolated horizontal geomagnetic fields. Using Valentia only as an input for the whole of Ireland underestimated the magnetic field, with the underestimation becoming more apparent at sites further North. Using only INTERMAGNET sites with SECS overestimated each site by approximately 40% at each site. Adding two of the three Irish sites to the SECS interpolation (SECS2) reduced the overestimation slightly in Armagh and Birr, and considerably reduced the overestimation in Leitrim.

	Armagh			Leitrim			Birr		
Interpolation	B_h^{obs}/B_h^{int}	RMSD (nT)	$B_h^{obs} - B_h^{int}$ (nT)	B_h^{obs}/B_h^{int}	RMSD (nT)	$B_h^{obs} - B_h^{int}$ (nT)	B_h^{obs}/B_h^{int}	RMSD (nT)	$B_h^{obs} - B_h^{int}$ (nT)
Valentia only	0.4	20.0	175	0.49	18.5	176	0.69	9.87	75
SECS with INTERMAGNET	1.41	14.528	-145	1.42	19.38	-147	1.40	12.45	-99
SECS with INTERMAGNET + MagIE	1.39	14.56	-137	1.14	12.345	-50	1.37	9.16	-93

Valentia as sole measurement for Ireland

If an area of interest is small enough, a single magnetic observatory can be used as an input for GIC simulations. The larger the area, the more spatially variable the geomagnetic field will be during a storm event, and therefore less suitable a single measurement will be. For Ireland, Valentia would be the obvious observatory to use in this manner, as it has been recording for the longest time. It is instructive to see how much the geomagnetic field changes between Valentia and the other observatory sites in Ireland during a storm. Figure 4.3 shows the measured B_x, B_y and B_h components at each observatory in Ireland. A baseline value for the two-day period was removed from each component.

The bottom plot shows largest difference between all of the observatories during the storm. To use the Valentia magnetometer for the whole of Ireland would underestimate the horizontal magnetic field, although those sites closer to Valentia were underestimated less than those further away. For example, the magnetic field at Valentia underestimated the measured field in Birr by 75 nT, but underestimated the magnetic field in Armagh by 176 nT during the peak activity of the storm.

SECS-interpolated geomagnetic field using INTERMAGNET sites only

Four sites were then used to interpolated the geomagnetic field across Ireland using SECS. These were Valentia, Eskdelmuir, Hartland and Lerwick. These sites are the only observatories near or in Ireland which have measured geomagnetic data during storm events pre-2012. They are therefore particularly important for reconstructing the geomagnetic field during events such as the October 2003 and March 1989 storms.

The measured and SECS interpolated horizontal geomagnetic fields at Birr, Armagh and Leitrim are shown in Figure 4.5a. For each site, SECS overestimates the geomagnetic field, particularly during the more disturbed parts of the storm. During the least well modelled part of the storm (0200 UT to 0300 UT 23 June), the modelled B_h overestimates the actual magnetic field at each site by approximately 40% (see Table 4.1).

SECS-interpolated geomagnetic field using INTERMAGNET and MagIE sites

The final test included the MagIE sites in the SECS interpolation. The SECS calculated horizontal magnetic field over all of Ireland using Valentia, Birr, Leitrim, Armagh, Eskdelmuir, Hartland and Lerwick at different times during the storm is shown in Figure 4.4.

To check how the addition of the MagIE sites affected the SECS calculation, the field was interpolated at each MagIE site using the INTERMAGNET sites and the two other MagIE sites as inputs. For example, the magnetic field at Armagh was interpolated using the magnetic inputs from Birr and Leitrim, as well as the INTERMAGNET sites.

The interpolated magnetic field at each of the MagIE sites is seen in Figure 4.5b, and the interpolation across Ireland is shown in Figure 4.4. The addition of two MagIE sites slightly improved the SECS simulation at Armagh and Birr, reducing the overestimate to approximately 39% when compared to only using INTERMAGNET sites as intputs. The modelled magnetic field at Leitrim improved significantly, reducing the overestimate to 50 nT, whereas using INTERMAGNET sites only had an overestimate of 147 nT.

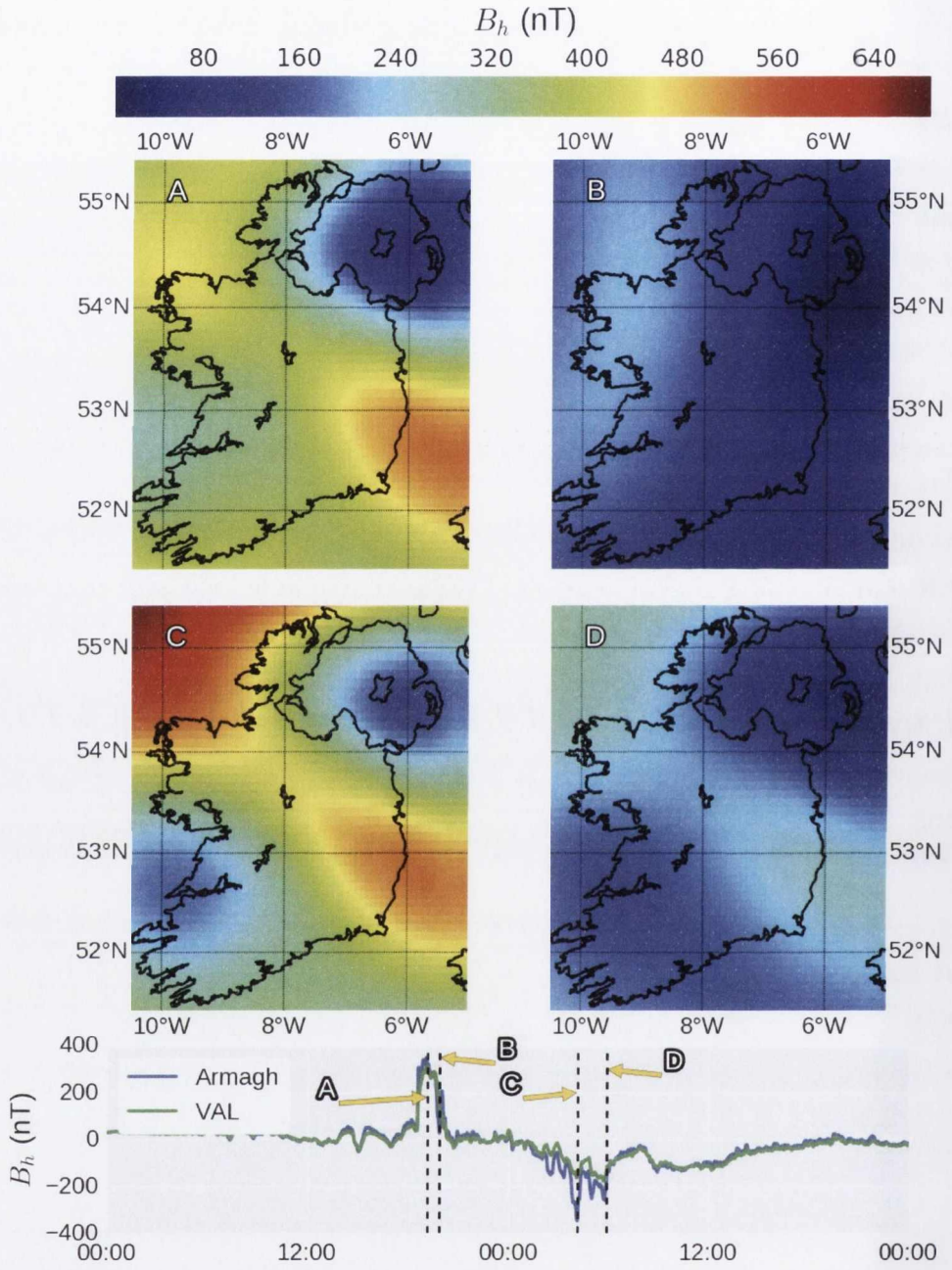
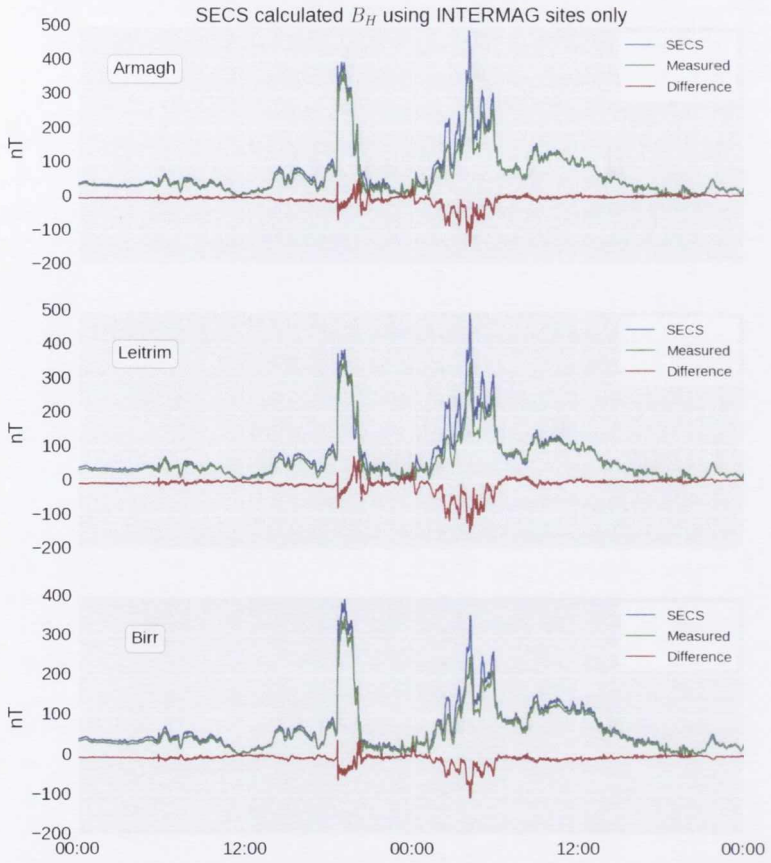
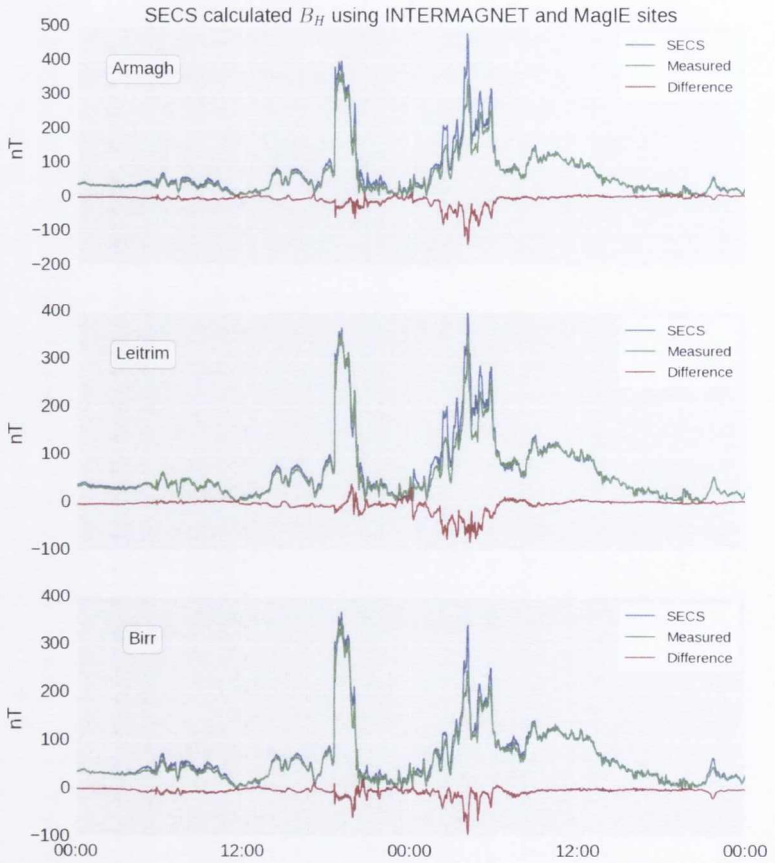


Figure 4.4: The SECS interpolated B_h across Ireland at four points during the June 2015 event using INTERMAGNET and MagIE sites as inputs. The top four plots (A, B, C and D) correspond to the dashed lines in the bottom plot, which shows the measured B_h time series for Armagh and Valentia. Armagh sees marginally larger variations in the magnetic field than Valentia.



(a) SECS using INTERMAGNET as inputs



(b) SECS using INTERMAGNET and MagIE as inputs

Figure 4.5: Measured and modelled horizontal geomagnetic field in three sites in Ireland for the 22-23 June 2015 event. (a) shows the modelled field using only INTERMAGNET sites as inputs. (b) shows the same sites using INTERMAGNET and two of the three MagIE sites as inputs. Overall, the addition of two MagIE sites improved the accuracy of the modelled geomagnetic fields around Ireland (see Table 4.1).

Summary

As can be seen from Table 4.1, there are errors in each of the three scenarios when interpolating or extrapolating the magnetic field across Ireland. Using Valentia alone as a measurement for the whole of Ireland underestimates the magnetic field at the more northerly MagIE sites by at least 75 nT. This error increases the further away from Valentia one travels, increasing to 176 nT for Armagh. The shape of the time-series also reflects this fact, with Birr having a lower RMSD error (9.87 nT) than Leitrim (18.5 nT) and Armagh (20.0 nT).

Using SECS with INTERMAGNET sites also has a large error, although it is an overestimate rather than an underestimate. Each of the MagIE sites were overestimated by approximately 40%. This was a uniform error across Ireland, at least for this particular event (22-23 June 2015). The RMSD errors range from 12.45 nT for Birr to 19.38 nT for Leitrim.

Adding two of the three MagIE sites to the SECS calculation improves the accuracy of the modelled magnetic fields at each of the MagIE sites, although it still overestimates the true values. This improvement is most clear in the Leitrim site. Including Armagh and Birr in the SECS calculation reduces the overestimate by 97 nT at the storm's peak at this site.

From the above, it is clear that SECS is not a perfect method of interpolating geomagnetic data across Ireland. However, even using only INTERMAGNET sites as inputs, it gives a more accurate representation of the geomagnetic field across Ireland when to using Valentia as a single uniform geomagnetic measurement. The addition of the MagIE sites leads to a marginal increase in accuracy in two of the three sites, and a considerable improvement in one (see Table 4.1). It can be concluded that in the case of Ireland for the June 2015 event, the more sites whose data is included in the SECS calculation, the greater the accuracy of the interpolated geomagnetic field.

Once a method of interpolating the geomagnetic field across a region is chosen, this magnetic field can be used as inputs to calculate surface electric fields which drive GICs. This process is explored in the next chapter.

5

Magnetotellurics and The Thin-Sheet Method

Due to the difficulty in acquiring long-term surface electric field measurements (see Chapter 3), it is often necessary to calculate surface electric fields when recreating GICs for historical events. To do this requires an input magnetic field (as calculated in Chapter 4 using SECS), and a regional model of the Earth's conductivity structure. The geoelectric field can then be calculated using a number of different electromagnetic methods. Two of the more popular methods of calculating electric fields in GIC studies are magnetotellurics (MT), and the thin-sheet method.

In this chapter, the MT method will be described in brief. Different simplifications to the method will be outlined, and the historical MT measurements taken in Ireland will be described. The resistivity model of Ireland's subsurface is derived from these historical measurements, and will also be described.

Following the description of MT, the thin-sheet method of electric field calculation will be briefly outlined, along with the different variables that need to be taken into account when using the thin-sheet method.

Using both the MT and thin-sheet methods to calculate electric fields outlined in this chapter, the geoelectric field response of Ireland will be simulated for several

storm events in Chapter 7.

Magnetotellurics

MT is a passive source geophysical exploration method which relates surface geomagnetic and geoelectric fields to the Earth's conductivity structure, and is historically accepted as being discovered by Tikhonov and Cagniard concurrently in the 1950s (Chave & Jones, 2012). By simultaneously measuring both surface electric and magnetic fields at a location, it allows one to infer the conductivity structure of the ground at varying depths. Once a model of the ground conductivity is constructed, the model can be mapped to the conductive properties of rocks which are measured in laboratory tests (Nover, 2005; Yoshino, 2010). This allows for the subsurface geology of a region to be identified.

Knowing the conductivity structure of the ground has many practical applications not limited to simulating electric fields for space weather studies. Depending on the conditions at a particular site and the method and equipment used, the conductivity of the subsurface from a few metres to several hundred kilometres deep can be investigated using MT (or more broadly, electromagnetic) methods. MT can be used for mineral exploration (Farquharson & Craven, 2009; Varentsov *et al.*, 2013), hydrocarbon exploration (Strack, 2012; Streich, 2016), carbon sequestration (Ogaya *et al.*, 2013, 2014) and thermal energy (Berktold, 1983; Munoz, 2014; Stegena, 1976), as well as for more academic studies to determine the nature of the subsurface.

In terms of space weather and the study of GICs, MT is commonly used to calculate electric fields as it is fast and easy to implement. It has been used across the globe for GIC studies including North America (Bedrosian & Love, 2015; Love *et al.*, 2016; Wei *et al.*, 2013), China (Zhang *et al.*, 2015), Australia (Marshall *et al.*, 2013), Spain (Torta *et al.*, 2014, 2017), Sweden (Wik *et al.*, 2008), Finland (Viljanen & Pirjola, 1994) and Ireland (Blake *et al.*, 2016b), among others.

The MT method has also been used specifically to create resistivity maps for later use with GIC calculations (Ádám *et al.*, 2012; Viljanen *et al.*, 2012). In this study, MT measurements taken around Ireland are used to make a resistivity

model of Ireland's subsurface. The MT method is then used to calculate electric fields for GIC simulations.

Description of MT

The following description of MT in this chapter is not intended to exhaustive. MT will be described only so far as it is used in this study to generate resistivity models of Ireland and replicate electric fields for GIC calculations. More detailed descriptions of the method can be found in Cagniard (1953); Chave & Jones (2012); Naidu (2012); Simpson & Bahr (2005) and Miensopust (2010), each of which are used for the description of MT given below.

MT Sources

Many different sources contribute to the time-varying electromagnetic fields which allow for the MT method. These can be from the core of the Earth itself to extra-terrestrial bodies and processes. The signals can be separated into two categories.

1. The first is the low frequency signals (< 1 Hz). These signals originate with the interaction of solar plasma with the ionosphere and magnetosphere (Chave & Jones, 2012). As the solar wind disturbs the Earth's ambient magnetic field, low-frequency electromagnetic waves are produced from the dynamic variations of plasma.

2. High frequency signals (>10 Hz) are caused by lightning strikes that propagate within the Earth-ionosphere boundaries, which act as a waveguide. These high frequency signals allow for audiomagnetotellurics (AMT). AMT is used for shallow studies of upper crustal features, for reasons which will be outlined below.

Between the two source ranges (at around 1 Hz), there is a lack of signal from sources. This is known as the MT dead-band. The lack of energy results in unreliable MT response estimates (Garcia & Jones, 2008). Long-period signals need to be measured for a longer period of time compared to the high-period signals, in order to get enough cycle samples. As such, a long-period MT site (<1 Hz) can be installed to collect data for months at a time.

Maxwell's Equations

To begin to describe MT, it is useful to start with Maxwell's Equations, which describe electromagnetic fields within materials (Fleisch, 2008). These are

$$\nabla \cdot \mathbf{E} = \frac{\rho_v}{\epsilon_0} \qquad \text{Gauss' Law} \tag{5.1}$$

where $\mathbf{E}$ is the electric field, ρ_v is charge density, ϵ_0 is electric permittivity of free space. Gauss' law states that the electric field given by an electric charge diverges from positive charge and converges upon negative charge .

$$\nabla \cdot \mathbf{B} = 0 \qquad \text{Gauss' Law for magnetism} \tag{5.2}$$

where $\mathbf{B}$ is the magnetic field. Gauss' law for magnetism states that the divergence of the magnetic field at any point is 0, or that no magnetic monopoles exist.

$$\nabla \times \mathbf{E} = -\frac{\partial B}{\partial t} \qquad \text{Faraday's Law} \tag{5.3}$$

Faraday's law states that a circulating electric field is produced by a magnetic field that changes with time.

$$\nabla \times \mathbf{B} = \mu_0\left(\mathbf{J} + \epsilon_0 \frac{\partial E}{\partial t}\right) \qquad \text{Ampère-Maxwell's Law} \tag{5.4}$$

where $\mathbf{J}$ is current density and μ_0 is magnetic permeability of free space. Ampère-Maxwell's law states that a circulating magnetic field is produced by an electric current and by an electric field that changes with time.

Maxwell's equations can also be expressed through the three constitutive relationships, which relate electromagnetic fields to the properties of materials through which they propagate:

$$\mathbf{J} = \sigma \mathbf{E} \qquad \text{Ohm's Law} \tag{5.5}$$

where σ is the electrical conductivity of a material (inverse of electrical resistivity ρ).

$$\mathbf{D} = \epsilon \mathbf{E} \tag{5.6}$$

where $\mathbf{D}$ is the displacement current, ϵ is the electric permittivity, which is defined as $\epsilon = \epsilon_r \cdot \epsilon_0$. The relative electrical permittivity (ϵ_r) ranges from 1 in a vacuum to around 80 for water.

$$\mathbf{B} = \mu\mathbf{H} \tag{5.7}$$

where μ is the magnetic permeability and $\mathbf{H}$ is the magnetic field strength. For most materials in the Earth, the magnetic permeability can be approximated to its value in a vacuum $\mu_0 = 4\pi \times 10^{-7}$.

Assumptions of MT

When considering EM induction in the Earth, the following simplifying assumptions are considered applicable (Naidu, 2012; Simpson & Bahr, 2005):

1. Maxwell's equations are always obeyed.
2. The Earth only absorbs and dissipates EM energy. It does not generate EM energy.
3. All fields are conservative and differentiable away from their sources.
4. EM source fields are treated as uniform plane-polarised EM waves generated at a distance, which propagate into the Earth at a near-vertical angle of incidence.
5. The Earth does not accumulate charges in a 1D Earth. In a 2/3D Earth, charges can accumulate along conductivity discontinuities.
6. The Earth acts as an Ohmic conductor, obeying Equation 5.5.
7. The 'quasi-static' approximation holds for the total current density. This means that time-varying displacement currents ($\partial\mathbf{D}/\partial t$) are negligible compared to conduction currents. This allows for EM induction in the Earth to be treated as a diffusive process.
8. The bulk electrical and magnetic properties of rocks are more important than the electrical and magnetic properties of minerals within rocks.

Boundary Conditions

Across a discontinuity between two materials 1 and 2, the following boundary conditions can be applied to EM fields and currents described by Maxwell's equations (Miensopust, 2010; Naidu, 2012), where $\hat{n}$ is the unit vector normal to the discontinuity boundary:

$$E_2^t - E_1^t = 0 \tag{5.8}$$

The tangential component of the electric field is continuous across the boundary between the materials.

$$H_2^t - H_1^t = 0 \tag{5.9}$$

If there is no surface current, the tangential components of the magnetic field are continuous across the boundary.

$$\hat{n} \times (D_2 - D_1) = \rho_s \tag{5.10}$$

As there are two materials with different properties, there is an accumulation of surface charge density ρ_s. This means that the displacement current D is discontinuous across the boundary.

$$\hat{n} \times (B_2 - B_1) = 0 \tag{5.11}$$

The normal magnetic field is continuous across the boundary.

$$\hat{n} \times (J_2 - J_1) = 0 \tag{5.12}$$

The normal components of the current density are continuous across the boundary, given that displacement currents are ignored.

Diffusion Equations and EM Skin-Depth

Taking the MT assumptions and boundary conditions into account, Maxwell's equations can be simplified in the following manner. When considering a plane

electromagnetic wave propagating to the ground ($+z$ direction), solutions to the the electric and magnetic waves can be expressed as

$$\mathbf{E} = \mathbf{E}_0 e^{i\omega t - \mathbf{k}z} \tag{5.13}$$

$$\mathbf{B} = \mathbf{B}_0 e^{i\omega t - \mathbf{k}z} \tag{5.14}$$

where $\mathbf{E}_0$ and $\mathbf{B}_0$ are the amplitudes of $\mathbf{E}$ and $\mathbf{B}$ at their origin, ω is angular frequency and $\mathbf{k}$ is wavenumber. From these, it can be seen that

$$\frac{\partial \mathbf{B}}{\partial t} = i\omega\mathbf{B} \qquad \text{and} \qquad \frac{\partial \mathbf{E}}{\partial t} = i\omega\mathbf{E} \tag{5.15}$$

Using these solutions, along with Equations 5.5 to 5.7, and the vector identity

$$\nabla \cdot (\nabla \times \mathbf{F}) = 0 \tag{5.16}$$

for a vector $\mathbf{F}$, Maxwell's equations can be rewritten as

$$\nabla \cdot \mathbf{E} = -\mathbf{E}\nabla \ln\sigma \tag{5.17}$$

$$\nabla \cdot \mathbf{B} = 0 \tag{5.18}$$

$$\nabla \times \mathbf{E} = -i\omega\mathbf{B} \tag{5.19}$$

$$\nabla \times \mathbf{B} = \mu_0\sigma\mathbf{E} \tag{5.20}$$

In the absence of charges, $\mathbf{E}$ and $\mathbf{B}$ depend only on ω and σ. Taking these equations, one can apply the following identities:

$$\nabla \times (\nabla \times \mathbf{F}) = \nabla(\nabla \cdot \mathbf{F}) - \nabla^2\mathbf{F} \tag{5.21}$$

$$\nabla \times (\chi\mathbf{F}) = \chi\nabla \times \mathbf{F} - \mathbf{F} \times \nabla\chi \tag{5.22}$$

where χ is a scalar. Taking the curl of the Equation 5.20, and assuming that in the Earth $\nabla \cdot \mathbf{E} = 0$:

$$\nabla \times \nabla \times \mathbf{E} = (\nabla \cdot \nabla \mathbf{E}) - \nabla^2 \mathbf{E}$$

$$\nabla \times \left(- \frac{\partial \mathbf{B}}{\partial t} \right) = 0 - \nabla^2 \mathbf{E}$$

$$\nabla^2 \mathbf{E} = \frac{\partial}{\partial t} (\nabla \times \mathbf{B})$$

$$\nabla^2 \mathbf{E} = \mu_0 \sigma \frac{\partial \mathbf{E}}{\partial t} = i\omega\mu_0\sigma\mathbf{E} \tag{5.23}$$

Assuming a plane wave, one can substitute Equation 5.15 into the right hand side to get

$$\nabla^2 \mathbf{E} = i\omega\mu_0\sigma\mathbf{E} \tag{5.24}$$

Similarly for the magnetic fields:

$$\nabla^2 \mathbf{B} = i\omega\mu_0\sigma\mathbf{B} \tag{5.25}$$

These are the diffusive equations which tell us how the EM signals are dissipated and attenuated when travelling through a medium. For example, in air, with a σ of approximately 0, there is no significant attenuation. Equations 5.24 and 5.25 are 2^{nd} order partial differential equations with solutions valid for a vertical external source field:

$$\mathbf{E} = \mathbf{E}_1 e^{i\omega t - qz} + \mathbf{E}_2 e^{i\omega t + qz} \tag{5.26}$$

$$\mathbf{B} = \mathbf{B}_1 e^{i\omega t - qz} + \mathbf{B}_2 e^{i\omega t + qz} \tag{5.27}$$

The 2^{nd} terms in Equations 5.26 and 5.27 increase with increasing depth (z), but as we assume that the Earth does not generate energy (assumption 2 in Section 5.1.1.3), we set $\mathbf{E}_2$ and $\mathbf{B}_2$ equal to 0.

In the case of a homogenous halfspace with uniform σ (i.e., $\frac{\partial \mathbf{E}}{\partial t} = \frac{\partial \mathbf{B}}{\partial t} = 0$), we can take a second derivative of Equation 5.26

$$\frac{\partial^2 \mathbf{E}}{\partial z^2} = q^2 \mathbf{E}_1 e^{i\omega t - qz} = q^2 \mathbf{E} \tag{5.28}$$

As our medium is a uniform halfspace with $\frac{\partial \mathbf{E}}{\partial t} = \frac{\partial \mathbf{B}}{\partial t} = 0$, it can be seen that

$$\nabla^2 \mathbf{E} = \frac{\partial^2 \mathbf{E}}{\partial z^2} \tag{5.29}$$

Equating Equation 5.24 with Equation 5.28:

$$q^2 \mathbf{E} = i\omega\mu_0\sigma\mathbf{E}$$

$$q = \sqrt{i\omega\mu_0\sigma} \tag{5.30}$$

The inverse of the real part of q is known as the electromagnetic skin depth. It describes the depth an electromagnetic wave with angular frequency ω will penetrate into a medium with electric conductivity σ before its amplitude is attenuated by a factor of 1/e. It is commonly given as

$$\delta(\omega) = \sqrt{\frac{2}{\omega\mu_0\sigma}} \approx 503\sqrt{\rho T} \tag{5.31}$$

where T is the period in seconds and ρ is resistivity (Chave & Jones, 2012). Figure 5.1 shows the calculated skin-depth for different resistivities and periods. As can be seen, higher frequency waves attenuate quicker than lower frequency waves. As such, longer periods are required to probe deeper into the Earth. It can also be seen that waves will attenuate quicker when propagating through conductive materials.

MT Transfer Function and Dimensionality

The MT transfer functions relate the measured electric and magnetic fields at different frequencies to the the conductivities of the local geology. There are a

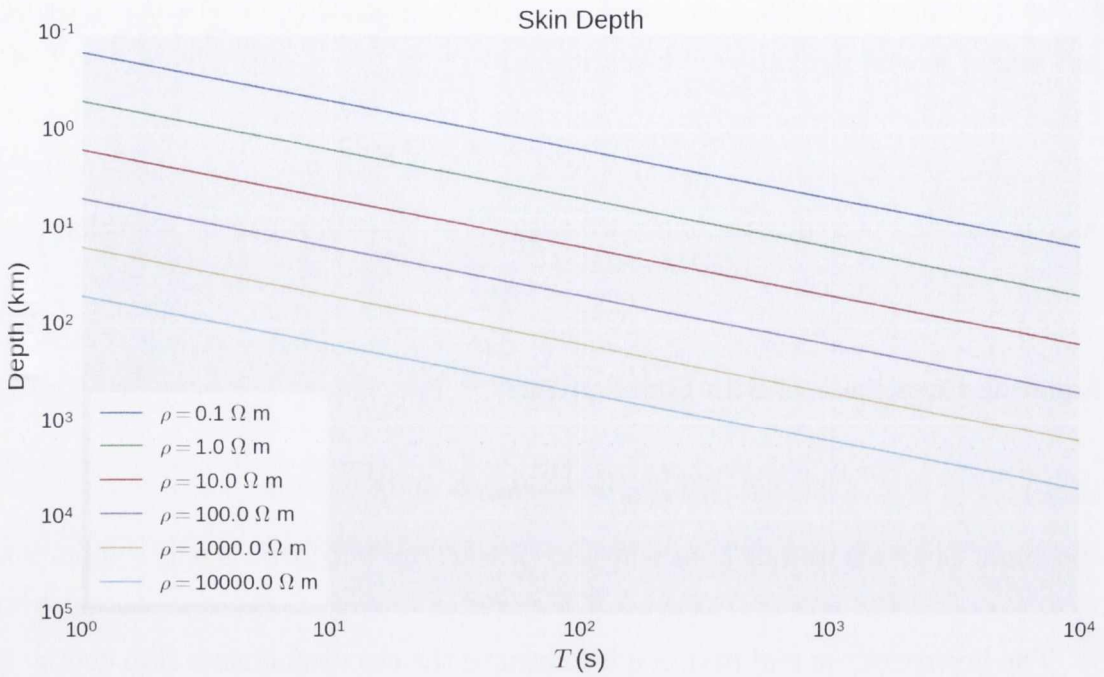


Figure 5.1: The skin-depth of signals of different period T propagating in media with different resistivities ρ.

number of different transfer functions in use in MT, but the most well known uses the MT impedance tensor (Z):

$$\mathbf{E}(\omega) = \left(\frac{1}{\mu_0}\right)\mathbf{Z}(\omega) \cdot \mathbf{B}(\omega) \tag{5.32}$$

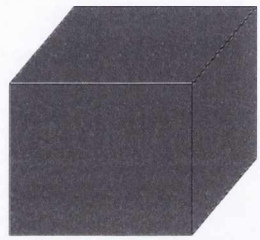
where ω is frequency. In its expanded form:

$$\begin{pmatrix} E_x(\omega) \\ E_y(\omega) \end{pmatrix} = \frac{1}{\mu_0} \begin{pmatrix} Z_{xx}(\omega) & Z_{xy}(\omega) \\ Z_{yx}(\omega) & Z_{yy}(\omega) \end{pmatrix} \begin{pmatrix} B_x(\omega) \\ B_y(\omega) \end{pmatrix} \tag{5.33}$$

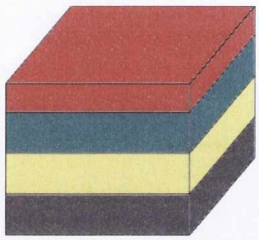
This outlines how the relationship between **E** and **B** depends on **Z**, the MT tensor or response function. The **Z** tensor contains information regarding the resistivity of the ground, and can be constructed for different resistivity profiles. The components of **Z** are complex.

The simplest case is for an homogenous Earth with uniform conductivity in all dimensions. For a simple, layered resistivity structure that varies only with depth,

$$\begin{pmatrix} E_x \\ E_y \end{pmatrix} = \frac{1}{\mu_0} \begin{pmatrix} 0 & Z_{xy} \\ -Z_{xy} & 0 \end{pmatrix} \begin{pmatrix} B_x \\ B_y \end{pmatrix} \qquad \begin{pmatrix} E_x \\ E_y \end{pmatrix} = \frac{1}{\mu_0} \begin{pmatrix} 0 & Z_{xy} \\ -Z_{xy} & 0 \end{pmatrix} \begin{pmatrix} B_x \\ B_y \end{pmatrix}$$

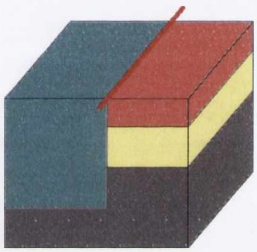


Homogenous Earth

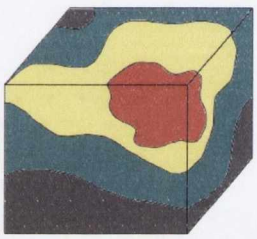


1-D Earth

$$\begin{pmatrix} E_x \\ E_y \end{pmatrix} = \frac{1}{\mu_0} \begin{pmatrix} 0 & Z_{xy} \\ Z_{yx} & 0 \end{pmatrix} \begin{pmatrix} B_x \\ B_y \end{pmatrix} \qquad \begin{pmatrix} E_x \\ E_y \end{pmatrix} = \frac{1}{\mu_0} \begin{pmatrix} Z_{xx} & Z_{xy} \\ Z_{yx} & Z_{yy} \end{pmatrix} \begin{pmatrix} B_x \\ B_y \end{pmatrix}$$



2-D Earth



3-D Earth

Figure 5.2: The different dimensionality regimes and their MT tensors. Different colours denote different resistivities. Its important to note that the different resistivity regions do not necessarily align with different rock types. The red line in the 2D Earth indicates the direction of the strike (or geological discontinuity). In this study, the homogenous, 1D Earth and 3D earth models are used to replicate E-fields for calculating GICs.

a 1D approach is used. A 2D approach is used when the geology changes with depth and in one horizontal direction. For complex areas, a full 3D MT approach is used (see Section 5.1.2.4). Each case is depicted in Figure 5.2, and explained below.

Homogenous Earth

The simplest scenario for modelling the Earth is to treat it as a uniform halfspace: i.e., the conductivity of the Earth does not vary with any direction. The trans-

fer function which describes this is the Schmucker-Weidelt function (C). This is defined as

$$C = \frac{1}{q} \tag{5.34}$$

where q is defined in Equation 5.30. C depends on frequency and is complex. For a homogenous half-space, the real and imaginary parts of C have equal magnitudes. With the following relationship

$$E_x = E_{1x} e^{i\omega t - qz} \quad , \quad \frac{\partial E_x}{\partial t} = -qE_x \tag{5.35}$$

and using Equation 5.15 with Equation 5.35, we get the following

$$qE_y = -i\omega B_x \qquad \text{and} \qquad qE_x = i\omega B_y \tag{5.36}$$

This gives us

$$C = \frac{1}{q} = \frac{E_x}{i\omega B_y} = -\frac{E_y}{i\omega B_x} \tag{5.37}$$

And rearranging for resistivity ρ using Equation 5.30

$$\rho = \frac{1}{\sigma} = \frac{1}{|q|^2}\mu_0\omega = |C|^2\mu_0\omega \tag{5.38}$$

By measuring the electric and magnetic fields simultaneously at a location, one can calculate a single value for the resistivity of the subsurface (Simpson & Bahr, 2005).

1D Earth

In the case of a 1-dimensional Earth (or layered Earth), the conductivity varies only with depth ($+z$). In this scenario

$$\frac{\partial E_x}{\partial x} = \frac{\partial E_y}{\partial y} = 0 \tag{5.39}$$

Because of this, the diagonal components of $\mathbf{Z}$ (Z_{xx} and Z_{yy}) are set to 0. As there is no lateral resistivity variation, the off-diagonal components (Z_{xy} and Z_{yx}) have

the same amplitude but different signs. Equation 5.33 is rewritten as

$$\begin{pmatrix} E_x \\ E_y \end{pmatrix} = \frac{1}{\mu_0} \begin{pmatrix} 0 & Z_{xy} \\ -Z_{xy} & 0 \end{pmatrix} \begin{pmatrix} B_x \\ B_y \end{pmatrix} \tag{5.40}$$

Expanding this for each horizontal component of the E-field gives:

$$E_x = \frac{1}{\mu_0} Z_{xy} B_y \qquad \text{and} \qquad E_y = \frac{-1}{\mu_0} Z_{xy} B_y \tag{5.41}$$

In the case where each layer in the 1D model has the same resistivity value, Equations 5.41 can be inverse Fourier transformed to obtain a time-domain relation between the electric and magnetic fields

$$E_{x,y}(t) = \pm \frac{1}{\sqrt{\pi \mu_0 \sigma}} \int_0^\infty \frac{1}{\sqrt{\tau}} \frac{dB_{y,x}(t-\tau)}{dt} d\tau \tag{5.42}$$

This method of calculating E-fields has been used in GIC studies in Blake *et al.* (2016b); Pirjola (1985); Torta *et al.* (2014), and is equivalent to Equation 5.37. In this study, Equation 5.42 was discretised according to the method found in Pirjola (1985)

Calculating the MT response (Z) from a 1D, N-layered Earth, with each layer n having a conductivity ρ_n is an iterative process, with each layer treated similarly to an homogenous Earth. This is known as Wait's recursion formula, and requires $N-1$ iterations to calculate for an earth, and is calculated in the following manner (Simpson & Bahr, 2005):

The electric and magnetic fields in the n^{th} layer have the following forms (similar to Equations 5.26 and 5.27):

$$E_{xn}(q_n, \omega) = E_{1n} e^{i\omega - q_n z} + E_{2n} e^{i\omega + q_n z} \tag{5.43}$$

$$B_{yn}(q_n, \omega) = \frac{q_n}{i\omega} \left(B_{1n} e^{i\omega - q_n z} + B_{2n} e^{i\omega + q_n z} \right) \tag{5.44}$$

In this case, the second terms E_{2n} and B_{2n} are not set to 0, as each layer has a

finite thickness. These can be rewrittem as

$$E_{xn}(q_n, \omega) = a_n(q_n, \omega)\mathrm{e}^{-q_n z} + b_n(q_n, \omega)\mathrm{e}^{q_n z} \tag{5.45}$$

$$B_{yn}(q_n, \omega) = \frac{q_n}{i\omega}\Big(a_n(q_n, \omega)\mathrm{e}^{-q_n z} + b_n(q_n, \omega)\mathrm{e}^{q_n z}\Big) \tag{5.46}$$

The n^{th} layer would have the following transfer function:

$$C_n(z) = \frac{E_{xn}(z)}{i\omega B_{yn}(z)}, \qquad q_n = \sqrt{i\mu_0\sigma_n\omega} \tag{5.47}$$

This is similar to the Schmucker-Weidelt equation (Equation 5.37), except with conductivity σ_n. Subbing Equations 5.45 and 5.46, we can get the transfer function for the top and bottom of the n^{th} layer ($C_n(z_{n-1})$ and $C_n(z_n)$ respectively).

$$C_n(z_{n-1}) = \frac{a_n\mathrm{e}^{-q_n z_{n-1}} + b_n\mathrm{e}^{q_n z_{n-1}}}{q_n(a_n\mathrm{e}^{-q_n z_{n-1}} + b_n\mathrm{e}^{q_n z_{n-1}})} \tag{5.48}$$

$$C_n(z_n) = \frac{a_n\mathrm{e}^{-q_n z_n} + b_n\mathrm{e}^{q_n z_n}}{q_n(a_n\mathrm{e}^{-q_n z_n} + b_n\mathrm{e}^{q_n z_n})} \tag{5.49}$$

Rearranging these, one arrives at a transfer function for the $n-1^{\text{th}}$ layer

$$C_n(z_{n-1}) = \frac{q_n C_n(z_n) + \tanh[q_n(z_n - z_{n-1})]}{q_n(1 + q_n C_n(z_n)\tanh[q_n(z_n - z_{n-1}])} \tag{5.50}$$

Assuming that the Schmucker-Weidelt transfer function is continuous at the boundary between layer n and $n-1$, such that

$$C_n(z_n) = \lim_{z \to n-0} C_n(z) = \lim_{z \to z_n + 0} C_{n+1}(z) = C_{n+1}(z_n) \tag{5.51}$$

We arrive at Wait's recursion formula:

$$C_n(z_{n-1}) = \frac{q_n C_{n+1}(z_n) + \tanh[q_n(z_n - z_{n-1})]}{q_n(1 + q_n C_{n+1}(z_n)\tanh[q_n(z_n - z_{n-1})])} \tag{5.52}$$

This formula allows you to calculate the transfer function at the top of the n^{th} layer so long as the transfer function at the top of the $n-1^{\text{th}}$ layer is known. As such, one can iteratively calculate C for each layer from the bottom layer to

the surface for each frequency. The bottom (or basement) layer is defined as an homogenous halfspace.

Two important characteristics in MT are the apparent resistivity ρ_a and the impedance phase (ϕ). The apparent resistivity is defined as the average resistivity of an equivalent homogenous halfspace for each frequency, and is related to Z with the following formula:

$$\rho_a = \frac{1}{\mu_0 \omega} |Z|^2 \tag{5.53}$$

In the case of the 1D layered Earth discussed, the apparent resistivity is expressed as

$$\rho_a(\omega) = |C|^2 \mu_0 \omega \tag{5.54}$$

As Z is complex, the impedance phase is expressed as

$$\phi = \tan^{-1}\left(\frac{\mathrm{Im}Z}{\mathrm{Re}Z}\right) = \tan^{-1}\left(\frac{E_x}{B_y}\right) \tag{5.55}$$

The apparent resistivity and impedance phase of different synthetic 1D resistivity profiles were calculated using Equation 5.52. These are shown in Figure 5.3. For an increasing resistivity, the impedance phase remains $< 45°$ for all periods. Conversely, for a decreasing resistivity, the impedance phase remains $> 45°$. For a homogenous resistivity profile, the apparent resistivity is uniform and equal to the actual resistivity. The impedance phase remains at $45°$ in this case.

An example of how different resistivity profiles affect calculated electric fields is shown in Figure 5.4. Two 2-layer resistivity profiles were used to calculate the surface electric field in Leitrim during the 17-18 March 2015 storm. The first is composed of 10^4 Ωm for the first 5 km, and 10^{-1} Ω thereafter, whereas the second has 10^{-1} Ωm for the first 5 km, and 10^4 Ω thereafter. The resulting electric fields give roughly the same amplitude, but the electric fields resulting from the resistivity profile with a conductive surface layer show much longer periods, whereas the second resistivity profile resulted in electric field with a strong short period signal.

This behaviour is seen as the two resistivity profiles quickly attenuate different parts of the input signal. The conductive surface layer in the first profile quickly attenuated the high-frequency signal, leaving the long periods. The second profile (with its conductive deeper layer) attenuated low-frequency signal, leaving the short periods.

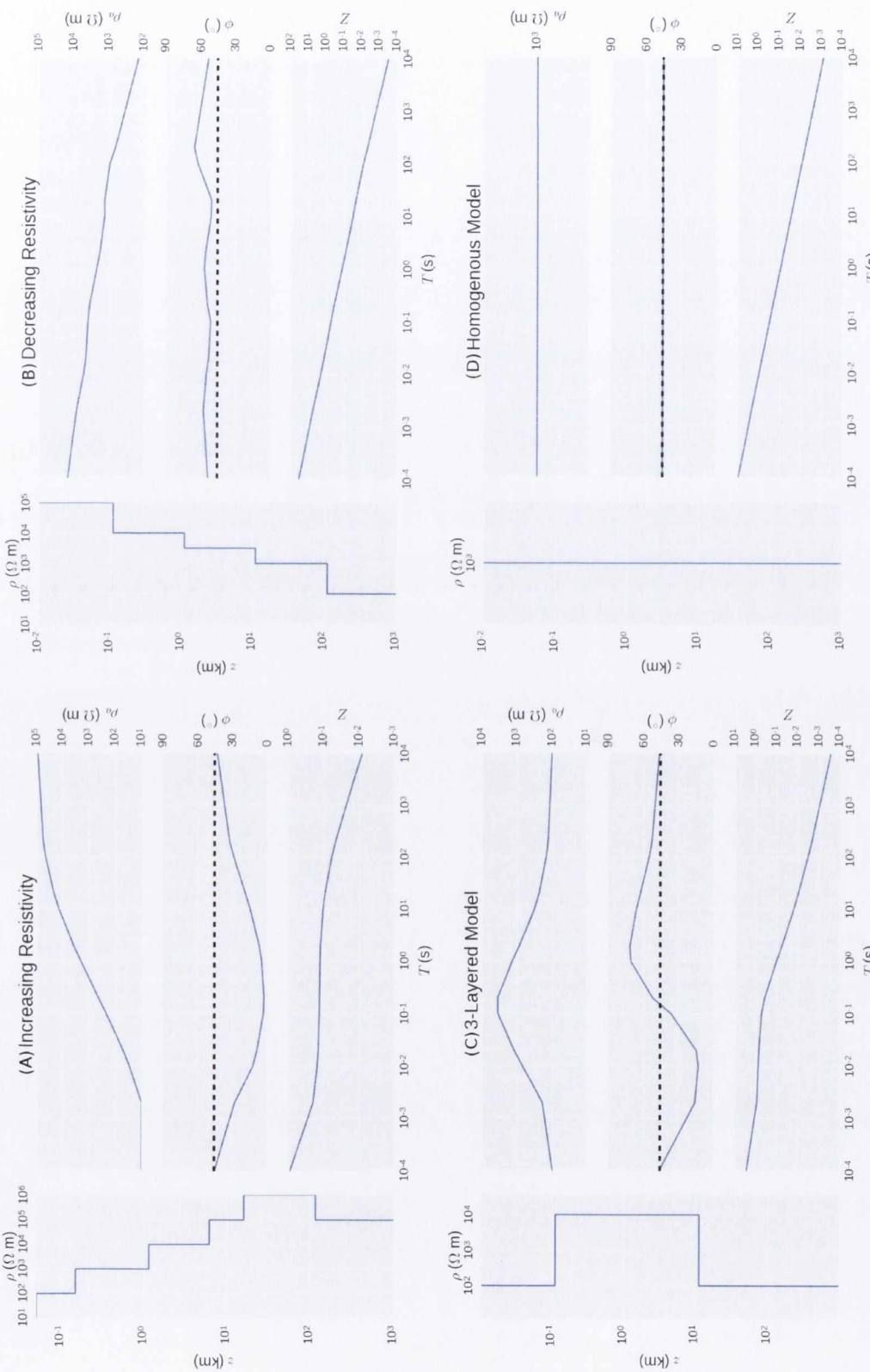


Figure 5.3: Four different synthetic resistivity (ρ) profiles, and their calculated apparent resistivity ρ_a, impedance phase ϕ and impedance tensor Z. The different resistivity profiles are (A) increasing with depth, (B) decreasing with depth, (C) conductive with resistive anomaly, (D) homogenous. The homogenous model gives an apparent resistivity which is equal to the given resistivity.

2D Earth

A 2D Earth is one where conductivity does not vary in one horizontal direction, but varies with the depth and the other horizontal direction. This simplification is often used when attempting to measure the conductivity at a geological fault or between two conductively distinct regions. The direction in which the conductivity is constant is known as the geo-electric strike (see Figure 5.2). Suppose the strike was directed along the x-axis. In this case there will be no along-strike variations ($\frac{\partial B}{\partial x} = \frac{\partial E}{\partial x} = 0$). Equations 5.19 and 5.20 can then be rewritten as

$$\left(\frac{\partial E_x}{\partial y} - \frac{\partial E_y}{\partial y} + \frac{\partial E_z}{\partial y}\right) + \left(\frac{\partial E_x}{\partial z} - \frac{\partial E_y}{\partial z} + \frac{\partial E_z}{\partial z}\right) = i\omega(B_x - B_y + B_z) \tag{5.56}$$

$$\left(\frac{\partial B_x}{\partial y} - \frac{\partial B_y}{\partial y} + \frac{\partial B_z}{\partial y}\right) + \left(\frac{\partial B_x}{\partial z} - \frac{\partial B_y}{\partial z} + \frac{\partial B_z}{\partial z}\right) = \mu_0\sigma(E_x - E_y + E_z) \tag{5.57}$$

In the case of an ideal 2D Earth, the E and B fields are orthogonal. This allows us to decompose Equations 5.56 and 5.57 into two distinct modes depending on how the magnetic and electric fields are oriented. When the E-field is parallel to the strike, we get the E-polarisation or transverse electric (TE) mode. When the B-field is parallel to the strike, we get the B-polarisation or transverse magnetic (TM) mode.

For the TE mode, we have the following:

$$\frac{\partial E_x}{\partial y} = \frac{\partial B_z}{\partial t} = i\omega B_z \tag{5.58}$$

$$\frac{\partial E_x}{\partial z} = \frac{\partial B_y}{\partial t} = -i\omega B_y \tag{5.59}$$

$$\frac{\partial B_z}{\partial y} - \frac{\partial B_y}{\partial z} = mu_0\sigma E_x \tag{5.60}$$

For the TM mode:

$$\frac{\partial B_x}{\partial y} = \mu_0\sigma E_z \tag{5.61}$$

$$-\frac{\partial B_x}{\partial y} = \mu_0 \sigma E_y \tag{5.62}$$

$$\frac{\partial E_z}{\partial y} - \frac{\partial E_y}{\partial z} = i\omega B_x \tag{5.63}$$

Since the electric components are only related to their orthogonal magnetic counterparts, $Z_{xx} = Z_{yy} = 0$. The Z_{xy} and Z_{yx} represent the TE and TM modes respectively. Equation 5.32 can then be written as:

$$\begin{pmatrix} E_x \\ E_y \end{pmatrix} = \frac{1}{\mu_0} \begin{pmatrix} 0 & Z_{TE} \\ Z_{TM} & 0 \end{pmatrix} \begin{pmatrix} B_x \\ B_y \end{pmatrix} \tag{5.64}$$

This equation is true when the impedance tensor is in the direction of the strike. It is possible to rotate the system around a vertical axis until the diagonal components are 0, in which case Equation 5.64 will be accurate. This is contingent on the subsurface being idealy represented by a 2D Earth, and the signals being noise-free.

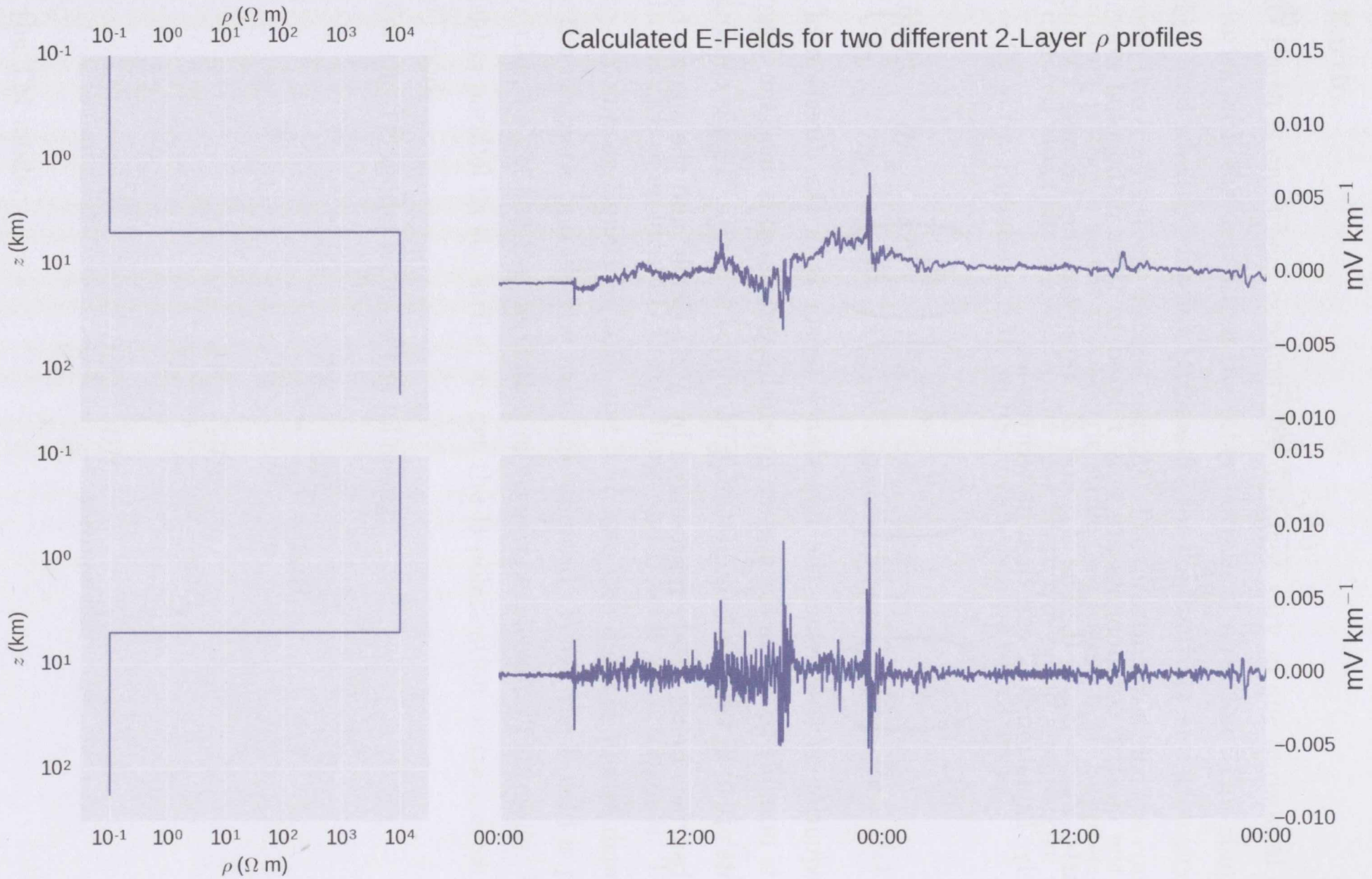


Figure 5.4: The effect of two different 2-layer resistivity profiles have on calculated E-fields using the same input magnetic field measurements. The first profile (top plots) has a conductive upper layer (0-5 km) and a resistive basement layer beneath. The second profile (bottom) has an inverted profile to the first. The resulting E-fields from each show different periods dominating, depending on where the conductive layer is. A conductive top layer attenuates shorter period signals, and a conductive basement layer attenuates longer period signals.

3D Earth

In a 3D Earth, the conductivity values vary with depth and both horizontal directions. No rotation is able to simplify the MT equation in the manner of a 2D Earth, and all four components of **Z** must be found. This means that the lateral proximity of conductive regions needs to be taken into account. This is particularly important when modeling the subsurface near bodies of water such as coasts. The full 3D MT tensor is then written as

$$\begin{pmatrix} E_x \\ E_y \end{pmatrix} = \frac{1}{\mu_0} \begin{pmatrix} Z_{xx} & Z_{xy} \\ Z_{yx} & Z_{yy} \end{pmatrix} \begin{pmatrix} B_x \\ B_y \end{pmatrix} \tag{5.65}$$

When expanded, this gives:

$$E_x = \frac{1}{\mu_0}[(Z_{xx})(B_x) + (Z_{xy})(B_y)] \tag{5.66}$$

$$E_y = \frac{1}{\mu_0}[(Z_{yx})(B_x) + (Z_{yy})(B_y)] \tag{5.67}$$

To map the conductivity of a region in 3D requires significantly more computation than for 1D or 2D MT, and it is usually preferable to utilise 1D and 2D MT wherever possible. In some cases, however, this can introduce significant errors in the modelling, and 3D is necessary (Newman *et al.*, 2015).

MT Inverse Problem

In Section 5.1.2.2, a method of calculating the MT transfer function from a known 1D subsurface conductivity model was outlined. This is known as the 1D MT forward problem. Most geophysical problems require that the inverse of this method is known: that is that a resistivity model is found from electric and magnetic measurements. This is known as the MT inverse problem.

This is not a trivial problem to solve, as for every apparent resistivity curve calculated, there will be a number of resistivity models that will approximate this signal, depending on the noise levels, error propagation and simplifications used.

The early methods of solving the inverse problem required significant use of trial-and-error (Chave & Jones, 2012). Synthetic resistivity profiles are created, their responses calculated, and compared to the measured response with least-square errors. This process is repeated until one arrives at a model which well represents the measured response. As can be expected, this can be a computationally intensive exercise if a complicated model is required, particularly with 3D Earth models.

A number of modern techniques exist to accurately replicate a resistivity model from MT measurements in a manner that is computationally efficient. These include finite difference approximations (Siripunvaraporn *et al.*, 2002), finite elements, and integral equations (Miensopust *et al.*, 2013). Other methods include the Monte-Carlo method (Simpson & Bahr, 2005).

An example of generating resistivity profiles from measured magnetic and electric data is shown in Figure 5.5 for a homogenous Earth and a 1D layered Earth. Data from the Leitrim site during the 17-18 March 2015 event was used. The homogenous Earth model has a resistivity value of 8 Ωm. This value was selected by repeatedly calculating electric fields using Equation 5.41, varying σ until a minimum least-squares error was found between the calculated and measured electric fields. The 1D resistivity profile was calculated using Occam's inversion (de Groot-Hedlin & Constable, 1990), and has values which range from 111 Ωm to 1 Ωm.

Both profiles were able to calculate the E_x component to a similar degree of accuracy, with the homogenous model slightly outperforming the layered model (the electric fields calculated with the homogenous model had a Pearson correlation coefficient of 0.763. This was 0.524 for the layered model).

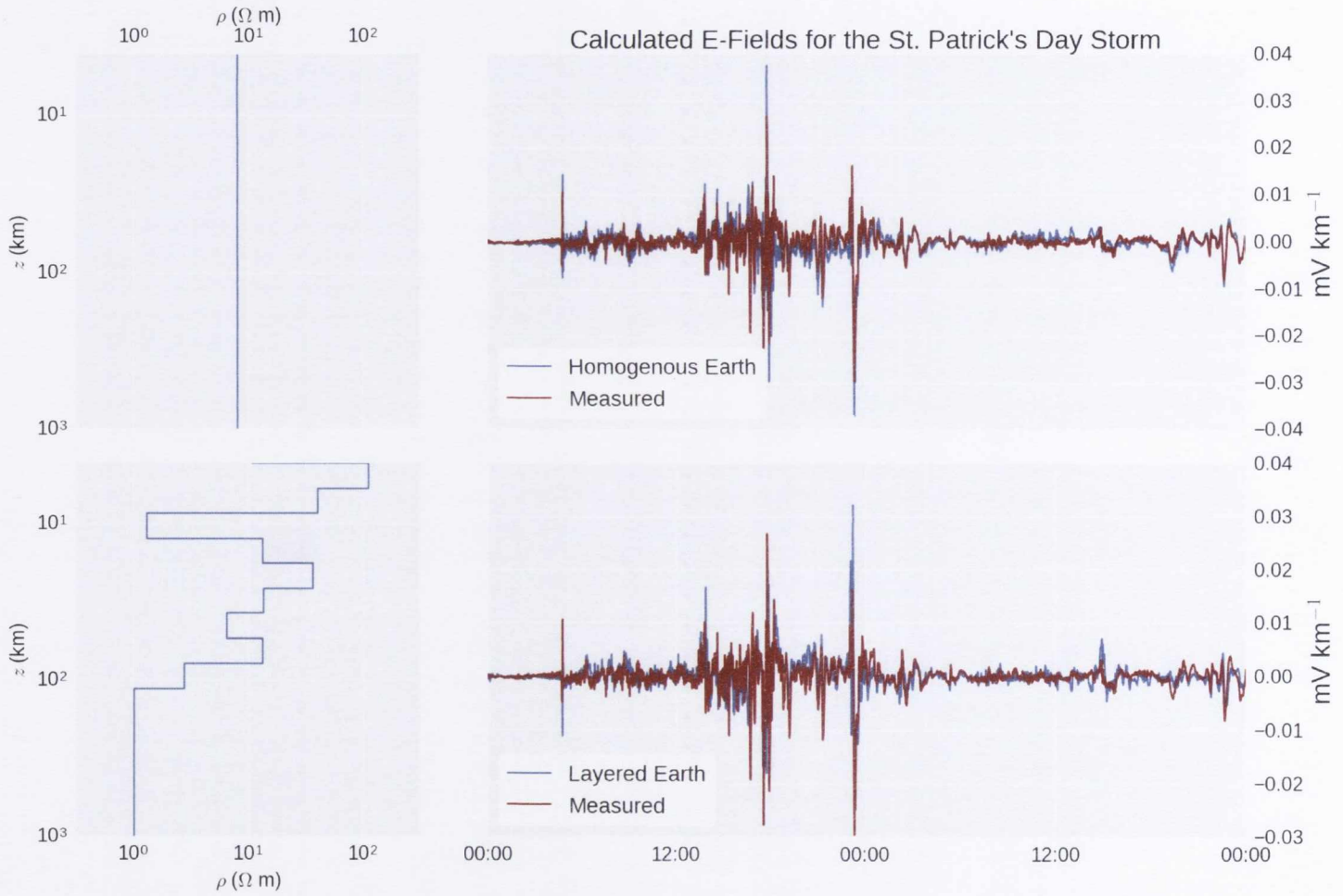


Figure 5.5: Calculated E_x in Leitrim using homogenous (top) and layered Earth (bottom) models. The homogenous model has a resistivity of 8 Ωm. This value was selected by using a least-squares fit. The layered Earth ranges from 111 Ω to 1 Ωm. The layered Earth resistivity profile was solved using Occam's 1D inversion algorithm (the details of which are given in de Groot-Hedlin & Constable (1990).

Other MT Considerations

A common problem encountered when trying to resolve the conductivity of the subsurface using the MT method is what is known as galvanic distortion. Galvanic distortion is caused by the accumulation of charges along the boundaries of shallow heterogeneities in the subsurface conductivity (Stephen *et al.*, 2003), which mostly affects the E-fields. The effects of galvanic distortion can modify the shape and the absolute value of the MT tensor, affecting both real and imaginary parts. In the case of 1-D or 2-D situation the effects of the galvanic distortion are simplified and are shown as a frequency independent shifts known as static shifts, vertically modifying the apparent resistivity curve (Sternberg *et al.*, 1988).

A method of correcting static shifts is to increase the number of sites which measure electric and magnetic fields in the area of study and compare between stations to identify the sites affected by galvanic distortion. If the number of stations which register static shift is small, their effect should be minimised when inverting the MT data to get a resistivity profile. Failing this, it is possible to decompose the MT impedance tensor into a combination of distortion parameters and the 1D or 2D response tensors. This separates local and regional parameters as much as possible, and assumes that the local structure causes the galvanic effects (Groom & Bailey, 1989).

MT Measurements in Ireland

From 2004 to 2014, DIAS conducted a number of geophysical projects around Ireland to map the conductivity of the Irish lithosphere at various depths using MT data. These projects were conducted with a number of different scientific objectives in mind. The three main projects (ISLE-MT, IRETHERM and IRCCSEM) are described here.

ISLE-MT (Irish Seismological Lithosphere Exploration - Magnetotellurics) ran from from 2004 to study the structure of the Iapetus suture below Ireland (Rao *et al.*, 2014). 39 long-period MT stations were set up to record for 6-8 weeks across central Ireland in a NNW-SSE direction.

IRETHERM, the Irish geothermal energy project, was initiated in 2011 to develop a strategic understanding of Ireland's geothermal potential (Jones *et al.*,

2015). This involved high-density broadband and high-frequency measurements in strategic locations around Ireland. These locations were focussed particularly on deep sedimentary basins (i.e., Rathlin Basin, Dublin Basin), granites (Galway, Leinster granites) and warm springs (in Dublin: see (Blake *et al.*, 2016a)). Work continues in DIAS on the data collected for IRETHERM.

IRECCSEM, which started in 2014, was set up to assess Ireland's potential for onshore carbon sequestration. Two regions were identified and had broadband and long-term MT systems installed. These were the Clare Basin and the Carboniferous Basin in Fermanagh. Work continues on IRECCSEM.

In all, approximately 750 MT sites were installed around Ireland gave data which were used for this study. The locations of these sites are given in the bottom right plot in Figure 5.6. Each site resolved the conductivity of the geology for different depths (i.e., AMT sites were shallow, with ISLE-MT sites resolving down to several hundred km). The data from each site was processed (Alan G. Jones, DIAS, personal communication, 2016) to give an average value of the subsurface at the following depths: 0-0.3 km, 0.3-1 km, 1-3 km, 3-10 km, 10-30 km, 30-60 km, 60-100 km and 100-200 km. The subsurface below 200 km was set at 100 Ωm.

For each depth interval, a radial basis function 2D interpolation scheme was used to interpolate the resistivity data beyond the MT sites to a roughly 10×10 km grid across Ireland. This made up the 1D MT model used in Blake *et al.* (2016b), which was used to calculate GICs during geomagnetic storms. Further details of these simulations are given in Chapter 7.

As can be seen from Figure 5.6, apart from the widely spaced ISLE-MT sites in the centre of Ireland, most of the sites were densely packed in areas of geophysical interest, leaving regions where no MT measurements existed to constrain the model. This is particularly apparent in the West and South West of Ireland. The resistivity values at these locations are suspect, as they are unconstrained by actual MT measurements. The crude method of interpolating the resistivity values also led to interpolation artifacts, such as is seen in the South-West of Ireland in the 30-60 km and 60-100 km depth intervals. No measurements exist at this location to explain such a conductive intrusion.

Despite these shortcomings, the MT model was able to replicate measured GICs with a simple model of the Irish power network, as will be shown in the next

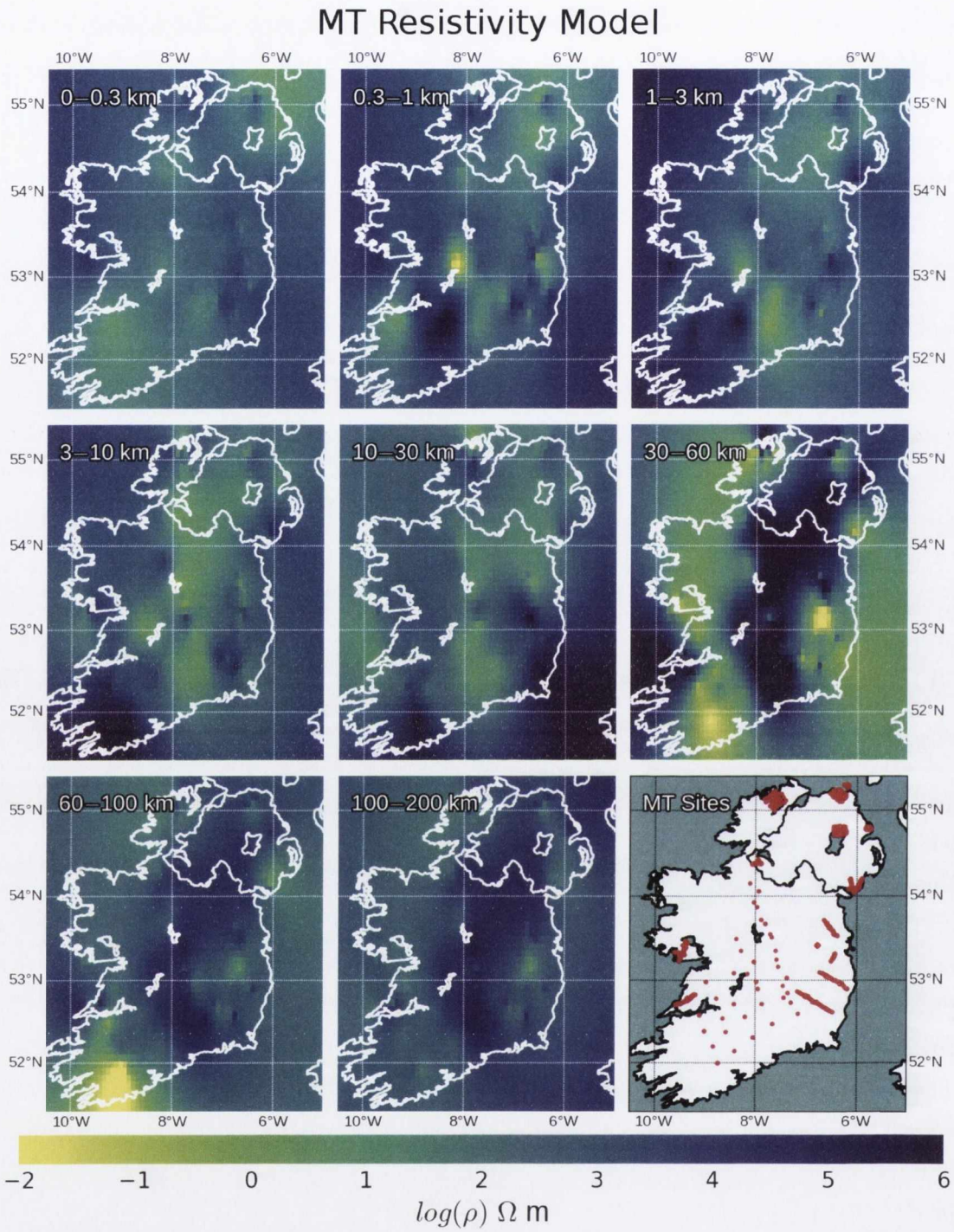


Figure 5.6: Resistivity of various depth intervals in the Irish geology down to 200 km as given by the MT model. The location of the sites from different MT surveys which informed the model are given in the bottom right subfigure. The values given by the MT sites were interpolated across Ireland using a radial basis function for different depths.

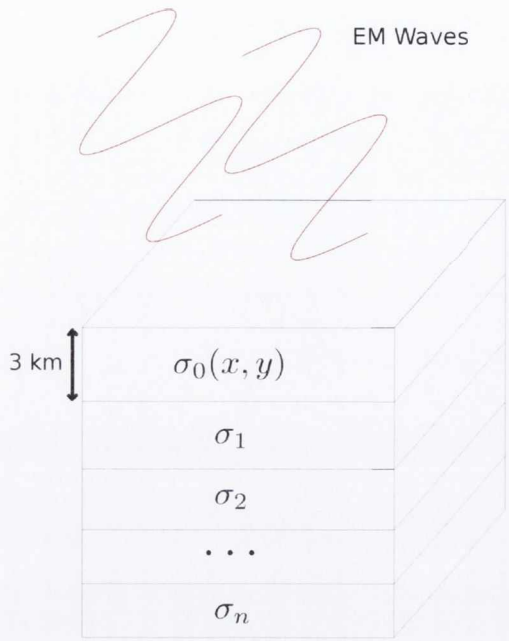


Figure 5.7: Resistivity structure used for the thin-sheet approximation method. The top layer has a varying conductance with a thickness of 3 km. This value is hard-coded in the Matlab program. Subsequent layers have a fixed conductance and varying thicknesses.

chapter.

The Thin-Sheet Method

Like MT, the thin-sheet approximation relates the horizontal surface electric fields and horizontal magnetic fields to a resistivity model. It is used to solve quasi-3D induction problems where the 3D conductivity variations have a limited vertical extent: i.e., lateral variations in conductivity occur near the surface (Grandis & Menvielle, 2015; McKay, 2003). As such, it has been used to for induction studies in the oceans (Vasseur & Weidelt, 1977). The benefits of the thin-sheet method is that only horizontal magnetic field components are necessary for calculating the electric field, and the method is valid for any external source (Weaver, 1994).

As mentioned above, the thin-sheet method is also used to calculate electric fields during geomagnetic storms for GIC simulations. It has been used particu-

larly in studies in Britain (Beggan, 2015; Kelly *et al.*, 2017; McKay, 2003; Thomson *et al.*, 2005) and has been used more recently to calculate GICs in Austria (Bailey *et al.*, 2017). Calculations were performed for this study using a Matlab program supplied by BGS (Ciarán Beggan, personal communication, 2016). This Matlab program was originally intended to be ported to Python but time-constraints prevented this from being achievable.

The thin-sheet model was first developed by Price (1949), and there are a number of different thin-sheet algorithms in use (Wang & Lilley, 1999). The method used in this study is that of Vasseur & Weidelt (1977). The thin-sheet method assumes that the surface of a model can be considered thin enough such that the electric field is unchanged in phase or magnitude across the layer. In the Vasseur implementation of the thin-sheet method, the top layer of the ground has varying conductance in two directions. Subsequent layers of the Earth have fixed resistivity in both horizontal directions. A schematic of this is shown in Figure 5.7.

The Thin-Sheet Equation

With the thin-sheet method, the displacement current is neglected, and vacuum permeability and a harmonic time factor ($e^{i\omega t}$) is assumed. The conductance (integrated conductivity) of the thin sheet can be expressed as a sum of its normal and anomalous (varying) parts

$$\tau(r) = \tau_n + \tau_a(r) \tag{5.68}$$

Similarly for the electric field:

$$E(r) = E_n + E_a(r) \tag{5.69}$$

The thin-sheet boundary condition relates the discontinuity of the tangential magnetic field to the sheet current density. This is given by

$$B(r, 0_+) - B(r, 0_-) = -\mu_0 \tau(r) \hat{z} \times E(r, 0) \tag{5.70}$$

The central thin-sheet equation given by Vasseur & Weidelt (1977) for a surface electric field at point r is given by

$$E(r,0) = E_n(r,0) + i\omega\mu_0 \int_S \tau_a(s) E(s,0) \cdot D(r|s) ds \tag{5.71}$$

where $D(r|s)$ is the 2×2 Green's tensor which relates the electric field of a unit electric dipole embedded in the normal model at s, observed at r. The Green's tensor generates the kernel of the integral.

This equation effectively sums the electrical effect every cell has on every other cell, and is discretized and reduced to $2 \times N$ linear equations, where N is the number of cells in a simulation. These equations are solved for a region using a Gauss-Seidel formulation, and are considered solved when the difference between iterative electric field calculations is less than some threshold.

A detailed discussion of this equation and full derivation can be found in Vasseur & Weidelt (1977) and Weaver (1994).

Computing the Thin-Sheet Approximation

When computing the thin-sheet approximation, there are a number of practical considerations that need to be taken into account. These are listed below:

Number of Squares in Grid

The electric field at one position is affected by the electric field at all other positions in the thin-sheet model. The size of N affects electric field amplitudes. An example of this is shown in Figure 5.8. The larger N is, the larger the calculated electric fields become. In this study, N was set at 4,920, to allow for a more manageable computing time for the program. A 2,880 minute event took approximately 1 day to calculate for a resistivity model with $N = 4,920$, whereas it took over a week to calculate electric fields for the same 2,880 minute event for $N = 23,449$. These times are for an Intel i7-4790 processor operating at 3.6 GHz using four cores in parallel. The grid size of 10×10 km squares is a hard-coded value in the thin-sheet program which was determined to best replicate surface electric fields (McKay, 2003).



Figure 5.8: The effect of grid size N on the calculated electric field with the thin-sheet approximation. Left column is the input horizontal magnetic. Right column shows the respective calculated electric field. As N decreases, the magnitude of the calculated electric field decreases marginally.

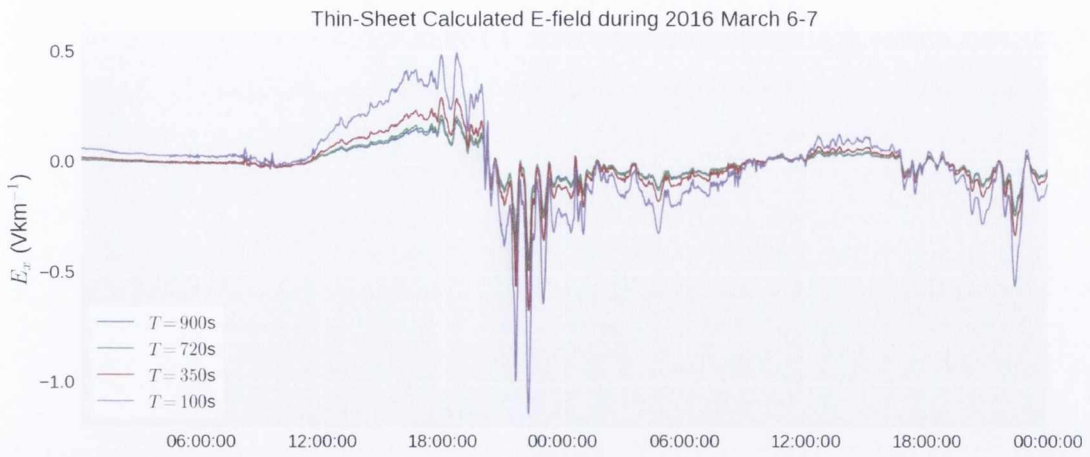


Figure 5.9: Thin-sheet calculated electric field response using different characteristic periods for the 6-7 March 2016 geomagnetic storm.

Input Period

The thin-sheet method calculates the surface electric field at a point using a single user-defined input period, and the amplitude of an input magnetic field. The chosen input period value has ranged from 750s to 300s in previous studies (Bailey *et al.*, 2017; Thomson *et al.*, 2005), with different periods chosen to match output calculated electric fields to measured electric fields. In addition, the input period may be chosen to maximise the availability of MT data for a conductivity model (e.g., when studying a high-resistance region, a larger input period may be chosen). It is important to note that a single frequency does not yield a full time-domain response, although it is possible to calculate representative electric field responses using a single period. Figure 5.9 shows how varying the characteristic period will change the calculated electric field at a point. There are limits on the range of values that can be chosen as an input period, so that thin-sheet boundary conditions are not violated. A discussion of this can be found in Weaver (1994).

Conductivity Model

Lateral variations need to be taken into account when using the thin-sheet method. This is important when considering an island such as Ireland, which is surrounded by conductive sea. For this study, a conductance model of the seas surrounding

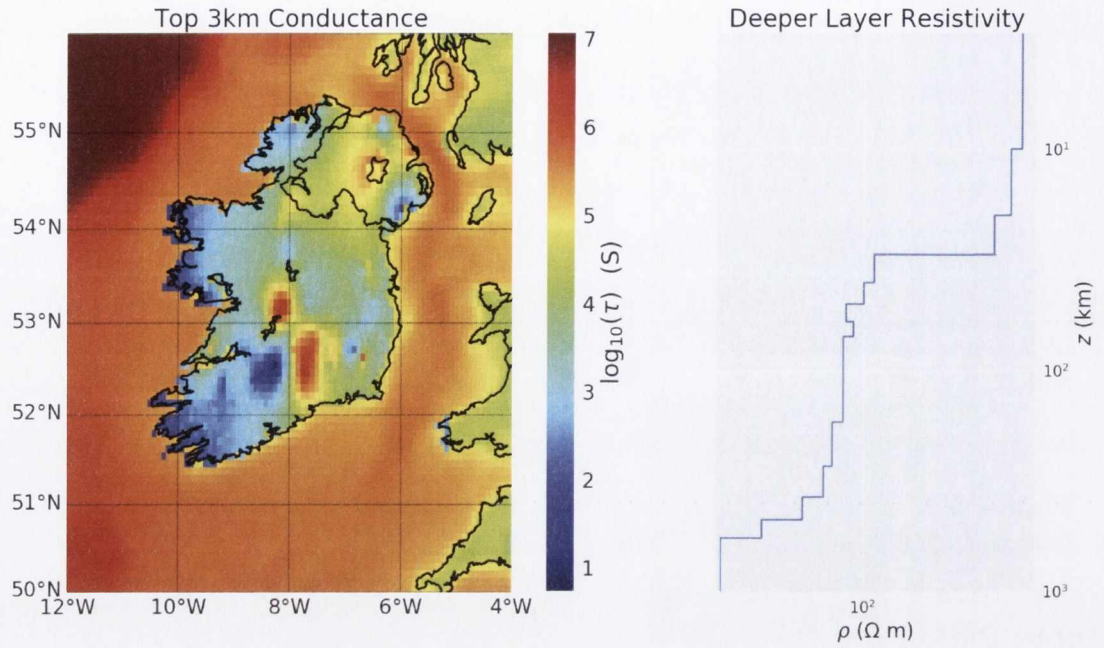


Figure 5.10: Thin-sheet conductivity model for Ireland. The left panel shows the conductance of the top 3 km of Ireland and the surrounding shelf seas. The right panel shows the resistivity of subsequent layers (i.e., layers at depths greater than 3 km).

Ireland and the UK was used. This model was supplied by BGS (Ciarán Beggan, personal communication, 2016), and incorporates bathymetry studies to determine the depth of the seas. The seawater was estimated as having a conductivity of 45 S m^{-1}. When this model is combined with the Irish MT model (outlined in Section 5.1.5, one gets a complete conductance model for the top 3 km for use in thin-sheet calculations. Subsequent layers used average values given by the MT model. Deeper layers were given gradually less resistive values, as is seen in the asthenosphere (Gaillard *et al.*, 2008). These can be seen in Figure 5.10.

The effect the discontinuity between the conductive sea and resistive land can be seen in Figure 5.11. For a northward directed magnetic field, the electric field is most prominent at East-West conductance boundaries between conductive and resistive regions. Similarly, for an eastward directed magnetic field, there is a larger electric field at north-south conductance boundaries.

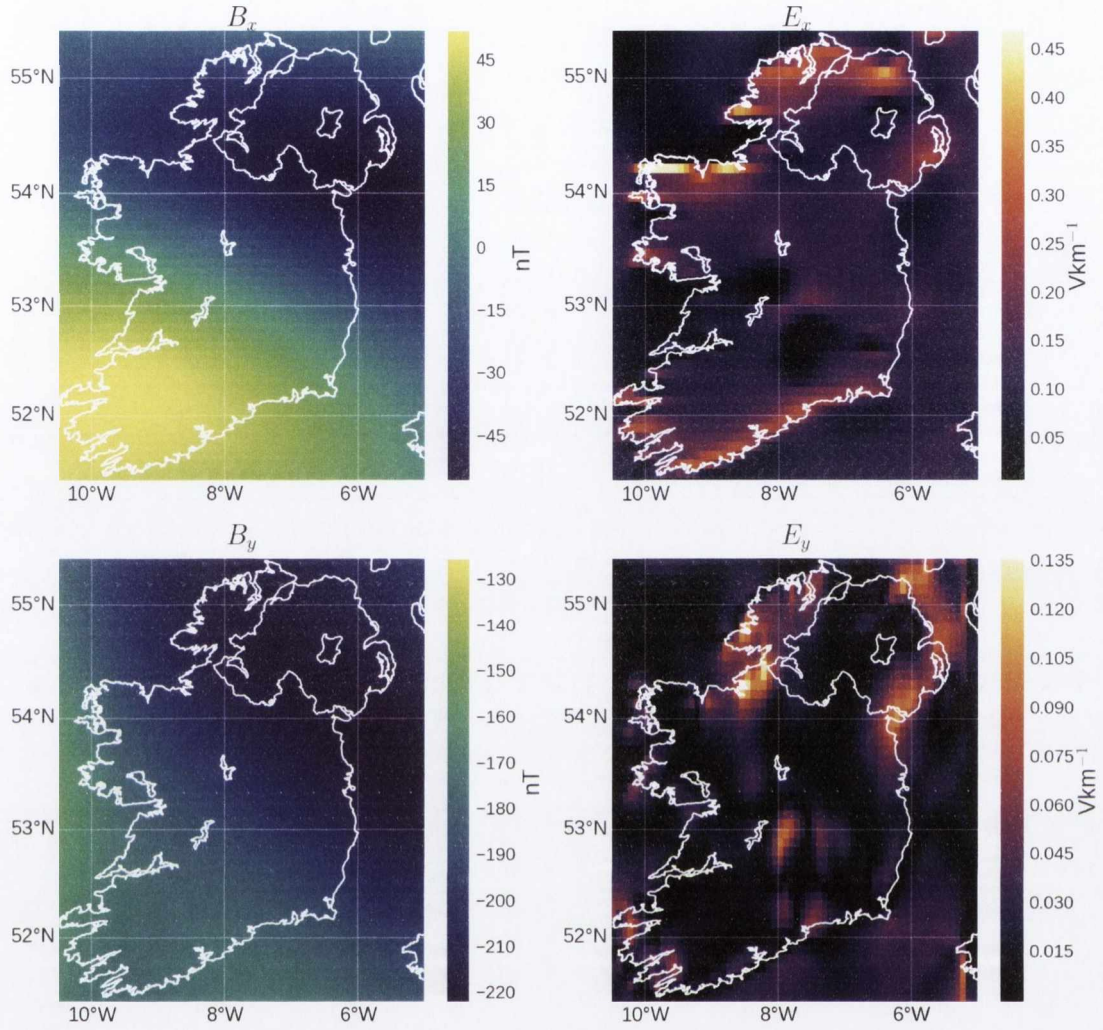


Figure 5.11: Calculate E_x and E_y for input B_x and B_y using the thin-sheet method during the 6-7 March 2016 geomagnetic storm. Larger electric fields can be seen at the boundaries between conductive and resistive regions (i.e., the sea and land). The structure of the land is also reflected in the electric fields, particularly the two conductive regions in the South of Ireland (see Figure 5.10).

Comparing MT and Thin-Sheet Methods

When calculating the surface electric field at a point, it is necessary to have both a resistivity model and input magnetic field, regardless as to whether the MT or thin-sheet method is used. As can be seen in the above sections, the manner in

which electric fields are calculated differ between the MT and thin-sheet method.

In order to see how they differ practically, the electric field at a point was calculated using a synthetic magnetic field and a homogenous 400 Ωm ground resistivity model. This can be seen in Figure 5.12, which shows (from top to bottom) a magnetic field, the rate of change of this field, the thin-sheet calculated electric field and the MT method calculated electric field.

If one wants to calculate the surface electric field across a region using the thin-sheet method, Equation 5.71 is solved for each minute independently. The electric field at some cell (x, y) and time t depends on the amplitude of the magnetic field across the region (for all values of x, y), but does not depend on magnetic field values at any time other than t. This is despite the fact that geomagnetic induction is a diffusive process which depends on previous geomagnetic conditions at a location.

In contrast to the thin-sheet approximation, the 1D MT method (given in Equation 5.42) requires a magnetic time-series to calculate electric fields at a single point, but is independent of the electromagnetic conditions of its neighbours (unless their effect is accounted for in a 3D MT tensor). The result of these differences in methods is different resulting electric fields for the same input magnetic field and conductivity models. The thin-sheet calculated electric field tends to follow the shape of the input magnetic field, whereas the MT calculated electric fields are more affected by the rate of change of the magnetic fields.

For the test case given in Figure 5.12, both methods give electric fields of similar amplitudes, although the thin-sheet method follows the long-period signal of the input magnetic field. This has implications for calculating GICs, as shall be seen in later chapters.

Summary

In this chapter, two methods of calculating surface electric fields using input magnetic fields and ground resistivity models were outlined. These are the MT and thin sheet methods.

The MT method is a popular method of determining the subsurface conductivity structure, and is widely used to calculate surface electric fields for GIC

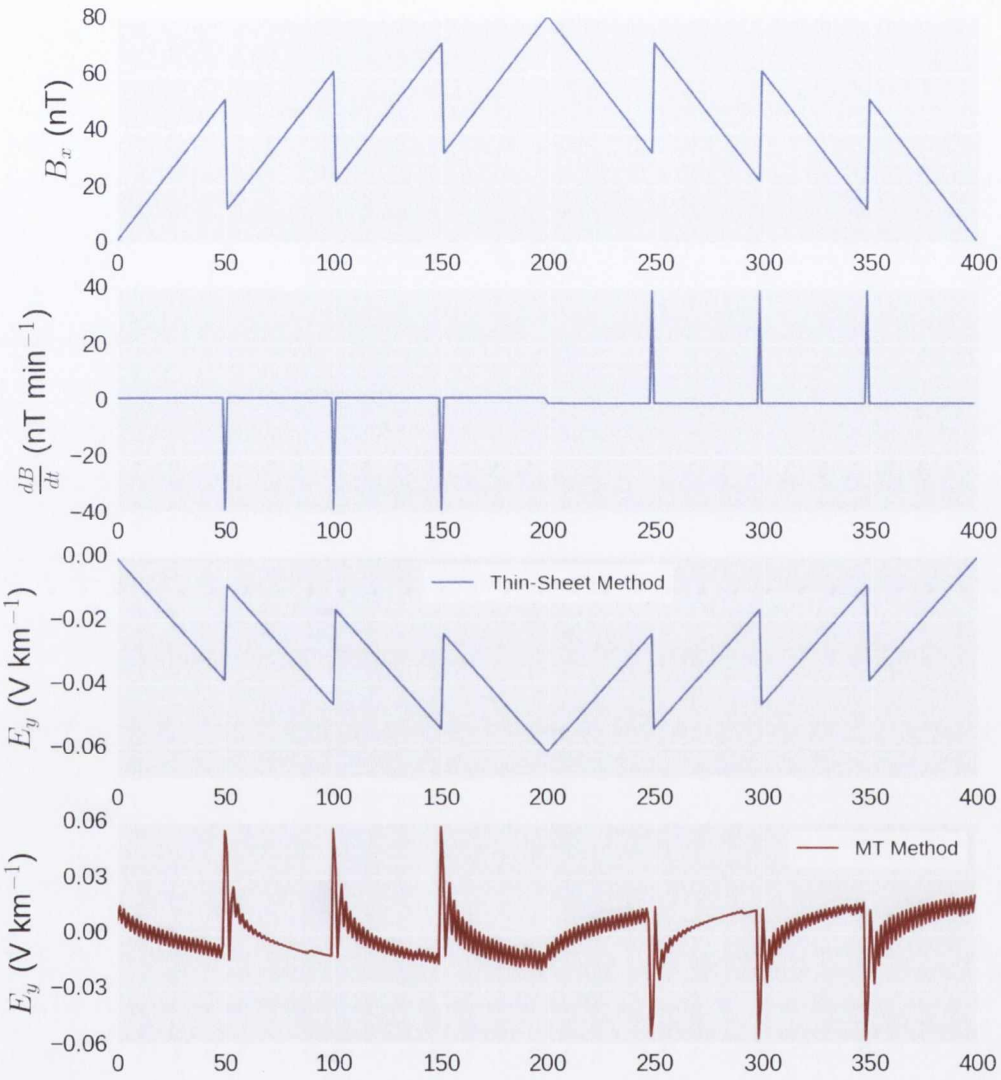


Figure 5.12: Comparison between thin-sheet and MT calculated electric field. The plots show from top to bottom: the synthetic magnetic signal, the rate of change of this signal, the calculated electric field using the MT method and the calculated electric field using the thin-sheet method. The oscillating signal in the electric field calculated using the 1-D MT approach is a result of the discretising of Equation 5.42 (MT calculation for uniform Earth). The approach of Pirjola (1985) was used in this instance.

simulations. The basic workings MT, along with the different simplifications one can make when utilising it, were outlined in this chapter. The calculated electric field response of different synthetic resistivity models was explored.

Also summarised were the several MT campaigns which mapped Ireland's geological resistivity since the early 2000s. Data from these campaigns form the basis of an all-Ireland resistivity model, which uses measured values down to 200 km.

The thin-sheet method is similar to MT in that it was originally used to determine the conductivity of subsurface geology, although it is now used to calculate electric fields specifically for GIC studies. In this chapter, the thin-sheet method was outlined, and different computational considerations explored. These included the effect grid size and characteristic frequency has on calculated electric field. The MT-derived resistivity model was coupled with a conductivity model of the seas around Ireland for use with the thin-sheet method.

Using these two methods of calculating electric fields and the MT derived resistivity map, the electric field response of Ireland can now be calculated and compared for historical geomagnetic disturbances. These case studies are explored in later chapters.

6

GIC Modelling in the Irish Power Network

In order to calculate GICs in a power network, it is necessary to have measured or calculated electric fields and a model of the subject power network. In this chapter, we describe the most commonly used method of calculating GICs. The software developed for constructing detailed power network models as part of this study is then described, along with details of the Irish 400, 275, 220 and 110 kV power network models. Finally, different aspects of the power network are explored with respect to GICs. Part of the work in this chapter appears in Blake *et al.* (2016b).

Modelling GICs in a Power Network

The most commonly used approach to modelling GICs in use in academia is the Lehtinen-Pirjola (LP) method (Lehtinen & Pirjola, 1985). This approach treats the subject power grid as a discretely earthed network, and applies Ohm and Kirchhoff's laws in order to estimate GICs. A BGS Matlab program which utilises the LP approach was ported to Python for use in this project (Ciarán Beggan, BGS, personal communication, 2014). As GICs are driven by magnetic field variations

which range from 10^{-5} to 1.0 Hz, it is appropriate to treat GICs as DC (Boteler & Pirjola, 2016). The LP method allows for modelling of any power network, so long as information about the network's transformers and connections are known. The following description of the LP method appears in Viljanen & Pirjola (1994). GIC earthing currents through N earthed nodes (transformers) can be calculated using the following equation

$$\mathbf{I} = (\mathbf{1} + \mathbf{YZ})^{-1}\mathbf{J} \tag{6.1}$$

where $\mathbf{1}$ is the unit matrix, $\mathbf{Y}$ is the network admittance matrix,and $\mathbf{Z}$ is the earthing impedance matrix. $\mathbf{I}$ is the matrix with elements I^i for $i = 1, ...N$. The admittance matrix $\mathbf{Y}$ is defined by the resistances of the conductors of the network:

$$Y_{ij} = -\frac{1}{R_{ij}}, \ (i \neq j) \quad , \quad Y_{ij} = \Sigma_{k \neq i} \frac{1}{R_{ik}}, \ (i = j) \tag{6.2}$$

where R_{ij} is the resistance between two nodes i and j. The column vector $\mathbf{J}$ has elements defined by

$$J_i = \Sigma_{k \neq i} \frac{V_{ki}}{R_{ki}} \tag{6.3}$$

The voltages affecting the conductors in a network depend on the path taken by the conductor. This is because, in general, the geoelectric field is not a gradient of a scalar potential, therefore the voltage is path-dependent (Pirjola, 2002). The calculation of V_{ki} is then

$$V_{ki} = \int_k^i \mathbf{E} \, ds \tag{6.4}$$

Once all of these components are known, the current which flows from node i to k can be calculated as

$$I_{ik} = \frac{V_{ij}}{R_{ij}} + \frac{(\mathbf{ZI})_i - (\mathbf{ZI})_j}{R_{ij}} \tag{6.5}$$

As mentioned above, AC power networks utilise three phase power lines. In these lines, the impedances of each phase of the power system are identical. In order to account for each of the phases when calculating GICs, the parallel paths

of each phase can be used to calculate an equivalent circuit for GIC calculation (Boteler & Pirjola, 2016). When the three phases are treated as parallel conductors, the equivalent circuit can be calculated by dividing line and transformer winding resistances by three:

$$\frac{1}{R_e} = \frac{1}{R_p} + \frac{1}{R_p} + \frac{1}{R_p}, \qquad R_e = \frac{R_p}{3} \tag{6.6}$$

Where R_e is the equivalent circuit resistance and R_p is the resistance of a single phase.

In practical terms, to simulate GICs in a network, the following information regarding the network is required: position of transformers, transformer winding resistances, substation grounding resistances, connections between substations and the resistances of these connections. Using only these, GICs can be calculated in a single voltage system.

Modelling Different Voltage Levels

In most transmission networks, there are different voltage levels which can be modelled. The flow of GICs in a network of multiple voltages will be through the windings of the transformers at each substation. The type of transformer determines the nature of the path for flow of GICs (Boteler & Pirjola, 2014). The two main types of transformers used are two-winding (or 'YY' transformers) and autotransformers. As they have different construction, they need to be treated differently (see Figure 6.1).

Two-winding transformers have two separate windings, each of which connects to either the higher or lower voltage busbar (or bus) in a substation. These are connected to a central ground or neutral point. Autotransformers have a single winding which acts as both the primary and secondary coil in a transformer.

For a two-winding transformer, if the high and low voltage windings are treated as nodes in the method described in Section 6.1, this introduces non-diagonal elements in the earthing impedance matrix $\mathbf{Z}$. Solving for GICs as in Equation 6.1 requires the inverse of $\mathbf{Z}$, which becomes impractical with the added non-diagonal elements.

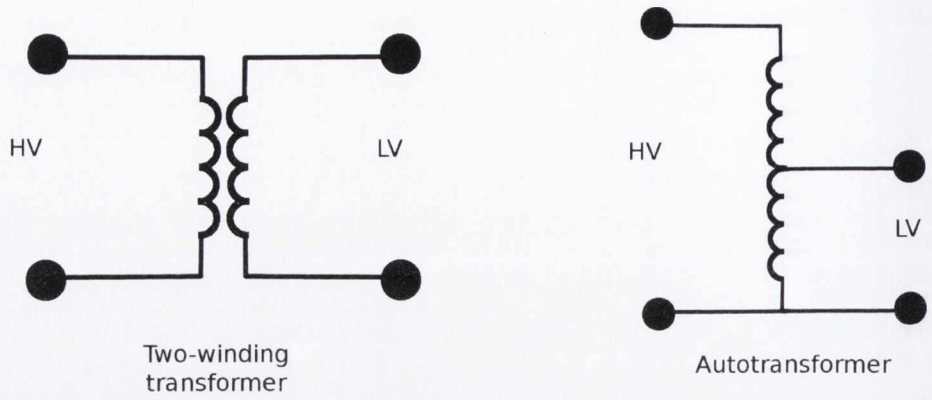


Figure 6.1: Schematics for two-winding transformer (left) and an autotransformer (right) for a single phase. The two-winding transformer has two separate windings (HV and LV) which connect to a common ground. The autotransformer has a single winding which each voltage regime shares. The LV connections on this autotransformer is currently connected halfway up the winding. This position of this connection will dictate the output voltage.

A solution involves the introduction of virtual nodes with infinite grounding resistances in a power network model (Boteler & Pirjola, 2016, 2014; Pirjola, 2005). For a two-winding transformer, the higher and lower voltage nodes are made to be 'virtual' nodes with infinite grounding resistance. These are connected to a single ground node which has the substation's true grounding resistance. These nodes are connected to other nodes with resistance equivalent to the higher and lower voltage winding resistances (see Figure 6.2). This leads to a diagonal earthing matrix $\mathbf{Z}$ which can be readily inverted. The infinite (or computationally large) grounding resistances ensure that no current flows through these virtual nodes to ground.

Similar to the treatment given to a YY-transformer, an autotransformer requires a single virtual node at the high voltage bus in order to be included in the calculation.

Power Network Model Generator

There are two difficult aspects of creating a power network model for calculating GICs. The first aspect involves collating the information on a power network,

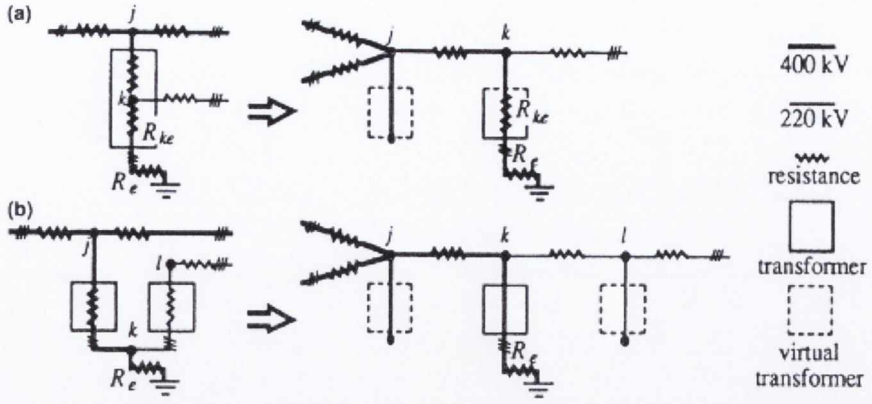


Figure 6.2: Virtual node treatment of an autotransformer (a) and two-winding transformer (b). For an autotransformer, a virtual node is placed at the point of the the HV bus j. The resistance of the conductor connecting j and k is set as the HV winding resistance. In (b), two virtual nodes are placed at j and l, the high and low voltage buses respectively. The resistances of jk and kl are the resistances of the high and low voltage windings (Pirjola, 2005).

including transformer types, high voltage and low voltage winding resistances, transmission line resistances, etc. This involves accessing information on elements of a power network which may not even be digitised. As power networks often have hundreds of substations, this can be a laborious and time-consuming task.

Assuming that one has enough information about a network in order to begin constructing a model, the issue of accounting for transformer type and multiple transformers per substation arises. For example, in a substation with three YY-transformers, one needs to create 11 nodes (including high and low voltage buses), and account for 12 connections between these real and virtual nodes. Included in this process is properly allocating the resistances of the windings to the internal connections between nodes.

As part of this study, a program was written in Python which constructs a power network model for GIC modelling using the methods outlined above. This program, the power network model generator (or PNMG), takes into account the two transformer types listed above, multiple transformers per substation, dual-circuit connections between substations and transformer grounding switches. The program takes in two comma-separated-value (.csv) files: one con-

taining transformer information, and the other containing connection data between substations. It outputs a single .csv file containing the model which can be used as an input to the LP method for GIC calculations. The program is available for download from the TCD Solar Physics Research Group GitHub page (www.github.com/TCDSolar). Using the program written for this study, one can create a detailed model of a power network down to a transformer level.

An example of a PNMG modelled substation with multiple transformers is shown in Figure 6.3. This shows a 220/110 kV substation as part of a model of the Irish power network (Model B, see Section 6.2). This substation consists of one autotransformer (far left) and three YY-transformers connected in parallel. They are each connected to high and low voltage buses, which connect to other 220 and 110 kV substations respectively. The filled circles are each connected to a common ground, and it is here that the GIC are calculated. Each of the unfilled circles are the virtual nodes with infinite grounding resistances.

In order to verify that the PNMG was accurately creating power networks given transformer and connection information, the test-case 500 and 345 kV power network featured in Horton *et al.* (2012) was used. This representative network (see Figure 6.4) consists of eight substations with a total of 15 auto and YY-transformers. Also included in the paper was a GIC blocking device at one substation, and some instances of multiple parallel connections between substations.

This information was fed into PNMG and the output model was subjected to a uniform 1 V km^{-1} electric field. GIC were then calculated for each of the substations, as in Horton *et al.* (2012). Figure 6.5 shows the comparison between the GIC values given in the paper and those calculated using the PNMG model. Substation 5, which has two YY-transformers exhibits the highest difference of 4 A. These differences are relatively small given the amplitude of GICs calculated. As such, the PNMG program was used to create a model of the Irish power network.

The Irish Power Network

The Irish power network consists of approximately 270 substations and 6,400 km of 400, 275, 220 and 110 kV transmission lines in both the Republic of Ireland

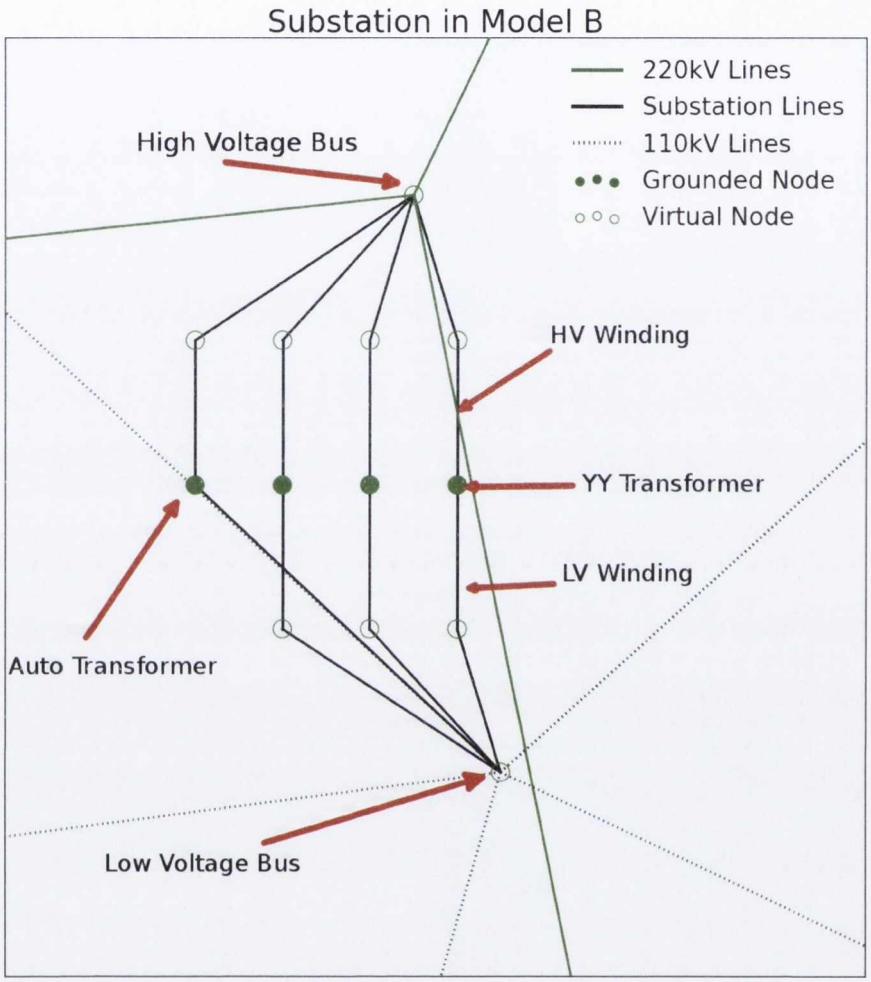


Figure 6.3: A 220/110 kV substation created by the power network model generator for the Irish power network. This substation has one autotransformer (far left) and three YY-transformers connected in parallel. The autotransformer has one internal connection which has the resistance of the HV winding. Each of the YY-transformers has two connections with resistances set to the HV and LV winding resistances. The solid black lines represent the internal substation connections, where all transformers are assumed to be in parallel.

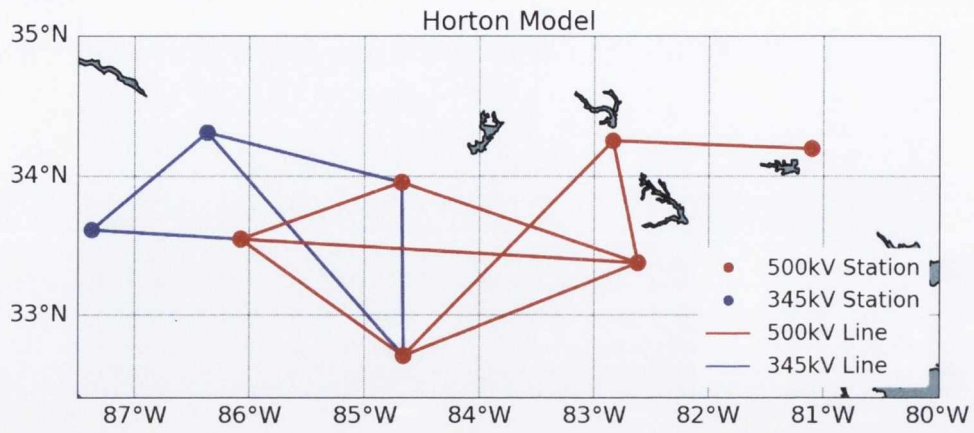


Figure 6.4: The Horton *et al.* (2012) model network for testing GIC calculations. This network consists of two voltage levels (500 and 345 kV), eight substations and 15 transformers of differing types.

and Northern Ireland. It is operated by EirGrid (Republic of Ireland) and SONI (Northern Ireland), and a schematic of the network is shown in Figure 6.6.

As Ireland is a small country (approximately 300×500 km in area), its network requires less high-voltage lines and substations than other larger countries. For example, Ireland currently has only four 400 kV substations, and three 400 kV transmission lines. These lines run roughly West-East, bringing power generated in the West to Dublin, Ireland's largest population centre. The Republic has approximately 34 substations which operate at 220 kV. These are located primarily along the East and South-East coasts. One of these substations connects to the 275 kV network in Northern Ireland, where there are ten 275 kV substations. These cluster around Lough Neagh and Belfast in Northern Ireland. Ireland's 110 kV network is composed of approximately 230 substations all across Ireland. In areas of the West and North-West of Ireland, 110 kV lines are the highest voltage network in use. Ireland also has two high-voltage DC connections to Britain. These are the Moyle and East-West interconnectors.

Modern national power systems are often heavily interconnected between countries. It is necessary to consider any networks which are physically connected to a subject network, as they may affect the flow of GICs. It is usually possible to

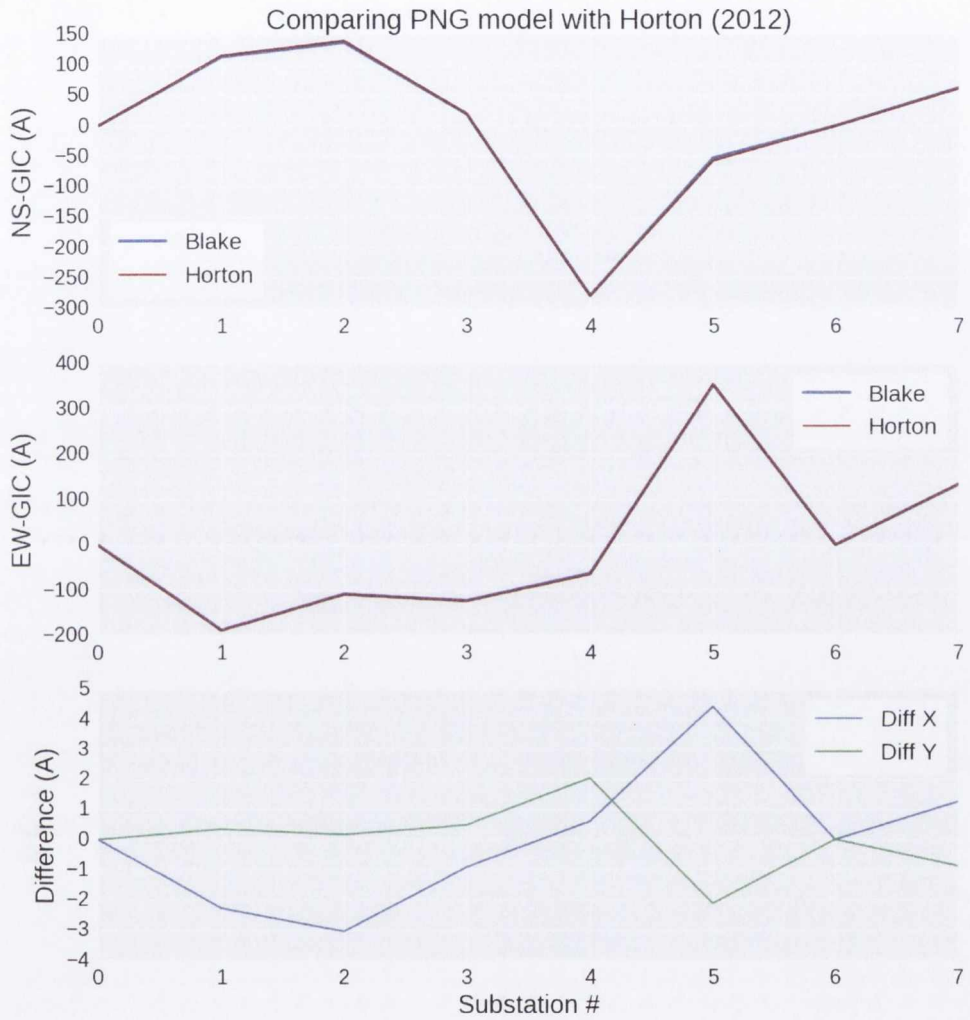


Figure 6.5: GIC values given in Horton *et al.* (2012) compared to GIC values calculated using a model created with the PNMG program. The plots from top to bottom show GIC due to a northward electric field, GIC due to an eastward directed field, and the difference between the Horton and PNMG-model GIC calculations. The largest deviation is seen in substation 5 which has two YY-transformers. This was off by just over 4 A out of around 350 A.

approximate such an adjacent network for GIC purposes.(Boteler & Pirjola, 2016). From a GIC calculation point of view, Ireland is a simple case, as it only has two HVDC connections to the British networks. This means that the Irish network can be considered as a whole without approximating peripheral power networks.

Ireland's power network also has a Hall Effect probe installed to directly measure GICs at a single transformer in the 400/220 kV Woodland substation (approximately 23 km North-West of Dublin). This is discussed further in Chapter 7, when the data it produces is replicated for several geomagnetic storm events.

Irish Network Models

Two models of the Irish power network were created for studying GICs during the course of this project. The first (Model A), is a simplified first-approximation model of the Irish 400, 275 and 220 kV substations and lines. This model was used in Blake *et al.* (2016b). The second model, (Model B) is a much more detailed model, and includes the 110 kV part of the network. All of the Irish power network data was provided by EirGrid (Sarah Walsh, EirGrid, 2014 and David Bell, EirGrid, 2016, personal communications). Both moels can be seen in Figure 6.7

A table of the characteristics of Model A and Model B can be seen in Table 6.1, and each model is described in detail below.

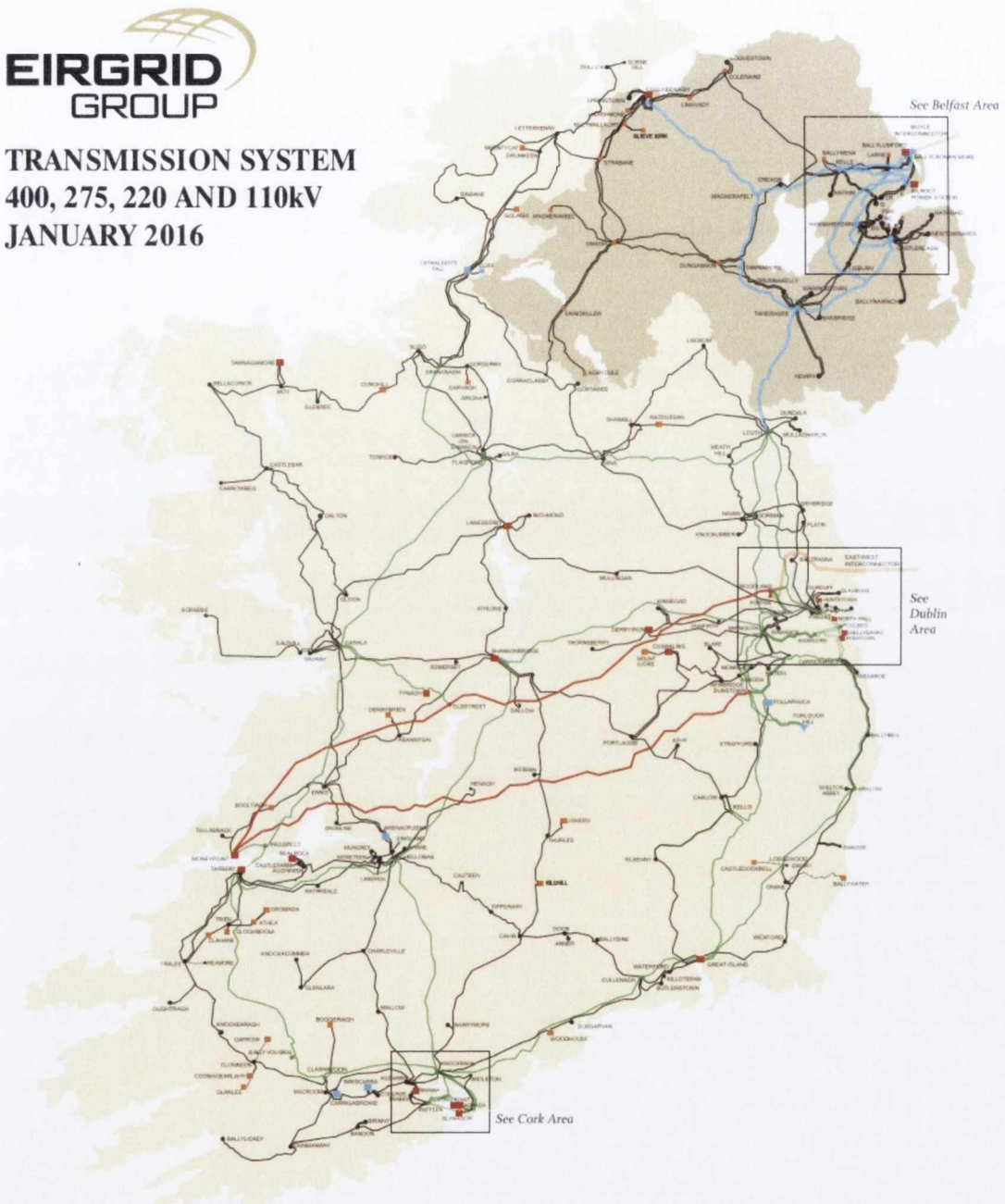


Figure 6.6: The 2016 EirGrid transmission system. The red, blue, green and black lines represent 400, 275, 220 and 110 kV transmission lines respectively. The highest voltage lines in Northern Ireland operate at 275 kV, whereas all of the 400 kV lines and substations are in the Republic of Ireland. The highest voltage lines in areas of the West and North-West of Ireland are 110 kV.

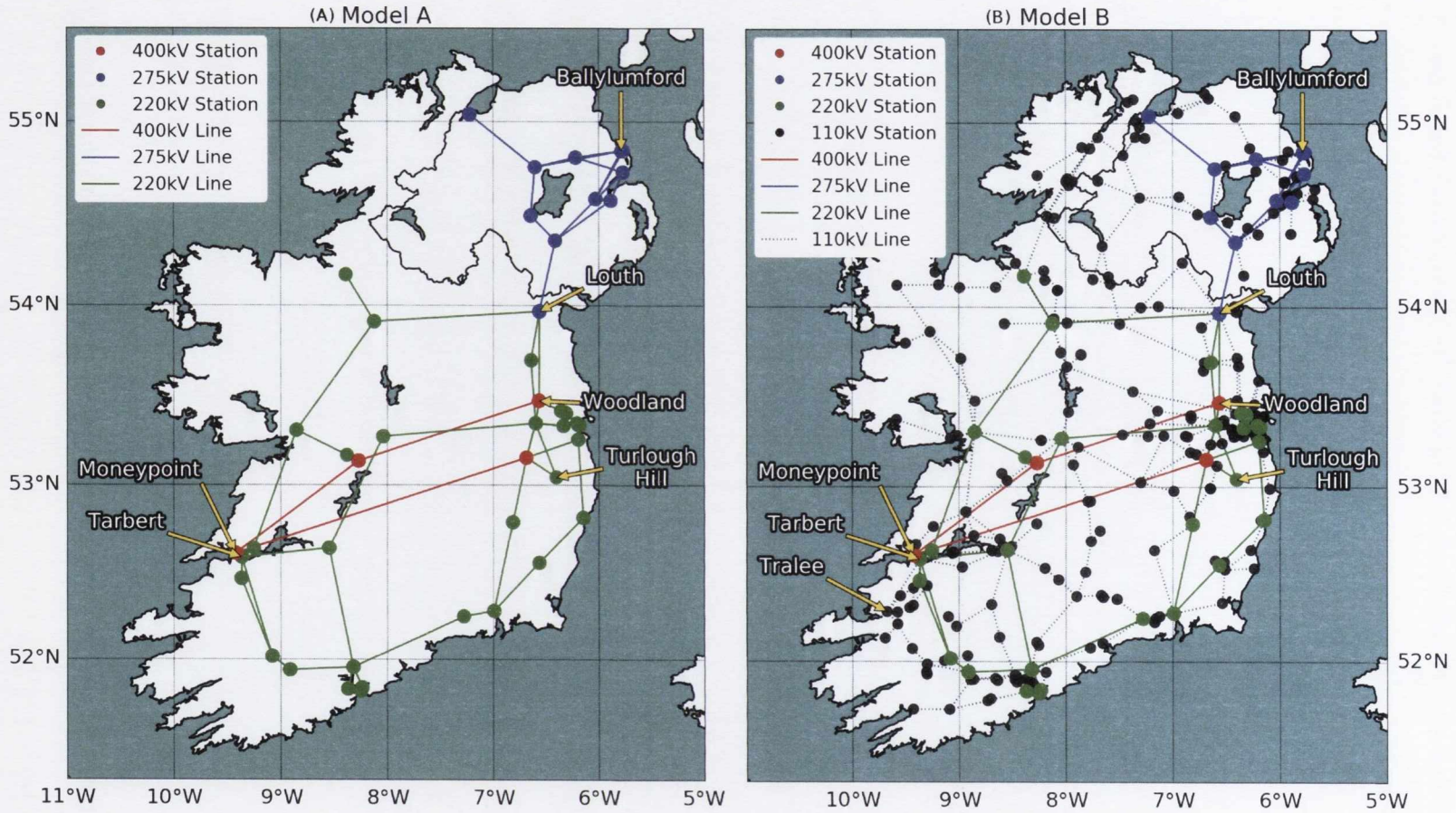


Figure 6.7: The two models of the Irish network used in this study. Model A appears in Blake *et al.* (2016b), and includes 400, 275 and 220 kV substations and transmission lines. Model B has the addition of the 110 kV substations and lines, as well as more detail on a substation level. Transformer numbers per substation and types of transformer are taken into account in this model. Named substations are Moneypoint, Ballylumford, Tarbert, Tralee, Louth, Turlough Hill, and Woodland.

Table 6.1: Details from the power network models A and B. Model B is a significantly expanded model of the Irish power network compared to Model A.

Values	Model A	Model B
Voltages (kV)	400, 275, 220	400, 275, 220, 110
Substations	46	274
Connections	78	404
Nodes	56	511
Line Type	single phase	three phase
Trafos per site	1	between 1–7
Trafo Res. (Ω)	estimated 0.5	between 0.04–0.68
Ground Res. (Ω)	estimated 0.1	between 0.25–6.35
Ground Switches	No	Yes
T-junction Connections	No	Yes

Model A

Model A consists of 46 substations with operating voltages of 400, 275 and 220 kV. Every substation consists of a single transformer with a fixed transformer resistance of 0.5 Ω, and a grounding resistance of 0.1Ω. These are estimated values which are used frequently where true resistance values are not known (Myllys *et al.*, 2014; Torta *et al.*, 2014). Only the four 400 kV substations and the single 220 kV substation which connects to the 275 kV network in Northern Ireland had transformers which were not composed of single nodes. Each of these were set as two-winding transformers.

Transformer nodes were connected with straight transmission lines and line resistances were calculated from line composition and true length. The transmission lines were treated as single phase lines, not as three-phase as reported in Blake *et al.* (2016b).

With all of the approximations and estimations listed above, Model A can be viewed as a 'first approximation' of the Irish power network. This model has been significantly improved with Model B.

Model B

Model B is an expanded and more realistic model of the complete Irish power network. It consists of 274 substations which operate at 400, 275, 220 and 110 kV.

Each substation consists of between one and seven transformers (an example of a 220/110 kV substation can be seen in Figure 6.3). The higher voltage substations (400, 275 and 220 kV) have the correct transformer types (auto or two-winding) and use true winding resistances which range from between 0.043 Ω and 0.685 Ω. Each of the 110 kV substations each contain a single transformer, which was given a winding resistance of 0.087 Ω. This value was chosen as it was a representative resistance of the LV windings in the 220/110 kV transformers in the model (David Bell, EirGrid, personal communication, 2017). Connections between substations used true line resistances and were treated as three-phase.

Model B also included 12 T-junction connections in the 110 kV network, a detail not seen in Model A. These junctions are where two transmission lines meet at a point that is not a substation. These were modelled as nodes with an infinitely high resistance. In addition to this, actual grounding resistances were supplied for 33 substations. These values range from 0.246 Ω to 6.35 Ω. Substations for which there was no grounding resistance data were given grounding resistances of 1 Ω. This is the value which EirGrid aims to have at each substation. All of this information was used as an input for the PNMG program to obtain a model which could be used for GIC calculations.

Network Sensitivity Tests

Once a network model has been created, it is informative to subject it to a number of test simulations using idealised electric fields. This helps to isolate the effect each of the characteristics of a power grid have on GICs calculation, independent of ionospheric or geological effects. It also allows one to estimate the errors each assumption has on GIC calculations.

Application of Uniform Electric Field

The general susceptibility of a power network to GICs can be examined by applying a uniform electric field of 1 V km^{-1} in different directions to the model networks and subsequently calculating GICs at the transformer nodes. In reality, geoelectric fields are affected by ionospheric conditions and subsurface geology, and will not

be uniform across a region. However, applying a uniform electric field to a network will give an indication as to which substations will favour GICs due solely to the makeup and orientation of a network. This exercise has been used on a number of different power networks in different studies (Horton *et al.*, 2012; Myllys *et al.*, 2014; Torta *et al.*, 2014; Turnbull, 2011).

Figure 6.8 shows the response of models A and B to uniform electric fields in the northward and eastward directions. For both models, there is a clear difference in the signs of GICs in substations across Ireland. When the electric field points northward, southern substations tend to have negative GIC (current flowing from the earth), and northern substations tend to have positive GIC (current flowing to the Earth). A similar divide can be seen with the eastward directed field.

With model A, an eastward electric field produced GICs greater than 20 A in only two of the 46 substations. The first of these is the 400/220 kV Moneypoint substation in County Clare in the West of Ireland, with 37 A. The other substation with greater than 20 A is the 220/110 kV substation in Tarbert, with 20.1 A.

With model B, Moneypoint is again the most affected substation, with 113 A induced with an eastward directed field. As can be seen in Figure 6.8, this value is much larger than the induced currents seen in other substations. Tarbert again sees 20 A, and the 110 kV substation at Tralee sees 28 A. Louth, the substation which connects the network in the Republic to that in Northern Ireland sees 37 A when the electric field points northward.

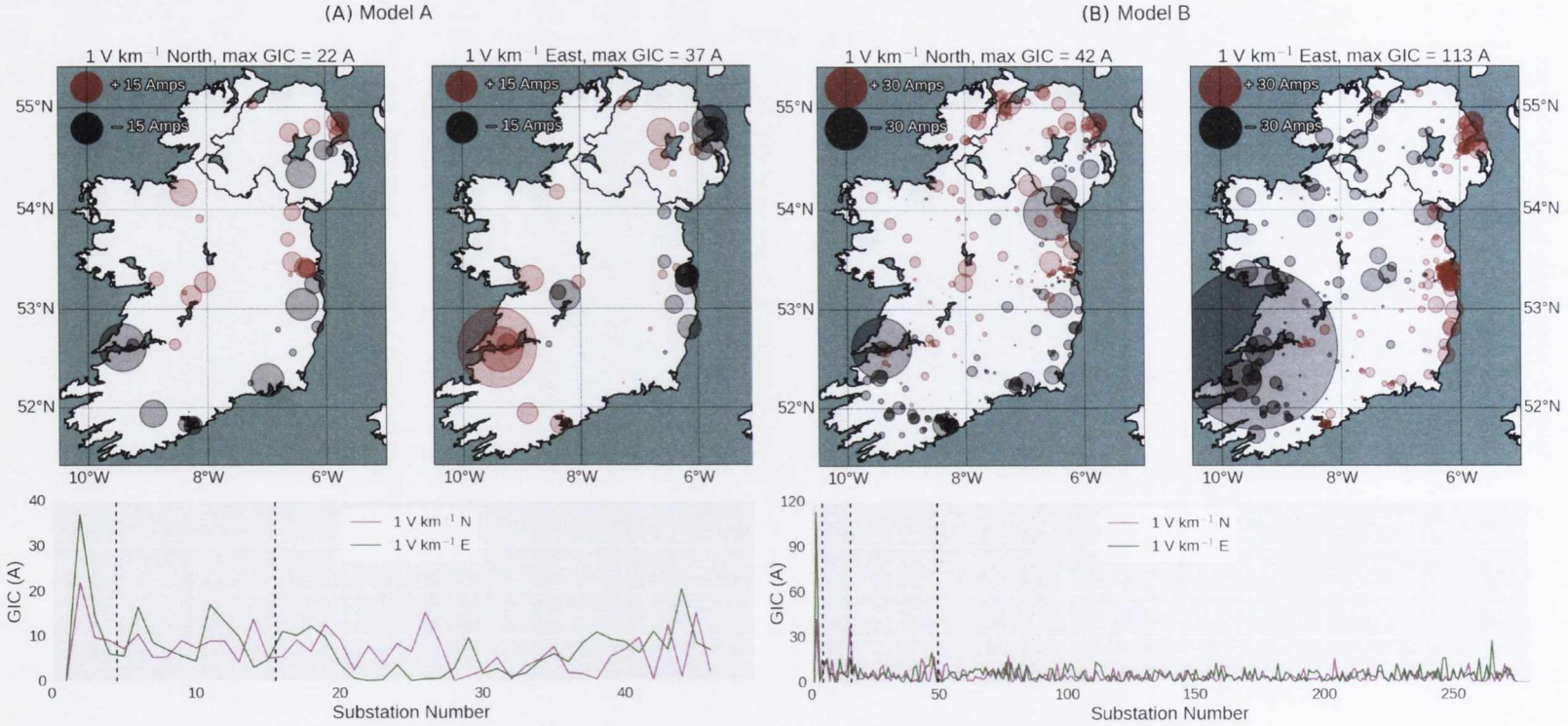


Figure 6.8: The response of the two power network models to uniform electric fields directed North and East. Model A has peak GICs of 37 A in Moneypoint with an eastward directed field (A), whereas model B has peak GICs of 113 A in Moneypoint (B). The bottom plots in subfigures (A) and (B) show the calculated GIC for each substation. The dashed black lines separate (from left to right) 400, 275, 220 and 110 kV substations. Substations are listed alphabetically for each voltage regime

Electric Field Orientation

The large GIC values in the Moneypoint substation are to be expected, given that it is connected to two of the largest transmission lines in the country (as larger lines allow for greater induced voltages; see Equation 6.4). Depending on the angle between transmission lines and the electric field, different values of GIC will be induced, with transmission lines parallel to an electric field giving the largest induced voltages and therefore the largest GIC. In contrast to this, transmission lines perpendicular to electric fields will have zero induced voltage. This can be seen in Moneypoint. When the electric field points East, it couples more strongly with the roughly East-West transmission lines which connect to Moneypoint substation, driving larger currents than a northward directed field.

A uniform 1 V km^{-1} field was applied to model B for every angle from 0 to 180° clockwise from North, in order to investigate the effect of a field in a direction other than North or East. It is unnecessary to continue to rotate the electric field between 180 and 360°, as induced GICs would have the same amplitude but different polarity as to when the field points from 0 to 180°.

The total sum of induced currents in all of the substations in model B for a uniform electric field directed different angles clockwise from North is shown in Figure 6.9. It shows that for an electric field pointing 82°, maximum GICs are induced in the network with a total of 1523 A. This is roughly eastward, and matches with the large GICs in Figure 6.8. A large proportion of the induced current is due to the Moneypoint substation. The green line in Figure 6.9 shows the sum of GICs minus Moneypoint's contribution. At its peak, Moneypoint accounts for approximately 8% of the total GICs in the network.

While the sum of GIC across a network is useful to know, it is the amplitude in individual substations which is concerning from an engineering point of view. Figure 6.10 shows the number of substations which experienced peak GICs per angle of uniform electric field. It shows that there is not a clearly identifiable angle which causes a clear peak in maximum GICs. 29 substations experienced peak GICs when the field pointed between 45–50° (NE), and 31 experienced the same between 145–150° (roughly SE).

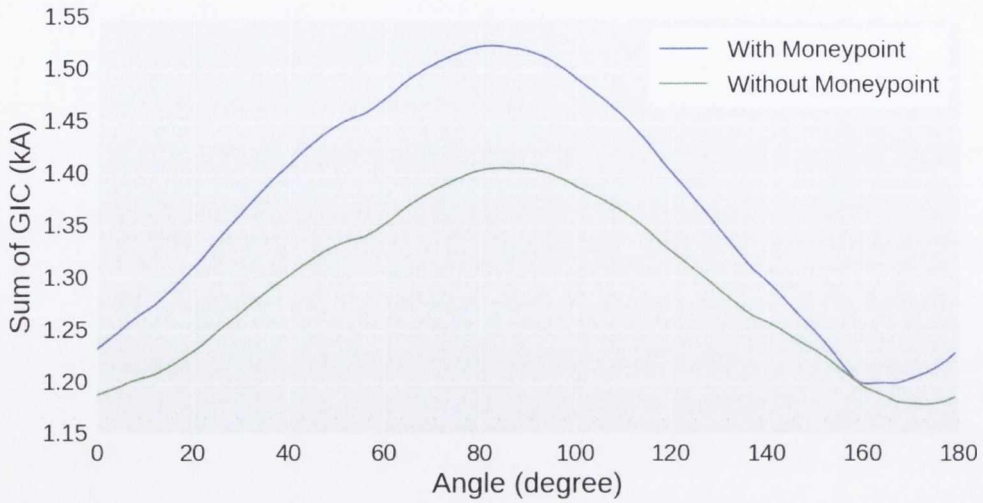


Figure 6.9: Sum of GICs generated in model B due to uniform electric field directed at angles clockwise from North. The green line indicates the sum of GICs excluding the GICs at Moneypoint.

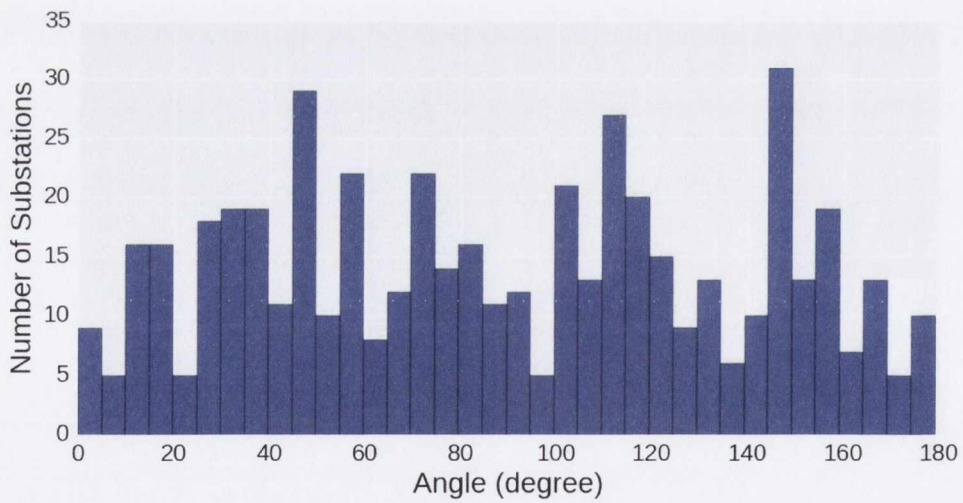


Figure 6.10: The number of substations which experienced a peak GIC due to a uniform electric field of 1 V km^{-1} pointing in different angles.

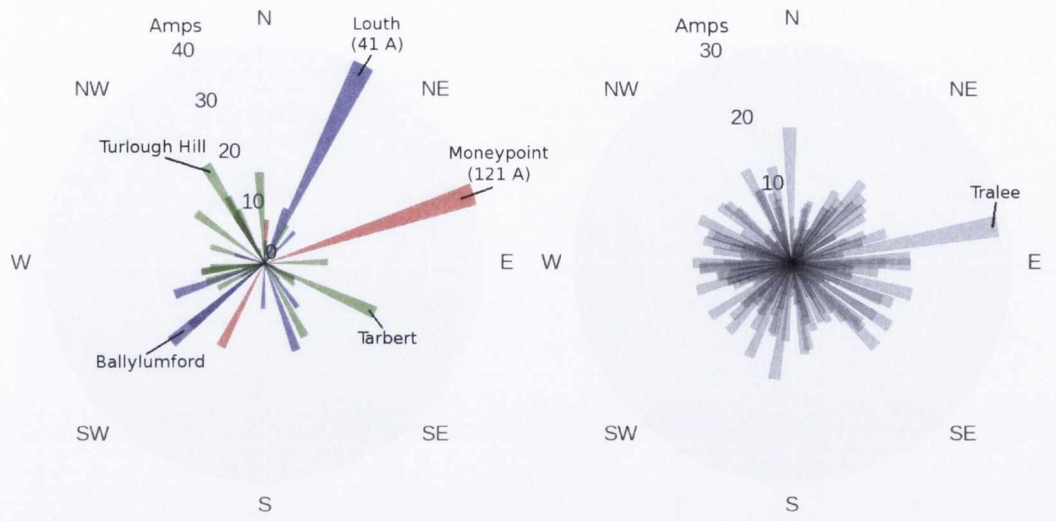


Figure 6.11: Direction of electric field in which the maximum positive GIC is generated per substation. In each subfigure, angle corresponds to direction of electric field, and length of each segment is the maximum current. The red, blue, green and gray segments correspond to 400, 275, 220 and 110 kV substations respectively. Moneypoint saw GICs of 121 A.

Figure 6.11 shows the angle of electric field for which each substation in model B experienced maximum GICs. Unsurprisingly, it is Moneypoint which again sees the largest GIC at 121 A, when the electric field points 69° clockwise from North. GICs of 41 A were calculated at Louth for a 24° electric field. This is roughly the same angle of the transmission line which connects the Louth substation to the 275 kV network. With the exception of Tralee, it can be seen that the 275 and 220 kV substations experienced marginally larger GICs than the 110 kV substations.

Ground Resistance Analysis

The grounding resistances (or GR for brevity) of substations are one of the characteristics of a network which influence the magnitude of induced currents. The neutrals of transformers are connected to a mesh of conductors buried in the sediment at the location of each substation. If the sediment is resistive, the substation will have a large GR, which will limit GICs. Likewise, conductive sediment will lead to a low GR. For safety, substations are built to have GRs as low as possible.

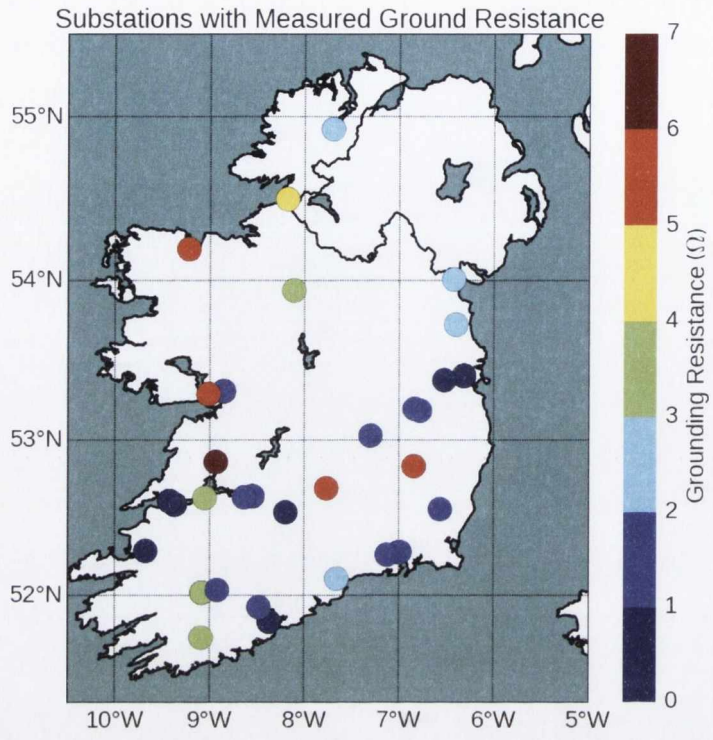


Figure 6.12: Locations of substations with measured grounding resistances. These range from 0.25–6.35 Ω.

As mentioned above, model B has information on the GR of 33 of its 274 substations. These sites are shown in Figure 6.12. These substations have GR which range from 0.25 to 6.35 Ω, with an average of 1.9 Ω. These values are much larger than the 0.1 Ω assumption used in other studies (Blake *et al.*, 2016b; Myllys *et al.*, 2014; Torta *et al.*, 2014; Turnbull, 2011). The distribution of known GR are shown in Figure 6.13. Those sites which did not have that information were set as having grounding mat resistances of 1 Ω in the previous section.

In order to investigate how this 1 Ω GR assumption affects calculated GICs, the substations with unknown GR were uniformly set at fixed values ranging from 0.25 to 7 Ω. For each different chosen GR for these substations, the network was subjected to a uniform 1 V km^{-1} electric field. The resulting GIC at these substations, along with the 33 substations with known GR, are shown in Figure 6.14.

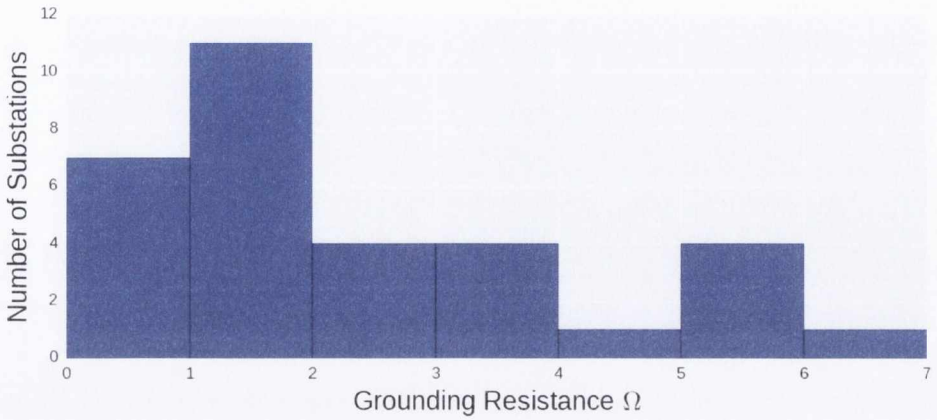


Figure 6.13: Histogram of known substation grounding resistances. 33 substations have known grounding resistance values. The average of these known values is 1.98 Ω. Roughly half of them are less than 2 Ω.

The figure shows from top to bottom, the GIC calculated at each substation for varying GR, the variation in GIC for each substation for the simulations, and GR value against average GIC per substation.

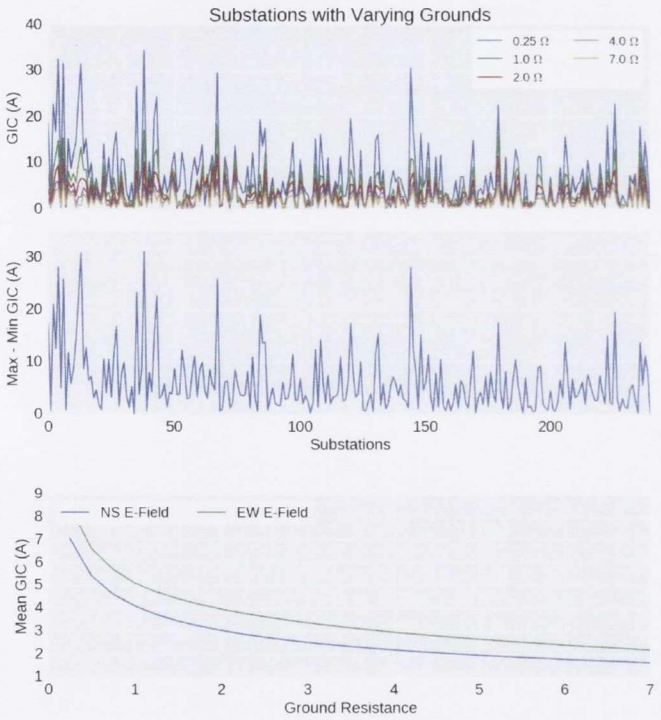
As one could expect, varying the GR from 0.25 up to 7 Ω gives greatly different GIC estimates at most of the substations. The larger the GR, the smaller the GICs in the substations with unknown grounds. The inverse of this is true at the 33 substations with fixed grounds. This is because as the GR increases for most of the network, the 33 substations with fixed grounds become relatively less resistive, becoming more suitable outlets for the induced currents in the network.

For the 241 substations which were given different GR, the maximum difference in GIC for each of the substations averaged to be 5.9 A, although individual substations varied from effectively 0 to 31 A. The substations with fixed values gave marginally more stable GIC for the simulations, with individual substations varying from 0 to 29.6 A. The average variation for the 33 substations was 5 A.

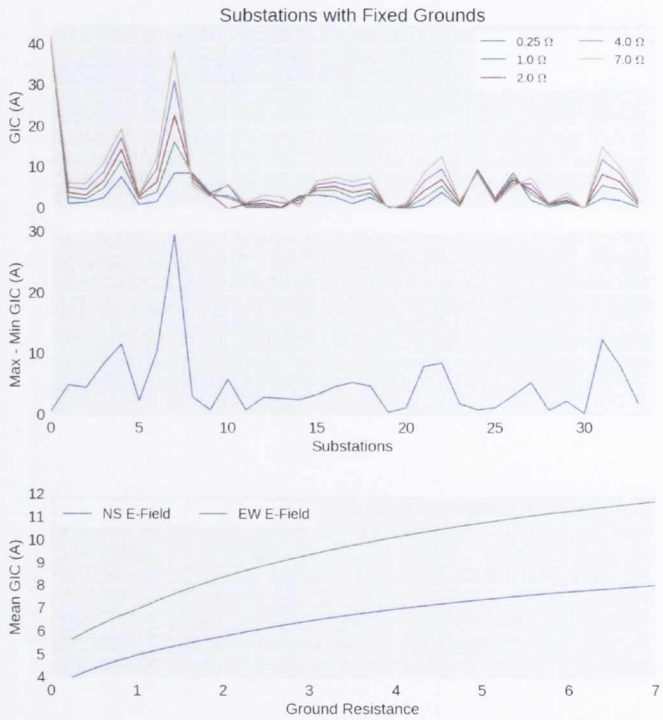
These simulations show that although we know the GR of 33 of the 274 substations, the calculated GICs in many of the substations with known GR were strongly affected by the assumed GR of the rest of the network. For example, four of the substations with known GR had GICs which varied by greater than 10 A depending on the value of GR chosen for the rest of the network. Whilst

10 A isn't a particularly large current, it is a large fraction of the typical calculated GICs seen in Section 6.3.1, meaning that there is considerable uncertainty for many substations based on the assumed GR for the network.

Of the 33 substations with known resistances, the 220/110 kV Raffeen substation changed the most (by 29 A) depending on the assumed GR for the network. Other strongly affected substations were Tralee (varying by 12.45 A) and Great Island (varying by 11.7 A). Tarbert and Moneypoint, two substations which gave large GICs in the uniform electric field test in Section 6.3.1, gave stable GIC values depending on the chosen GR for the network. Tarbert varied by 3.1 A, whereas Moneypoint varied by only 0.7 A. This indicates that, for these sites, the chosen GR for the network is less important than the orientation of the network and the transmission line resistances.



(a) Substations with Varying Ground Resistances



(b) Substations with Known (Fixed) Ground Resistances

Figure 6.14: The GIC response of substations due to a northward 1 V km^{-1} electric field when the grounding resistances assumption of 1 Ω is altered. Subfigure (a) shows the response of those substations whose grounding resistances are unknown, whereas Subfigure (b) shows the response of the 33 substations with known and fixed grounding resistances. The bottom plot shows the average GIC per substation as the grounding resistance is altered.

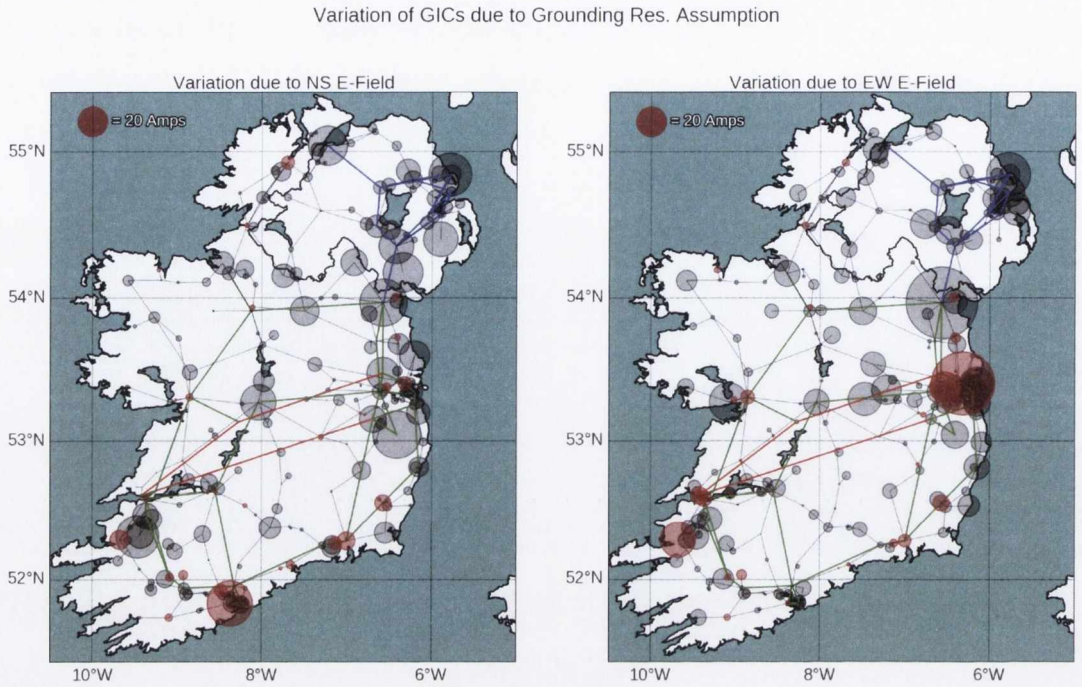


Figure 6.15: Plot of maximum variations per substation for different grounding resistances from 0.25–7 Ω. Red circles are for substations with known grounds, and black are for those with assumed grounding resistances.

A spatial plot of the maximum variations of GIC for the network for different grounding resistance values is given in Figure 6.15. It shows the variations (a proxy for uncertainty due to assumed grounding resistances) for each substation, where red circles are the substations with known resistances, and the black circles are for substations with assumed grounding resistances (those which were varied).

Effect of Adding Lower Voltages to Network

Higher voltage transmission lines will have lower resistances by construction, and can thus expect larger GICs (Boteler & Pirjola, 2016). As lower-voltage levels are therefore less important for GIC calculations, many studies have neglected to model them in a network. However, it has been shown that lower-voltage levels can have a significant impact on calculated GICs (Guo *et al.*, 2015; Torta *et al.*, 2014), although this is highly dependent on the makeup of an individual network.

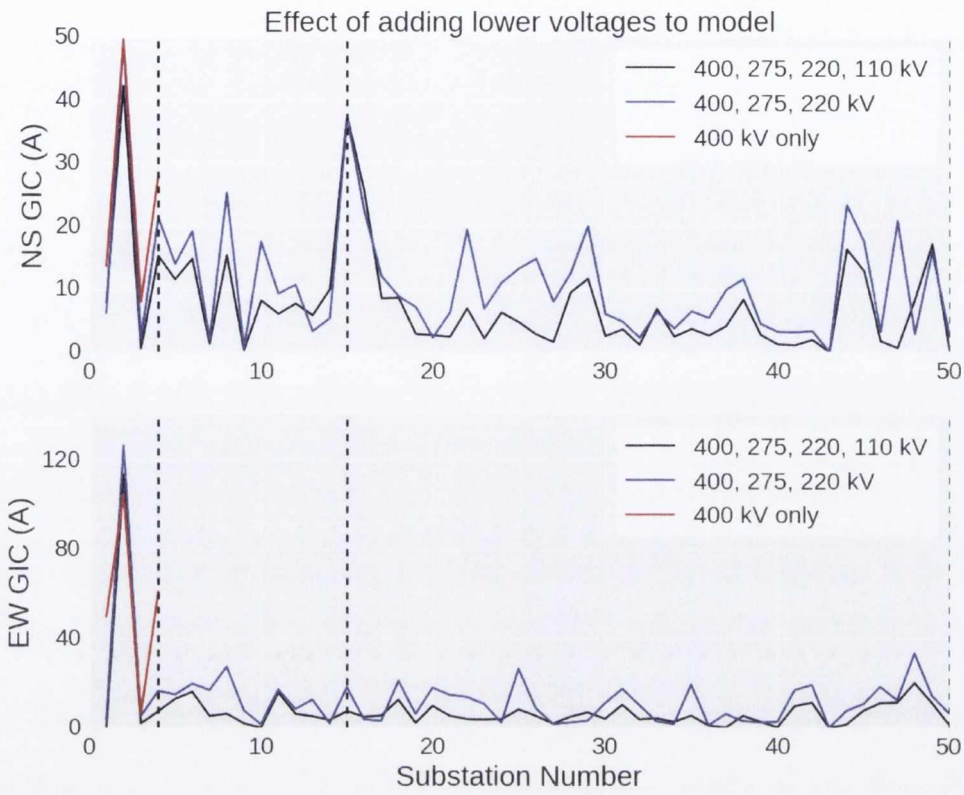


Figure 6.16: Calculated GICs for different voltage levels in the Irish network. The top and bottom plots are for northward and eastward electric fields respectively. The dashed lines separate from left to right the 400, 275, 220 and 110 kV substations.

The effect including all of the different voltage levels in the Irish power network model has on calculated GICs is explored in this section. Three calculations were made for northward and eastward electric fields. These are for the 400 kV network, the 400, 275 and 220 kV network, and the complete 400, 275, 220 and 110 kV network. The resulting GICs for each substation are shown in Figure 6.16.

When the 400 kV only network is compared to the 400, 275 and 220 kV network, the 400 kV substations experience marginally smaller GICs. The exception to this is Moneypoint with an eastward directed field, which experienced a slight increase in calculated GIC. Moneypoint is connected to a single 220 kV substation.

Generally, for each of the 400, 275 and 220 kV networks, the addition of the 110 kV network decreases the calculated GICs, as the currents are directed into

the lower voltage substations. Of the ten substations which experienced the largest absolute difference in GICs, all experienced reduced GICs. Furthermore, all (except Moneypoint) were connected to at least three 110 kV substations. It is to be expected that those substations most affected by the addition of the lower voltages are themselves connected to lower voltages, so the affected substations are not surprising.

The proportional changes in GICs when the 110 kV substations are added are shown in Figure 6.17. This shows that there is a general decrease in GICs. There are exceptions to this however, especially with the eastward directed field, with 11 substations experiencing increases in GIC. The largest proportional increase occurs in the 220 kV Turlough Hill substation, increasing by 192% with a northward directed field. Whilst this is quite a large increase, in absolute terms, the GIC at this substation only increased from 2.86 to 8.37 A. Five of the 50 substations had GICs which decreased by over 90%. Each of these substations had at least three connections to lower voltage substations.

The above analysis highlights the importance of including the lower voltage levels in a network model for GIC calculations. In the case of the Irish power network, with some exceptions, omitting the lower voltages would lead to overestimating the 'true' GIC at the higher voltage substations, especially at those substations with direct connections to the lower voltages.

Minimising GIC with Ground Switches

Some transformers are fitted with netural earth switches which are used to connect and disconnect from the substation ground. These are sometimes opened for operational reasons to reduce the potential short-circuit currents that could arise during a fault on the power grid. In terms of calculating GICs, these could be used to isolate a transformer from its ground, preventing a transformer from being a conduit for GICs to or from the ground.

In addition to grounding resistances, model B has information regarding ground switches in 15 of the 319 transformers. These transformers are in 10 substations. Figure 6.18 shows the effect an eastward 1 V km^{-1} will have on the network when all of the 15 transformers are grounded and isolated. The maximum difference is

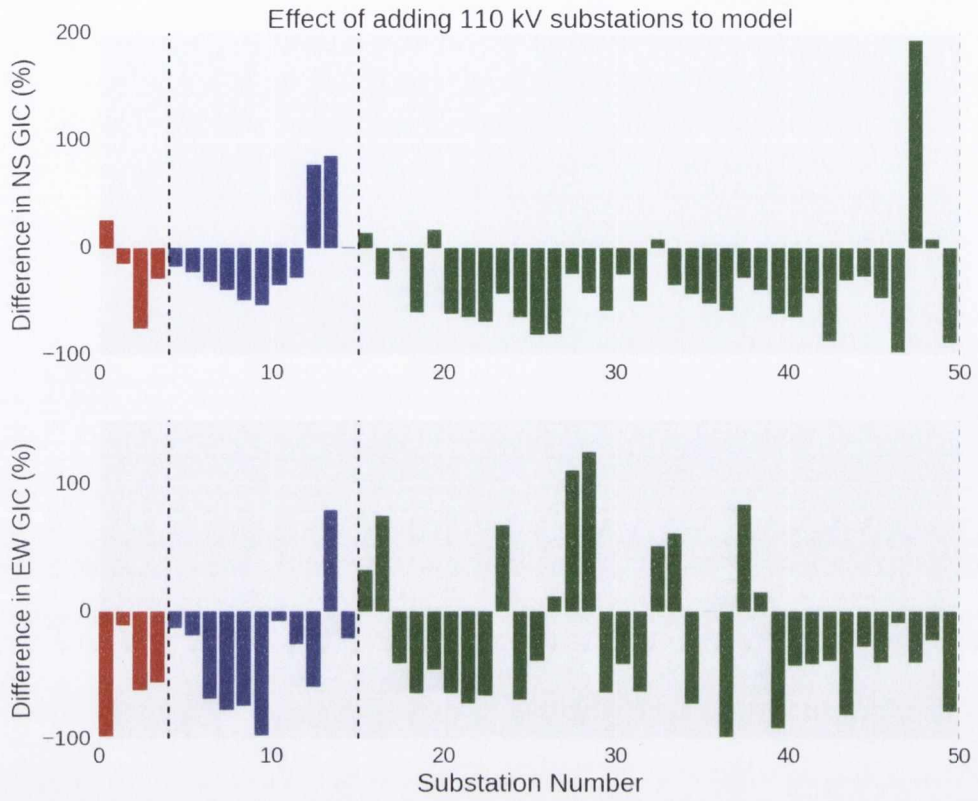


Figure 6.17: Proportional difference in calculated GICs when the 110 kV network is added to the model. The top and bottom plots are for northward and eastward electric fields respectively. The dashed lines separate from left to right the 400, 275, 220 and 110 kV substations.

a reduction of 10 A in the 220 kV Ballyvouskill substation. Other substations in the network are minimally affected and, unfortunately, none of the transformers with these switches are in any of the more 'at-risk' substations identified in the previous sections.

In an ideal scenario, those transformers most at risk from large amplitude GICs would be equipped with such ground switches. Provided with sufficient forewarning, they could be opened, thus preventing damage to vulnerable transformers. The following test was performed on the Irish power network model in order to determine the minimum number of ground switches needed to minimise GICs.

All transformers in the Irish power network model were set as grounded, and

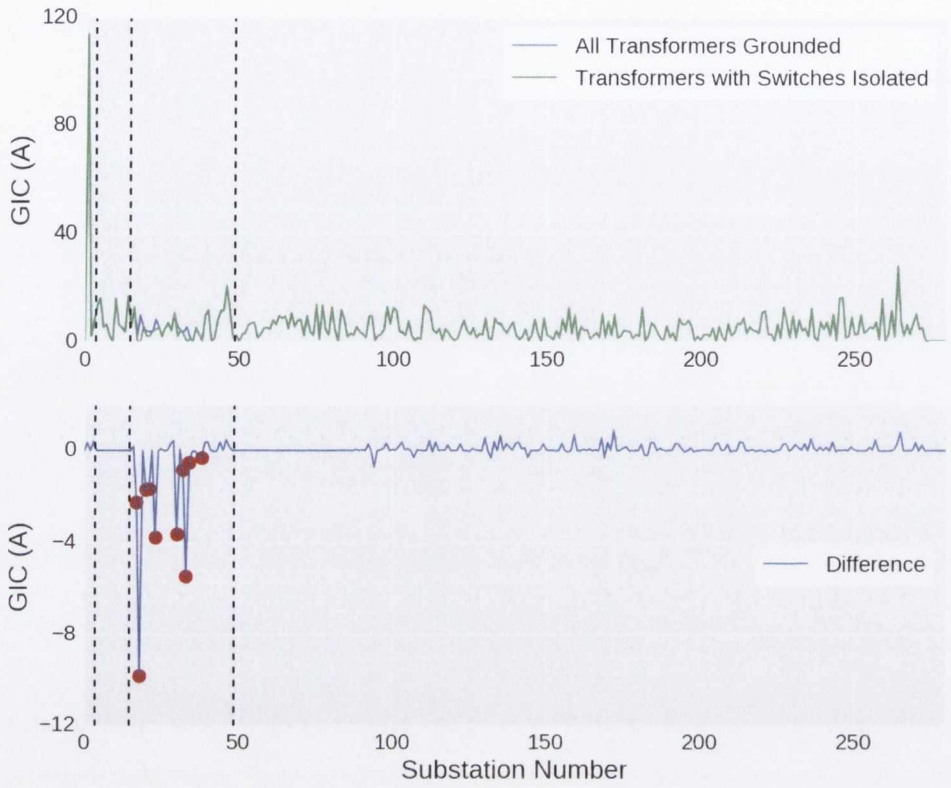


Figure 6.18: The effect of an eastward 1 V km^{-1} electric field on the network when transformers are grounded and isolated. An eastward directed field was chosen as it generates larger GICs than a northward directed field. The top plot shows the absolute values for all transformers grounded (blue) and all transformers except 15 with switches grounded (green). Bottom plot shows the difference between the two, with red circles indicating the substations with transformers with switches.

an eastern 1 V km^{-1} was applied to generate GICs. The transformers at the substation with the largest calculated GIC were isolated from the ground, and GICs were calculated again using the 1 V km^{-1} electric field. The electric field was repeatedly applied to the model, isolating the transformers in the most affected substations, until all substations were isolated. The calculated maximum GIC and sum of GICs for the whole network are shown in Figure 6.19.

This shows that the sum of GICs in the network decreases roughly linearly with each substation isolated from the ground. However, as mentioned before, it

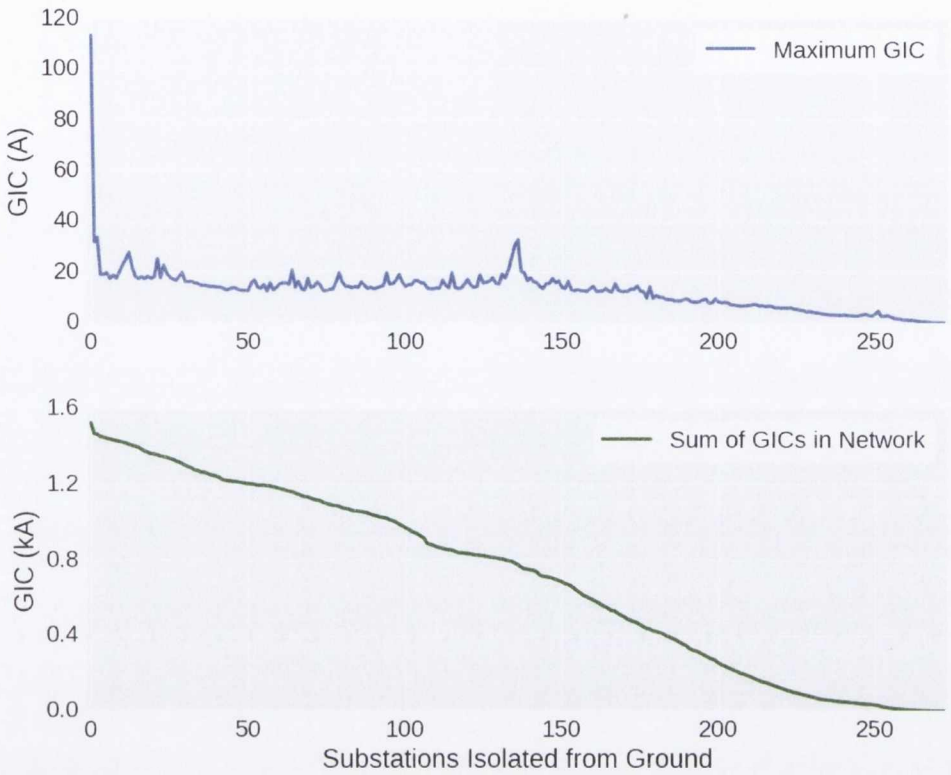


Figure 6.19: The maximum calculated GIC (top) and sum of GICs (bottom) for the Irish network model due to a uniform field, as substations have their transformers isolated from the ground.

is the amplitude of a GIC in an individual substation which is concerning from an engineering perspective. After isolating only four substations (five transformers), the maximum GIC in the Irish network due to an eastward directed field was reduced to less than 20 A. A single ground switch at the Moneypoint substation (which has a single transformer in the model) reduces the maximum calculated GIC in the network to 32 A.

Summary

Two models of the Irish power grid were created for GIC calculation using the Lehtinen & Pirjola (1985) method. The second of these models, Model B, includes

the entirety of the Irish high voltage network, with 400, 275, 220 and 110 kV substations. Each of the 400, 275 and 220 kV substations have correct transformer data including high and low-voltage winding resistances. The 110 kV substations have estimated winding resistances.

This model was subjected to a number of tests involving uniform electric fields in order to gauge the general GIC response of the network when storm dynamics and geology are omitted. With an eastward directed 1 V km^{-1} electric field, a current of 113 A was measured in a single substation. Four other substations saw GICs greater than 20 A. When the electric field pointed 82° clockwise from North, there was the greatest GIC response across the network.

In the model, 33 of the 274 substations have actual grounding resistances which varied from 0.25 – 7 Ω. The remaining substations had grounding resistances set at 1 Ω. In order to check the affect this assumption has on calculated GICs, the grounding resistances of the other 241 substations were varied uniformly. The calculated GIC at some substations changed considerably with the assumed grounding resistance, while others changed very little. This was true for some of the 33 substations with fixed known grounding resistances. This test was used as a proxy for uncertainty introduced by our assumption of a 1 Ω grounding resistance.

Adding the 110 kV substations to the model changed some of the GICs in the substations by up to 200%. It was shown that to omit the lower voltage networks would lead to overestimating GICs in the higher voltage systems. As could be expected, the substations most affected by the introduction of lower voltage levels were those with multiple direct galvanic connections to lower voltage levels.

Finally, the effect using grounding switches in the Irish network was explored. It was shown that the 15 transformers in the Irish network with grounding switches are not positioned in particularly vulnerable parts of the Irish network. Isolating these 15 transformers would not decrease the GICs in any substation by more than 10 A for a 1 V km^{-1} electric field. It was shown that with switches on five chosen transformers, the maximum GIC due to a uniform electric field could be reduced to less than 20 A.

The above tests show that Ireland's network is less susceptible to GICs than other networks. The Norwegian, British and Spanish networks each saw larger and more widespread GICs for the 1 V km^{-1} tests described above (Myllys *et al.*,

2014; Torta *et al.*, 2014; Turnbull, 2011). For example, the Spanish network had widespread calculated GICs greater than 100 A. The networks for those countries span much larger areas than Ireland, which measures approximately 300×500 km. The addition of the lower voltage levels in Ireland also ensures that the network is quite dense, with approximately one grounded transformer for every 220 km^2, providing many outlets for GICs.

Despite this, the more vulnerable substations in Ireland were identified. Foremost among these is the 400 kV Moneypoint substation. This is connected to two of the largest high-voltage lines in Ireland, and has a low grounding resistance (0.246 Ω). For these reasons, the GIC at this substation dominates the values given by the other substations. Currently, Moneypoint has one transformer in operation, although more are planned in the future (Ray Doyle, EirGrid, personal communication, 2017), and this would effectively 'dilute' the GIC at the substation between transformers. Other notable substations were Louth, Tarbert and Tralee. Each of these saw above 20 A for the uniform electric field tests.

This chapter showed how the Irish model network was developed, and how the various characteristics of the model contribute to the distribution of GICs. The next step in studying GICs in this model is to subject it to real geomagnetic storm events. This is done in the following chapters, first for recent events, then for larger historical events.

7

Modelling GICs During Recent Storm Events

In Chapter 4, the SECS method of interpolating geomagnetic fields during geomagnetic storm events was explored. In Chapter 5, the MT and thin-sheet methods of calculating electric fields using subsurface resistivity models was outlined. In Chapter 6, a model of the complete HV Irish power network was presented and subjected to idealised surface electric fields.

In this chapter, the effects of several geomagnetic storms in the Irish power network are calculated. This process begins with measured geomagnetic fields around Ireland and Britain. These fields are interpolated across Ireland, and coupled with different Earth resistivity models to calculate surface electric fields. Finally, GICs are calculated in two different models of the Irish power network.

These calculated GICs are then compared to measured GIC data at the Woodland 400/220 kV substation for recent geomagnetic storms. The resistivity model that best reproduces the measured GICs is identified, so that it can then be used to simulate larger historical geomagnetic storms. This enables us to get a qualitative estimation of how Ireland's power network is affected by geomagnetic storms. Part of the work that appears in this chapter is published in Blake *et al.* (2016b).

Measured GIC Data in Ireland

Ireland's power network has no recorded instances of transformer damage which have been attributed to geomagnetic activity (David Bell, EirGrid, personal communication). Until recently, Ireland has had no direct measurements of GICs. This was changed in mid-August 2015, when a Hall effect probe was installed on one of two transformers in Woodland, a 400/220 kV substation in Meath (labeled in Figure 6.7). This Hall effect probe measures the changing magnetic field produced by any GIC which flows through the transformer ground. The intensity of the measured magnetic field is proportional to the magnitude of the current flowing through the transformer ground, giving an almost direct measurement of GIC.

The device in Woodland (shown in Figure 7.1) samples the magnetic field at a frequency of 6.4 kHz. It averages these values into one-minute bins, producing 1440 GIC values per day. These data are stored and emailed automatically to interested parties the morning after each day. The device has undergone several calibrations by EirGrid engineers, and has been running continuously since its installation.

The recent date of installation and lack of multiple GIC measurements in Ireland presents a problem when studying GICs. Since August 2015, there have been few large geomagnetic events, so few events that can be used to validate GIC simulations exist. Furthermore, none of the 'large' events have registed larger than Kp7+ on the planetary K-index scale (see Section 3.3.2). This means that when simulating GICs in the Irish power network, the calculated current in only one transformer can be confirmed, and only for small sample of relatively minor geomagnetic events. Nevertheless, the general method of simulating GICs in the Irish network in this study is as follows:

1. Different combinations of resistivity models and electric field calculation methods are combined to calculate GICs in the transformer in Woodland. The models that give calculated GICs which best fit the measured GICs are assumed to best fit the calculated GIC for the entirety of the network.

2. These 'correct' models can then used to simulate historical storms in later chapters.

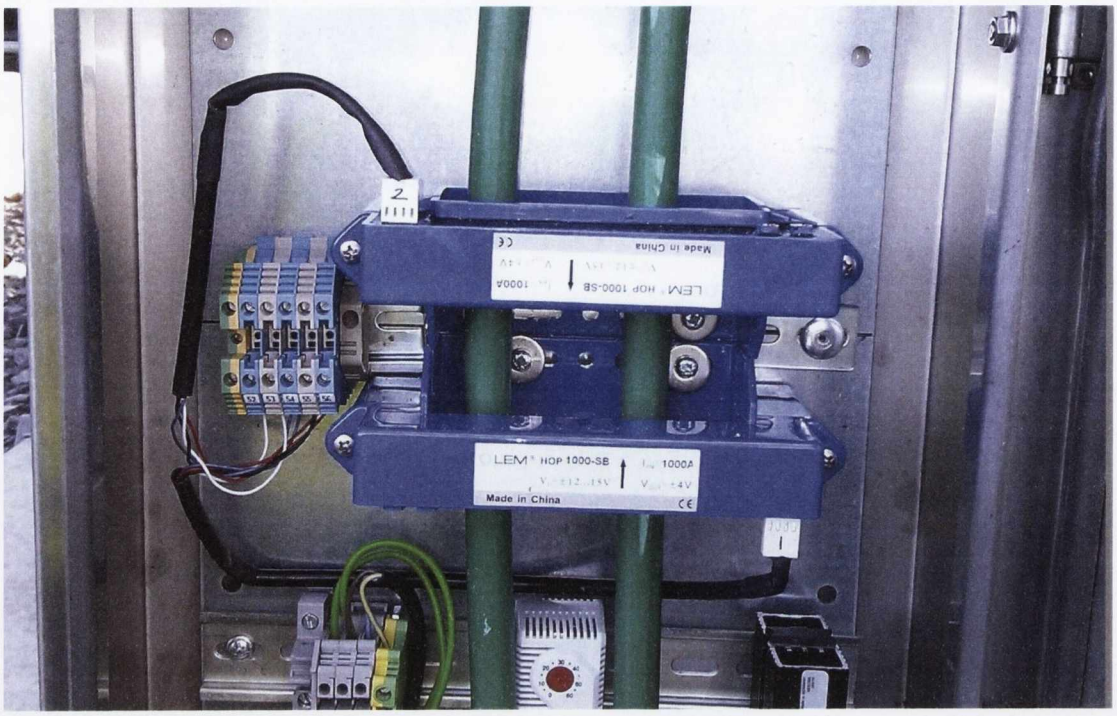


Figure 7.1: The Hall effect sensor at the ground of a transformer in the Woodland substation. This devices bins the data into minute bins *in situ*, and a daily file is emailed to interested parties (David Bell, EirGrid, personal communication).

Choosing Recent Events

Five geomagnetic storms which occurred after the installation of the Hall effect probe were chosen to test GIC simulations. These five events were chosen as they gave the largest unambiguous GIC measurements at the Woodland substation. The dates of these events are: 26-28 August 2015, 07-08 September 2015, 07-08 October 2015, 20-21 December 2015 and 06-07 March 2016. The horizontal magnetic field components measured at the Birr observatory during each event are given in Figure 7.2 and Table 7.1 lists the geomagnetic conditions and operational geomagnetic observatories for each event.

As the Hall effect probe has only been functioning since 2015, it has been operating near solar minimum. Most of the recent events (three of five) are caused by high speed solar wind from coronal holes rather than CMEs or solar flares. A brief description of the solar and geomagnetic conditions which caused the storm events follows.

Table 7.1: The recent events chosen to test GIC calculations. This table gives the geomagnetic conditions and the MagIE and INTERMAGNET stations which were available for each. Kp and Dst values were taken from http://wdc.kugi.kyoto-u.ac.jp/.

Event	Kp	Dst (nT)	Sites Available
26-28 Aug. 2015	6+	-90	Birr, Leitrim, VAL, CLF, DOU, ESK, HAD, LER
07-08 Sep. 2015	6+	-70	Birr, Leitrim, VAL, ESK, HAD, LER
07-08 Oct. 2015	7+	-124	Birr, VAL, CLF, DOU, ESK, HAD, LER
20-21 Dec. 2015	7-	-155	Birr, Sligo, ESK, HAD, LER
06-07 Mar. 2016	6+	-98	Birr, Sligo, VAL, ESK, HAD, LER

26-28 August 2015

A large active region (NOAA number 12403) on the western limb of the Sun produced several C-class flares after its appearance on the Earth-facing side of the Sun on 18 August. An extended period of southward oriented B_z interplanetary magnetic field elevated geomagnetic activity for several hours. At 04:48 UT, the active region produced a M2.1-class flare, further disturbing the geomagnetic field. Another M2.1-class flare occurred from the same region at 18:56 UT on the 28th. The peak of the geomagnetic disturbance occurred around 21:00 UT on the 28th, with a Dst of -92 nT, and a maximum planetary K-index of 6+.

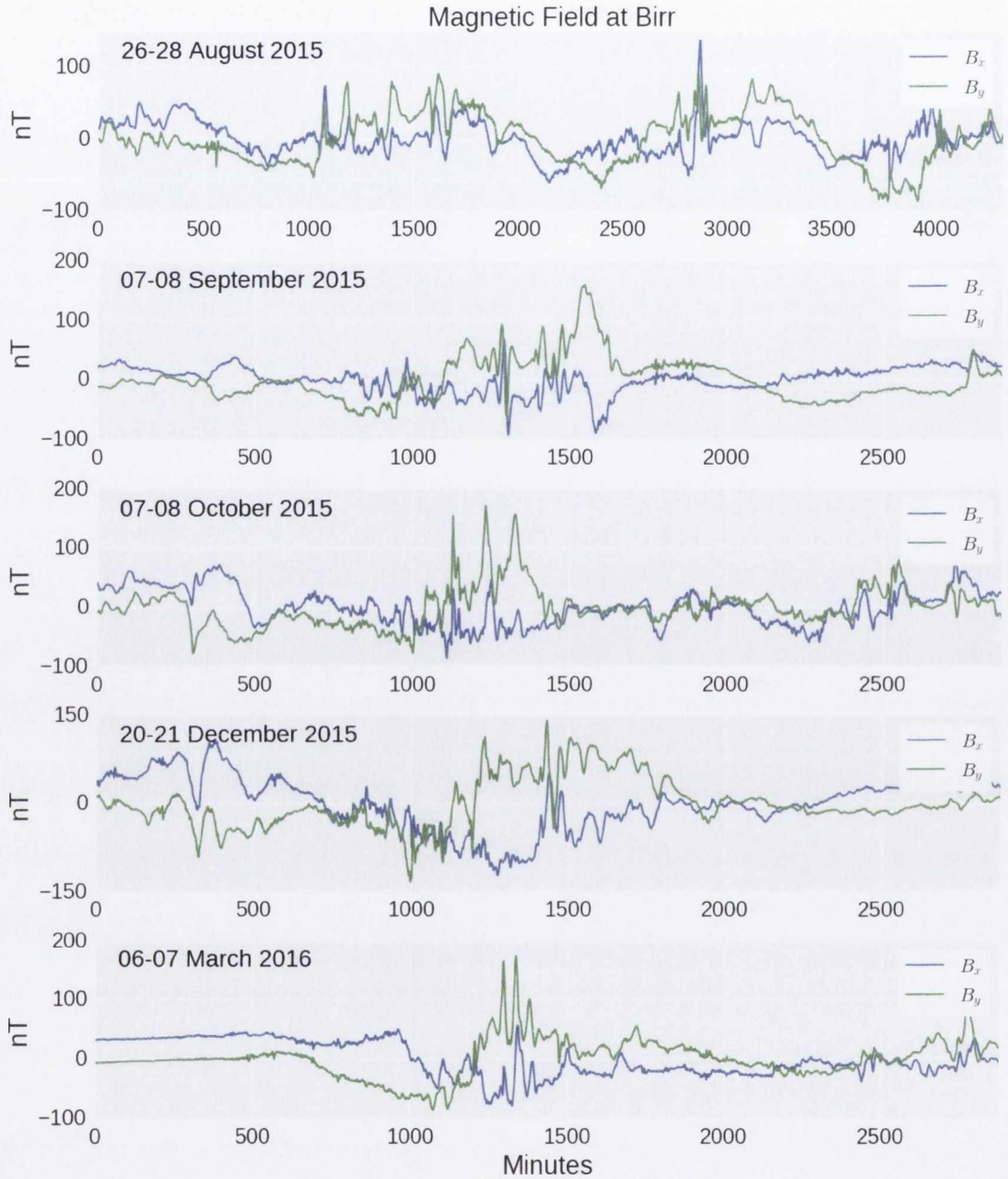


Figure 7.2: Measured horizontal magnetic field components in Birr during the five recent events. The daily baseline has been subtracted from the data in the above plots.

07-08 September 2015

The Sun was quiescent in the days leading up to this event, with no flaring active regions or CMEs occurring. However, there was a large coronal hole on the centre of the solar disk with a solar wind speed of around 580 kms^{-1}. The geomagnetic storm began at approximately 21:30 UT on the 7th, and continued until 0500 UT the next day. This storm had a peak Dst of -70 nT, and a Kp-index of 6+.

07-08 October 2015

Like the September event, there were no active regions of flaring that led to geomagnetic activity for this event. Once again, there was a large mid-latitude coronal hole with a high-speed solar wind of about 780 kms^{-1}. This high speed wind continued to the 9th, when it dropped to less than 600 kms^{-1}. The geomagnetic storm began in earnest before 18:00 UT on the 7th, with a peak Dst of -124 nT, and a Kp-index of 7+.

20-21 December 2015

A CME eruption on 16 December had a glancing impact with Earth's magnetosphere on the 19th. A southward directed IMF (approximately -18 nT) exacerbated the effect of the CME, which led to a minor geomagnetic storm. The storm had a peak Dst of -155 nT, and a Kp-index of 7-.

06-07 March 2016

The Sun exhibited no flaring and only small and stable active regions in the days preceding this event. Again it was a high speed solar wind which caused this geomagnetic disturbance. The southward directed portions of this wind coupled well with the magnetosphere, leading to a Dst of -98 nT and a Kp-index of 6+.

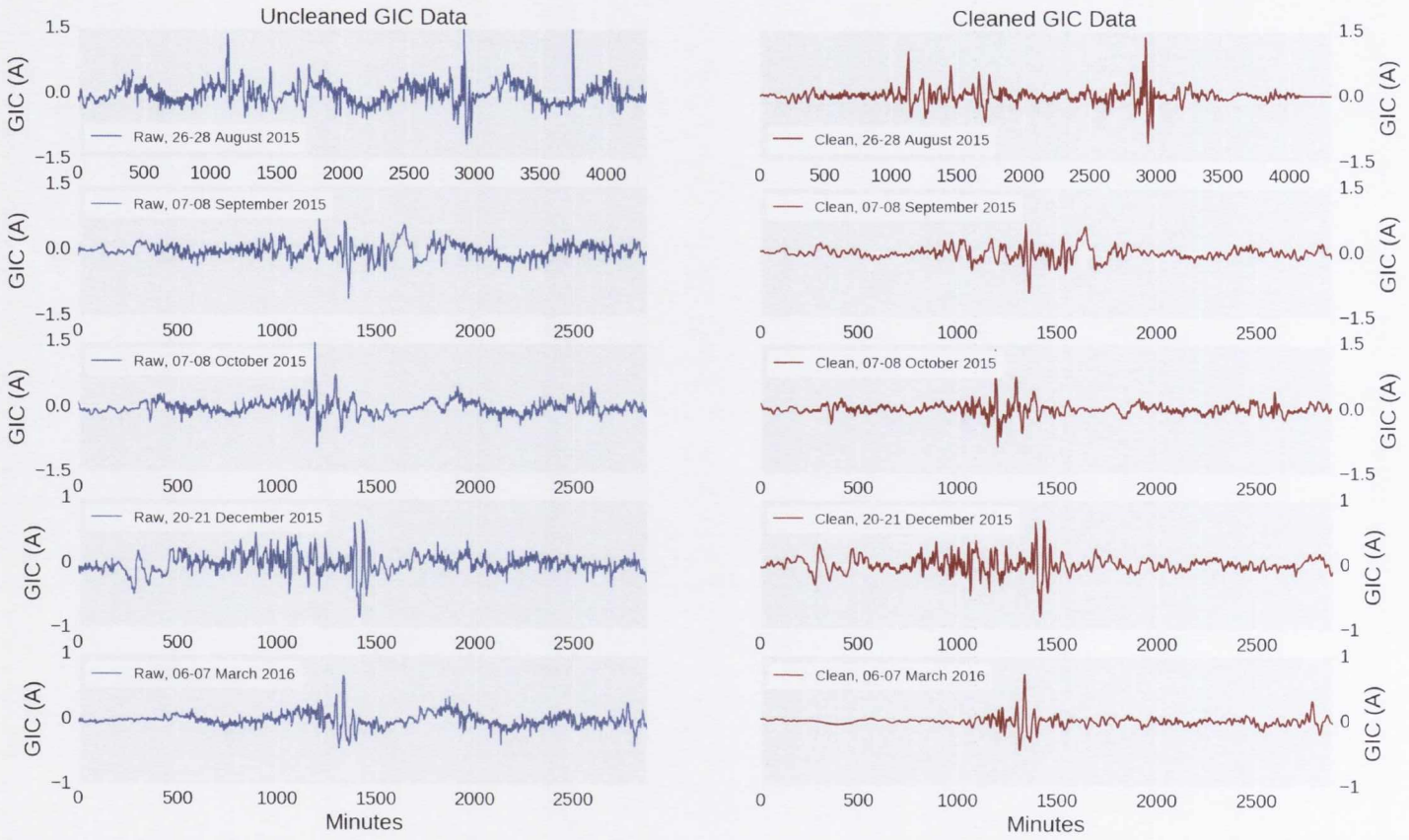


Figure 7.3: Untreated and cleaned GIC data for each of the five recent events used in this study as measured in the Hall effect probe in Woodland. The diurnal variation and high frequency noise can be seen in each of the raw data events. Also seen are stray large-amplitude spikes unrelated to GIC activity (see for example 26-28 August 2015 plot). These spikes were manually removed and interpolated across. The cleaning process is outlined in Figure 7.4

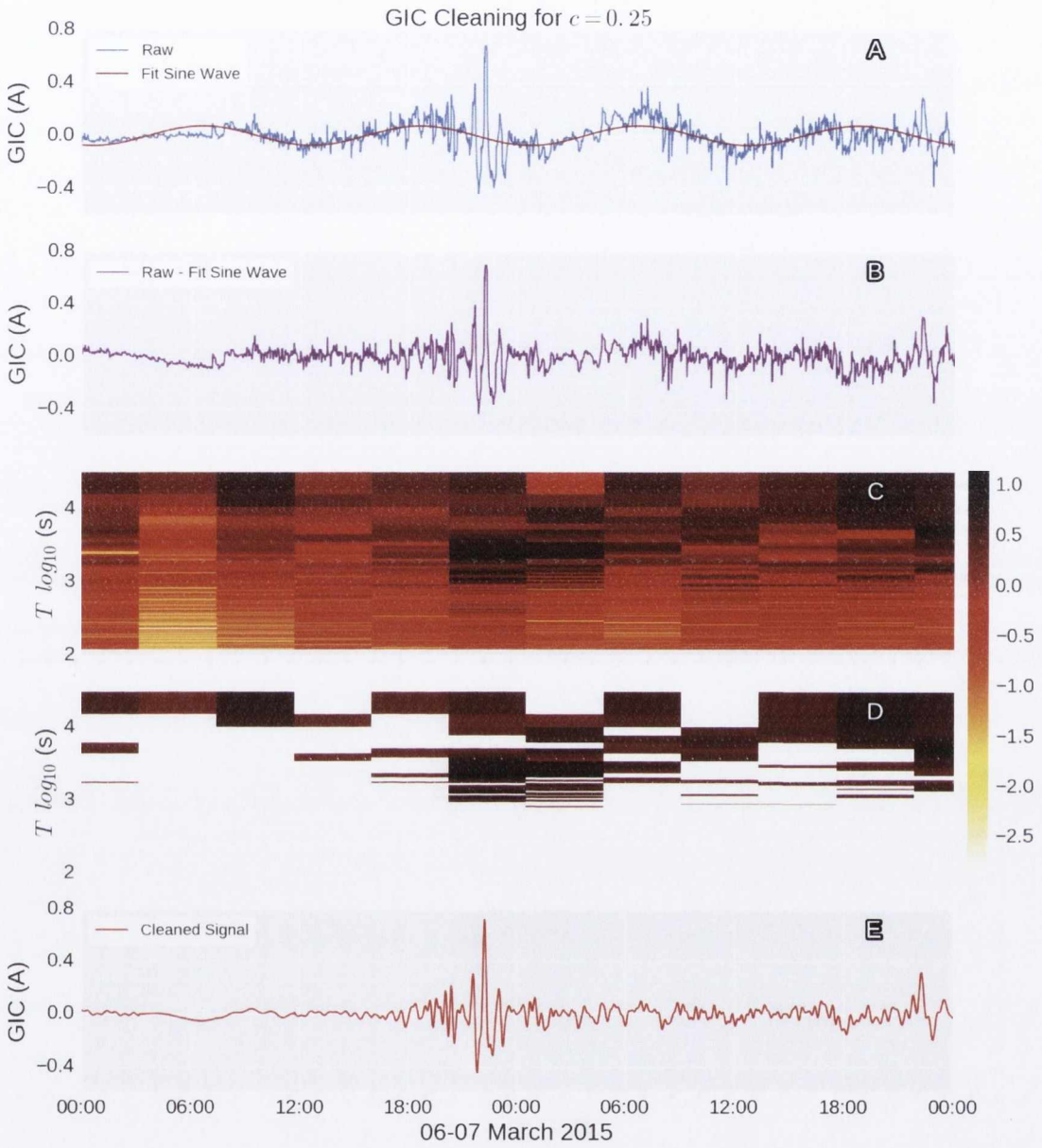


Figure 7.4: The cleaning process for raw GIC data for the 06-07 March 2015 event. First, a sine wave is fit to the data (A) and subtracted to give (B). A spectrogram of this signal is created with four-hour bins (C). The lowest contributing bins are discarded from the spectrogram, according to some proportion c (D). The signal is then recreated (E). The resulting signal is primarily GIC, with the noise spikes greatly reduced. As can be seen from subfigure D, most of the shorter periods of the signal were the lowest contributors, and were thus discarded.

Cleaning GIC Measurements

In order to properly measure the fit of GIC data, it is necessary that whatever noise or artifacts unrelated to GIC in the measured data are removed. A 2.1 A baseline, a quasi-diurnal sinusoidal variation and high frequency noise of ~0.1 A are present in the GIC data from Woodland. The measured data for each of the events (minus the 2.1 A baseline) are shown in the left column plots of Figure 7.3.

For each of the events, the raw data exhibits the long-period sinusoidal variation and higher frequency noise of about 0.1 A. In addition to this persistent noise, some events exhibit large spikes of several A. These spikes are unrelated to geomagnetic activity, and probably relate to the operation of the Woodland substation. Different elements of a substation may be connected or disconnected from the high-voltage network depending on the load on a network. These spikes can be seen in the August 2015 and September 2015 events. In addition to these sources of noise, there is a curious lessening of the signal present for the first eight hours of every day. This is also unrelated to geomagnetic conditions.

The data are cleaned using the following method. Firstly, every instance of large noise spikes which were unrelated to geomagnetic activity are manually removed, and filled with a linear interpolation (for example, the large spike near the end of the August 2015 event). The baseline is then removed from the measured GIC, and a sine wave is fit to the data using least squares error fit. This sinusoidal signal is taken away from the data, and a spectrogram of the residual data is created. The bins in the spectrogram show power per period contribution to the GIC signal. A value, c, is chosen, which indicates a proportion of the spectrogram periods to be kept. For example, if $c = 0.25$, only the 25% of the bins with the largest contributions to the spectrogram are kept. The GIC signal is then reconstructed using this reduced spectrogram. For the different events, different values of c were manually selected to keep as much of the long-period signal as possible. The values for c ranged from 0.25 to 0.5.

Provided the GIC signal is much larger than the background noise level, the noise contributions will be removed, leaving only the GIC contribution to the signal. Figure 7.4 shows the complete cleaning process when applied to the 06-07

March 2016 event. For this particular event, c was set as 0.25, The largest contributors to the signal were the long periods (after the diurnal signal was removed), which are associated with GICs ($> 10^3$ s). Most of the shorter period noise was discarded, although not all.

The cleaned time-series are shown in the right column of Figure 7.3. In the following sections, the GIC will be modelled, firstly using a simple power network model, and then with the full 400, 275, 220 and 110 kV power network model.

Goodness-Of-Fit Measures

To quanitatively assess the goodness-of-fits between the measured and modelled GICs, three tests were employed. The first of these is the root mean-square-deviation RMSD_{oc}, which is defined in Chapter 4. This gives a measure of the average difference between a series of measurements and predictions.

The second is the Torta *et al.* (2014) defined performance parameter P_{oc}. This is defined as

$$P_{oc} = 1 - \frac{\mathrm{RMSD}_{oc}}{\sigma_o} \tag{7.1}$$

where subscripts o and c refer to the observed and calculated time-series, and σ is the standard deviation. A P_{oc} value of 1 denotes a complete match between observed and measured values.

The final measure is the Pearson correlation coefficient R_{oc}. This is a measure of linear correlation, with 1 being total positive linear correlation, -1 being total negative linear correlation, and 0 being no linear correlation.

For every combination of ground resistivity and power network models, the predicted and measured GICs at Woodland were assessed using these three methods.

Simple Power Network Response

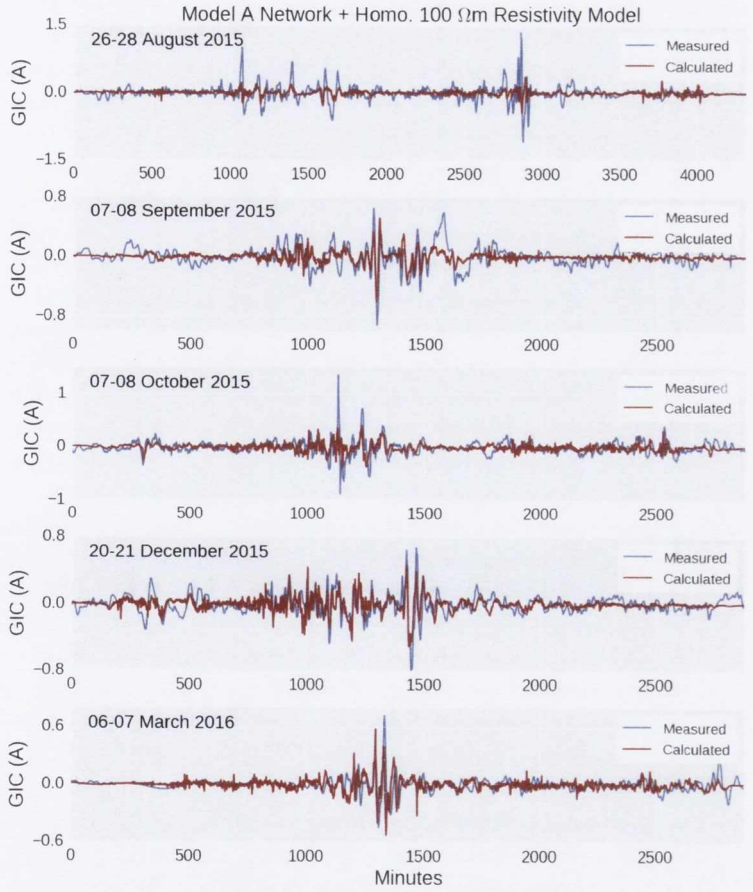
As in Blake *et al.* (2016b), the first simulations were performed using the simple 400, 275 and 220 kV network model (Model A outlined in Chapter 6). For each of the events, the electric field was calculated using a homogenous 100 Ωm

ground resistivity model, as well as the MT-derived resistivity model outlined in Chapter 5 (hereafter referred to as the 1D Earth model). These calculations were performed using the MT method. The GIC data calculated at the Woodland station (which was represented as a single transformer in Model A) were compared to the measured and cleaned data. These time-series comparisons can be seen in Figure 7.5.

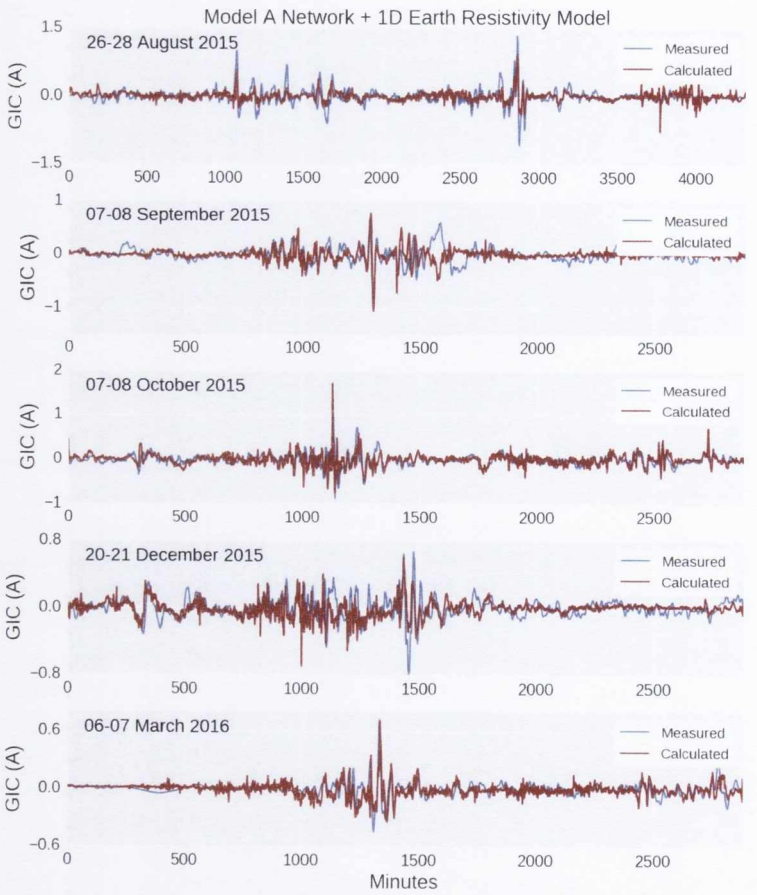
From a qualitative perspective, both the 1D and homogenous Earth models result in GICs which approximate the measured GICs well for most of the storm events. The 1D Earth model appears to fit the largest GIC spikes better than the homogenous model, which tended to underestimate their amplitude. This is particularly evident during the September 2015 event where the largest GIC activity during the peak of the storm (minutes 1253-1361) were underestimated by the homogenous model by approximately 0.2 A. This is similar to the most active parts of the October 2015 and the March 2016 storm events.

For each of the events in Figure 7.5, these calculated performance parameters are given in Table 7.2. From these calculated values, the 1D model performed better than the homogenous model only during the August 2015 storm, with a lower RMSD_{oc}, higher P_{oc} and higher R_{oc}.

Each of the other four events were better fitted by the homogenous resistivity model, as per the three chosen goodness-of-fit metrics. This appears to be contrary to our qualitative assessment. This discrepancy is likely due to the fact that the goodness-of-fit metrics are applied to the entirety of the time-series, not only the particularly disturbed parts of the time-series. The larger spikes are the more important parts of the time-series to fit, as they are the times where damage to transformers are most likely to happen.



(a) Model A with homogenous 100 Ωm ground model.



(b) Model A with 1D ground model.

Figure 7.5: Measured and calculated GIC at a transformer in Woodland during the five recent geomagnetic storms using the simple network Model A. Subfigure (a) shows the the calculated GIC using a 100 Ωm homogenous model, while subfigure (b) shows the same using the 1D Earth model.

Table 7.2: Goodness-of-fit measures for the calculated GICs using network Model A. These were calculated for a homogenous 100 Ωm ground resistivity model, as well as the 1D Earth model. As in Blake *et al.* (2016b), both were calculated using the MT method.

	Network Model A					
	Homogenous 100Ωm			1D Earth Model		
	RMSD_{oc}	P_{oc}	R_{oc}	RMSD_{oc}	P_{oc}	R_{oc}
26-28 Aug. 2015	0.153	0.064	0.355	0.133	0.186	0.573
07-08 Sep. 2015	0.121	0.138	0.509	0.159	-0.129	0.238
07-08 Oct. 2015	0.114	0.134	0.5	0.137	-0.046	0.45
20-21 Dec. 2015	0.106	0.157	0.551	0.159	-0.26	-0.0044
06-07 Mar. 2016	0.064	0.135	0.57	0.073	0.021	0.509

The distribution of the GICs in the simple power network model for each event are given in Figure 7.6. In all of the storms, the 400 and 275 kV substations appear to experience the largest GICs. This is to be expected, as the higher voltage networks tend to have lower transmission line resistances, which contributes to larger GICs. In particular, the 400 kV Woodland (#4 in Figure 7.6), 275 kV Ballylumford (#6) and the 275 kV Coolkeeragh (#11) substations tended to experience the largest proportion of the current for every event and resistivity model. Woodland and Ballylumford were identified in Chapter 6 as being relatively susceptible to GICs due to the orientation and resistive characteristics of the power network model.

In the case of the homogenous model (plotted in blue), the distribution of GIC is broadly the same as when a uniform electric field is applied to Ireland (as seen in Figure 6.8). This is to be expected with a uniform Earth model, as then only the power network makeup and magnetic field will determine the distribution of the GICs.

When the 1D Earth model is used, the proportion of GIC which flows through Woodland, Ballylumford and Coolkeeragh is elevated, each experiencing at least 8% of the total GIC for each event. In the case of Ballylumford, the 1D Earth model nearly doubles the proportion of GIC for some events, when compared to the homogenous model.

The fact that the signal given for Woodland is so similar for both the homogenous and 1D Earth resistivity models is not surprising. It is a well known side

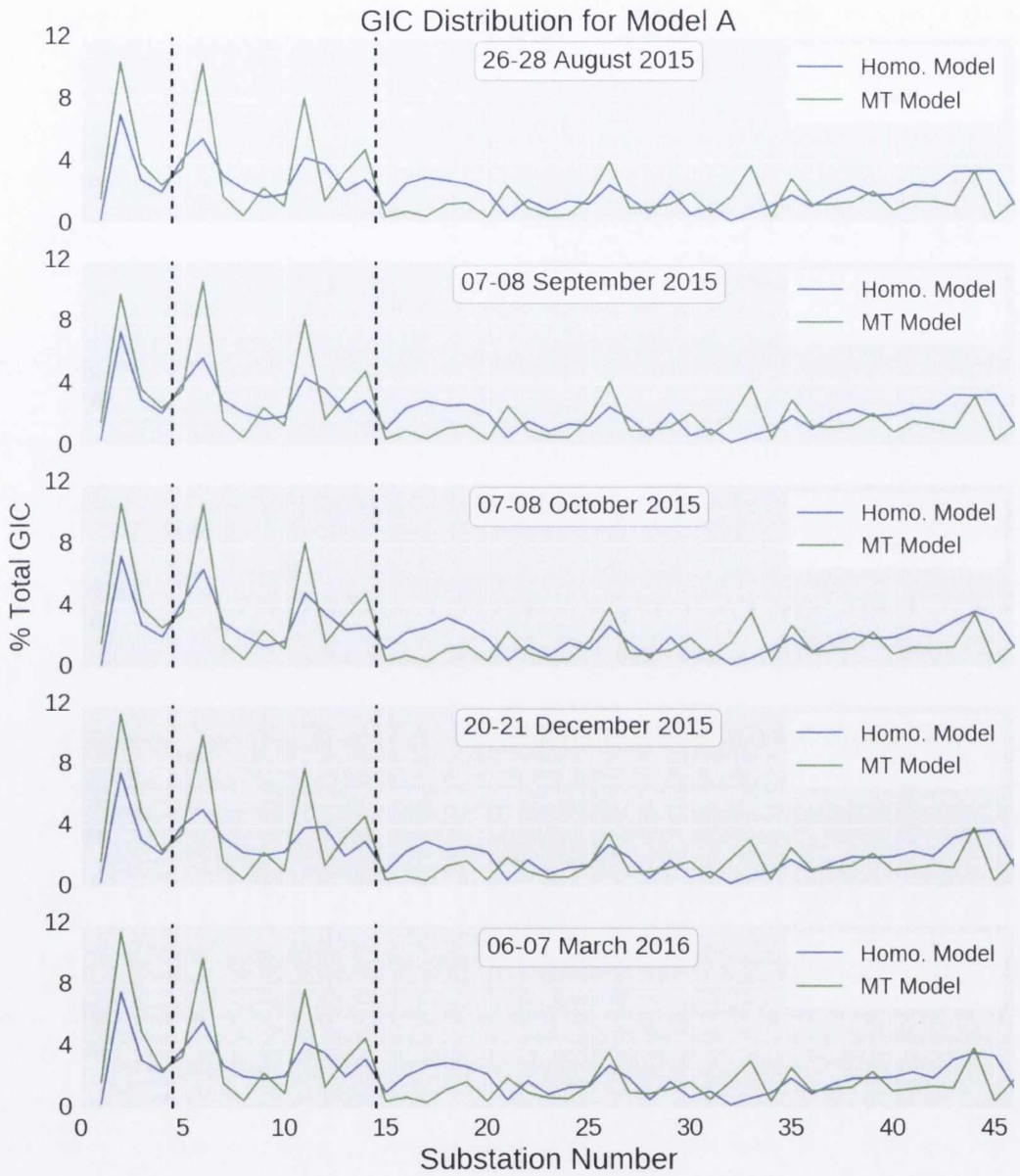


Figure 7.6: The GIC distribution in the simple power network model for each recent event and resistivity model. The dashed lines separate (from left to right) the 400, 275 and 220 kV substations, each of which are modelled as having a single operating transformer. The Woodland substation is number four in these plots

effect of the voltage calculation equation (Equation 6.4) that integrating the electric field along a transmission line effectively smooths the electric field between nodes, meaning that a high-resolution conductivity model may lead to similar GICs to those given by a more simple model (Viljanen & Pirjola, 1994).

From Figure 7.5, the measured GIC at Woodland can be seen to be reasonably approximated when using a simple power network model. As discussed in Chapter 6, this model incorporates some significant simplifications. In particular, Model A uses single-phase power lines and models the Woodland substation as a single transformer, when in reality, two transformers operate there. In the following section, GIC are calculated in the comple power network model (Model B) for the recent events.

Detailed Power Network Response

In this section, GICs are modelled in the detailed power network model (Model B in Chapter 6) using electric fields calculated using both the MT and thin-sheet methods. For both electric field calculation methods, three different resistivity models were used. These were: a homogenous 400 Ωm Earth, a 400 Ωm land model which incorporated a conductive sea, and the MT derived 1D Earth ground model with a 400 Ωm basement.

In order to best fit the measured GIC at Woodland in the detailed power network model, it was found that more resistive ground resistivity models were required when compared to the simple network mode. This is due to the differences in the network model assumptions. Although Model B uses three phase power lines (effectively reducing transmission line resistance and increasing GIC magnitude), it correctly models Woodland as having two transformers. In effect, this means that larger GICs for the Woodland substation need to be modelled in order to fit the measured data at the single transformer. This required larger electric fields, which in turn require higher resistive Earth models.

This change was accounted for by using 400 Ωm rather than 100 Ωm ground resistivity models. In the case of the MT derived 1D Earth resistivity model, a basement value of 400 Ωm was used instead of 100 Ω. When calculating GICs using the thin-sheet method, the calculated GICs needed to be detrended in order

for them to correctly fit the measured GICs. In order to achieve this, periods larger than $10^{4.2}$ s (approximately four and a half hours) were removed from the calculated signal. This step was necessary as a consequence of the thin-sheet calculation method (see Section 5.2.3).

Homogenous 400 Ωm Earth

The first resitivity model used with the power network Model B is the homogenous 400 Ωm halfspace. For each of the five events, the MT and thin-sheet methods were used to calculate the electric field. Corresponding GICs were then calculated in the network. These resulting GICs are shown in Figure 7.7 for each event. The left column of plots are the GICs modelled using the MT method, and the right column shows the GICs modelled using the thin-sheet method. Qualitatively, both electric field calculation methods fit the calculated GICs well, with some events faring better than the others. As with the Model A calculations in the previous section, the peaks during the August 2015 event are underestimated by both the MT and thin-sheet methods, whereas the peaks during the March 2016 event appears to be overestimated by both.

With the thin-sheet calculations, the general shape of the time-series appears to match the measured data at Woodland, and the peaks are approximated well for most of the events. Despite this, there appears to be a slight phase shift of a few minutes in some of the events. This is most noticeable during the September 2015 and Dececmber 2015 events. A similar phase shift was exhibited with the thin-sheet method by Bailey *et al.* (2017) when GICs were calculated for Austria.

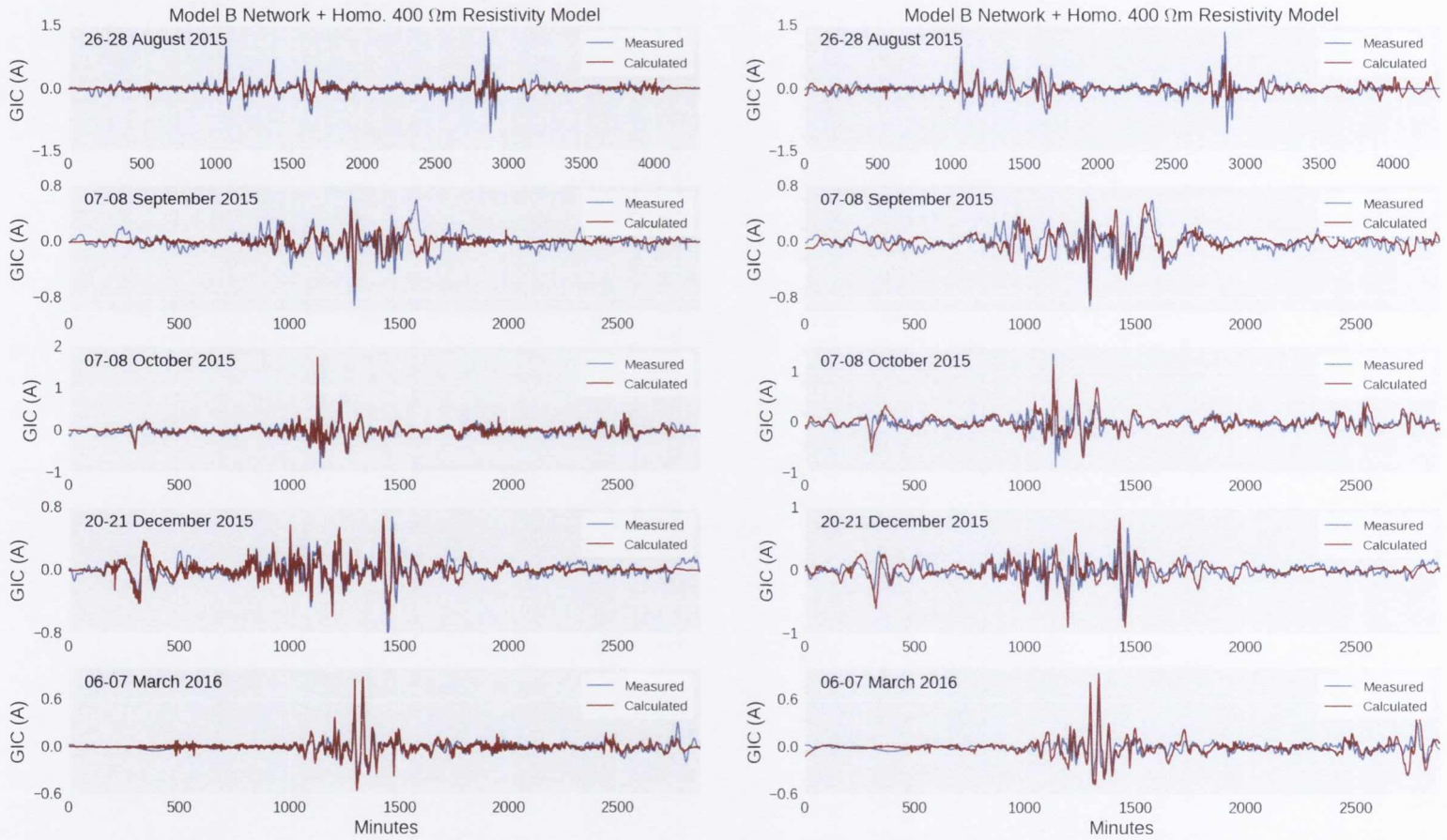
The goodness-of-fit measures for the 400 Ωm homogenous Earth resistivity model are given in Table 7.3. From these measures, the MT method yielded more accurate results, with lower RMSD_{oc} and higher P_{oc} for every event when compared to the thin-sheet method.

The MT method also exhibited higher R_{oc} values than the thin-sheet method for all of the events except the September 2015 event. This exception is likely due to the large peak which occured between minutes 1500-1650 during the September 2015 event. The MT method failed to approximate this peak, underestimating

Table 7.3: Goodness of fit measures for the calculated GICs using network Model B and a 400 Ωm Earth. Both the MT and thin-sheet methods of calculating electric fields were used.

	Network Model B, 400 Ωm Halfspace					
	MT method			Thin-Sheet Method		
	RMSD_{oc}	P_{oc}	R_{oc}	RMSD_{oc}	P_{oc}	R_{oc}
26-28 Aug. 2015	0.122	0.252	0.723	0.152	0.069	0.446
07-08 Sep. 2015	0.129	0.081	0.414	0.136	0.033	0.521
07-08 Oct. 2015	0.100	0.235	0.682	0.126	0.039	0.629
20-21 Dec. 2015	0.102	0.188	0.639	0.137	-0.083	0.505
06-07 Mar. 2016	0.054	0.260	0.779	0.084	-0.133	0.668

its amplitude, whereas the thin-sheet method approximated it well. This peak is quite noticeable in the magnetic field data for the day.



(a) MT method with network Model B

(b) Thin-sheet method with network Model B

Figure 7.7: Measured and calculated GIC at a transformer in Woodland using network Model B for a homogenous 400 Ωm Earth. Subfigure (a) shows the MT calculated GICs, and subfigure (b) shows the thin-sheet calculated GICs after removing long-periods.

400 Ωm Earth with Conductive Sea

The next ground resistivity model that was used had a 400 Ωm halfspace beneath Ireland, and conductive seas everywhere else. For the MT method of calculation, 3D MT tensors for locations near the coastlines were synthesized to incorporate the conductive effect of the sea. These were made using the ModeEM program Egbert & Kelbert (2012); Kelbert *et al.* (2014). In the case of the thin-sheet method, the cells which were on land were given a uniform resistivity of 400 Ωm, and the sea conductivity was calculated as in Section 5.2.2.

The measured and calculated GICs in Woodland for this scenario are shown in Figure 7.8, and the fitness measures are given in Table 7.4. Including the sea appears to have had little effect on the calculated GIC in Woodland for either the thin-sheet or MT calculation methods.

The goodness-of-fit measures show that for each of the events the addition of the sea effect in the 3D MT tensors marginally reduced the accuracy of the fit. In the case of the thin-sheet method, including a conductive sea also reduced the fit for the majority of the events. The August, October and December 2015 each saw larger R_{oc} values compared with the 400 Ωm halfspace model, although they also saw larger RMSD_{oc} errors.

The addition of the conductive sea leads to larger electric fields near coastlines, which should in turn lead to larger calculated GIC in these areas. To investigate this, the change in GIC for the 400 Ωm halfspace versus the 400 Ωm + conductive sea was plotted in Figure 7.9. This figure shows the difference in sum of GIC for the August 2015 event for both methods of calculating electric fields.

The addition of the sea increased the total calculated GIC by 11.3% for the MT method, and 18.3% for the thin-sheet method. In the case of the 3D MT tensors, the increase seems to be spread accross substations both near the coast and inland, although certain coastal areas (such as the South-West) experience significant increases. The largest increase was a factor of 2.12 for the MT method.

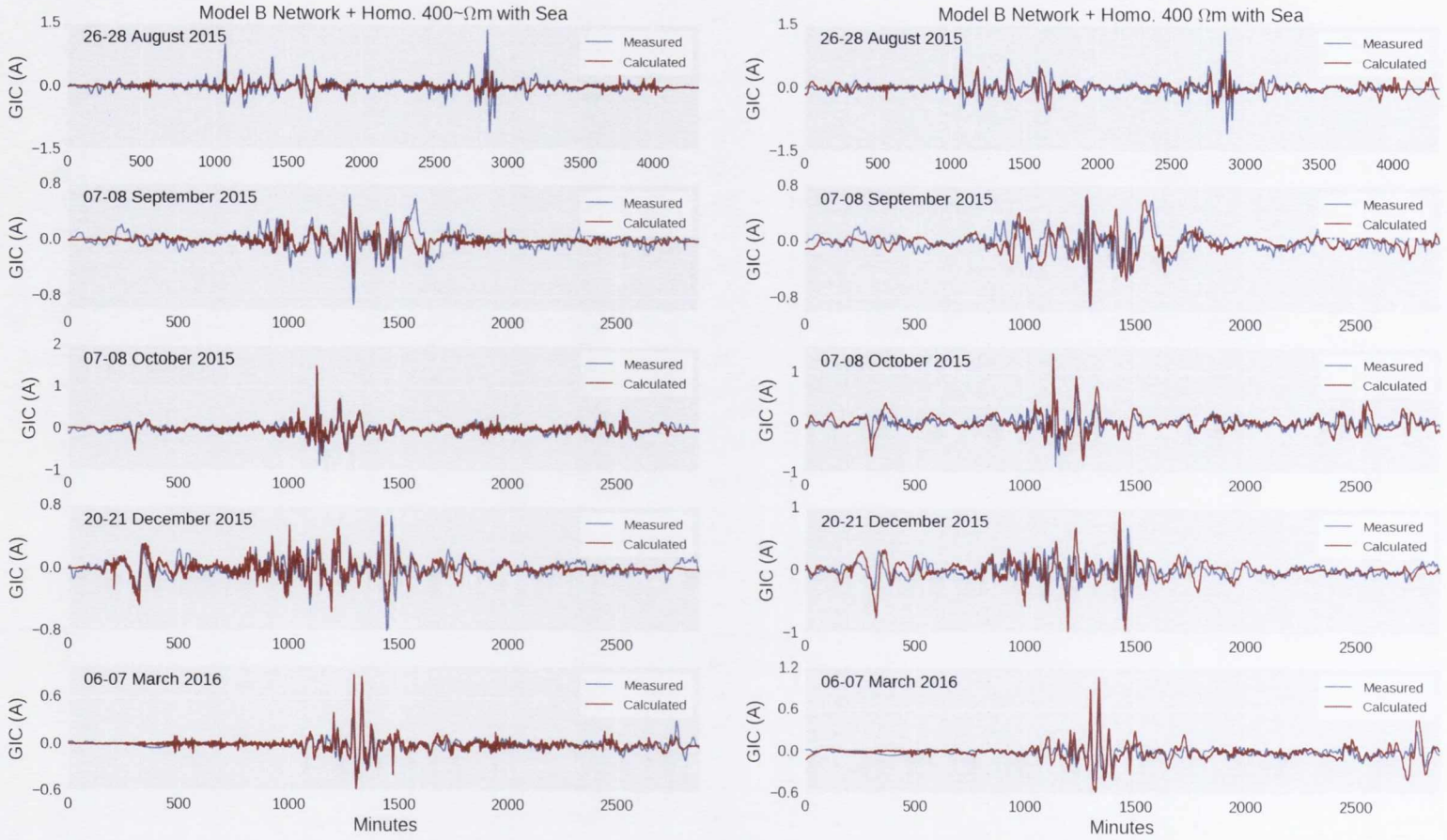
In the case of the thin-sheet method, fewer substations experienced an increase in GICs, although the few substations which did had a larger increase when compared with the MT method. These substations tended to be near inlets, or areas where the land is 'pinched', leading to large conductive discontinuities and larger

Table 7.4: Goodness of fit measures for the calculated GICs using network Model B and a 400 Ωm Earth with a conductive sea. Both the MT and thin-sheet methods of calculating electric fields were used.

	Network Model B, 400 Ωm Halfspace + Sea					
	MT method			Thin-Sheet Method		
	RMSD_{oc}	P_{oc}	R_{oc}	RMSD_{oc}	P_{oc}	R_{oc}
26-28 Aug. 2015	0.136	0.166	0.568	0.154	0.053	0.456
07-08 Sep. 2015	0.134	0.051	0.367	0.140	0.018	0.507
07-08 Oct. 2015	0.106	0.193	0.651	0.137	0.04	0.635
20-21 Dec. 2015	0.108	0.148	0.599	0.215	-0.139	0.53
06-07 Mar. 2016	0.059	0.199	0.725	0.094	-0.28	0.664

electric fields (as can be seen in Figure 5.11). The 110 kV Waterford substation experienced an increase in total GIC by a factor of 3.45 with the addition of the sea.

Unfortunately, for both methods of calculation, the GIC calculated at Woodland appears not to change much with the effect of the sea taken into account. This is likely due to the fact that Woodland is inland by some 30 km, and the largest line to the substation lies West, to Ireland's midland. This means that the sea effect calculations cannot be verified using the Woodland substation.



(a) Model B network with homogenous Earth and conductive sea, MT method

(b) Model B network with homogenous Earth and conductive sea, thin-sheet method

Figure 7.8: Measured and calculated GIC at a transformer in Woodland using network Model B for a 400 Ωm Earth with a conductive sea. Subfigure (a) shows the MT calculated GICs, and subfigure (b) shows the thin-sheet calculated GICs.

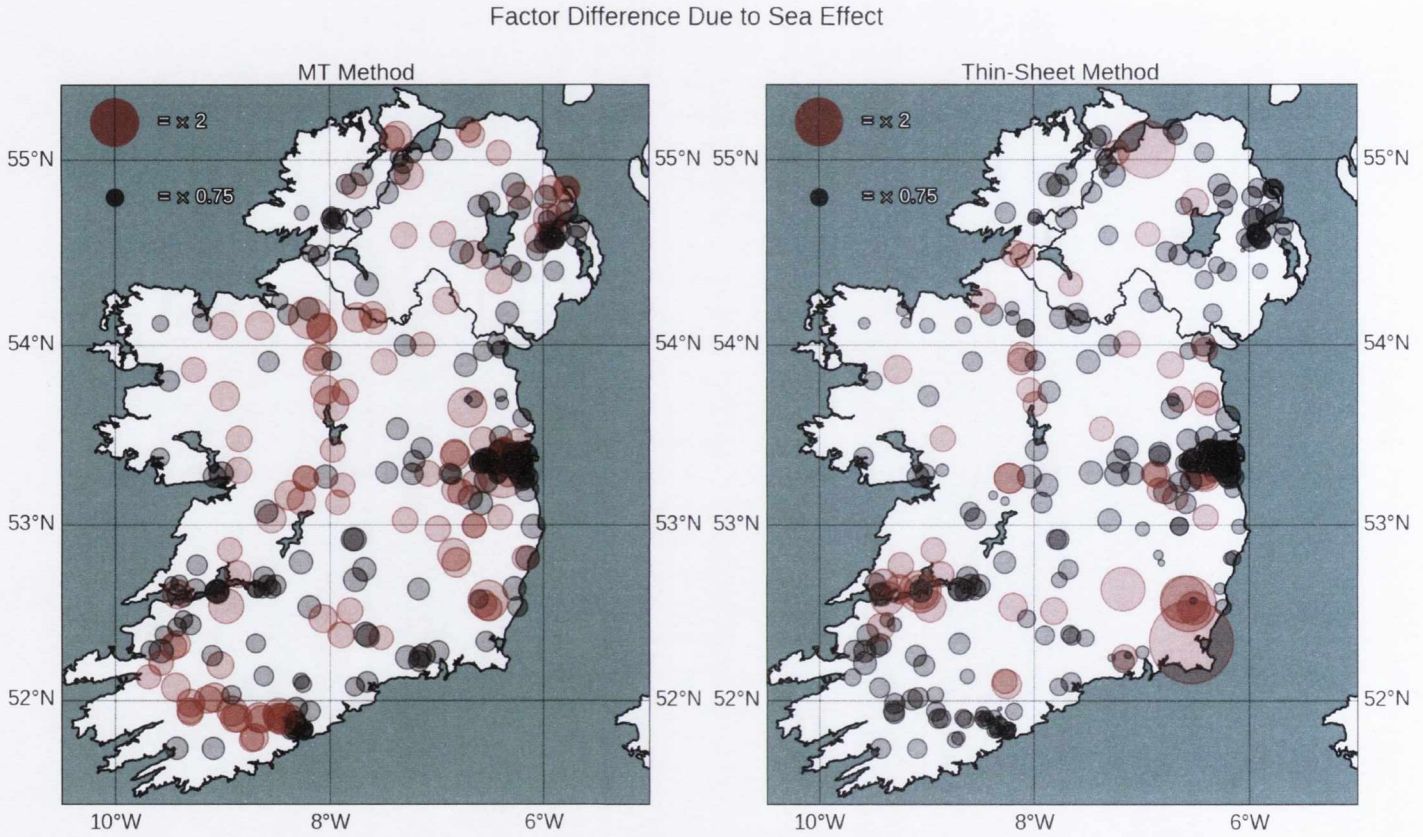


Figure 7.9: Factor difference in calculated GIC at substations when the conductive sea is added to a 400 Ωm halfspace Earth resistivity model. The left plot shows the factor difference in GICs when electric fields are calculated with 3D MT tensors. The right plot shows the differences when electric fields are calculated with the thin-sheet method. Red circles indicate an increase in GIC, and black circles indicate a decrease in GIC.

Table 7.5: Goodness of fit measures for the calculated GICs using network Model B and the MT derived resistivity model.

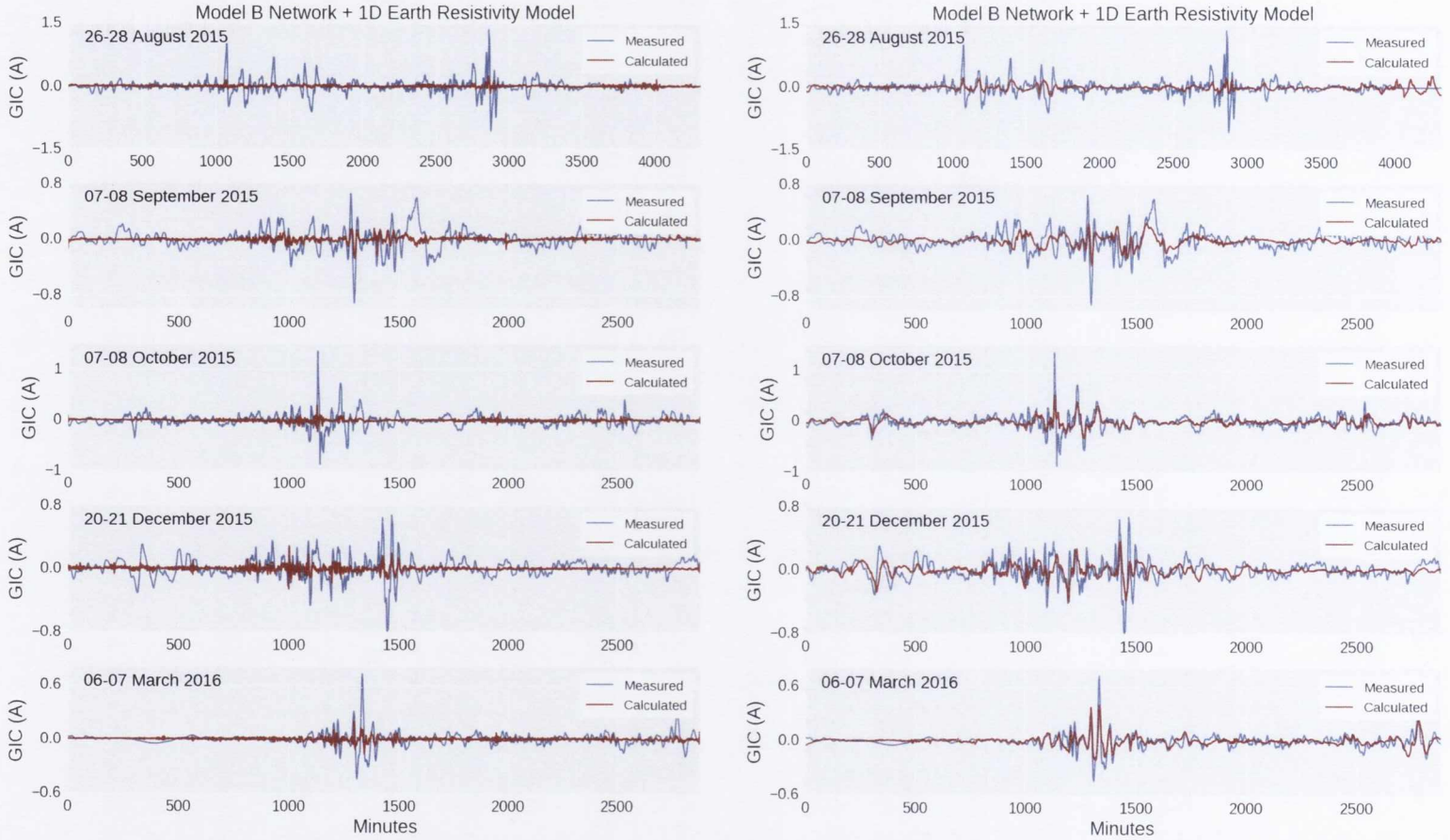
	Network Model B, MT Resistivity Model					
	MT method			Thin-Sheet Method		
	RMSD_{oc}	P_{oc}	R_{oc}	RMSD_{oc}	P_{oc}	R_{oc}
26-28 Aug. 2015	0.153	0.058	0.482	0.155	0.054	0.326
07-08 Sep. 2015	0.134	0.042	0.304	0.121	0.139	0.515
07-08 Oct. 2015	0.131	0.006	0.123	0.103	0.218	0.629
20-21 Dec. 2015	0.114	0.089	0.500	0.111	0.124	0.486
06-07 Mar. 2016	0.069	0.058	0.355	0.056	0.243	0.654

MT Derived Resistivity Model

The final resistivity model to be used with the detailed power network model was the MT derived model outlined in Chapter 5. As mentioned above, a basement value of 400 Ωm was used. The results of the calculated GIC for both the MT and thin-sheet methods can be seen in Figure 7.10. Goodness of fit measures are given in Table 7.5

From a brief glance at the plots, it is clear that the MT model underestimates the peaks of all the events, for both the MT and thin-sheet method of calculating GIC. The thin-sheet method fares marginally better, although peak GICs are underestimated by a factor of approximately 1.5 for the March 2016 event, to a factor greater than 5 for the August 2015 event.

The R_{oc} values given show that the shape of the GIC time-series produced matches the signal well, despite failing to match the amplitudes.



(a) Model B network with MT-derived ground model, MT method

(b) Model B network with MT-derived ground model, thin-sheet method

Figure 7.10: Measured and calculated GIC at a transformer in Woodland using network Model B for the MT derived ground model. Subfigure (a) shows the MT calculated GICs, and subfigure (b) shows the thin-sheet calculated GICs.

Summary and Discussion

In this chapter, the operation of the Woodland Hall effect probe was outlined, along with the processing methods used to clean the GIC data that it produces. Five recent events were used to test the GIC calculation methods. This involved interpolating measured magnetic fields for each event using SECS, calculating the surface electric field using both the MT and thin-sheet methods, and calculating GICs in an Irish power network model.

The cleaning process was tailored to remove frequencies that contributed least to the raw GIC signal measured the Woodland transformer. For most of the GIC signal in the five events, the persistent noise of approximately 0.1 A was removed (the cleaning process in Section 7.1.2 acted in effect as a low-pass band filter). This made the fitting of calculated GIC a simpler task, but it may not be a process that is suited for all GIC measurements. Where a long-period peak in the GIC signal coincides with a positive addition of the 0.1 A noise, a larger GIC signal will arise. Removing the 0.1 A noise from this signal will leave a cleaned GIC signal that under-reports the true current measured at a transformer neutral (whether the entirety of the signal is due to geophysical effects or not). As such, using such a frequency cleaning method should be used with caution.

Calculated GICs at Woodland were compared to the cleaned measured data recorded by the Woodland Hall effect probe, and analysis was conducted to see which combination of electric field calculation method and resistivity model produced GICs which best fit the measured GICs. Despite all of the cumulative errors and assumptions involved in every step of calculating GICs (these are explored in detail in Chapters 6, 4 and 5), the data at Woodland was reproduced for most of the events with a reasonable level of accuracy for some of the events (particularly the 06-07 March 2016 event).

In particular, the 400 Ωm Earth with a conductive sea and the homogenous 400 Ωm Earth resistivity models produced electric fields which drove accurate GICs in Woodland (with the detailed Model B power network) for most of the events. This is true for both the MT and thin-sheet methods of calculating electric fields. Overall, the combination of a homogenous 400 Ωm Earth with the MT method of calculating electric fields produced the best fit for the GICs over all five events.

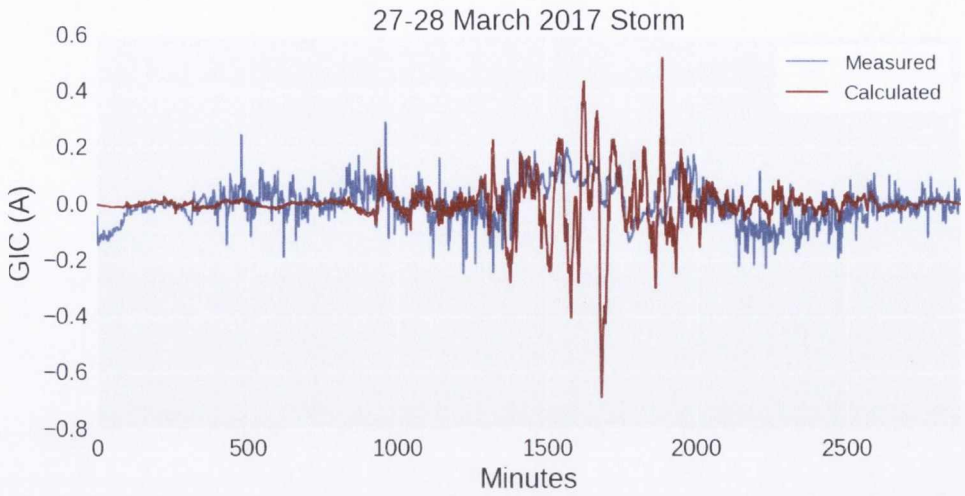


Figure 7.11: Measured and calculated GIC in Woodland for the 27-28 March 2017 event. The GIC were calculated using a 400 Ωm uniform resistivity model.

Some events were better fitted than others. In particular, the March 2016 event was generally reproduced to a high degree of accuracy, while the measured GICs during the August 2015 event were consistently underestimated. It is possible that the network experienced a change in operation between August 2015 and March 2016. It is not unusual for network elements to be taken out of service for repairs or testing, which would reroute any potential GICs. Unfortunately, we do not yet have the sufficient information which would enable the altering of the power network model for individual events.

A stark highlight of this information defecit is given with the 27-28 March 2017 geomagnetic storm. This storm registered as a Kp 6+ event, and simulated GIC at Woodland for the event (using a uniform 400 Ωm Earth with the MT method) had a peak of 0.7 A. However, in the measured GIC data for the event, there was no indication of any GIC activity. This can be seen in Figure 7.11. It is likely that elements of the network had either been connected or disconnected for this event, however, we do not have this information at hand.

Another explanation for the difference in accuracy between the five events in this chapter may be due to terrestrial weather. Of the five events simulated in this chapter, Woodland only experienced rainfall immediately before the August

event (raining for several hours in the preceding days). This would have increased the conductivity of the ground at the substation, which may have increased its susceptibility to GICs while the ground was sodden. As our network model did not change ground conductivity to reflect this, the calculated GIC values underestimated the measured GICs.

It was found that the MT-derived 1D Earth resistivity model was sufficient for producing GICs in a simple network which assumed that the Woodland substation operated a single transformer. With the detailed power network Model B, however, the electric fields it produced were insufficient to drive GICs of amplitudes seen at Woodland. A limitation of the MT model used in this study is that it is constructed from independent 1D MT soundings at different locations (see Section 5.1.5). Future work should incorporate the full 3D tensors that provided the data for this model, as including 3D MT tensors has been shown to increase the accuracy of GIC modelling at substations (Torta *et al.*, 2017).

As it stands, the simulations show that the measured GIC in a single transformer in Ireland can be replicated during storm events using the detailed model of the Irish power network, along with a uniform 400 Ωm Earth resistivity model. In order to fully validate the models and methods used, more GIC measurements need to be taken concurrently in different locations around the Irish power network. An obvious location for another Hall Effect probe would be Moneypoint. This substation can expect large GICs, according to our simulations. In the next chapter, a number of historical events will be simulated in detail and analysed using the 400 Ωm halfspace model with the MT method.

8

Simulating Historical Storm Events

In the first part of this chapter, three large historical geomagnetic events are simulated in Ireland. Geommagnetic field data from INTERMAGNET sites are interpolated across Ireland using SECS. Electric fields are then calculated using a 400 Ωm homogenous Earth resistivity model with the MT method. Finally, GICs are calculated in the detailed model of the Irish power network. The distribution and magnitude of the calculated GICs in these events are analysed.

The second part of this chapter deals with the statistics of infrequent superstorm events in Ireland. The size of events Ireland can expect over long timescales is estimated using two methods: an historical storm is scaled according to estimates of large geomagnetic events, and 25 years of geomagnetic data are used to predict the scale of 1-in-100 year events.

Historical Event Case Studies

Three historical events were chosen to be simulated in Ireland. These are the 13-14 March 1989, 08-10 November 1991 and 29-31 October 2003 storm events. These were chosen because they are amongst the largest recent geomagnetic storms to occur with INTERMAGNET coverage (each event happened after 1989). As

Table 8.1: Maximum measured and calculated values for the three historical storms analysed in this chapter. The maximum dB_H/dt was measured at Valentia. The maximum E_H and GIC are calculated values. Kp and Dst values are obtained from the World Data Centre for Geomagnetism, Kyoto (http://www.wdc.kugi.kyoto-u.ac.jp).

Storm	Kp	Dst (nT)	dB_H/dt (nT min^{-1})	E_H (V km^{-1})	GIC (A)
13-14 Mar. 1989	9o	-589	253	2.7	159
08-10 Nov. 1991	9-	-354	146	1.0	67
29-31 Oct. 2003	9o	-383	250	1.4	125

with the recent events in Chapter 7, the magnetic field was interpolated across Ireland using SECS. This field was coupled with a 400 Ωm homgenous Earth model, and surface electric fields were calculated using the MT method. The detailed network model (Model B) was then imposed onto the electric field and GICs were calculated.

As the events all occurred before August 2015, there are no GIC measurements to verify the calculated GICs. Furthermore, there are no reports of damage or disruption to any elements of the Irish power network that have been attributed to geomagnetic activity. This means that there is, unfortunately, no way to verify these simulations with our current information. We have shown in the previous chapter that GICs in Woodland can be replicated during minor to moderate geomagnetic storms using the same inputs described above. However, this leaves considerable uncertainty in the calculated GIC in other substations in the network and for large storm events.

One further consideration is the orientation of the grid. The following simulations use information of the Irish power grid from 2016 to construct a model. The Irish power grid has certainly changed since 1989, although the higher voltage parts of the network (400, 275 and 220 kV) have remained largely the same in the intervening time. This adds uncertainty to calculated GICs in the lower voltage levels.

Table 8.1 lists the characteristics of the four historical storms, including the peak calculated electric fields and GICs in the Irish power network.

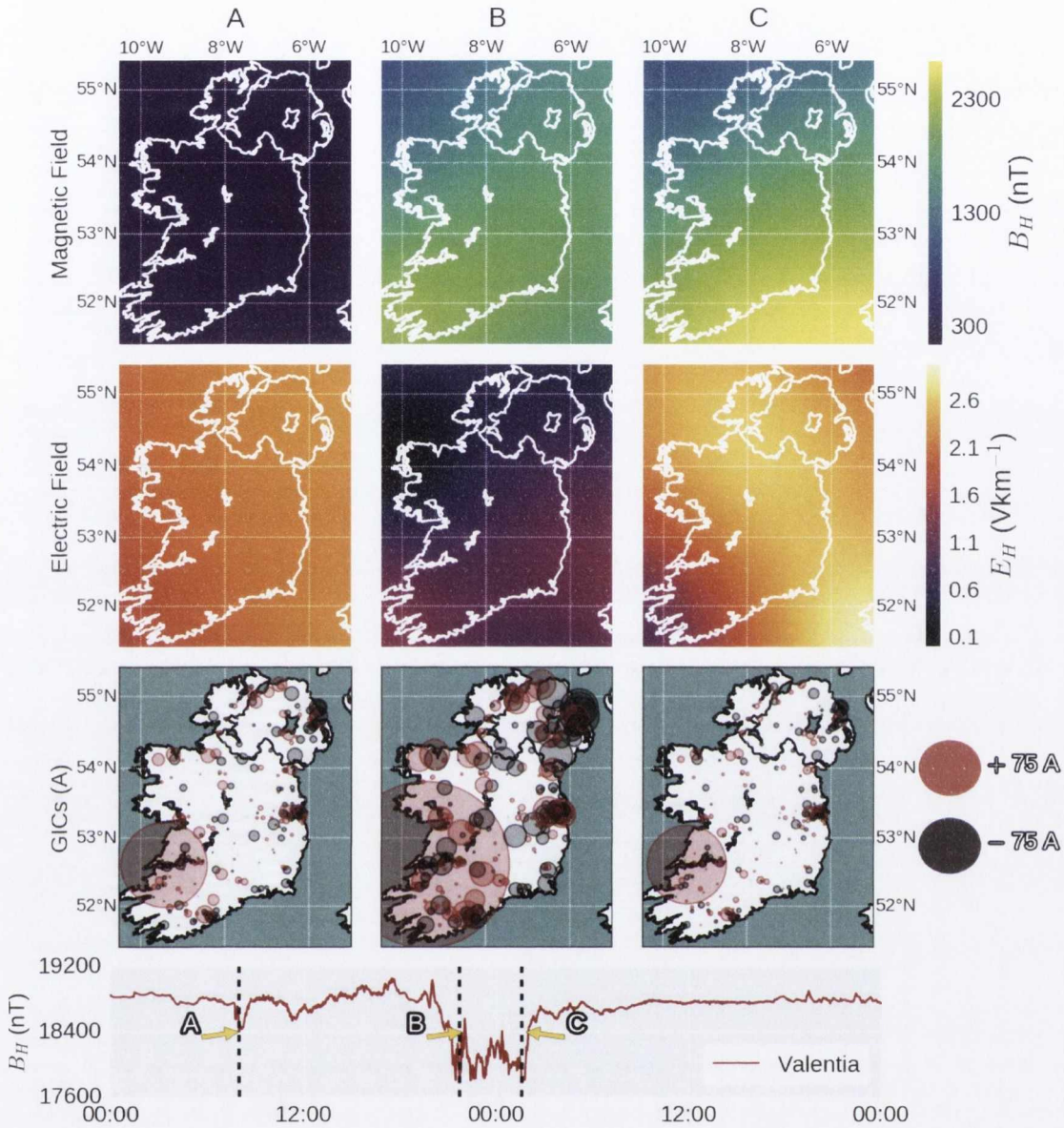


Figure 8.1: Results for the simulation of the March 1989 storm. Rows from top to bottom show the SECS interpolated magnetic field, simulated electric field, simulated GICs and measured magnetic field at Valentia. Columns left to right show three different times (indicated on the bottom plot with dashed lines and labels). Maximum GIC calculated was 159 A in Moneypoint.

13-14 March 1989

The 13-14 March 1989 event is the largest and most famous example of geomagnetic storms in the modern age. It is the clearest example of space weather disrupting a power grid, leading to a blackout in Canada and a damaged transformer in New Jersey (Allen *et al.*, 1989), as well as causing disruption to radio communications and satellite damage.

The 13-14 March 1989 event is the largest disturbance to occur during the 06-20 March 1989 interval, when there were repeated solar events and subsequent geomagnetic activity. This activity was precipitated by a large and complex sunspot group which produced several large flares (many surpassing the X1.0 level) from the 6th of March. This, coupled with repeated CMEs, drove the continued geomagnetic activity, with effects experienced worldwide.

On March 10, a particularly large CME erupted towards the Earth's magnetosphere, which it impacted approximately 50 hours later (Bolduc, 2002). For approximately 30 hours from 0200 UT on 13 March, the geomagnetic storm was measured at ground observatories around the world. Aurorae were seen as far south as London (Allen *et al.*, 1989), and the storm registered as a Kp 9o event, with a minimum Dst of -589 nT. Valentia saw a maximum change in the horizontal magnetic component of 253 nT min^{-1}.

Figure 8.1 shows the results of the simulations for the March 1989 event in Ireland. The figure shows the SECS-interpolated horizontal magnetic field (top row), calculated horizontal electric field (middle row), and resultant calculated GICs in the grid (bottom row). The bottommost plot shows the measured horizontal magnetic field at Valentia observatory during the event. Dashed lines in this plot indicate the three different times shown in the above plots (A, B and C).

Using a 400 Ωm halfspace resistivity model, the largest calculated electric field in Ireland was 2.7 Vkm^{-1} during the peak of the storm in the North of Ireland. This corresponded to GICs of 159 A in the 400 kV Moneypoint substation. Despite this large value at Moneypoint, absolute GICs greater than 100 A were only calculated for six minutes for the 1989 storm in Moneypoint (see Figure 8.2). Substations along Irelands north-eastern coast also seemed to experience larger GICs than the

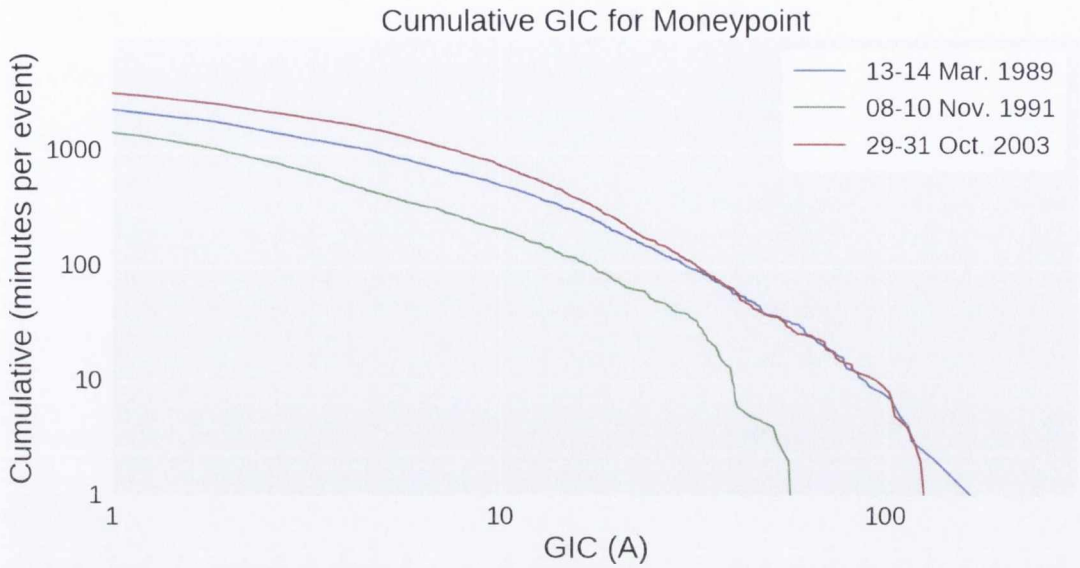


Figure 8.2: Cumulative GIC amplitudes in Moneypoint for each of the three historical storms. The calculated GICs at Moneypoint were greater than 100 A for six minutes of the March 1989 storm, and 8 minutes for the October 2003 storms.

rest of the network (barring Moneypoint), with nine substations experiencing GICs greater than 30 A.

The 275 kV Kilroot and Ballylumford substations experienced the next largest GICs after Moneypoint. They saw calculated GICs of 38.4 and 37.5 A respectively.

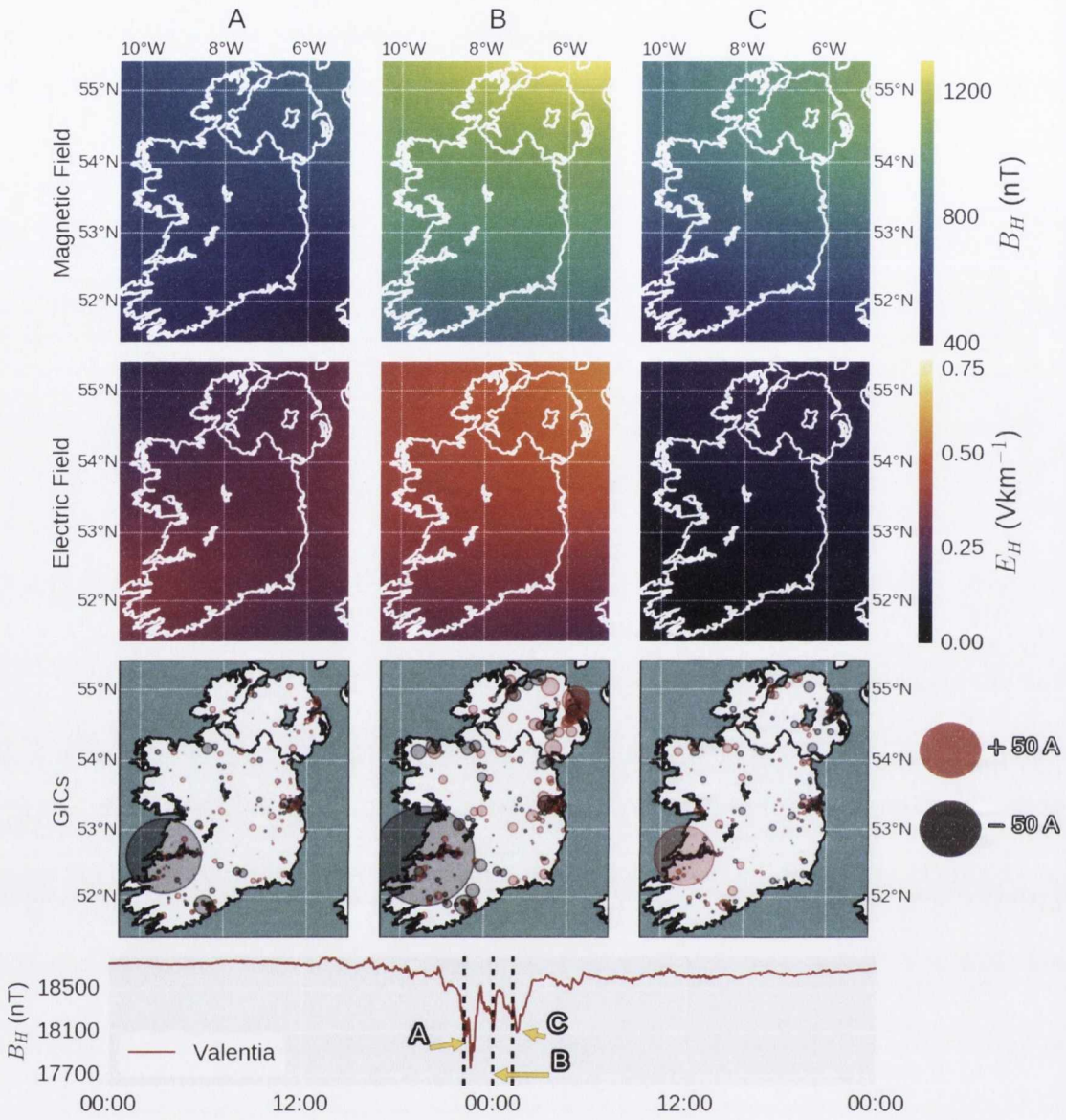


Figure 8.3: Results for the simulation of the November 1991 storm. Rows from top to bottom show the SECS interpolated magnetic field, simulated electric field, simulated GICs and measured magnetic field at Valentia. Columns left to right show three different times (indicated on the bottom plot with dashed lines and labels). Maximum GIC calculated was 67 A in Moneypoint.

08-10 November 1991

The November 1991 storm is one of the largest storms of the space age. It arose from the collapse of a solar filament outside of an active region on the Sun (Cliver *et al.*, 2009). This led to a large-scale CME eruption which impacted in the evening of 8 November, leading to a storm which lasted approximately 14 hours. The peak of the storm occurred on 2251 UT on 8 November with a minimum Dst of -354 nT, and a Kp value of 9-. The maximum variation measured in the horizontal magnetic component in Valentia for this event was 146 nT min^{-1}.

This storm is notable in that it was not predicted to occur beforehand. This was due to a lack of coronagraph and soft-X-ray images available at the time, as well as the fact that the Sun was otherwise quiescent in the days preceding the event.

The interpolated magnetic fields, calculated electric fields and calculated GICs are shown in Figure 8.3. The maximum calculated electric field for this event was 1.0 Vkm^{-1}, and the corresponding maximum GIC was 67 A in Moneypoint. The two substations which experienced the next largest GICs were the 275 kV Ballylumford and 275 kV Kilroot substations, with 18.7 and 15.4 A respectively.

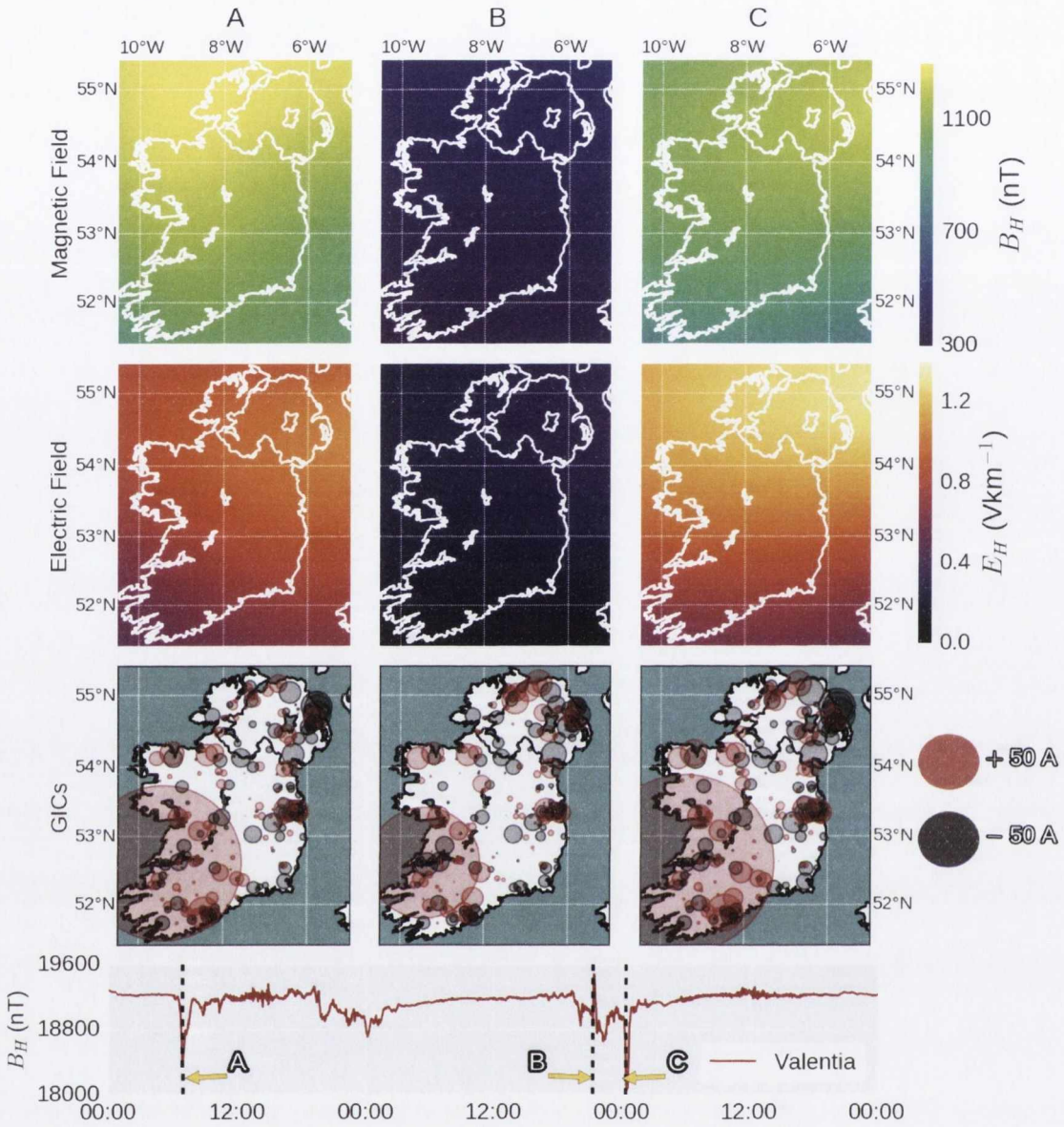


Figure 8.4: Results for the simulation of the October 2003 Halloween storm. Rows from top to bottom show the SECS interpolated magnetic field, simulated electric field, simulated GICs and measured magnetic field at Valentia. Columns left to right show three different times (indicated on the bottom plot with dashed lines and labels). Maximum GIC calculated was 125 A in Moneypoint.

29-31 October 2003

The famous 'Halloween' storms are part of a period of extreme solar activity from late October to early November in 2003. During this period, the NOAA Space Environment Center issued over 250 solar energetic event warnings and alerts due to three of the largest sunspot clusters for over a decade emerging on the surface of the Sun (NOAA, 2003). Nine significant flares occurred between 22-27 Occtober. On 28 October at 11:10 UT, an X17 flare from disk center erupted. This began the subject period of geomagnetic storms, and was accompanied by a large Earth-directed CME. This CME impacted the Earth's magnetosphere on the morning of the 29th, and geomagnetic activity lasted for over 24 hours.

Several different ground and near-space infrastructures were disrupted by these storm events. A large number of spacecraft had to turn off their instruments or take protective action due to the storm, aircraft were redirected from polar routes, and radio-based communications were degraded during the storms (NOAA, 2003). Unlike the 1989 event, there were no reported failures in power networks in America. Sweden, however, experienced very large GICs and a resulting transformer failure. This led to a blackout which affected roughly 50,000 customers (Pulkkinen *et al.*, 2003c). Currents of 40 A were also measured in transformers in Scotland during this storm (Thomson *et al.*, 2005).

This storm had three separate periods of Kp9o, and had a minimum Dst of -383 nT. The maximum variation measured in the horizontal magnetic component in Valentia for this event was 250 nT min^{-1} at 1455 UT on the 29th. The interpolated magnetic fields, calculated electric fields and calculated GICs are shown in Figure 8.4. The maximum calculated horizontal electric field for this event was 1.4 Vkm^{-1}, and the maximum GICs calculated was 125 A, again in Moneypoint. The two substations which experienced the next largest GICs were the 275 kV Ballylumford and 220 kV Trabeg substations, with 29.0 and 26.5 A respectively.

Historical Simulations Discussion

The top plot in Figure 8.5 shows the maximum calculated GIC for each substation during each of the three events. In all three of the historical events, the 400 kV Moneypoint substation experienced the largest currents by a large margin

(maximum GICs in Moneypoint were 159, 67 and 125 A for the three respective events). As can be expected, the largest storm event (March 1989) saw the largest widespread currents of the three events.

In terms of proportion of GIC which flowed through each substation (bottom plot of Figure 8.5), Moneypoint accounted for at 5.8% , 5.4% and 5.0% of the total GICs calculated for each of the events (1989, 1991 and 2003 respectively). The importance of Moneypoint for GIC calculations is not surprising. As shown in Chapter 6, Moneypoint is connected to two of the largest transmission lines in the country. These are low-resistance 400 kV lines. In addition to this, Moneypoint has a low grounding resistance of 0.25 Ω, which aids the flow of GICs.

No substation (other than Moneypoint) experienced GICs greater than 38.4 A for the 1989 storm and 29.0 A for the 2003 storm. These values are lower than those calculated or measured in other countries for the 2003 event (Pulkkinen *et al.*, 2003c; Thomson *et al.*, 2005; Torta *et al.*, 2014; Turnbull, 2011; Viljanen *et al.*, 2012). These low values are likely due to a combination of Ireland's mid-latitude location (which leads to lower magnetic variations) coupled with Ireland's small size.

The distribution of GICs in the power network (bottom plot in Figure 8.5) is very similar to the distribution of GICs one gets when Ireland's network is subjected to a uniform 1 Vkm^{-1} electric field (Figure 6.8). With these simulations, a uniform Earth was used to calculate electric fields. As such, only variations in the magnetic field and the characteristics of the power network model dictate the distribution of GICs. With a varying Earth resistivity model, this distribution may change to a lesser or larger extent (depending on the ground model).

Figure 8.6 shows the ten substations which experienced the largest peak GICs for each of the three events. Six substations appear in the top ten for each of the events. The majority of these substations were in the North of Ireland. This is where the largest magnetic variations (and therefore electric fields, if one uses a homogenous Earth model) were calculated. Six of the substations which experienced the largest GICs were 110 kV substations. This is despite the lower voltage transmission lines having higher resistances than their HV counterparts.

The large currents seen in Moneypoint ($>$ 100 A) would be cause for concern for power network operators, especially if they were sustained for several hours.

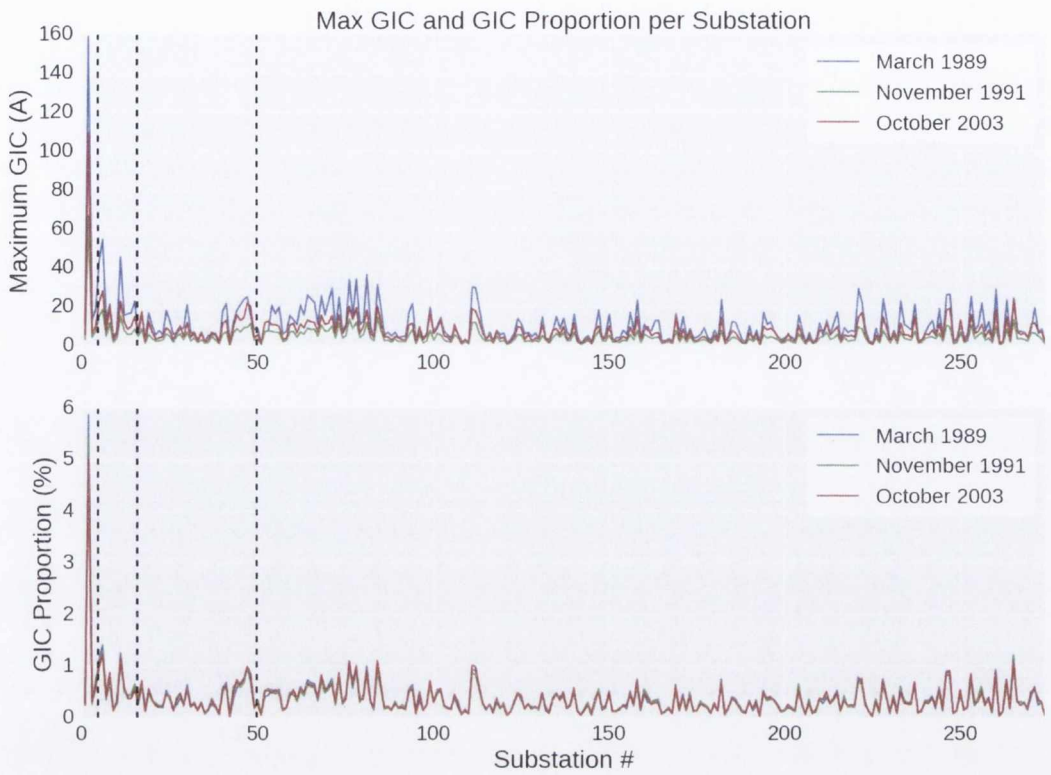


Figure 8.5: Maximum GIC (top) and proportion of GIC (bottom) per substation for each of the three historical events. The dashed lines separate from left to right 400, 275, 220 and 110 kV substations.

As mentioned above, there are no reports of transformer damage at Moneypoint during these events. It may be the case that transformer difficulties may have occurred in Moneypoint in the months after each event due to degradation from GICs, without the root cause being identified. It may equally be that the transformers at Moneypoint are resilient to currents of this magnitude. Currents greater than 100 A were calculated to occur for only 6 minutes during the 1989 storm, and 8 minutes during the three day Halloween 2003 storms. Simulations of the thermal properties of specific transformers in the Irish power network under GIC excitation would shed light on the response of transformers to the simulated GIC amplitudes for historical storms.

It may also be that no currents of this magnitude were seen at Moneypoint at all. At every step of the geomagnetic storm simulations (SECS for magnetic fields,

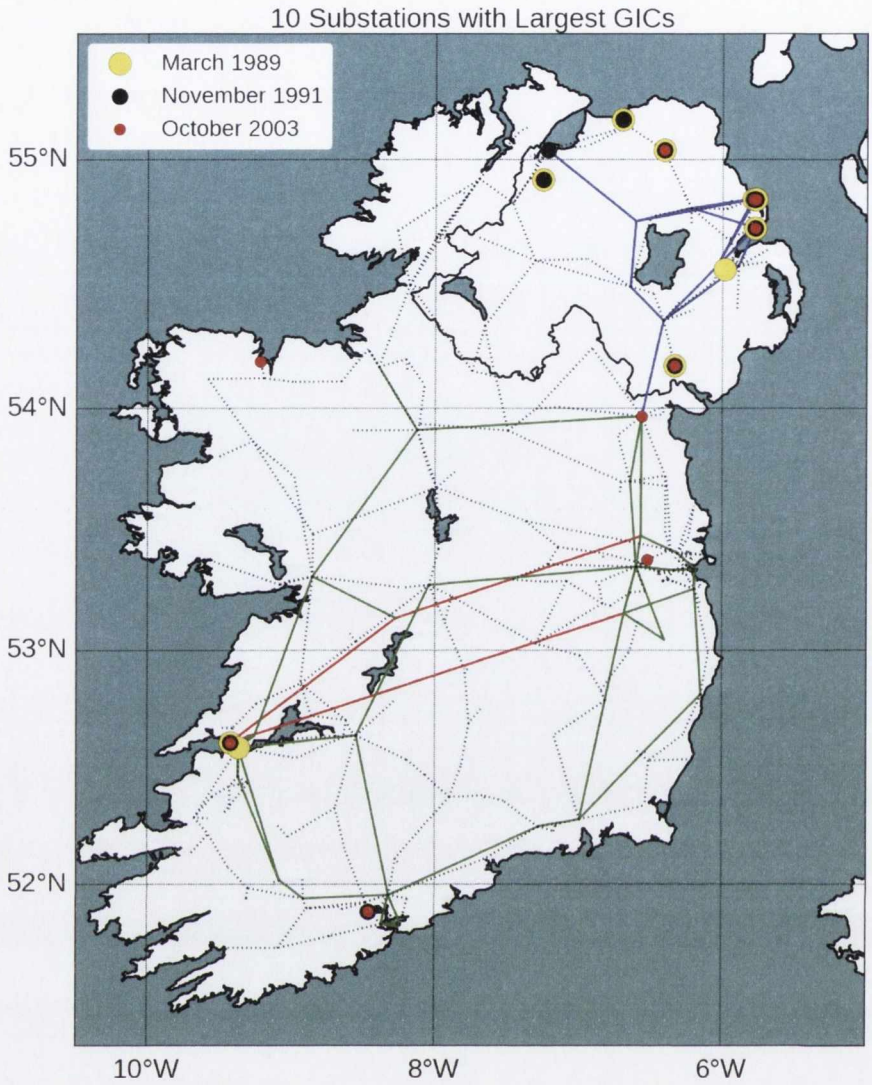


Figure 8.6: The ten substations which experienced the largest GICs during each of the three historical events simulated. Nine of the 15 substations are more northerly than 54° N.

MT method for electric field, LP method for GIC calculation), there are significant assumptions taken and uncertainties around currents in transformers outside of Woodland. As such, the above calculations can only be taken as qualitative estimates of GICs in the Irish power network. The most direct way to circumvent this obstacle is to get GIC measurements on multiple transformers around Ireland.

Extreme Event Analysis

The potential economic fallout from a large-scale geomagnetic storm has prompted a number of studies which look at rare large-scale geomagnetic events. In 2012, Earth experienced a near-miss with a powerful CME (Baker *et al.*, 2013). This particular CME, had it been Earthward directed, would have given rise to a geomagnetic event larger than even the 1859 Carrington storm. This storm serves as a reminder that large events can and will occur with time. It is therefore useful to estimate the magnitude and frequency of worst-case geomagnetic storm scenarios.

By measuring geomagnetic and electric fields over long periods, one can fit the distribution of measurements, and thereby estimate the frequency of much larger events. This approach can be seen in papers such as Love *et al.* (2016); Pulkkinen *et al.* (2012) and references therein. Once estimates for the 100-year (or longer) geoelectric variations are made, GICs can be calculated using model power networks. Such GIC estimates for infrequent events have been performed for the British (Beggan *et al.*, 2013) and Spanish (Torta *et al.*, 2014) power networks.

100-year GIC values in the Irish power networks were estimated in two ways. The first way uses previously calculated 100-year estimates for the geomagnetic field at Valentia. These are then used to scale the 2003 Halloween storm, and calculate corresponding GIC values. The second method used 25 years of geomagnetic data from four INTERMAGNET observatories to calculate GICs in the power network directly (as in the start of this chapter). From this large body of GIC calculations, a power law and lognormal distribution were fit to the tail of the data distribution, and estimates for GICs were made. Both methods are explored below.

Scaled Geomagnetic Storm

Thomson *et al.* (2011) estimated the 100, and 200-year maximum return values for the geomagnetic field at a number of different INTERMAGNET sites using several decades of available data. By using generalized Pareto distributions, they were able to fit the tail of their data (infrequent and large amplitude values). In this manner an estimate of the maximum horizontal intensity and declination (along with derivatives for both) over different timescales were estimated.

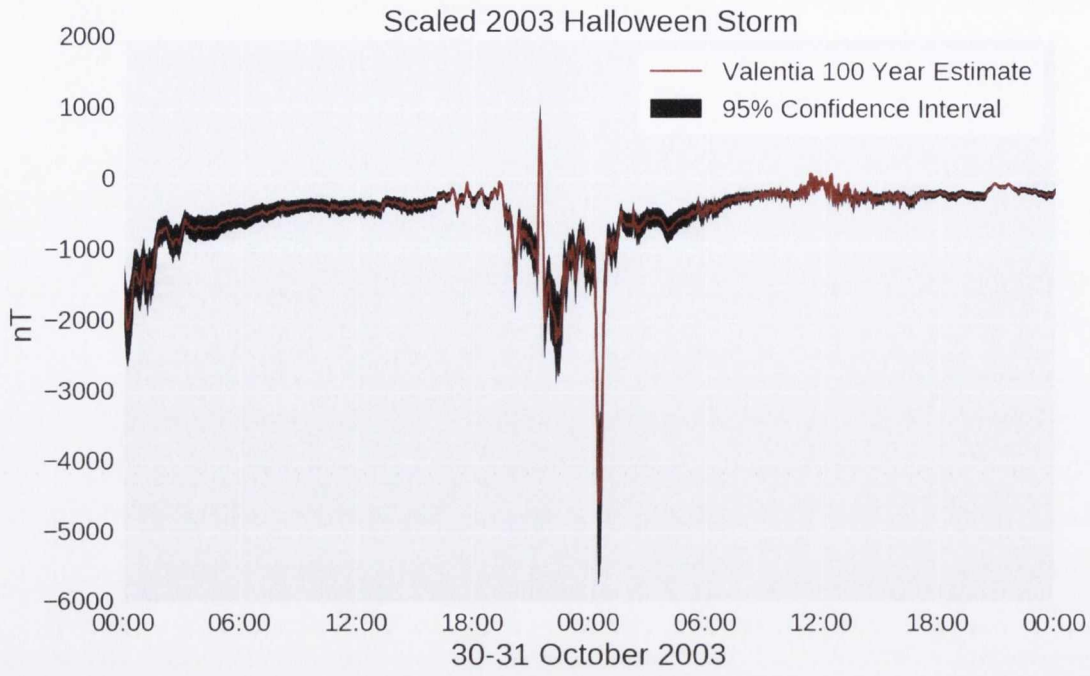


Figure 8.7: B_x component of the scaled 2003 Halloween storm according to the estimated 100-year dB/dt values from Thomson *et al.* (2011).

For a period of 100-years, the maximum change in the horizontal magnetic intensity in Valentia observatory was estimated as approximately 666 nTmin^{-1}. The lower and upper bounds for the 95% confidence interval were approximately 500 and 833 nTmin^{-1} respectively. In order to generate a realistic representation of a geomagnetic storm, the 2003 Halloween storm was used as a template. The maximum variation in the B_x component was scaled according to the 100-year value (and its 95% confidence boundaries). The scaled timeseries is shown in Figure 8.7. This reconstructed magnetic timeseries was assumed to be uniform across Ireland.

Electric field values were calculated using the scaled magnetic data and a 400 Ωm homogenous Earth model. At its peak, the scaled 100-year storm generated an electric field of 2.25 Vkm^{-1}. Corresponding GICs were calculated for the Irish power network. The maximum GIC for each substation are shown in Figure 8.8. These GIC values were calculated for a northerly and easterly directed

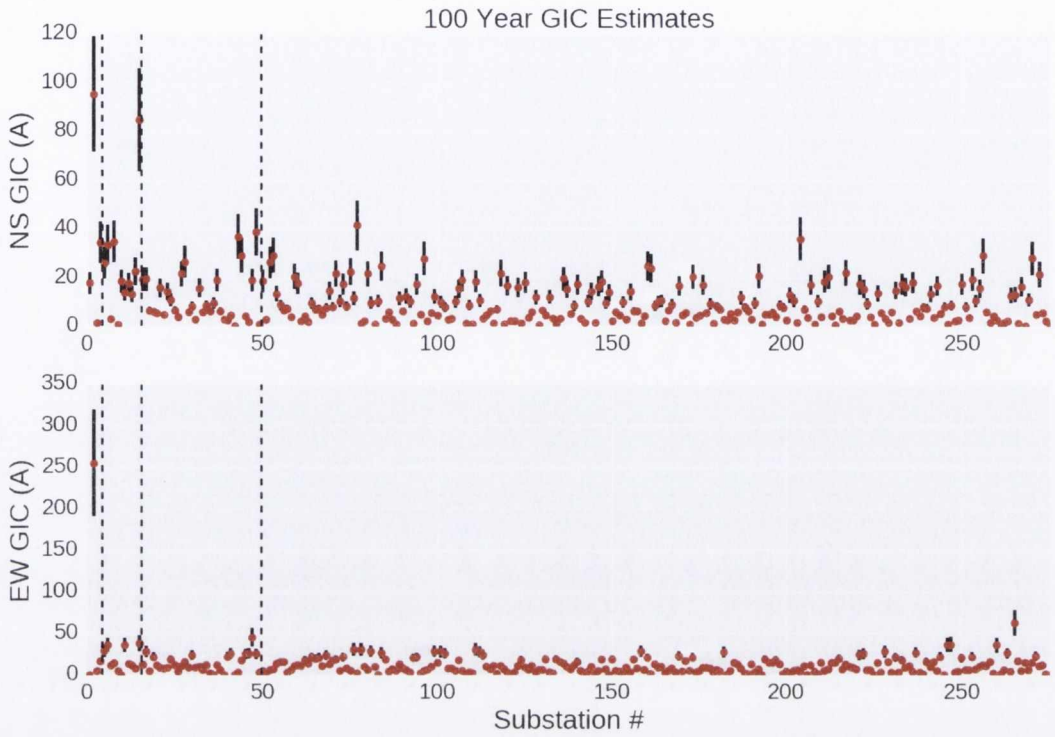


Figure 8.8: Maximum calculated GICs per substation for the 100-year extreme event magnetic estimates. Top plot shows the GIC from a purely north-south alignment. Bottom shows the GIC from an east-west alignment. The black bars indicate the 95% confidence interval for each substation. The dashed black lines separate the 400, 275, 220 and 110 kV substations.

electric field.

The largest GIC value was calculated in Moneypoint for an easterly electric field. This was calculated as 255 A. As with the various GIC simulations in this thesis, the other substations saw much lower GIC amplitudes. The next largest GIC was calculated in the 275 kV Louth substation for a northerly electric field. This substation saw 84 A.

Extrapolating 25 Years of GIC Calculations

Geomagnetic data sourced from four INTERMAGNET stations from January 1991 to the end of 2015 were used along with a 400 Ωm Earth model to calculate GICs. These sites are Valentia, Hartland, Eskdelmuir and Lerwick. Their data

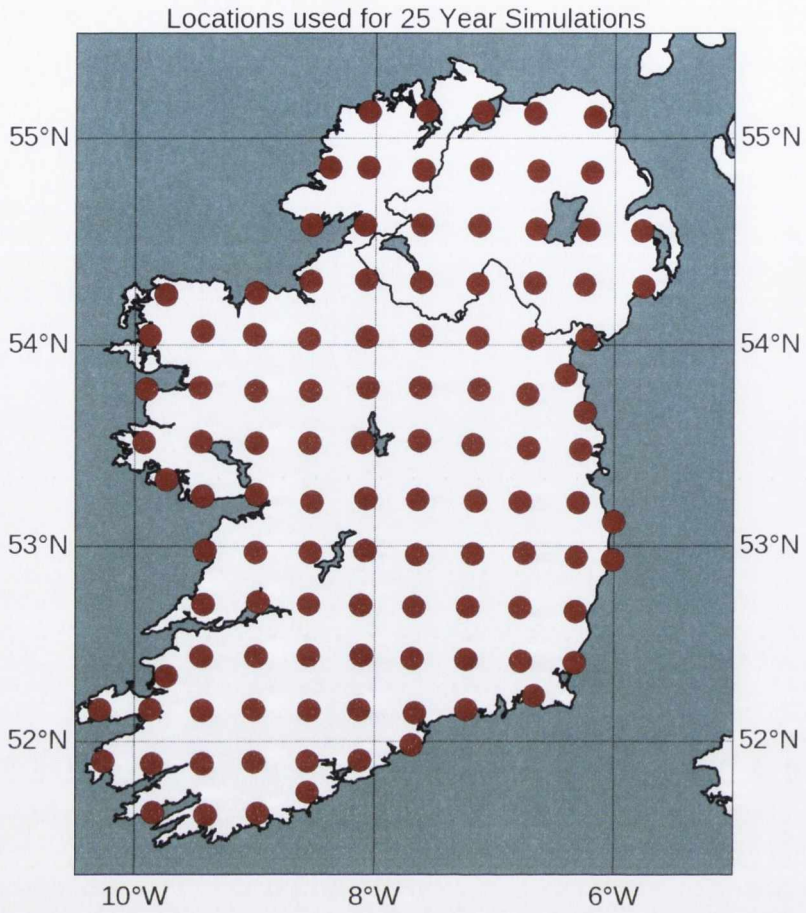


Figure 8.9: The 111 locations used for 25 year GIC simulations. Magnetic fields were only interpolated at these points to speed up the calculation of GICs.

were collected from http://supermag.jhuapl.edu/ for ease of use. These magnetic timeseries were interpolated across Ireland at 111 points using SECS. The location of these points are shown in Figure 8.9.

For simplicity, only those times where there were magnetic data available at all four stations were interpolated. Of the roughly 13.14 million minutes from 1991–2015, 12.65 million minutes were interpolated. Approximately 340 days were cut from the data, although these were not always contiguous. The year 1993 had the most data missing, with three months of data unavailable from Valentia

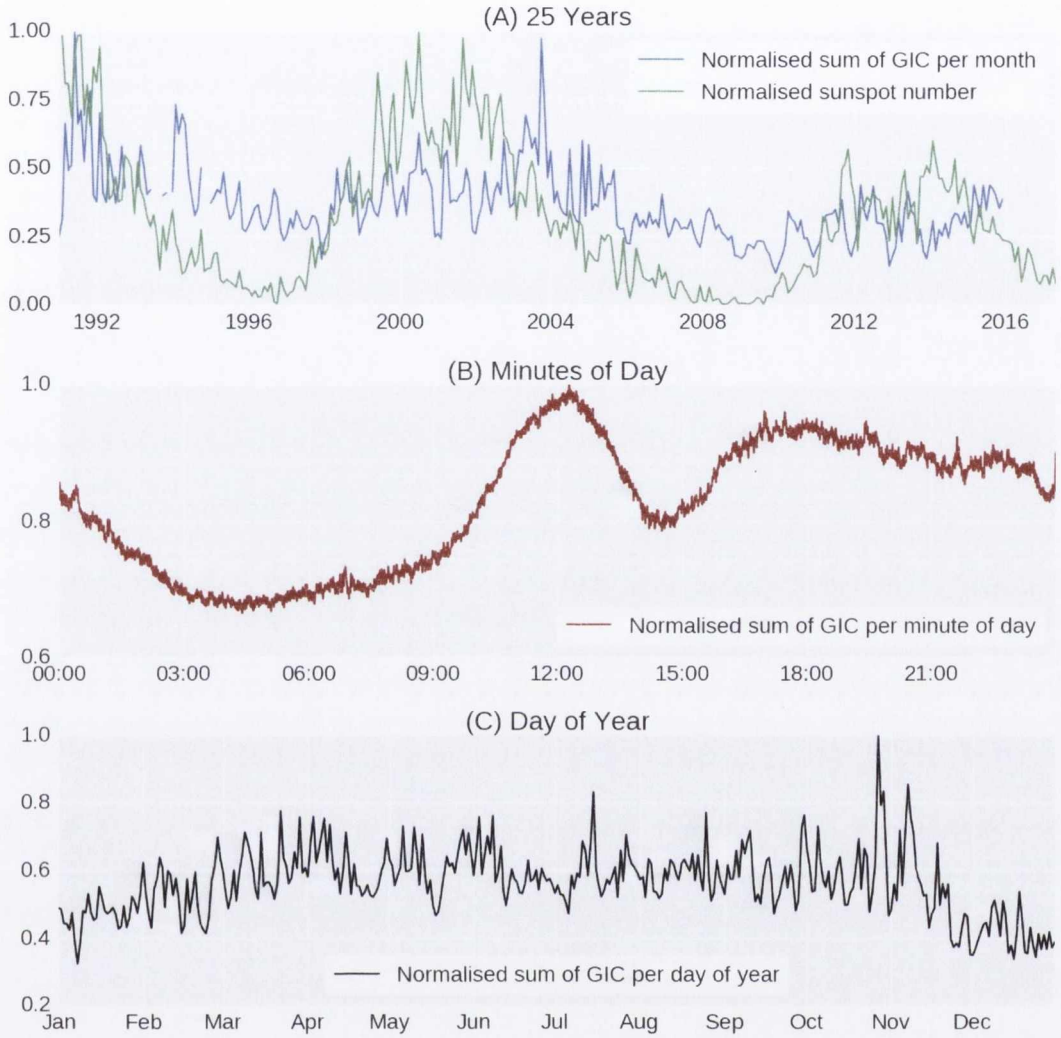


Figure 8.10: Normalised sum of GIC values from the 25 years of simulations. (A) shows the sum of GIC over the whole 25 years of simulations in monthly bins. Also plotted here is the sunspot number. (B) shows the normalised sum of GIC per minute of day. (C) shows the normalised sum of GIC per day of year.

observatory. Future simulations should take advantage of the INTERMAGNET database, which has is a more complete database.

The electric field at each of the 111 points was calculated for all of the interpolated magnetic field data using a 400 Ωm homogenous Earth, as described in previous sections. GICs were then calculated. To save time, 20 steps were used in the integration of the electric field under power lines (Equation 6.4), as opposed to

200 steps used for the rest of this thesis. When compared to the historical event simulations at the beginning of this chapter, the differences in GIC due to the simplifications taken are minimal (within a fe percent). The GIC calculations took approximately 3.5 thousand core-hours to run in total. The end result is roughly 3.46 billion individual GICs calculations, with one GIC value per substation per minute.

Figure 8.10 shows the normalised sum of GIC values for different time bins. The top plot shows the sum of GIC over the whole 25 years of simulations in monthly bins. Also in the top plot are the normalised sunspot numbers, showing the sunspot cycle. The normalised GIC values appear to follow the sunspot cycle, albeit with a lag of a few years. The middle plot shows the normalised sum of GIC per minute of day. The curve after midday is similar to the solar-quiet curve that appears during geomagnetically quiet times in the geomagnetic field (see Figure 3.13). The bottom plot shows the normalised sum of GIC per day of year. There appears to be less GIC calculated between the months of December and March, when the entire dataset is taken into account. The large peak at the end of October is due to the 2003 storms.

A histogram of the logarithmically binned GIC data is shown in the top of Figure 8.11. The bottom plot of the same figure shows the cumulative of the tail (right hand side) of the histogram. This shows the expected number of events greater than some amplitude x per year, for $x > 20$ A.

Two different distributions were fit to the data. The first is a power law. A power law is a probability distribution which has the form:

$$p(x) \propto Cx^{-\alpha} \tag{8.1}$$

where C is a normalisation constant and α is the exponent. On a log-log plot, a power law gives a straight line, with a slope of α (although this is not the only requirement for a power law). Power laws are frequently used to describe many different physical phenomena whose amplitudes or frequencies span many orders of magnitude (Newman *et al.*, 2015). The power law fit used in this study was generated using the approach of Alsott *et al.* (2014).

From the top plot in Figure 8.11, the histogram is clearly not a straight line. A minimum GIC amplitude (x_{min}) needs to be chosen in order to truncate the data to be fit with a power law. This value was chosen by minimising the Kolmogorov-Smirnov (KS) values for different x_{min}. The KS value measures the difference between empirical and idealised probability distribution functions. An x_{min} value of 20 A minimised the KS value. The best-fit for the power law gave an α value of 4.26. The corresponding cumulative plot, when extrapolated beyond the measured data, gives a 1-in-100 year GIC amplitude of 258 A.

The second fit used is the lognormal distribution. A random positive variable x is the realization of a lognormal statistical process if its probability density is (Love *et al.*, 2016):

$$p(X|\mu,\sigma^2) = \frac{1}{x\sqrt{2\pi\sigma^2}}\exp\Big[-\frac{(\ln x-\mu)^2}{2\sigma^2}\Big] \tag{8.2}$$

where μ and σ are model parameters. When plotted with a logarithmic x-axis, a lognormal distribution has the same shape as a normal distribution. Lognormal distributions have been used to model geomagnetic disturbances over decade timescales by Pulkkinen *et al.* (2008) and Love *et al.* (2015). As pointed out in Love *et al.* (2016), power laws are capable of fitting only a small portion of some distributions, and a lognormal distribution can often be fit to more of a distribution. Different values of μ and σ were chosen such that the χ^2 value between the generated lognormal distribution cumulatives and measured cumulatives were minimised. The χ^2 value is defined as:

$$\chi^2 = \sum\Big[\frac{o_x - e_x}{o_x}\Big]^2 \tag{8.3}$$

where o and e are the observed and estimated cumulative values for different values of x. The best-fit lognormal distribution had a μ of -4.62, and a σ of 8.23. The yearly cumulative for this distribution estimates that an event with a 100-year period will have an amplitude of 179 A.

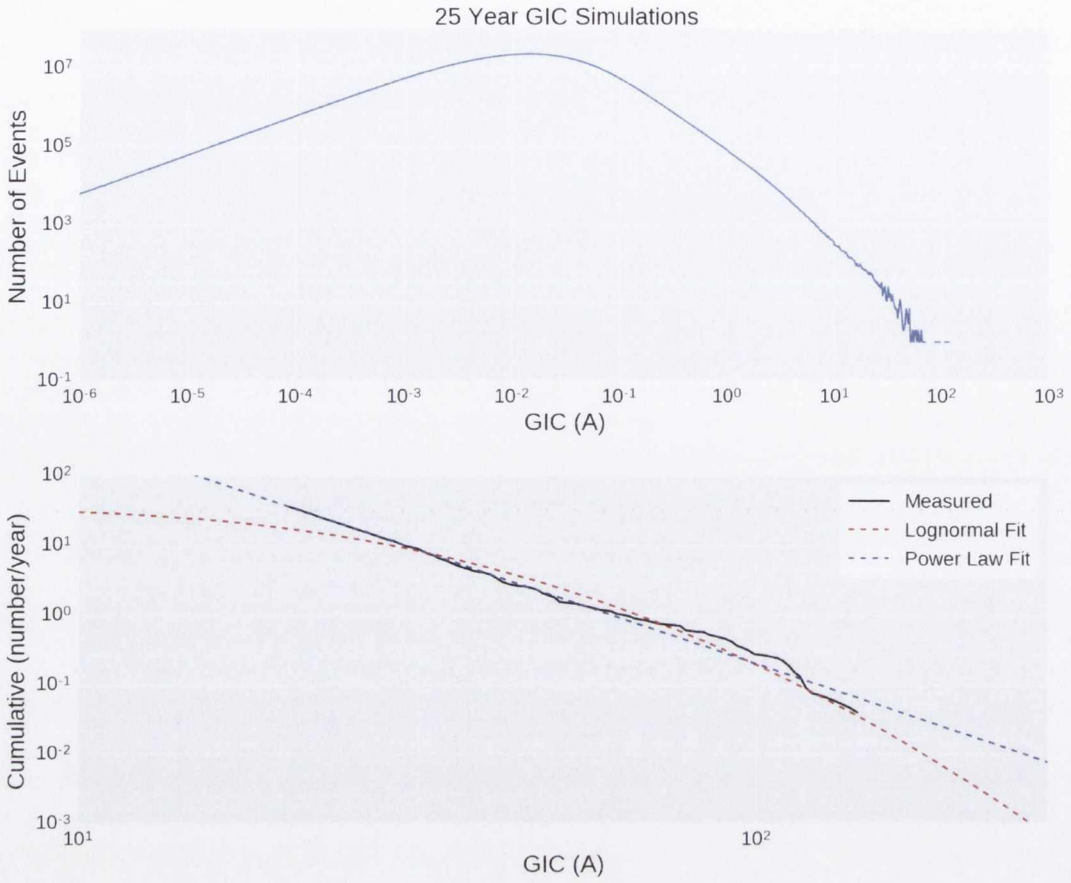


Figure 8.11: Top: histogram of the entire set of 25 years of GICs in logarithmic bins. Bottom: the exceedance cumulatives for one year. Also shown are the fit to the cumulative using power law (blue dashed lines) and lognormal (dashed red) distributions. Extrapolating the power law yields a 258 A event with a period of 100 years. The lognormal equivalent is 178 A.

Extreme Event Discussion

The amplitude of a 1-in-100 year GIC event in Ireland was estimated using two different methods. The first scaled the 2003 Halloween storm according to maximum variations in the horizontal geomagnetic field values calculated in Thomson *et al.* (2011). This yielded a GIC value in the Moneypoint substation of 255 A. The second method calculated GICs for 25 years and fit power law and lognormal distributions to the data. The fitted power law estimated a one in a 1-in-100 year GIC value of 258 A. The corresponding value for the lognormal distribution was

179 A.

Each of the listed methods above suffer from the same simplifications and uncertainties as the other simulations in this thesis. This is a consequence of the steps taken in acquiring GIC values (SECS, E-field, GIC calculations), and the limits on the available information for each step taken. In addition, they inevitably involve estimating the amplitude of events which haven't occurred yet. In the case of the scaled geomagnetic storm method, the 2003 storm was chosen as a representative historical storm. No accounting for the spatial variations of large geomagnetic storms, or how geomagnetic storms scale was taken into account in order to arrive at the 255 A value.

Both the fitting of the power law and lognormal distribution to the 25 years of calculated GICs can also be more rigorously expanded upon. For example, in the case of the lognormal distribution, a fit could be performed using maximum likelihood estimates (MLE) as well as a simple χ^2 fit. No tests were performed to determine which distribution was a more statistically probable fit for the calculated data.

For all of these caveats, the maximum GIC that can be expected in the Irish power network for a 100-year period is roughly in the region of 180-260 A (assuming a uniform 400 Ωm resistivity model). It is difficult to estimate the effect of a current of this magnitude on a transformer. It would undoubtedly be a cause for concern for engineers, given that the addition of a small GIC (10s of A) to a transformer's operation can lead to problems (see Section 1.2.1).

9

Conclusions and Future Work

This work is the first detailed study of GICs in the Irish power network, some of which has been published in Blake *et al.* (2016b). In order to monitor geomagnetic storms in real-time, a network of geomagnetic observatories has been established across Ireland. A detailed model of the Irish power network has been created for simulating GICs, and substations vulnerable to GICs have been identified. The Irish power network model was used to replicate measured GICs at a transformer in an Irish substation. Finally, historical geomagnetic storms were simulated, and estimates for large-scale and rare GIC events were made. The main results from this work are summarised below.

MagIE

Geomagnetic variations in Ireland are now being measured at multiple locations as part of the MagIE network. Data from the Armagh and Birr observatories are available in real time at www.rosseobservatory.ie, and K-indices are calculated for each, alerting end-users of activity in Ireland. These sites, in addition to Met Éireann's Valentia, ensure that Ireland has dense coverage for geomagnetic disturbances for its small size. In addition to these sites, long-term geoelectric fields

were measured in Leitrim and Sligo during some moderate geomagnetic storms. These data can aid in testing geoelectric field calculations.

The addition of the MagIE geomagnetic observatories was shown to increase the accuracy of geomagnetic field interpolations throughout Ireland for a single geomagnetic event, when using the SECS method of interpolation. Future geomagnetic storms will be measured at multiple sites in Ireland, which will aid simulations for phenomena such as GICs.

Power Network Modelling

The complete high voltage Irish power network was modelled for use in GIC simulations. The high voltage Irish power network consists of 274 substations which operate at 400, 275, 200 and 110 kV. As part of the detailed model, the resistances and types of the higher voltage (> 110 kV) transformers were taken into account. Some of the substations also had ground resistance values, as well as ground switches. A Python program was developed to correctly construct such a model from power network information, for use with the Lehtinen & Pirjola (1985) method of calculating GICs. This program was tested with the Horton *et al.* (2012) power network model, and was found to correctly recreate GIC values.

The power network model was subjected to a number of different tests. Firstly, a uniform electric field of 1 V km^{-1} was applied to the network at different angles. The substations most susceptible to GICs were identified. In particular, the 400 kV Moneypoint substation was most affected, with a maximum 121 A calculated when the electric field was oriented roughly ENE. The vulnerability of Moneypoint was a recurring factor to all GIC simulations in this work. This is due to its low grounding resistance and long low resistance transmission lines which connect it to the rest of the grid.

The effect of substation grounding resistances have on GIC calculations were explored. For those substations where grounding resistance information was unavailable, it was assumed to be 1 Ω. By changing this assumption from 1 Ω to 7 Ω in increments, the response of the power network to a uniform electric field was gauged. It was found that for some substations, altering the grounding resistance

altered the calculated GIC very little, indicating that the network orientation was more important than the grounding resistance in some cases.

The effect of omitting the lower voltage parts of the Irish network was explored. It was found that adding the 110 kV substations to the model changed some of the GICs in the substations by up to 200%. Omitting the lower voltage networks would lead to overestimating GICs in the higher voltage systems. Those substations most affected by adding the lower voltages were those with direct connections to the lower voltage substations.

It was shown that the 15 ground switches which can currently isolate transformers from their grounds in Ireland would play a negligible role in protecting the network from GICs. This is due to the location of the ground switches. In a simulation, it was shown that by using ground switches on five select transformers, the maximum GIC induced in Ireland from a 1 V km^{-1} electric field could be reduced to less than 20 A.

Simulating GICs in Ireland During Geomagnetic Storms

Data from a Hall effect probe at the Woodland substation were processed and cleaned. Five recent geomagnetic storm events were used to test the GIC calculation methods with measured GIC data. Two different electric field calculation methods (MT and thin-sheet) and three different resistivity models (homogenous 400 Ωm, homogenous 400 Ωm land with conductive sea and MT-derived 3D Earth) were used. It was found that the calculated GICs best fit the measured GICs when the MT method was used with an homogenous 400 Ωm resistivity model. For the five events used, some were better modelled than others. In particular, the geomagnetic storm on the 27-28 March 2017 appeared to have no measurable effect on the Woodland probe, despite currents of 0.7 A being predicted.

Larger historical storms were then simulated, using the MT method of electric field calculation and the 400 Ωm resistivity model. The March 1989, November 1991 and October 2003 storms were each simulated and analysed. In each case, the Moneypoint substation saw the largest calculated GIC values (159, 67 and 125 A respectively). The majority of the substations which saw the largest GICs were situated above 54° N. Despite the large GIC values in Moneypoint for the 1989

storm, GICs with an amplitude larger than 100 A only occurred for 6 minutes. This shows that such GIC spikes were not sustained for long periods during this storm.

Three estimates for a 1-in-100 year GIC event were made as the final part of this study. The 2003 storm was scaled according to maximum GIC variation estimates made by Thomson *et al.* (2011) for Valentia observatory. GICs were then calculated in a similar manner to previous simulations, using this scaled magnetic timeseries as an input. Moneypoint saw a maximum GIC value of 255 A. This is a large current, which would likely cause operational problems in a transformer.

Using INTERMAGNET geomagnetic data from 1991 to end of 2015, GICs were calculated for approximately 25 years. Power law and lognormal distributions were fit to the GIC calculations, and extrapolated to estimate 1-in-100 year GIC return values. These were found to be ~179 A and ~258 A for the power law and lognormal distributions respectively.

Future Work

The work in this thesis is the first step in studying GICs in Ireland. Many aspects of the work done can be improved and expanded upon.

MagIE currently has only two sites permanently installed with realtime communications (Birr and Armagh), and a real-time connection to Valentia observatory is currently being established. Malin Head, in the northernmost tip of Ireland, has been identified as a suitable location for a magnetometer installation, but is yet to be permanently installed. In the future, Malin Head would be welcome addition to MagIE. MagIE currently has no long-term electric field measurements currently being taken. Ideally, MagIE would have multiple electric field measurements at different locations. Current work being undertaken in TCD is seeking to extend electric field measurements around Ireland for space weather and GIC simulations.

In this study, MT data taken by DIAS was used to make a crude resistivity model (see Section 5.1.5). It was found that this model was sufficient to calculate GICs for a simple model of the Irish power network as appeared in Blake *et al.* (2016b). However, for the updated model of the Irish power network, the MT derived resistivity model gave GICs which underestimated measured GICs at

Woodland. It was found that a simple 400 Ωm model worked better for GIC simulations. Future work should properly avail of the decades of MT data in Ireland, and use it to create a realistic full 3D model of the Irish subsurface. Creating a single resistivity model for the Irish subsurface which utilizes historical broadband and long-period MT measurements would be a significant endeavour. At the time of writing, work is being undertaken in both Trinity College Dublin and the Dublin Institute for Advanced studies to gather more long-period MT measurements around Ireland to make a single resistivity model for space weather and geophysics applications. The SWEMDI (Space Weather ElectroMagnetic Database for Ireland) project should yield resistivity models which will constrain e-field calculations.

None of the GIC simulations in this work had measured GICs at more than a single transformer. While the power network model was created to be as detailed as possible, there were naturally assumptions which needed to be made in order to calculate GICs. Outside of Woodland, it is not possible to verify that these assumptions give correct GICs for different storm simulations. More GIC measurements are needed in order to comprehensively validate the models used in this thesis. These can be acquired through more Hall effect probes at different transformers around Ireland, or by using magnetometers beneath power lines (Matandirotya *et al.*, 2015).

In particular, the Moneypoint substation requires scrutiny. In all simulations, it is consistently the most affected by GICs: it has a single operational transformer and a low grounding resistance. For future GIC work, it would be immensely beneficial for measurements at this substation. Other substations which were identified as being 'at risk' included those 275 kV substations on the north-east coast of Northern Ireland, although to a lesser extent than Moneypoint. Thermal analysis of the Moneypoint substation would be beneficial for understanding the effect on GICs on a transformer level.

The analysis of the 1-in-100 years GIC values can also be greatly expanded upon. Different distributions can be fit to the 25 years of data, and statistical errors can be estimated with greater accuracy. Should a full MT resistivity map be developed for calculating GICs with full 3D MT tensors, as opposed to the

crude resistivity model seen in Chapter 5, the 25 years of simulations should be repeated, to get another estimate of infrequent GIC events.

For future events, Ireland is now equipped with at least three functioning magnetometic observatories, a detailed power network model and data from a GIC probe. As time goes on and more geomagnetic storms occur, Ireland will have a more complete database to draw upon for geomagnetic simulations.

References

Ádám, A., Prácser, E. & Wesztergom, V. (2012). Estimation of the electric resistivity distribution (EUROHM) in the European lithosphere in the frame of the EURISGIC WP2 project. *Acta Geod Geophys*, **47**, 4. (Cited on page 64.)

Akasofu, S. (1989). Several contoversial issues on substorms. *Space Science Reviews*, **113**, 1–40. (Cited on page 23.)

Allen, J., Frank, L., Sauer, H. & Reiff, P. (1989). Effects of the March 1989 Solar Activity. *EOS*, **70**, 46. (Cited on page 160.)

Alsott, J., Bullmore, E. & Plenz, D. (2014). powerlaw: A Python Package for Analysis of Heavy-Tailed Distributions. *PLoS ONE*, **9**. (Cited on page 174.)

Amm, O. (1997). Ionospheric Elementary Current Systems in Spherical Coordinates and Their Application. *J. Geomag. Geoelectr.*, **49**, 947–955. (Cited on pages 50 and 51.)

Amm, O. (2001). The elementary current method for calculating ionpspheric current systems from multisatellite and ground magnetometer data. *J. Geophys Res.*, **106**, 24843–24855. (Cited on page 49.)

Amm, O. & Viljanen, A. (1999). Ionospheric disturbance magnetic field continuation from the ground to the ionosphere using spherical elementary current systems. *Earth Planets Space*, **51**, 431–440. (Cited on pages 50, 51 and 52.)

Atkinson, G. (1966). A theory of polar substorms. *Journal of Geophys. Res.*, **71**, 5157–5163. (Cited on page 23.)

Bailey, R., Halbedl, T., Schattauer, I., Romer, A., Achleitner, G., Beggan, C., Wesztergom, V., Egli, R. & Leonhardt, R. (2017). Modelling geomagnetically induced currents in midlatitude Central Europe using a thin-sheet approach. *Ann. Geophys.*, **35**, 751–761. (Cited on pages 5, 90, 93 and 145.)

Baker, D.N., Li, X., Pulkinnen, A., Ngwira, C.M., Mays, M.L., Galvin, A.B. & Simunac, K.D.C. (2013). A major solar eruptive event in July 2012: Defining extreme space weather scenarios,. *Space Weather*, **11**, 585–591. (Cited on page 169.)

Bartels, J., Heck, N. & Johnston, H. (1939). The three-hour range index measuring geomagnetic activity. *Geophysical Research*, **44**, 411–454. (Cited on pages 42 and 43.)

Bedrosian, P. & Love, J. (2015). Mapping geoelectric fields during magnetic storms: Synthetic analysis of empirical United States impedances. *Space Weather*, **42**. (Cited on page 64.)

BEGGAN, C. (2015). Sensitivity of geomagnetically induced currents to varying auroral electrojet and conductivity models. *Earth, Planets, Space*, **67**, 1–12. (Cited on pages 5 and 90.)

BEGGAN, C.D., BEAMISH, D., RICHARDS, A., KELLY, G.S. & THOMSON, A.W.P. (2013). Prediction of extreme geomagnetically induced currents in the UK high-voltage network,. *Space Weather*, **11**, 407–419. (Cited on page 169.)

BERKTOLD, A. (1983). Electromagnetic studies in geothermal regions. *Geophysical Surveys*, **6**, 173–200. (Cited on page 64.)

BIRKELAND, K. (1908). *The Norwegian Polaris Expedition 1902-1903, Vol. 1.*. Christiania, H. Aschelhoug, 1st edn. (Cited on page 21.)

BITTERLY, M., MENVIELLE, M., BITTERLY, J. & BERTHELIER, A. (1997). A comparison between computer derived (FMI Method) and hand scaled K indices at Port-Aux-Francais and Port Alfred French Observatories. *Proceedings of the VIth International workshop on geomagnetic instruments, data acquisition and processing*, 136–143. (Cited on page 43.)

BLAKE, S., HENRY, T., JONES, A., MOORE, J., MURRAY, J., CAMPANYÀ, J., VOZAR, J., WALSH, J. & RATH, V. (2016a). Understanding hydrothermal circulation patterns at a low-enthalphy thermal spring using audio-magnetotelluric data: A case study from Ireland. *Journal of Applied Geophysics*, **132**, 1–16. (Cited on page 87.)

BLAKE, S.P., GALLAGHER, P.T., MCCAULEY, J., JONES, A.G., HOGG, C., CAMPANYÀ, J., BEGGAN, C.D., THOMSON, A.W.P., KELLY, G.S. & BELL, D. (2016b). Geomagnetically Induced Currents in the Irish Power Network During Geomagnetic Storms. *Space Weather*, **14**, 1136–1154. (Cited on pages 5, 64, 75, 87, 99, 108, 110, 111, 118, 130, 139, 142, 178 and 181.)

BOLDUC, L. (2002). GIC observations and studies in the Hydro-Qubec power system. *J. Atmos. Sol.-Terr. Phys.*, **64**, 1793–1802. (Cited on pages 4, 5, 8 and 160.)

BOTELER, D. (2006). The super storms of August/September 1859 and their effects on the telegraph system. *Adv. in Space Res.*, **38**, 159–17 2. (Cited on page 3.)

BOTELER, D. & PIRJOLA, R.J. (2016). Modeling Geomagnetically Induced Currents. *Space Weather*, **15**, 1. (Cited on pages 23, 24, 100, 101, 102, 108 and 122.)

BOTELER, D.H. & PIRJOLA, R.J. (2014). Comparison of methods for modelling geomagnetically induced currents. *Ann. Geophys.*, **32**, 1177–1187. (Cited on pages 6, 101 and 102.)

BOTELER, D.H., SHIER, R., WATANABE, T. & HORITA, R. (1989). Effects of Geomagnetically Induced Currents in the B.C. Hydro 500 kV System. *IEEE Trans. Power Delivery*, **4**, 818–823. (Cited on page 5.)

BYRNE, J., MALONEY, S., MCATEER, J., REFOJO, J. & GALLAGHER, P. (2010). Propagation of an earth-directed coronal mass ejection in three dimensions. *Nature Communications*, **1**. (Cited on page 15.)

CAGNIARD, L. (1953). Basic theory of magnetotelluric method of geophysical prospecting. *Geophysics*, **18**, 605–635. (Cited on pages 25 and 65.)

CARRINGTON, R. (1860). Singular Appearance in the Sun. *Monthly Notices Royal Astron. Soc.*, **20**, 13–15. (Cited on pages 3 and 17.)

CAWOOD, J. (1979). The magnetic crusade: Science and politics in early victorian britain. *Isis*, **70**, 493–518. (Cited on page 26.)

CENTRA TECH (2011). *OECD/IFP Futures Project on Future Global Shocks: Geomagnetic Storms*. On behalf of the Office of Risk Management and Analysis, US Department of Homeland Security. (Cited on page 4.)

CHAVE, A.D. & JONES, A.G. (2012). *The Magnetotelluric Method, Theory and Practice*. Cambridge University Press, Cambridge UK, 1st edn. (Cited on pages 18, 22, 23, 32, 34, 47, 64, 65, 71 and 84.)

CHEN, P. (2011). Coronal Mass Ejections: Models and Their Observational Basis. *Living Rev. Solar Phys.*, **8**. (Cited on page 15.)

CLARK, S. (2007). *The Sun Kings*. Princeton University Press, New Jersey, USA, 1st edn. (Cited on page 27.)

CLARK, T. (1992). Computer generated K indices adopted by the British Geological Survey. *J. Atmos. Terr. Phys.*, **54**, 447–456. (Cited on pages 42 and 43.)

CLIVER, E. (2006). The 1859 space weather event: Then and now. *Adv. in Space Res.*, **38**, 119–129. (Cited on page 3.)

CLIVER, E., BALASUBRAMANIAM, K., NITTA, N. & LI, X. (2004). The 1859 solar-terrestrial disturbance and the current limits of extreme space weather activity. *Solar Physics*, **224**, 407–422. (Cited on page 2.)

CLIVER, E., BALASUBRAMANIAM, K., NITTA, N. & LI, X. (2009). Great geomagnetic storm of 9 November 1991: Association with a disappearing solar filament. *J. Geophys. Res.*, **114**, 1–9. (Cited on page 163.)

CLIVER, E.W. (1994). Solar Activity and Geomagnetic Storms: The First 40 Years. *Eos. Trans. Amer. Geophys. Union*, **75**, 569–584. (Cited on page 26.)

CLIVER, E.W. & DIETRICH, W. (2013). The 1859 space weather event revisited: limits of extreme activity. *J. Space Weather Space Clim.*, **3**, 1–14. (Cited on pages 27 and 28.)

CRANMER, S. (2009). Coronal Holes. *Living Rev. Solar Phys.*, **3**. (Cited on page 14.)

CULLUM, J. & FITZGERALD, G. (1889). Reports on the Magnetic Observatories at Valentia. *Proceedings of the Royal Irish Academy*, **1**, 221–228. (Cited on page 29.)

DAGLIS, I., THORNE, R., BAUMJOHANN, W. & ORSINI, S. (1999). The Terrestrial Ring Current: Origin, Formation and Decay. *Reviews of Geophysics*, **8**, 407–438. (Cited on page 20.)

DAVY, H. (1821). On the Magnetic Phenomena Produced by Electricity. *Phil. Trans. R. Soc. Lond.*, **111**, 7–19. (Cited on page 2.)

de Groot-Hedlin, C. & Constable, S. (1990). Occam's inversion to generate smooth, two-dimensional models from magnetotelluric data. *Geophysics*, **55**, 1613–1624. (Cited on pages 84 and 85.)

DeRosa, M., Brun, A. & Hoeksema, J. (2012). Solar magnetic field reversals and the role of dynamo families. *The Astrophysical Journal*, **757**. (Cited on page 14.)

Dong, X., Liu, Y. & Kappenman, J.G. (2001). Comparative analysis of exciting current harmonics and reactive power consumption from gic saturated transformers. In *2001 IEEE Power Engineering Society Winter Meeting. Conference Proceedings (Cat. No.01CH37194)*, vol. 1, 318–322 vol.1. (Cited on page 8.)

Dungey, J. (1961). Interplanetary magnetic field and the auroral zones. *Physical Review Letters*, **6**, 47–48. (Cited on page 23.)

Egbert, G. & Kelbert, A. (2012). Computational recipes for electromagnetic inverse problems. *Geophys J Int*, **189**, 251–267. (Cited on page 148.)

Eroshenko, E., Belov, A., Boteler, D., Gaidash, S., Lobkov, S., Pirjola, R. & Trichtchenko, L. (2010). Effects of strong geomagnetic storms on Northern railways in Russia. *Adv. in Space Res.*, **46**, 1102–1110. (Cited on page 2.)

Farquharson, C. & Craven, J. (2009). Three-dimensional inversion of magnetotelluric data for mineral exploration: An example from the McArthur River uranium deposit, Saskatchewan, Canada. *Journal of Applied Geophysics*, **68**, 450–458. (Cited on page 64.)

Fleisch, D. (2008). *A Student's Guide to Maxwell's Equations*. Cambridge University Press, Cambridge, UK, 1st edn. (Cited on page 66.)

Forbes, T. (2000). A review on the genesis of coronal mass ejections. *Journal of Geophysical Research*, **105**, 23153–23165. (Cited on page 15.)

Gaillard, F., Malki, M., Iancono-Marziano, G., Pichavant, M. & Scaillet, B. (2008). Carbonatite Melts and Electrical Conductivity in the Asthenosphere. *Science*, **322**, 1363–1365. (Cited on page 94.)

Garcia, X. & Jones, A. (2008). Robust processing of magnetotelluric data in the AMT dead band using the coninuous wavelet transform. *Geophysics*, **6**, 223–234. (Cited on page 65.)

Gaunt, C.T. (2014). Reducing uncertainty - responses for electricity utilities to severe solar storms,. *J. Space Weather Space Clim.*, **4**, 27. (Cited on page 5.)

Gaunt, C.T. & Coetzee, G. (2007). Transformer failures in regions incorrectly considered to have low GIC-risk. *IEEE, PowerTech*, **4**, 27. (Cited on pages 5, 7 and 8.)

Girgis, R. & Vedante, K. (2012). Effects of gic on power transformers and power systems. In *Transmission and Distribution Conference and Exposition (T&D), 2012 IEEE PES*, 1–8, IEEE. (Cited on page 8.)

Grandis, H. & Menvielle, M. (2015). Thin-sheet electromagnetic modeling of magnetovariational data for a regional-scale study. *Earth, Planets and Space*, **67**, 1–8. (Cited on page 89.)

GREEN, J. & BOARDSEN, S. (2006). Duration and extent of the great auroral storm of 1859. *Adv. in Space Res.*, **38**, 130–135. (Cited on page 3.)

GROOM, R.W. & BAILEY, R.C. (1989). Decomposition of magnetotelluric impedance tensors in the presence of local three-dimensional galvanic distortion. *Journal of Geophysical Research: Solid Earth*, **94**, 1913–1925. (Cited on page 86.)

GUO, S.X., LIU, L.G., PIRJOLA, R., WANG, K.R. & DONG, B. (2015). Impact of the EHV Power System on Geomagnetically Induced Currents in the UHV Power System. *IEEE Trans. Power Delivery*, **30**, 2163–2170. (Cited on page 122.)

HAMACHER, D. (2014). Aurorae in Australian Aboriginal Traditions. *J. Astron. Hist. Herit*, **17**, 1–20. (Cited on page 2.)

HODGSON, R. (1860). On a curious Appearance seen in the Sun. *Monthly Notices Royal Astron. Soc.*, **20**, 15–16. (Cited on page 3.)

HORTON, R., BOTELER, D., OVERBYE, T., PIRJOLA, R. & DUGAN, R. (2012). A test case for the calculation of geomagnetically induced currents. *IEEE Trans. Power Del.*, **27**, 2368–2373. (Cited on pages xii, 104, 106, 107, 113 and 179.)

HUDSON, M., KRESS, B., MUELLER, H., ZASTROW, J. & BLAKE, J. (2008). Relationship of the Van Allen radiation belts to solar wind drivers. *J. Atmos. and Sol-Terr. Phys.*, **70**, 708–729. (Cited on page 19.)

JONES, A. *et al.* (2015). IRETHERM: Developing a strategic and holistic understanding of Ireland's geothermal energy potential through integrated modelling of new and existing geophysical geochemical and geological data. *Proceedings World Geothermal Congress*. (Cited on page 86.)

KAPPENMAN, J., ZANETTI, L. & RADASKY, W. (1997). Geomagnetic Storm Forecasts and the Power Industry. *Eos, Trans. AGU*, **78**. (Cited on page 9.)

KATAOKA, R. *et al.* (2017). Historical space weather monitoring of prolonged activities in Japan and in China. *Space Weather*, **15**, 392–402. (Cited on page 2.)

KELBERT, A., MEQBEL, N., EGBERT, G. & K., T. (2014). ModEM: A modular system for inversion of electromagnetic geophysical data. *Computers and Geosciences*, **66**, 40–53. (Cited on page 148.)

KELLY, G., VILJANEN, A., BEGGAN, C. & THOMSON, A. (2017). Understanding GIC in the UK and French high-voltage transmission systems during severe magnetic storms. *Space Weather*, **15**, 99–114. (Cited on pages 5 and 90.)

KOEN, J. & GAUNT, T. (2003). Geomagnetically Induced Currents in the Southern African Electricity Transmission Network. *IEEE Bologna PowerTech Conference*. (Cited on pages 5 and 8.)

LE, G., SLAVIN, J. & STRANGEWAY, R. (2010). Space Technology 5 observations of the imbalance of regions 1 and 2 field-aligned currents and its implication to the cross polar cap Pedersen currents. *J. Geophys. Res.*, **115**. (Cited on pages 20 and 21.)

LEHTINEN, M. & PIRJOLA, R. (1985). Currents produced in earthed conductor networks by geomagnetically-induced electric fields. *Ann. Geophys.*, **3**, 479–484. (Cited on pages 12, 99, 127 and 179.)

LEWIS, J. (2004). *Physics and Chemistry of the Solar System*. Elsevier Academic Press, Massachusetts, USA, 2nd edn. (Cited on page 14.)

LIU, J., WANG, C., LIU, L. & W.H., S. (2016). The response of local power grid at low-latitude to geomagnetic storm: an application of the Hilbert Huang Transform. *Space Weather*, **14**, 300–312. (Cited on page 5.)

LOVE, J., JOSHUA RIGLER, E., PULKKINEN, A. & RILEY, P. (2015). On the lognormality of historical magnetic storm intensity statistics: Implications for extreme-event probabilities. *Geophysical Research Letters*, **42**. (Cited on page 175.)

LOVE, J. *et al.* (2016). Geoelectric hazard maps for the continental United States. *Space Weather*, **43**. (Cited on pages 64, 169 and 175.)

LOWRIE, W. (2007). *Fundamentals of Geophysics*. Cambridge University Press, Cambridge, UK, 2nd edn. (Cited on page 14.)

MACMANUS, D. *et al.* (2017). Long-term geomagnetically induced current observations in New Zealand: Earth return corrections and geomagnetic field driver. *Space Weather*, **15**. (Cited on pages 5 and 10.)

MALONEY, S. & GALLAGHER, P. (2010). Solar Wind Drag and the Kinematics of Interplanetary Coronal Mass Ejections. *The Astrophysical Journal Letters*, **24**. (Cited on page 15.)

MARSHALL, R.A., DALZELL, M., WATERS, C.L., GOLDTHORPE, P. & SMITH, E. (2012). Geomagnetically induced currents in the New Zealand power network. *Space Weather*, **10**, 1–13. (Cited on pages 5 and 47.)

MARSHALL, R.A., GORNIAK, H., VAN DER WALT, T., WATERS, C., SCIFFER, M., MILLER, M., DALZELL, M., DALY, T., POUFERIS, G., HESSE, G. & WILKINSON, P. (2013). Observations of geomagnetically induced currents in the Australian power network. *Space Weather*, **11**, 6–16. (Cited on pages 5 and 64.)

MATANDIROTYA, E., CILLIERS, P.J. & VAN ZYL, R. (2015). Differential magnetometer method (DMM) for the measurement of geomagnetically induced currents (GIC) in a power line: technical aspects. *Journal of Electrical Engineering*, **66**, 50–53. (Cited on pages 10 and 182.)

MATANDIROTYA, E., CILLIERS, P.J., VAN ZYL, R.R., OYEDOKUN, D.T. & DE VILLIERS, J. (2016). Differential magnetometer method applied to measurement of geomagnetically induced currents in Southern African power networks. *Space Weather*, **14**, 221–232. (Cited on page 10.)

MCCLOSKEY, A., GALLAGHER, P. & BLOOMFIELD, D. (2010). Flaring Rates and the Evolution of Sunspot Group McIntosh Classifications. *Sol. Phys.*, **291**, 1711–1738. (Cited on page 17.)

MCFADDEN, P., MERRILL, R., MCELHINNY, M. & LEE, S. (1991). Reversals of the Earth's Magnetic Field and Temporal Variations of the Dynamo Families. *J. Geophys. Res.*, **96**, 3923–3933. (Cited on page 18.)

McKay, A. (2003). *Geoelectric Fields and Geomagnetically Induced Currents in the United Kingdom*. Ph.D. thesis, University of Edinburgh. (Cited on pages 5, 89, 90 and 91.)

McKay, A. & Whaler, K. (2006). The electric field in northern England and southern Scotland: implications for geomagnetically induced currents. *Geophys. J. Int.*, **167**, 613–625. (Cited on page 5.)

McLay, S.A. & Beggan, C.D. (2010). Interpolation of externally-caused magnetic fields over large sparse arrays using Spherical Elementary Current Systems. *Ann. Geophys.*, **28**, 1795–1805. (Cited on page 50.)

Menvielle, M., Papitashvili, N., Häkkinen, L. & Sucksdorff, C. (1995). Computer production of K indices: review and comparison of methods. *Geophys. J. Int.*, **123**, 866–886. (Cited on page 43.)

Miensopust, M., Queralt, P., Jones, A. & 3D MT modellers (2013). Magnetotelluric 3-D inversion- a review of two successful workshops on forward and inversion code testing and comparison. *Geophys. J. Int.*, **193**, 1216–1238. (Cited on page 84.)

Miensopust, M.P. (2010). *Multidimensional Magnetotellurics: A 2D case study and a 3D approach to simultaneously invert for resistivity structure and distortion paramaters*. Ph.D. thesis, National University Of Ireland, Galway. (Cited on pages 65 and 68.)

Moodley, N. & Gaunt, C.T. (2012). Developing a power transformer low energy degradation assessment triangle. In *IEEE Power and Energy Society Conference and Exposition in Africa: Intelligent Grid Integration of Renewable Energy Resources (PowerAfrica)*, 1–6. (Cited on page 10.)

Munoz, G. (2014). Exploring for Geothermal Resources with Electromagnetic Methods. *Surv. Geophys.*, **35**, 101–122. (Cited on page 64.)

Myllys, M., Viljanen, A., Rui, O.A. & Magne Ohnstad, T. (2014). Geomagnetically induced currents in Norway: the northernmost high-voltage power grid in the world,. *J. Space Weather Space Clim.*, **4**, 27. (Cited on pages 5, 111, 113, 118 and 128.)

Naidu, G. (2012). *Deep Crustal Structure of the Son-Narmada-Tapti Lineament, Central India*. Springer Press, New York, USA. (Cited on pages 65, 67 and 68.)

Nevanlinna, H. (2005). A study on the great geomagnetic storm of 1859: Comparisons with other storms in the 19th century. *Adv. Space Res.*, **38**, 180–187. (Cited on page 3.)

Newman, G., Lindsey, N., Gasperikova, E., Bertrand, E. & Caldwell, T. (2015). The importance of full impedance tensor analysis for 3D magnetotelluric imaging the roots of high temperature geothermal systems: application to the Taupo Volcanic Zone, New Zealand. *Proceedings World Geothermal Congress*. (Cited on pages 83 and 174.)

Ngwira, C.M., McKinnell, L. & Cilliers, P.J. (2011). Geomagnetic activity indicators for geomagnetically induced current studies in South Africa. *Adv. Space Res.*, **48**, 529–534. (Cited on page 5.)

NOAA (2003). *Service Assessment: Intense Space Weather Storms October 19-November 07*. (Cited on pages 17 and 165.)

NOVER, G. (2005). Electrical properties of crustal and mantle rocks- a review of laboratory measurements and their explanation. *Surveys in Geophysics*, **26**, 593–651. (Cited on page 64.)

OGAYA, X., LEDO, J., QUERALT, P., MARCUELLO, A. & QUINTA, A. (2013). First geoelectrical image of the subsurface of the Hontomin site (Spain) for CO2 geological storage: A magnetotelluric 2D characterization. *International Journal of Greehouse Gas Control*, **13**, 168–179. (Cited on page 64.)

OGAYA, X., QUERALT, P., LEDO, J., MARCUELLO, A., QUINTA, A. & JONES, A. (2014). First geoelectrical image of the subsurface of the Hontomin site (Spain) for CO2 geological storage: A 3D magnetotelluric characterization. *International Journal of Greehouse Gas Control*, **27**, 120–138. (Cited on page 64.)

OHMI, T., KOJIMA, M., TOKUMARU, M., FUJIKI, K. & HAKAMADA, K. (2004). Origin of the slow solar wind. *Adv. Space Res.*, **33**, 689–695. (Cited on page 14.)

OLSEN, N. & CLAUDIA, S. (2016). Magnetic Signatures of Ionospheric and Magnetospheric Current Systems During Geomagnetic Quiet Conditions - An Overview. *Space Sci. Rev.*, **206**, 5–25. (Cited on page 20.)

OUGHTON, E., SKELTON, A., HORNE, R., THOMSON, A. & GAUNT, C. (2017). Quantifying the daily economic impact of extreme space weather due to failure in electricity transmission infrastructure. *Space Weather*, **15**, 1–19. (Cited on page 4.)

OUGHTON, E. *et al.* (2016). Helios Solar Storm Scenario. *Cambridge Risk Framework series; Centre for Risk Studies*. (Cited on page 4.)

PARKER, E. (1965). Dynamical Theory of the Solar Wind. *Space Science Reviews*, **4**, 666–708. (Cited on page 14.)

PAYNTER, R.T. & TOBY-BOYDELL, B.J. (2011). *Introduction to Electricity*. Pearson Publishing, London, UK. (Cited on page 5.)

PETIAU, G. & DUPIS, A. (1980). Noise temperature coefficient and long-time stability of electrodes for telluric observations. *Geophys. Prosp.*, **28**, 792–804. (Cited on page 32.)

PHILLIPS, K. (1992). *Guide to the Sun*. Cambridge University Press, Cambridge, UK, 1st edn. (Cited on pages 14, 15 and 16.)

PIRJOLA, R. (1985). On currents induced in power transmission systems during geomagnetic variations. *IEEE Trans. Power App. Syst*, 10. (Cited on pages 75 and 97.)

PIRJOLA, R. (2000). Geomagnetically induced currents during magnetic storms,. *IEEE Trans. Plasma Sci*, **28**, 1867–1873. (Cited on pages 2 and 5.)

PIRJOLA, R. (2002). Review on the calculation of surface electric and magnetic fields and of geomagnetically induced currents in ground-based technological systems,. *Surv. Geophys.*, **23**, 71–90. (Cited on pages 10 and 100.)

PIRJOLA, R. (2005). Effects of space weather on high-latitude ground systems. *Adv. Space Res.*, **36**, 2231–2240. (Cited on pages 102 and 103.)

PIRJOLA, R. & VILJANEN, A. (1998). Complex image method for calculating electric and magnetic fields produced by an auroral electrojet of finite length,. *Ann. Geophys.*, **16**, 1434. (Cited on page 25.)

PRICE, A. (1949). The induction of electric currents in non-uniform sheets and shells. *Q. J. Mech. appl. Math*, **2**, 283–310. (Cited on page 90.)

PULKKINEN, A., VILJANEN, A., PAJUNPÄÄ, K. & PIRJOLA, R. (2001). Recordings and occurrence of geomagnetically induced currents in the Finnish natural gas pipeline network. *J. Appl. Geophys.*, **48**, 219–231. (Cited on page 5.)

PULKKINEN, A., AMM, O., VILJANEN, A. & BEAR WORKING GROUP (2003a). Ionospheric equivalent current distributions determined with the method of spherical elementary current systems. *J. Geophys. Res.*, **108**, 1053. (Cited on page 50.)

PULKKINEN, A., AMM, O., VILJANEN, A. & BEAR WORKING GROUP (2003b). Separation of the geomagnetic variation field on the ground into external and internal parts using the spherical elementary current system method. *Earth Planets Space*, **55**, 117–129. (Cited on page 50.)

PULKKINEN, A., LINDAHL, S., VILJANEN, A. & PIRJOLA, R. (2003c). Geomagnetic storm of 29-31 October 2003: Geomagnetically induced currents and their relation to problems in the Swedish high-voltage power transmission system. *J. Geophys. Res.*, **108**, 1053. (Cited on pages 5, 165 and 166.)

PULKKINEN, A., PIRJOLA, R. & VILJANEN, A. (2008). Satistics of extreme geomagnetically induced currents. *Space Weather*, **6**. (Cited on page 175.)

PULKKINEN, A., BERNABEU, E., EICHNER, J., BEGGAN, C. & THOMSON, A. (2012). Generation of 100-year geomagnetically induced current scenarios. *Space Weather*, **10**. (Cited on page 169.)

PULKKINEN, A. *et al.* (2017). Geomagnetically induced currents: Science, engineering and applications readiness. *Space Weather*, **15**, 1053. (Cited on pages 4 and 8.)

RAO, C.K., JONES, A.G., MOORKAMP, M. & WECKMANN, U. (2014). Implications for the lithospheric geometry of the Iapetus suture beneath Ireland based on electrical resistivity models from deep-probing magnetotelluric. *Geophys. J. Int.*, **198**, 737–759. (Cited on pages 35 and 86.)

REAY, S.J., CLARKE, E. & HAMILTON, B. (2011). First Steps Towards K Indices from South Atlantic Observatories: Port Stanley Observatory. *Data Science Journal*, **10**, 117–129. (Cited on pages 42 and 43.)

RISHBETH, H. (1988). Basic physics of the ionosphere: a tutorial review. *IEREJ*, **58**, 207–223. (Cited on page 20.)

ROTHWELL, P. & MCILWAIN, C. (1960). Magnetic Storms and the Van Allen Radiation Belts-Observations from Satellite 1958ϵ (Explorer IV). *J. Geophys. Res.*, **65**, 799–805. (Cited on page 19.)

RUSSELL, C. (1993). Planetary Magnetospheres. *Rep. Prog. Phys.*, **56**, 687–732. (Cited on page 19.)

RYAN, J.M., LOCKWOOD, J. & DEBRUNNER, H. (2000). Solar Energetic Particles. *Space Science Reviews*, **93**, 33–53. (Cited on page 18.)

SABINE, E. (1852). On Periodical Laws Discoverable in the Mean Effects of the Larger Magnetic Disturbances. No. II. *phil. Trans. R. Soc. Lond.*, **142**, 103–124. (Cited on page 27.)

SCHRIJVER, C. & SISCOE, G. (2010). *Heliophysics II Space Storms and Radiation: Causes and Effects*. Cambridge University Press, Cambridge, UK. (Cited on pages 16 and 22.)

SCHRIJVER, C.J. (2009). Driving major solar flares and eruptions: A review. *Adv. in Space Res.*, **43**, 739–755. (Cited on page 16.)

SCHRIJVER, C.J., DOBBINS, R., MURTAGH, W. & PETRINEC, S.M. (2014). Assessing the impact of space weather on the electric power grid based on insurance claims for industrial electrical equipment. *Space Weather*, **10**, 488–498. (Cited on page 4.)

SCHUBERT, G., ROMANOWICZ, B. & DZIEWONSKI, A. (2015). *Treatise on Geophysics Volume 1: Deep Earth Seismology*. Elsevier Academic Press, Massachusetts, USA, 1st edn. (Cited on pages 20 and 21.)

SCOTT, D. (2015). Birkeland Currents: A Force-Free Field Aligned Model. *Progress in Physics*, **11**, 167–179. (Cited on page 20.)

SEKI, K., HIRAHARA, M., HOSHINO, M., TERASAWA, T., ELPHIC, R., SAITO, Y., MUKAI, T., HAYAKAWA, H., KOJIMA, H. & MATSUMOTO, H. (2003). Cold ions in the hot plasma sheet of Earth's magnetotail. *Nature*, **422**, 589–592. (Cited on page 19.)

SIMPSON, F. & BAHR, K. (2005). *Practical Magnetotellurics*. Cambridge University Press, Cambridge, UK. (Cited on pages 65, 67, 74, 75 and 84.)

SIRIPUNVARAPORN, W., EGBERT, G. & LENBURY, Y. (2002). Numerical accuracy of magnetotelluric modeling: A comparison of finite difference approximations. *Earth Planets Space*, **54**, 721–725. (Cited on page 84.)

SISCOE, G., CROOKER, N.U. & CLAUER, C. (2006). Dst of the Carrington storm of 1859. *Adv. Space Res.*, **38**, 173–179. (Cited on pages 3 and 47.)

ST-LOUIS, B. (2012). INTERMAGNET Technical Reference Manual. *INTERMAGNET*, **1**, 1–100. (Cited on page 28.)

STANKOV, S., STEGEN, K. & WARNANT, R. (2010). Local Operational Geomagnetic Index K Calculation (K-LOGIC) from digital ground-based magnetic measurements, operational manual. *Royal Meteorological Institute*, **1**, 1–32. (Cited on page 44.)

STEGENA, L. (1976). Electric Conductivity Structure and Geothermal Resevoirs. *Acta Geodaet. Geophys et Montanist. Acad. Sci. Hung.*, **3**, 377–397. (Cited on page 64.)

STEPHEN, J., GOKARN, S., MANOJ, C. & SINGH, S. (2003). Effects of galvanic distortions on magnetotelluric data: Interpretation and its correction using deep electrical data. *Journal of Earth System Science*. (Cited on page 86.)

STEPHENSON, F., WILLIS, D. & HALLINAN, T. (2004). The earliest datable observation of the aurora borealis. *Astronomy & Geophysics*, **45**, 615–617. (Cited on page 2.)

STERN, D. (2002). A Millenium of Geomagnetism. *Reviews of Geophysics*, **4**, 1–30. (Cited on page 27.)

STERNBERG, B., WASHBURNE, J. & PELLERIN, L. (1988). Correction for the static shift in magnetotellurics using tansient electromagnetic soundings. *Geophysics*, **53**. (Cited on page 86.)

STRACK, K. (2012). Future Directions of Electromagnetic Methods for Hydrocarbon Applications. *Surv. Geophys.*, **35**, 157–177. (Cited on page 64.)

STREICH, R. (2016). Controlled-Source Electromagnetic Approaches for Hydrocarbon Exploration and Monitoring on Land. *Surv. Geophys.*, **37**, 47–80. (Cited on page 64.)

TEMMER, M., ROLLETT, T., MÖSTL, C., VERONIG, A., VRSNAK, B. & ODSTRCIL, D. (2015). Influence of the ambient solar wind flow on the propagation behavior of interplanetary coronal mass ejections. *The Astrophysical Journal*, **743**. (Cited on page 15.)

THÉBAULT, E., FINLAY, C. & TOH, H. (2015). Preface: International Geomagnetic Reference Field-the twelfth generation. *Earth, Planets and Space*, **67**, 1–4. (Cited on page 27.)

THOMSON, A.W.P., MCKAY, A.J., CLARKE, E. & REAY, S.J. (2005). Surface electric fields and geomagnetically induced currents in the Scottish Power grid during the 30 October 2003 geomagnetic storm,. *Space Weather*, **3**, S11002. (Cited on pages 5, 90, 93, 165 and 166.)

THOMSON, A.W.P., DAWSON, E. & REAY, S. (2011). Quantifying extreme behaviour in geomagnetic activity. *Space Weather*, **9**. (Cited on pages 169, 170, 176 and 181.)

TORTA, J.M., MARSAL, S. & QUINTANA, M. (2014). Assessing the hazard from geomagnetically induced currents to the entire high-voltage power network in Spain,. *Earth, Planets and Space*, **66**, 87. (Cited on pages 5, 64, 75, 111, 113, 118, 122, 129, 139, 166 and 169.)

TORTA, J.M., MARCUELLO, A., CAMPANYÀ, J., MARSAL, S., QUERALT, P. & LEDO, J. (2017). Improving the modeling of geomagnetically induced currents in Spain. *Space Weather*, **15**, 691–703. (Cited on pages 5, 64 and 156.)

TRIVEDI, N., VITORELLO, I., WANDERLI, D., L.G., S., PADILHA, A., BOLOGNA, M., DE PADUA, M., SOARES, A., LUZ, G., PINTO, F., PIRJOLA, R. & VILJANEN, A. (2007). Geomagnetically induced currents in an electric power transmission system at low latitudes in brazil: A case study. *Space Weather*, **5**. (Cited on page 5.)

TURNBULL, K. (2011). *A study of geomagnetically induced currents in the UK national grid*. Ph.D. thesis, Lancaster University, Lancaster, UK. (Cited on pages 113, 118, 129 and 166.)

VARENTSOV, V., IV.M. AMD KULIKOV, YAKOLEV, A. & YAKOLEV, D. (2013). Possibilities of Magnetotelluric Methods in Geophysical Exploration for Ore Minerals. *Physics of the Solid Earth*, **49**, 309–328. (Cited on page 64.)

VASSEUR, G. & WEIDELT, P. (1977). Bimodal electromagnetic induction in non-uniform thin sheets with an application to the northern Pyrenean induction anomaly,. *Geophys. J. R. astr. SOC.*, **51**, 669–690. (Cited on pages 25, 89, 90 and 91.)

VILJANEN, A. & PIRJOLA, R. (1994). Geomagnetically induced currents in the Finnish high-voltage power system,. *Surv. Geophys.*, **15**, 383–408. (Cited on pages 10, 64, 100 and 144.)

VILJANEN, A., PULKKINEN, A., AMM, O., PIRJOLA, R., KORJA, T. & BEAR WORKING GROUP (2004). Fast computation of the geoelectric field using the method of elementary current systems and planar Earth models. *Ann. Geophys.*, **22**, 101–113. (Cited on page 5.)

VILJANEN, A., PIRJOLA, R., WIK, M., ADAM, A., PRASCER, E., SAKHAROV, Y. & KATKALOV, K. (2012). Continental scale modelling of geomagnetically induced currents. *J. Space Weather Space Clim.*, **2**. (Cited on pages 64 and 166.)

WANG, L. & LILLEY, F. (1999). Inversion of magnetometer array data by thin-sheet modelling. *Geophys. J. Int.*, **137**, 128–138. (Cited on page 90.)

WEAVER, J. (1994). *Mathematical Methods for Geo-Electromagnetic Induction*. Wiley Publishing, New Jersey, USA, 1st edn. (Cited on pages 89, 91 and 93.)

WEI, L.H., HOMEIER, N. & GANNON, L. (2013). Surface electric fields for North America during historical geomagnetic storms. *Space Weather*, **11**, 451–462. (Cited on page 64.)

WIK, M., VILJANEN, A., PIRJOLA, R., PULKKINEN, A., WINTOFT, P. & LUNDSTEDT, H. (2008). Calculation of geomagnetically induced currents in the 400 kV power grid in southern Sweden,. *Space Weather*, **6**, 7005. (Cited on pages 5 and 64.)

WILLIS, D., VAQUERO, J. & STEPHENSON, F. (2009). Early observation of the aurora australis: AD 1640. *A&G*, **50**, 20–24. (Cited on page 2.)

YERMOLAEV, Y., YERMOLAEV, M., ZASTENKER, G., ZELENYI, L., PETRUKOVICH, A. & SAUVAUD, J. (2005). Statistical studies of geomagnetic storm dependencies on solar and interplanetary events: a review. *Planetary and Space Science*, **53**, 189–196. (Cited on page 16.)

YOSHINO, T. (2010). Laboratory Electrical Conductivity Measurement of Mantle Minerals. *Surv. Geophys.*, **31**, 163–206. (Cited on page 64.)

ZHANG, J.J., WANG, C., SUN, T.R., LIU, C.M. & WANG, K.R. (2015). GIC due to storm sudden commencement in low-latitude high-voltage power network in China: Observation and Simulation,. *Space Weather*, **13**, 643–655. (Cited on pages 5 and 64.)

ZOIS, I. (2013). Solar activity and transformer failures in the Greek national electric grid. *J. Space Weather Space Clim.*, **3**. (Cited on page 5.)